To Yan & Taige

for your patience, suffering and love ···

Search for the Standard Model Higgs Boson and Study of the Scaling Property of QCD Dynamical Fluctuations at LEP

Doctoral Dissertation

to obtain the degree of doctor
from the University of Nijmegen,
according to the decision of the Council of Deans
to be defended in public
on Monday, November 11, 2002,
at 3.30 pm

by

Yuan Hu

born on January 4, 1967 in Huarong, China.

Search for the Standard Model Higgs Boson and Study of the Scaling Property of QCD Dynamical Fluctuations at LEP

Een wetenschappelijke proeve op het gebied
van de Natuurwetenschappen, Wiskunde en Informatica.

Proefschrift

ter verkrijging van de graad van doctor
aan de Katholieke Universiteit Nijmegen,
volgens besluit van het College van Decanen
in het openbaar te verdedigen
op maandag 11 november 2002,
des namiddags om 3.30 uur precies,

door

Yuan Hu

geboren op 4 januari 1967 te Huarong, China.

Promotor:	Prof. Dr. S.J. de Jong	
	Prof. Dr. E.W. Kittel	
Co-promotor:	Dr.Ir. D.J. Schotanus	
Manuscriptcommissie:	Dr. G.G. Bobbink	(NIKHEF)
	Prof. Dr. P. Duinker	(NIKHEF)
	Prof. L.S. Liu	(Huazhong Normal University, China)
	Dr. W.J. Metzger	(Katholieke Universiteit Nijmegen)
	Prof. Dr. C.G. Tully	(Princeton University, USA)

Front cover: A candidate event of the Higgs-strahlung process with decay channel HZ$\rightarrow$ $q\bar{q}e^+e^-$.

Het werk beschreven in dit proefschrift maakt deel uit van het onderzoeksprogramma van de Stichting voor Fundamenteel Onderzoek der Materie (FOM), die financieel wordt ondersteund door de Nederlandse Organisatie voor Wetenschappelijk Onderzoek (NWO).
The author was financially supported by the "Stichting voor Fundamenteel Onderzoek der Materie (FOM)", which is part of the "Nederlandse Organisatie voor Wetenschappelijk Onderzoek (NWO)".

ISBN 90-9016184-8

Contents

Preface

As the only creature under heaven that is gifted with the ability to reason, man has been, for many centuries, fascinated by questions as: why does the universe exist like it is and what is it made up of?

Ancient Chinese philosophers believed that the world was made of five elements: metal, wood, water, fire and earth. Their interactions (production and elimination) display what the world looks like. Likewise, ancient Indians chose another five fundamentals: space, earth, air, fire and water. Similar thoughts were developed by the ancient Greeks. Democritus (about 400 B.C.) argued that everything consists of the smallest indivisible pieces called "atoms" – fire is made of fire-atoms, wood is made of wood-atoms. This might be regarded as the earliest particle physics, which, as a unique discipline , tries to address the fundamental questions of the physical world: What are the building blocks (so called fundamental particles) of this world? How do they interact with each other? Why do they interact that way?

From the 18th century, chemistry was actively studied and developed. Scientists found that all of the matter in the world is composed of a number of chemical elements, *i.e.*, atoms (which is not of Democritus's kind). Between 1869 and 1871, Dimitri Mendeleyev successfully grouped atoms into what we call the Periodic Table. The mere fact that there are more than 100 kinds of atoms categorized in an orderly way in the Periodic Table strongly suggests that these elements are not the fundamental (meaning, indivisible) particles. Then, Thompson discovered the electron in 1897, and Rutherford showed in 1911, from his experiment in which α particles were scattered off gold foils, that the atoms had a small, heavy and positively charged nucleus centered in a small core surrounded by electrons which are bound to the nucleus by the electro-magnetic force. Soon afterwards, Bohr built a mathematical description of the atom using Planck's theory of quantization of energy. In his model, electrons move around the nucleus in fixed orbits and can only switch between orbits when a certain discrete amount of energy is absorbed or emitted. This amount of energy is the energy of a photon of a specific wavelength. By the late 1920's, with the development of quantum mechanics and more experiments, physicists generally agreed that the nucleus consisted of two kinds of nucleons: the proton, which has one unit of positive charge, found by Rutherford in 1919, and the neutron, a neutral counterpart of the proton predicted by Heisenberg and finally discovered by Chadwick in 1932. Protons and neutrons in a nucleus are bound by a strong force than can overcome the repulsive electric force of the protons.

The existence of the positron, as an anti-particle of the electron with the same mass but opposite electric charge, was predicted by Dirac in 1928 and established experimentally in 1933. In 1938, the muon which has the same electromagnetic property as the electron but is about 206 times heavier was found in cosmic rays. The energy loss problem in radioactive β decay was solved by Fermi, by assuming a new particle called the neutrino, that later in 1947 was observed in cosmic ray experiments.

Just when physicists thought that they finally had found all the building blocks of the world namely the electron, proton, neutron, photon, muon and neutrino, the study of cosmic rays and the nuclear force led to the inference of new elementary particles which were not needed to build known matter. This led to the construction of particle accelerators and the subsequent observation of many hundreds of new particles which interact strongly like the proton, neutron. These particles are called "hadrons" and were further divided into "mesons" with integer spin and "baryons" with half-integer spin. All these discoveries suggested that there was something more fundamental.

Just as experimental particle physics was making great progress, so was theoretical physics. Dirac, Schwinger, Feynman, *et al.*, incorporated Einstein's relativity into quantum mechanics and developed so-called Quantum ElectroDynamics (QED). Yang and Mills constructed what was later called a gauge theory as the foundation of modern quantum field theory. In 1964, Gell-Mann and Zweig put forth the static quark model. They postulated that the mesons and baryons consisted of three types of quarks: up, down and strange. The model beautifully simplified and organized the meson and baryon spectra. By that time, four types of fundamental forces were known: the well-understood electromagnetic force explains the interaction between electrons and the nucleus. The strong force describes the interactions between nucleons and the stability of the nucleus, the weak force results in the decay of heavy nuclei, and the gravitational force happens on every massive body. The notion that not just electromagnetism but all forces could be interpreted as the result of exchange of virtual gauge boson quanta got confirmed, the gluon and the intermediate bosons W and Z bosons became for the strong and the weak force, respectively, what the photon was to the electromagnetic one. In 1967, Weinberg and Salam proposed a theory that unified electromagnetic and weak forces and predicted the existence of massive and weakly interacting gauge bosons: $W^{\pm}$ and Z, for which, the so-called Higgs mechnism and Higgs boson were introduced into this theory. Insight in the dynamics of the gluon exchange led to Quantum ChromoDynamics (QCD). The subsequent unification of the electroweak and the strong forces results in what is presently known as the Standard Model.

In 1968, there came another experimental breakthrough. At the Stanford Linear Accelerator Center (SLAC), physicists found dynamical evidence of quarks inside the proton and the neutron. Later, more quarks were discovered: charm in 1974, bottom in 1977 and top in 1995. Next to the electron and the muon, the third lepton called the tau lepton was discovered in 1975. The first evidence of a gluon was observed in 1979 at Deutsches Elektronen-SYnchrotron laboratory (DESY). The $W^{\pm}$ and Z bosons were discovered in 1983 at the European Organization for Nuclear Research (CERN), which was a major triumph for the Standard Model. So far, six types (flavors) of quarks (up, down, charm, strong, bottom, top) each in three colors (blue, green and red), three types of leptons (electron, muon, tau, together with their three massless counterparts: neutrinos) and four interaction-intermediators (photon, $W^{\pm}$, Z and gluon) were found and considered as the fundamental particles. The Standard Model, especially its electroweak sector, has been extensively tested and found to be extremely successful in describing the properties of these particles and their interactions over a wide range of energies.

However, the Standard Model is still incomplete and a lot of problems must still be solved. One of the most important flaws is that the Higgs boson is still missing experimentally. The Higgs boson is needed in the Standard Model to give masses to the particles, in particular also to the massive gauge bosons: $W^{\pm}$, Z. Without the Higgs boson, the Standard Model would give an incorrect interpretation to the particles and their interaction. Currently, the search for the Standard Model Higgs boson is one of the hottest topics in particle physics.

Experiment not only tests theory. Experimental phenomena and results also spur the development of theory, and may even bring about a new theory. Quantum ChromoDynamics

(QCD) is the theory of strong interaction. The strong interactions, especially the way in which quarks and gluons combine to form the colorless hadrons that are observed, are still not well understood and described quantitatively within the framework of QCD. Thus, QCD is far from being precisely tested by experiements. More regularities are expected to be ruled out from experiments to get a deeper understanding of strong interactions. This is also a very important task of experimental particle physics.

The Large Electron Positron Collider (LEP) at CERN was a very good place to search for the Higgs boson, as well as to study QCD properties, by providing high center-of-mass energy e^+e^- collisions in an experimentally “clean” environment.

This thesis will discuss two topics: searches for the Standard Model Higgs boson and study of the scaling property of QCD dynamical fluctuations, using data collected with the L3 detector at LEP. The outline of this thesis is as follows: Chapter 1 describes the LEP collider and the L3 detector, the other chapters are divided into two parts. The first part will discuss the searches for the Standard Model Higgs boson. In Chapter 2, the electroweak section of the Standard Model and Higgs boson are introduced. Then the main analysis methods used for the Higgs search are discussed in Chapter 3, and the analysis strategy and corresponding results are presented in Chapter 4. Chapter 5 will give the combined results on the Higgs search. Finally, the prospects of future Higgs searches after LEP will be discussed in Chapter 6. The second part of this thesis will discuss the scaling property of dynamical fluctuations in QCD. The relevant conception and analysis tools will be discussed, after a short introduction of QCD, in Chapter 7. Chapter 8 will discuss the selection of hadronic events from Z decay. The analysis results will be presented in Chapter 9, and Chapter 10 will give the conclusions for part II. Finally, there will be a summary for this thesis.

Unless specified otherwise, all quantities used in this thesis are expressed in so-called natural units having $\hbar = c = 1$.

Chapter 1

LEP and L3

1.1 The LEP Collider

The Large Electron Positron (LEP) Collider [1], as part of CERN (European Organization for Nuclear Research), is located at the Swiss-French border (see Fig. 1.1) near the city of Geneva. The LEP-ring, with a circumference of 26.7 km, is housed in a tunnel, 50 to 150 m below the surface. It consists of eight circular and eight straight sections.

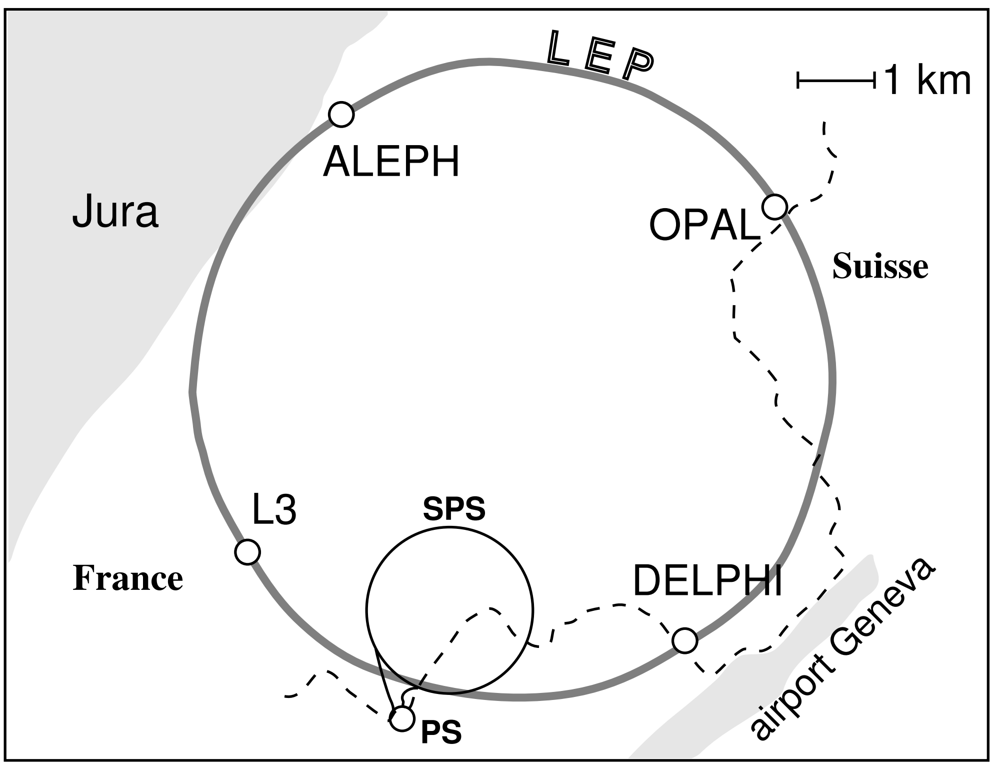

Figure 1.1: Schematic view of the **LEP** Collider.

In the LEP beam pipe, discrete packets (bunches or bunch trains) of electrons and positrons are accelerated and circulate in opposite directions. The injection of electrons and positrons into LEP is done in the following steps by four other accelerators. The LEP Injector Linacs (LIL) generate the electrons and positrons and accelerate them to 600 MeV. The Electron

Positron Accumulator (EPA) accumulates the electron and positron pulses into bunches. The bunches are injected into the Proton Synchrotron (PS) and accelerated to 3.5 GeV. The Super Proton Synchrotron (SPS) accelerates the bunches to 20 GeV and injects them into the LEP ring. The particle bunches are accelerated to the final beam energy in the LEP ring by radio-frequency (RF) cavities placed in two of the straight sections. These cavities, which provide up to 16 MW of power, are also used to replenish energy lost by synchrotron radiation when the bunches circulate in the ring. To keep the electrons and positrons in their orbits, 3304 dipole magnets, which produce a field of 0.048 T each, are installed in the curved sections, while focusing quadrupole and sextupole magnets are used to limit the lateral spread of the beams. The electrons and positrons are brought into collision at four interaction points (IP's) at four of the eight short straight sections in the LEP ring, where four large detectors: ALEPH [2], DELPHI [3], L3 [4–13] and OPAL [14] are installed, to register the particles which arise from the e^+e^- collisions, and measure their energy and momentum as well.

The collision rate in the interaction point divided by the interaction cross section is called the luminosity L, which, typically of the order of $10^{31}\text{cm}^{-2}\text{s}^{-1}$, is a function of LEP parameters such as the beam energy, the number of bunches, the current per bunch, the vertical beam-beam strength parameter, the single-turn frequency, and the focusing strength at the interaction point. Some of these parameters are difficult to measure precisely. The time integrated luminosity $\mathcal{L}$ can be more conveniently measured using small-angle Bhabha scattering ($e^+e^- \to e^+e^-$) as

$$\mathcal{L} = \int_0^T L\mathrm{d}t = \frac{N_{\text{Bhabha}}}{\sigma_{\text{Bhabha}}}, \tag{1.1}$$

because the Bhabha cross section, σ_{Bhabha}, can be accurately calculated for small scattering angles. Furthermore, Bhabha scattering has high rates at small angles. Here, N_{Bhabha} is the collected number of small-angle Bhabha events in time T.

The LEP collider was constructed to perform precision measurements of the electroweak interaction up to the center-of-mass energy about 200 GeV. This is achieved in two phases. In the first phase (1989-1995), LEP ran at center-of-mass energies around 91 GeV, close to the mass of the Z boson. The collected data were used for precise measurements of Standard Model parameters. From the fall of 1995 onwards, superconducting RF cavities were installed to raise the center-of-mass energy in steps to about 210 GeV. In 1996, the threshold for W^+W^- pair production was reached. In 2000, the highest energy, 210 GeV was attained. The collected data allow the precise measurement of important parameters such as mass, couplings and branching fractions of the $W^\pm$ bosons as well as the search for new particles.

The integrated luminosity delivered by LEP is shown as a function of time in Fig. 1.2. Detailed information on the LEP machine and its performance can be found in [1].

1.2 The L3 Detector

The L3 detector is located at IP 2 of the LEP ring, about 50 m underground. A perspective view of the detector is shown in Fig. 1.3. The design of the detector is optimised for precise energy measurement of muons, electrons and photons. The detector is installed inside a 7.8 kton octagonally shaped solenoidal magnet. The inner radius of this enormous magnet is 6 m and it is 12 m long. It provides a uniform field strength of 0.5 T which points along the direction of flight of the beam of electrons and is used to measure the momentum of charged particles as they traverse the volume of the detector.

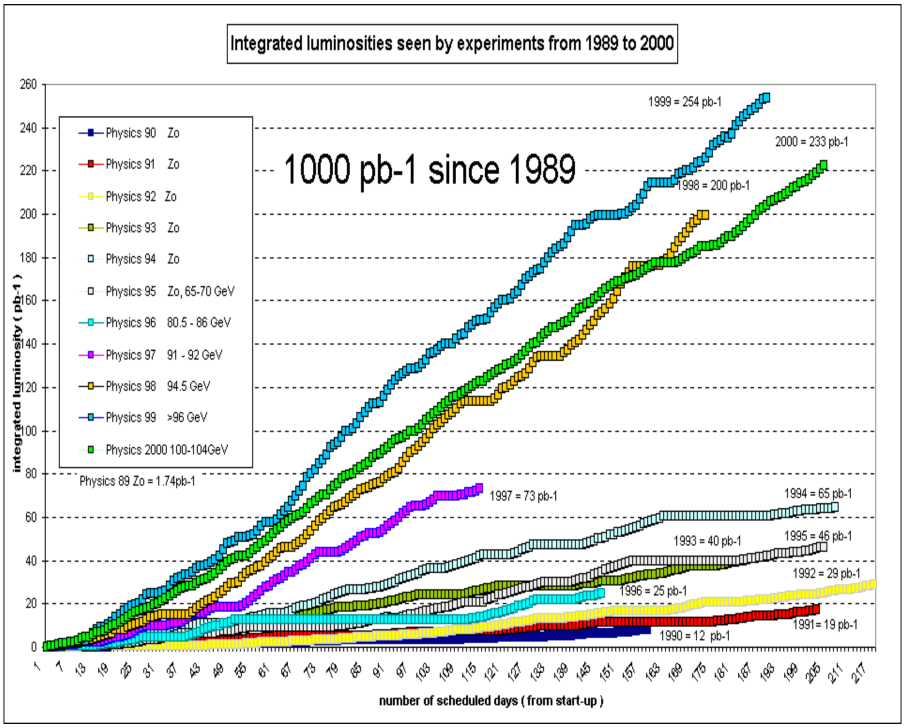

Figure 1.2: The averaged integrated luminosity delivered by LEP from 1989 to 2000.

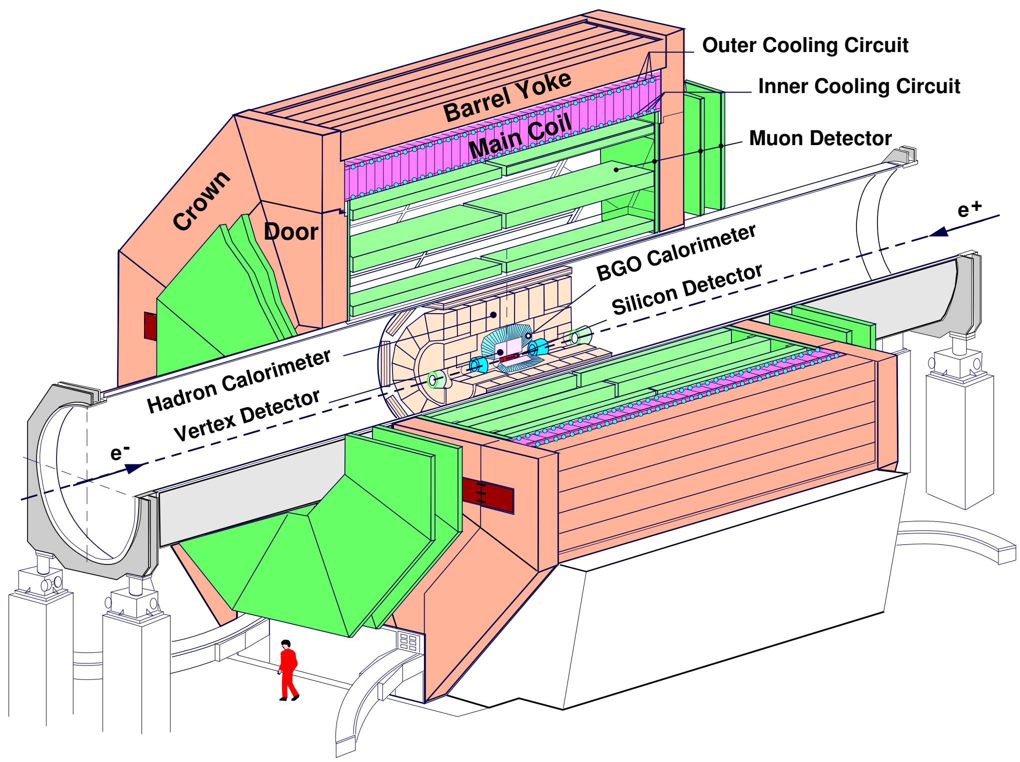

Figure 1.3: A perspective view of the L3 detector.

The right-handed L3 coordinate system is defined as follows. The origin is the geometric center of the detector, which is the interaction point of the colliding electron and positron beams. The x-axis points towards the center of the LEP ring, the y-axis points vertically upwards, the z-axis points along the direction of the electron beam. The distance between a point in the x-y plane and the geometric center of the detector is the radius r. The polar angle $\theta \in [0, \pi]$ is defined as the angle between the direction of a particle and the positive z-axis. The azimuthal angle $\phi \in [0, 2\pi]$ is that between the radius vector $\vec{r}$ and the positive x-axis.

The L3 detector is symmetric with respect to the interaction point and is divided into several specialized sub-detectors. From the inside out, the major components of the detector are:

- the Silicon Microvertex Detector (SMD) to measure accurately points along a charged particle's trajectory immediately outside the beam pipe,
- the Central Tracking Chambers consisting of a time expansion chamber (TEC) and the Z chambers to measure the curved trajectory of a charged particle bent by the magnetic field,
- the Electromagnetic Calorimeter (ECAL) to measure the energy of electrons and photons,
- the Hadron Calorimeter (HCAL) to measure the energy of hadronic particles, and
- the Muon Detector to measure the momenta of muons.

All of the subdetectors consist of a central part (the barrel) and a forward and backward part (the endcaps), except the SMD and the TEC which have only a barrel part. In the following sections, the major subdetectors will be discussed in more detail.

1.2.1 The Silicon Microvertex Detector

The Silicon Microvertex Detector (SMD) was installed in 1993. It is used to measure the charged particle positions close to the interaction point in order to resolve possible secondary vertices which arise from the decay of short-lived particles such as hadrons containing b quarks. This detector is directly attached to the beryllium beam pipe and made up of two cylindrical layers of double-sided silicon detector ladders, at radius 61.7 mm and 77.4 mm, respectively. The length of the SMD is 30 cm which covers the polar angle range $22^\circ \leq \theta \leq 158^\circ$. Each of the layers has 12 ladders which are made up of two electrically independent half-ladders. Each of the half-ladders consists of two 300 μm thin high resistivity n-type silicon wafers with microstrips of doped silicon on both the signal (p^+) and ohmic (n^+) surfaces. Electron-hole pairs created in the wafer by a traversing charged particle are collected on these strips. The strips on the signal and ohmic surfaces are orthogonal: one side measures the $r\phi$ coordinate and the other measures the z coordinate. The SMD can reach a position resolution of 7.5 μm in the $r\phi$ direction and 14.3 μm in the z direction. [15]

1.2.2 The Time Expansion Chamber and Z Chamber

The Time Expansion Chamber (TEC) and Z Chamber are used to reconstruct the trajectory (track) of a charged particle in $r - \phi$ (TEC) and z (Z Chamber). An xy-view of SMD, TEC, and Z Chamber is shown in Fig. 1.5.

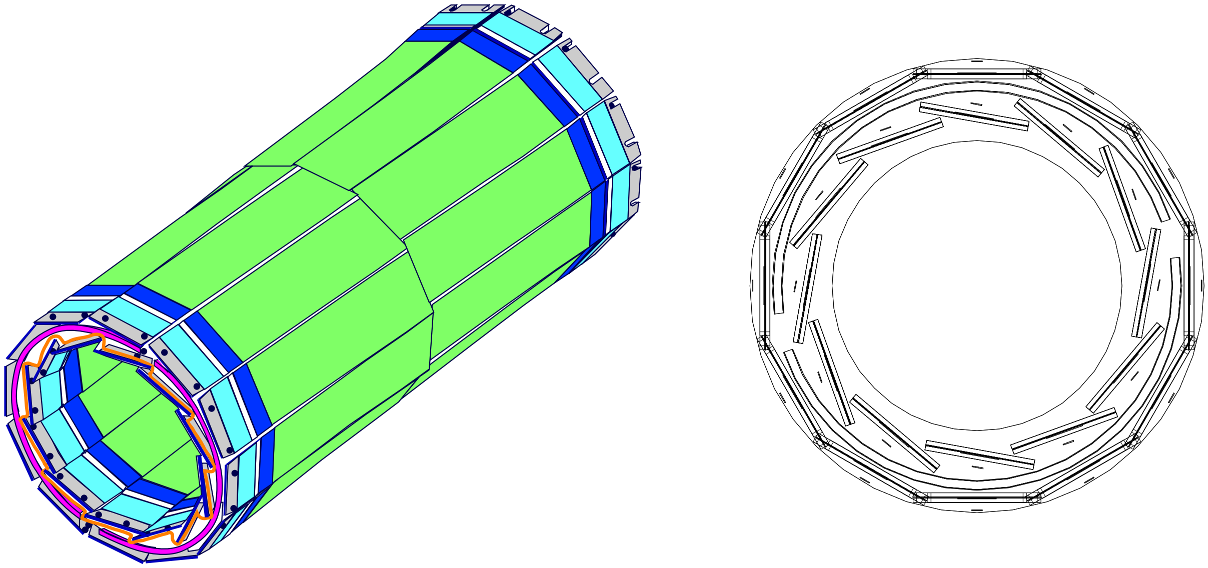

Figure 1.4: The Silicon Microvertex Detector. Left: 3-D view. Right: xy view.

The TEC consists of a closed gas volume with a gas mixture of 20% CO_2 and 80% Isobutane. Wires running parallel to the z-axis are kept at high voltage. Charged particles traversing the gas volume cause ionization of the gas atoms. While the positive ions drift to the negative cathode wires, the ionized electrons drift to the positive anode wires, where they cause an avalanche of secondary electrons which give a detectable signal. The average arrival time of the drift electrons is related to the distance at which the charged particle passed the wire. The amount of charge detected at the anodes is a measure of the energy loss of the particle in the TEC.

The TEC is subdivided into two parts: the inner TEC and the outer TEC. The inner TEC consists of 12 sectors in ϕ, each containing 8 anode wires. The outer TEC has 24 sectors, with 54 anode wires each, resulting in 62 anode wires over the full r-range. The inner and the outer radii of the TEC are 9.15 cm and 45.6 cm respectively. The length in z is 126 cm. Charge division wires, 2 in the inner TEC and 9 in the outer TEC, are read out on both sides, providing some z-information. Only a track with polar angle $44° < \theta < 136°$ can reach all 62 wires, while a track with $\theta < 10°$ or $\theta > 170°$ misses the TEC completely.

A particle with a polar angle between 42° and 138° will pass through the Z Chamber [8]. This detector supplements the measurements of TEC and SMD with a z coordinate at $r = 50$ cm. It consists of two cylindrical proportional wire chambers with cathode strip readout. The anode wires are aligned in the z direction. The two chambers contain two cathode layers each. The cathode layers are made of 240 strips with a pitch of 4.45 mm. The strips of two of the layers are arranged perpendicular to the z direction (z layer) and the strips of the other 2 layers run under a stereo angle of $\pm 60°$. The gas mixture consists of 80% argon, 16% CO_2, and 4% isobutane. A charged particle traversing the chamber ionizes the gas. The resulting electron avalanche around the anode wire induces image charges on the cathode layers. The relative amount of the signal measured on the individual cathode strips is used for the coordinate determination. The ϕ component of the stereo layer allows the matching of the cluster with a TEC track. The z layers are used for the measurement of the z coordinate. The resolution varies depending on the polar angle. At $\cos\theta = 0$ the resolution is about 0.2 mm whereas at $|\cos\theta| = 0.74$ the resolution is about 1 mm.

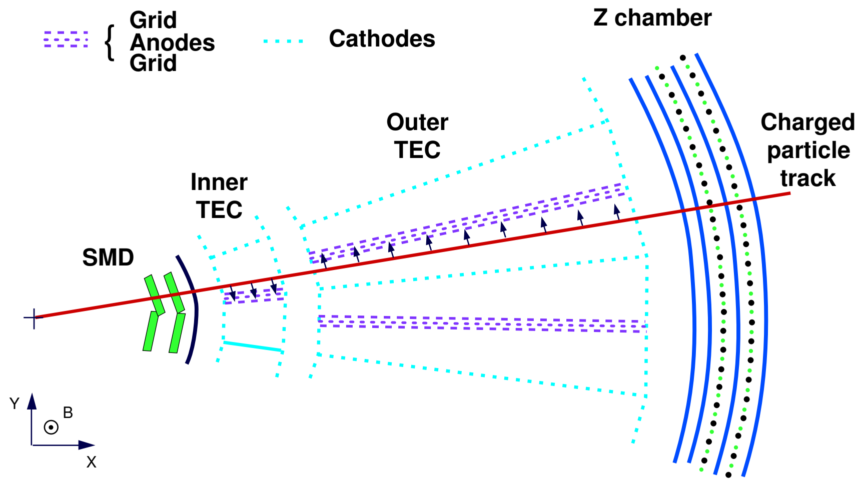

Figure 1.5: xy view of a section of the central tracking system: the SMD, the TEC and the Z-chamber.

1.2.3 The Electromagnetic Calorimeter

The Electromagnetic Calorimeter (ECAL) is designed to measure precisely the energy of electrons (positrons) and photons. It consists of 10734 Bismuth Germanium Oxide (BGO) crystals pointing to the interaction region. In dense matter, electrons with an energy of at least an order of magnitude higher than the electron mass lose energy primarily through Bremsstrahlung, while photons with such energies will interact through pair creation. These processes occur typically every radiation length (1.12 cm for BGO), resulting in an exponentially growing number of particles with smaller and smaller energies deeper in the material: an electromagnetic shower. This process continues until a critical energy (about 10 MeV for BGO) is reached. Below this energy, the electron energy loss is dominated by the ionization and excitation of the atoms in the crystal. This causes the atoms to emit green light, which is collected at the end of the crystals in photodiodes and converted into an electrical signal. For charged particles other than electrons, the critical energy is much higher, so that they only lose energy through ionization in the crystal. If such particles have an energy of about 1 GeV or higher, their energy loss becomes approximately independent of their initial energy, and they are called Minimum Ionizing Particles (MIPs). Hadronic particles lose a large part of their energy in a medium by nuclear interactions. These nuclear reactions can already take place inside the BGO, albeit with a much smaller probability than the Bremsstrahlung and pair-production processes for electrons/positrons and photons in the BGO. Therefore, hadrons will on average only lose a small fraction of their energy in the BGO.

The BGO crystals in the ECAL have a length of 24 cm, equivalent to 22 radiation lengths. The front face of each crystal is $2{\times}2$ cm^2 and the rear face is $3{\times}3$ cm^2. The barrel part covers the polar angle $42° < \theta < 138°$, and the endcap part covers the polar angle $11.6° < \theta < 36°$ and $144° < \theta < 168.4°$. The scintillation light of the BGO crystals is collected by two photodiodes which are mounted at the rear face of the crystals. The energy resolution is 5% at 100 MeV and less than 2% at energies larger than 1 GeV [16].

The gaps between the barrel and the endcap BGO crystals are filled with lead-scintillating fiber calorimeters (SPACAL). They consist of 24 modules (bricks) containing a lead structure

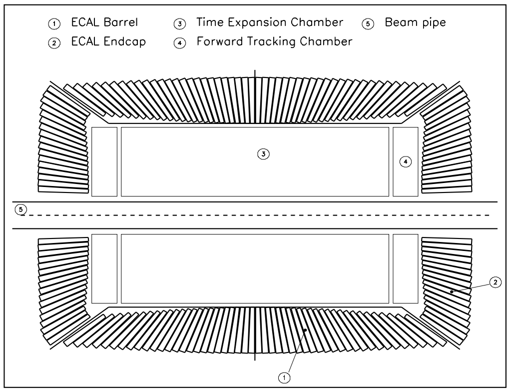

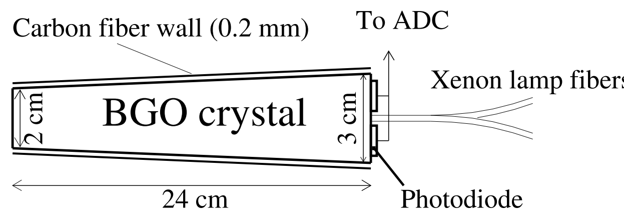

Figure 1.6: Left: the arrangement of the BGO crystals. Right: a BGO crystal.

filled with scintillating fibers. The scintillation light is collected by photodiodes glued onto the back end of the bricks. The resolution of the SPACAL is 15% at 45 GeV [11].

1.2.4 The Hadron Calorimeter

The Hadron Calorimeter (HCAL) is designed to measure the energy of hadrons. It consists of uranium absorber plates interspersed with proportional chambers, which act as the sampling medium. As in the case of the BGO calorimeter, it also consists of a barrel part (covering $35° < \theta < 145°$ region) and two endcap parts (covering $6° < \theta < 35°$ and $145° < \theta < 174°$ region). Both the barrel and endcap part cover the whole azimuthal angle. The barrel contains 9 rings with 16 modules. These modules consist of uranium absorber plates with a width of 5.5 mm interspersed with proportional chambers. There are in total 7968 chambers in the barrel part. The 2 endcaps are each built up of one outer and two inner rings. Each of these rings contains 12 modules. The hadronic jet energy resolution of HCAL is $(55/\sqrt{E} + 8)$ GeV. The direction of the jet axis can be measured with a resolution of about 2.5° [6].

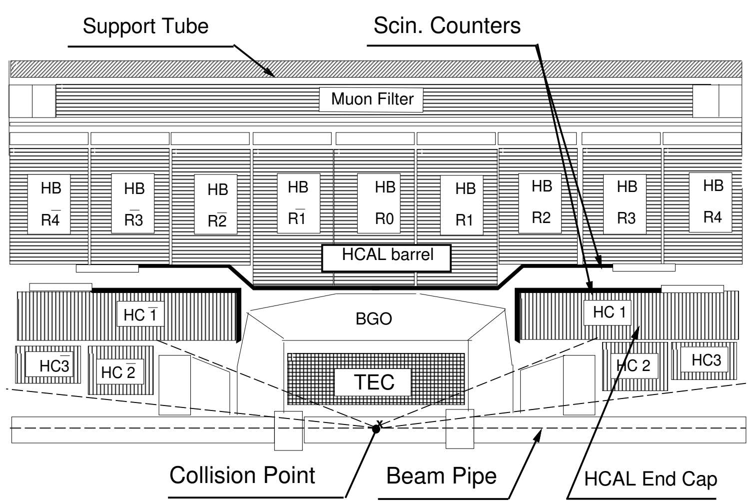

Figure 1.7: xz view of the structure of Hadron Calorimeter.

1.2.5 The Muon Detector

The muon detector consists of three layers of drift chambers, labeled from inside out as MI, MM, MO. It is used to measure muon momenta with high precision. The barrel part of the detector covers the polar angle range from 44° to 136° . It consists of two halves with a gap at $z = 0$. Each of the halves is subdivided into 8 octants, covering the whole azimuthal angle. Each octant consists of five drift chambers (P-chambers) which are arranged in three layers (see Fig. 1.8). The middle and outer layers are horizontally divided in two. The outer and inner chambers contain 16 wires each whereas the middle chambers are equipped with 24 wires. P-chambers are used to measure the muon track in the bending plane. To measure the muon track in the non-bending direction (z direction), so-called Z-chambers are mounted on both the inside and the outside of each MI and MO chambers. The design resolution for muons measured in all 3 layers is $\sigma_p/p \approx 2.5\%$ at 45 GeV [7, 13].

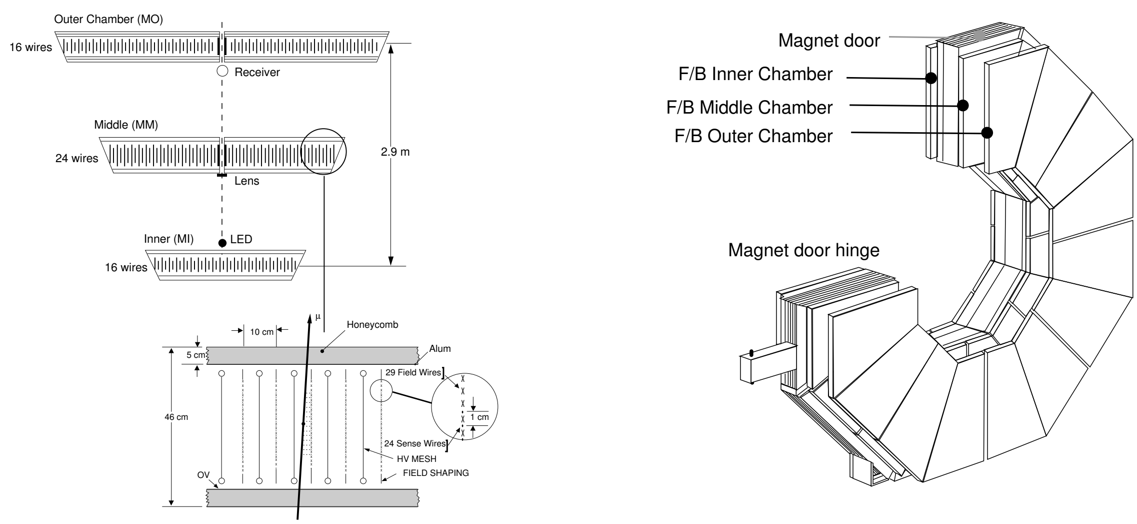

Figure 1.8: Left: The 3-layer structure of a muon octant in the barrel. Right: The forward-backward muon chambers.

The barrel part of the muon detector is complemented by a forward-backward spectrometer covering the polar angles $24° < \theta < 44°$ and $136° < \theta < 156°$. Three rings consisting of 16 drift chambers are attached to the magnet doors (Fig. 1.8). The magnet doors are wrapped with coils producing a toroidal magnetic field of 1.2 T.

1.2.6 Other Detector Components

Apart from the above major components, the L3 detector comprises several other important systems. The luminosity monitor [12] is mounted near the beam pipe in the very forward regions of the detector and is responsible for precisely measuring the luminosity delivered by the LEP accelerator by counting the number of small angle Bhabha scattering ($e^+e^- \rightarrow e^+e^-$) events. A series of large scintillating panels [17], installed between the HCAL and the ECAL, provide precise (<1 ns) timing information, which is used, among other things, to reject cosmic rays.

1.3 Trigger, Data Acquisition and Processing

The LEP beams collide at a rate of 45 kHz, but only some of the processes that take place are considered interesting physics. An efficient trigger system is responsible for making very fast decisions in between the beam crossings about whether or not to accept an event for further reconstruction. There are 3 trigger steps: level-1, level-2 and level-3 triggers [18]. This reduces the rate of events to about 5-10 Hz.

If the final trigger decision is positive, the digitized data from the various subdetectors are collected and built into one event by a FASTBUS based data acquisition system, and subsequently written to tape. A run is defined by the number of events that fit on a 200 MB tape (about 4500 events), the standard tape capacity at the start of LEP.

Afterwards, the data on the tape are processed by the L3 offline reconstruction program. Firstly, information from the databases such as calibration constants, alignment parameters, temperatures, and high voltages, is used to convert the digitized data to energy deposits, drift times, *etc.*. Secondly, the pattern recognition is performed for each subdetector. For example, crystal energies are converted to energy "bumps" (groups of BGO crystals containing energy deposits) and hits to tracks. Finally, tracks are matched to bumps in the ECAL and HCAL, and jet finding algorithms can be performed.

The data are stored in several formats. Candidate events for the luminosity calculation and events triggered by the Very Small Angle Tagger (VSAT) Bhabha trigger are sent to a separate event stream. The data format used for physics analysis, the DVN, contains only final objects such as tracks and energy bumps. The information of all individual channels of all subdetectors is kept on much larger tapes, which can be used to re-process the data if better calibrations or reconstruction software become available.

1.4 Detector Simulation

Monte Carlo (MC) simulation is needed to simulate the detector response to a given physics process, since this cannot be calculated with an analytical program.

Firstly, for a specific physics process, a number of events is randomly generated according to the distributions predicted by a theoretical model. This step is independent of the experimental setup, and is called generator level Monto Carlo.

The second step is to simulate the detector. The simulation program is based on the GEANT [19] and the GHEISHA [20] packages. It tracks the generated particles through the detector, taking into account their interaction cross sections with the detector materials and their lifetimes, thus mimicking as closely as possible the response of the real detector. The output of the simulation are TEC hits, energy deposits in calorimeters, *etc.*.

The third step, the reconstruction, is almost exactly the same as for real data. The trigger is also simulated. The data and the Monte Carlo events are stored in exactly the same format. Therefore, distributions can be easily compared, and the acceptance and efficiency can be calculated for a specific process.

Part I

Standard Model Higgs Boson Searches at LEP

Chapter 2

The Standard Model and the Higgs Boson

2.1 Introduction

The minimal theory of particle physics, the so-called Standard Model [21], describes the constituents of matter currently believed to be fundamental: quarks and leptons, and their interactions through three of the four basic forces: the electromagnetic, weak, and strong force. It was developed by Glashow, Weinberg, and Salam in the late 1960's and early 1970's, and has withstood nearly thirty years of experimental tests amazingly well. One of the most striking and convincing arguments in favor of this theory was the prediction of the heavy gauge bosons $W^{\pm}$ and Z, which were eventually observed by the UA1 and UA2 experiments at CERN [22,23].

Based upon Quantum Field Theory (QFT), the Standard Model is a gauge field theory which unifies the electromagnetic and weak interactions into an electroweak force via the gauge group $SU(2) \times U(1)$. The idea of gauge invariance is central to the Standard Model. The Standard Model Lagrangian density is required to be locally gauge invariant based upon the existence of conserved quantities in the interactions of fundamental particles. These gauge invariances give rise to the above mentioned three forces. The force carrying particles are represented by gauge boson fields. However, QFTs based on gauge invariance only accommodate massless gauge bosons. To keep agreement with the experimental evidence that there exist massive weak gauge bosons, the Higgs mechanism [24] is introduced into the Standard Model. This mechanism spontaneously breaks the gauge symmetries, leading to the existence of the Higgs boson. The fundamental particles acquire mass through their coupling to the Higgs field.

The fundamental particles and their properties are summarized in Tab. 2.1 (quarks and leptons which are fermions with spin $\frac{1}{2}$) and Tab. 2.2 (gauge bosons with spin 1).

The next sections give a cursory introduction to aspects of gauge symmetries, the Higgs mechanism and the Standard Model.

2.2 Symmetry and Gauge Invariance

The conserved quantities in the interactions of fundamental particles are associated with space-time or internal symmetries. The internal symmetries, which do not involve space-time, manifest themselves through interactions. An unmeasurable phase or set of phases corresponds to

Quarks			
Particle Name	Symbol	Electric Charge (e)	Mass GeV [25]
up	u	+2/3	0.0015 to 0.005
down	d	–1/3	0.003 to 0.009
charm	c	+2/3	1.1 to 1.4
strange	s	–1/3	0.060 to 0.170
top	t	+2/3	173.8 ± 5.2
bottom	b	–1/3	4.1 to 4.4

Leptons			
Particle Name	Symbol	Electric Charge (e)	Mass MeV [25]
electron	e	-1	0.51099907± 0.00000015
electron neutrino	ν_{e}	0	< 0.000015
muon	μ	-1	105.658389± 0.000034
muon neutrino	ν_μ	0	< 0.17
tau	τ	-1	$1777.05^{+0.29}_{-0.26}$
tau neutrino	ν_τ	0	< 18.2

Table 2.1: A summary of properties of quarks and leptons. Each of the particles has a corresponding antiparticle of opposite charge.

Gauge Bosons				
Force	Particle Name	Symbol	Electric Charge (e)	Mass GeV [25]
Electromagnetism	Photon	γ	0	0
Weak	W boson	$\mathrm{W}^{\pm}$	±1	80.41±0.10
Weak	Z boson	Z(or Z^0)	0	91.187±0.007
Strong	gluon	g	0	0

Table 2.2: A summary of properties of gauge bosons of the Standard Model.

each internal symmetry. A space-time independent transformation of the fermion fields with respect to this unobservable phase is expressed as

$$\psi(x) \to \psi'(x) = e^{-i\sum_j \tau_j \cdot \theta_j}\psi(x), \tag{2.1}$$

where $\tau_j (j = 1, 2, ..., N)$ are $n \times n$ matrix representations of the N generators of a group G of the internal symmetry, $\theta_j (j = 1, 2, ..., N)$ are a set of arbitrary phases, and $\psi(x)$ is a set of fields ($\psi_1(x)$,$\psi_2(x)$,..., $\psi_n(x)$) grouped together in a multiplet representation. This is called a global gauge transformation. If one considers, for instance, the Lagrangian of a free fermion with mass m:

$$\mathcal{L} = i\bar{\psi}\gamma^{\mu}\partial_{\mu}\psi - m\bar{\psi}\psi, \tag{2.2}$$

it appears that the global gauge transformation does not affect the Lagrangian describing the behavior of the fields. Since a conservation law exists for every continuous symmetry of a Lagrangian, fundamental particles possess conserved gauge charges.

However, the phase can be allowed to vary locally at different space-time coordinates, in which case the local gauge transformation can be expressed as

$$\psi(x) \rightarrow \psi'(x) = e^{-i\sum_j \tau_j \cdot \theta_j(x)}\psi(x), \tag{2.3}$$

where $\theta_j(x)$ is now dependent on space-time coordinates ($x = x^{\mu}$). However, the Lagarangian is not locally gauge invariant due to terms involving derivatives of $\psi(x)$. Gauge invariance is recovered by replacing the derivative ∂_{μ} in the Lagrangian with the gauge-covariant derivative $\mathcal{D}_{\mu}$. Yang and Mills developed a formalism for local gauge theory which includes non-Abelian as well as Abelian groups [26]. This requires the introduction of a massless vector gauge boson field $A^j_{\mu}(x)$ for each generator of the gauge group and a coupling constant g for each gauge group. The gauge-covariant derivative is then

$$\mathcal{D}_{\mu} \equiv \partial_{\mu} + ig\tau_j A^j_{\mu}(x). \tag{2.4}$$

A gauge invariant energy term ($\frac{1}{4}A^j_{\mu\nu}A^{\mu\nu}_j$) associated with these new gauge fields must also be added to the Lagrangian where $A^j_{\mu\nu}$ is a generalized field tensor given as

$$A^j_{\mu\nu} \equiv \partial_{\mu}A^j_{\nu} - \partial_{\nu}A^j_{\mu} - gf_{jkl}A^k_{\mu}A^l_{\nu}, \tag{2.5}$$

where f_{jkl} are the structure constants of the gauge group. One arrives at a new Lagrangian

$$\mathcal{L} = i\bar{\psi}\gamma^{\mu}\mathcal{D}_{\mu}\psi - m\bar{\psi}\psi - \frac{1}{4}A^j_{\mu\nu}A^{\mu\nu}_j, \tag{2.6}$$

which has the desired invariance under a transformation given by Eq. (2.3).

The N massless gauge boson fields interact with the fundamental fermion fields. If the gauge group G is non-Abelian (*e.g.*, $SU(2)$ and $SU(3)$), the structure constants f_{jkl} are non-zero and the resulting gauge boson fields are also self-interacting, *i.e.*, carry gauge "charges" themselves, and are able to transform one member of a multiplet into another.

2.3 The Higgs Mechanism

Weak interactions operate on extremely short distance scales, and the masses of the weak gauge bosons, $W^{\pm}$ and Z, have been measured to be large (see Tab. 2.2). However, a Quantum Field Theory which is based upon local gauge invariance only accommodates massless gauge bosons. Explicit mass terms for the gauge boson fields spoil gauge invariance. In the Standard Model, the Higgs mechanism is introduced to give masses to $W^{\pm}$ and Z bosons while retaining local gauge invariance.

A given symmetry is said to be spontaneously broken if the vacuum does not possess the same symmetry as the Lagrangian. This can be illustrated with a $U(1)$ locally gauge invariant Lagrangian describing the interaction of a scalar field $\Phi(x)$ and a gauge field $A_{\mu}(x)$:

$$\mathcal{L} = (\mathcal{D}_{\mu}\Phi)^{\dagger}(\mathcal{D}^{\mu}\Phi) - V(\Phi) - \frac{1}{4}A_{\mu\nu}A^{\mu\nu}, \tag{2.7}$$

where the covariant derivative is

$$\mathcal{D}_\mu = \partial_\mu + igA_\mu, \tag{2.8}$$

and the scalar potential $V(\Phi)$ is defined as

$$V(\Phi) = \mu^2\Phi^\dagger\Phi + \lambda(\Phi^\dagger\Phi)^2 \qquad (\lambda > 0). \tag{2.9}$$

When $\mu^2 > 0$, the potential has one minimum at $\Phi = 0$ (Fig. 2.1(a)), while when $\mu^2 < 0$, the potential has one local maximum at $\Phi = 0$ and a ring of minima at $|\Phi| = v$ where

$$v = \sqrt{\frac{-\mu^2}{\lambda}}, \tag{2.10}$$

as illustrated in Fig. 2.1(b). When Φ takes one specific minimum (*e.g.*, $\Phi = v$) as vacuum state, the vacuum is no longer $U(1)$ locally gauge invariant although the Lagrangian still is. The symmetry is spontaneously broken.

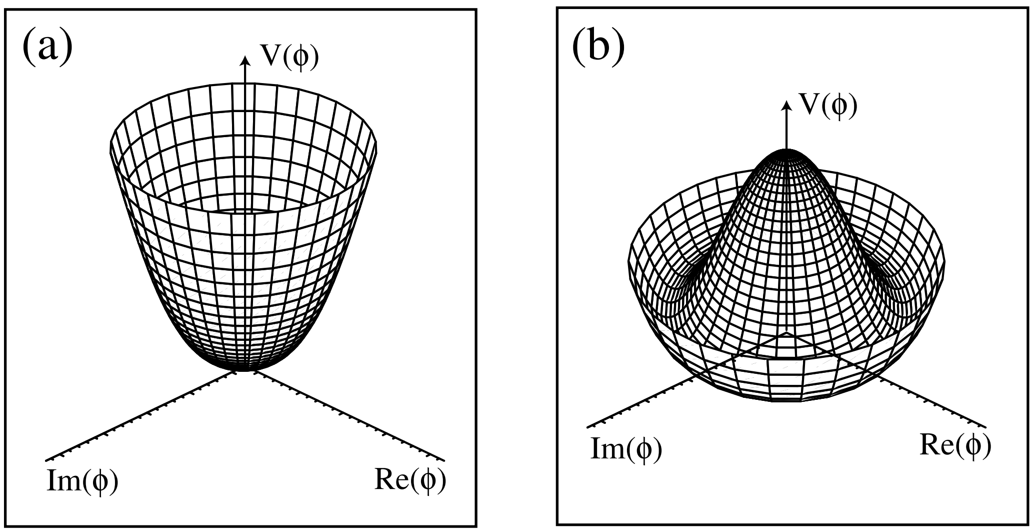

Figure 2.1: The scalar potential $V(\Phi) = \mu^2\Phi^\dagger\Phi + \lambda(\Phi^\dagger\Phi)^2$ (a) for $\mu^2 > 0$, in which case the potential has a minimum at $\Phi = 0$, and (b) for $\mu^2 < 0$, in which case the potential has a ring of minima at $|\Phi| = \sqrt{-\mu^2/\lambda}$.

Particles are quantum excitations of the vacuum state. Therefore, the scalar field can be expanded around the vacuum state and substituted into the Lagrangian:

$$\Phi(x) = \frac{1}{\sqrt{2}}e^{i\xi(x)/v}(v + H(x)); \tag{2.11}$$

$$\begin{aligned}\mathcal{L} &= \tfrac{1}{2}(\partial_\mu H)(\partial^\mu H) + \mu^2 H^2 + \tfrac{1}{2}(\partial_\mu \xi)(\partial^\mu \xi)\\ &+ gvA_\mu(\partial^\mu\xi) + \frac{1}{2}g^2v^2A_\mu A^\mu - \frac{1}{4}A_{\mu\nu}A^{\mu\nu} + \cdots.\end{aligned} \tag{2.12}$$

The massless $\xi(x)$ field is referred to as a Goldstone boson. In the case of a local gauge invariant Lagrangian, the Goldstone boson does not correspond to a physical particle. With a special choice of a local $U(1)$ gauge transformation, terms in the Lagrangian involving $\xi(x)$ and $\partial\xi(x)$ cancel, and the Lagrangian can be rewritten as

$$\mathcal{L} = \frac{1}{2}(\partial_\mu H)(\partial^\mu H) + \mu^2 H^2 + \frac{1}{2}g^2 v^2 A_\mu A^\mu - \frac{1}{4}A_{\mu\nu}A^{\mu\nu}. \tag{2.13}$$

The Goldstone boson can then be interpreted as the longitudinal polarization degree of freedom for the massive gauge field $A_\mu(x)$. Thus, this Lagrangian now describes a massive real scalar field $H(x)$ with a mass $\sqrt{-2\mu^2}$, and, most importantly, a massive gauge field $A_\mu(x)$ with mass gv.

The above formalism of spontaneously breaking a local gauge symmetry to yield a massive gauge boson is known as the Higgs mechanism. The surviving massive scalar field $H(x)$ is the Higgs boson. The parameters which appear in the scalar potential are important for determining the phenomenology of the Higgs boson: μ is the tree-level Higgs boson mass, and λ is the quartic Higgs self-coupling. The quantity $v/\sqrt{2}$ is the Higgs vacuum expectation value.

2.4 The Standard Model

The construction of the Standard Model begins with a local $SU(2)$ gauge symmetry associated with a conserved gauge charge, weak isospin (T). Another local $U(1)_Y$ gauge symmetry is associated with another conserved gauge charge: hypercharge (Y). The Yang-Mills formalism requires the introduction of a massless weak isospin triplet of gauge bosons $\vec{W}_\mu = (W^1_\mu, W^2_\mu, W^3_\mu)$ and a single massless hypercharge singlet gauge boson B_μ. Hence the covariant derivative is

$$\mathcal{D}_\mu = \partial_\mu + i\frac{g}{2}\tau_j \cdot W^j_\mu + ig'\frac{Y}{2}B_\mu. \tag{2.14}$$

The normal electric charge Q is a linear combination of the third component of weak isospin and hypercharge: $Q = T_3 + Y/2$.

Parity violation in the weak interaction is introduced by grouping left-handed and right-handed chirality states of particles in different weak isospin multiplets. Left-handed fermions are grouped in doublets whereas right-handed fermions are singlets. Tab. 2.3 displays the multiplet and quantum number assignments for the fermions in the Standard Model.

	Generation 1	Generation 2	Generation 3	T_3	Y	Q
Leptons	$\begin{pmatrix}\nu_e \\ e\end{pmatrix}_L$	$\begin{pmatrix}\nu_\mu \\ \mu\end{pmatrix}_L$	$\begin{pmatrix}\nu_\tau \\ \tau\end{pmatrix}_L$	$1/2$ $-1/2$	-1 -1	0 -1
	e_R	μ_R	τ_R	0	-2	-1
Quarks	$\begin{pmatrix}u \\ d'\end{pmatrix}_L$	$\begin{pmatrix}c \\ s'\end{pmatrix}_L$	$\begin{pmatrix}t \\ b'\end{pmatrix}_L$	$1/2$ $-1/2$	$1/3$ $1/3$	$2/3$ $-1/3$
	u_R	c_R	t_R	0	4/3	2/3
	d_R	s_R	b_R	0	-2/3	-1/3

Table 2.3: Multiplet and quantum number assignments for the fermions in the Standard Model. The prime indicates that the weak eigenstates of the quarks are not their mass eigenstates. The indices $L(R)$ denote left(right)-handed fermions.

To accommodate massive gauge bosons by the Higgs mechanism, a complex weak isospin scalar doublet Φ is introduced along with the scalar potential $V(\Phi)$ discussed in the previous section:

$$\Phi = \begin{pmatrix} \phi^+ \\ \phi^0 \end{pmatrix} = \frac{1}{\sqrt{2}} \begin{pmatrix} \phi_1 + i\phi_2 \\ \phi_3 + i\phi_4 \end{pmatrix}; \qquad V(\Phi) = \mu^2 \Phi^\dagger \Phi + \lambda (\Phi^\dagger \Phi)^2 \quad (\lambda > 0). \tag{2.15}$$

The Lagrangian of the electroweak standard can be written as the sum of four independent terms:

$$\mathcal{L} = \mathcal{L}_{\text{Fermion}} + \mathcal{L}_{\text{Gauge}} + \mathcal{L}_{\text{Higgs}} + \mathcal{L}_{\text{Yukawa}}, \tag{2.16}$$

where $\mathcal{L}_{\text{Fermion}}$ describes massless fermion fields and their interaction with the gauge fields:

$$\mathcal{L}_{\text{Fermion}} = i\bar{\psi}\gamma^\mu \mathcal{D}_\mu \psi. \tag{2.17}$$

The term $\mathcal{L}_{\text{Gauge}}$ contains the kinetic energy of the massless gauge fields B and $\vec{W}$ and the self interaction of the $\vec{W}$ fields:

$$\mathcal{L}_{\text{Gauge}} = -\frac{1}{4}\vec{W}_{\mu\nu}\vec{W}^{\mu\nu} - \frac{1}{4}B_{\mu\nu}B^{\mu\nu}, \tag{2.18}$$

where

$$\vec{W}_{\mu\nu} = \partial_\mu \vec{W}_\nu - \partial_\nu \vec{W}_\mu + g\vec{W}_\mu \times \vec{W}_\nu. \tag{2.19}$$

The third term in above equation is the self interaction of the $\vec{W}$ fields. It arises from the non-abelian character of the $SU(2)$ group, and

$$B_{\mu\nu} = \partial_\mu B_\nu - \partial_\nu B_\mu. \tag{2.20}$$

The mass eigenstates of the W particles are:

$$W_\mu^\pm = \frac{1}{\sqrt{2}}(W_\mu^1 \mp iW_\mu^2). \tag{2.21}$$

The photon field A_μ and the field of the Z boson Z_μ are linear combinations of B_μ and W_μ^3:

$$A_\mu = B_\mu \cos\theta_{\text{W}} + W_\mu^3 \sin\theta_{\text{W}} \tag{2.22}$$

$$Z_\mu = -B_\mu \sin\theta_{\text{W}} + W_\mu^3 \cos\theta_{\text{W}}. \tag{2.23}$$

The weak mixing angle θ_{W} depends on the coupling constants g and g':

$$\tan\theta_{\text{W}} = \frac{g'}{g}. \tag{2.24}$$

The term $\mathcal{L}_{\text{Higgs}}$ describes the interaction of the Higgs field and gauge boson fields:

$$\mathcal{L}_{\text{Higgs}} = (\mathcal{D}_\mu \Phi)^\dagger (\mathcal{D}^\mu \Phi) - \mu^2 \Phi^\dagger \Phi + \lambda (\Phi^\dagger \Phi)^2, \tag{2.25}$$

where λ is the Higgs self-coupling parameter.

The minima of the Higgs potential for $\mu^2 < 0$ are at

$$\Phi^\dagger\Phi = \frac{\Phi_1^2+\Phi_2^2+\Phi_3^2+\Phi_4^2}{2} = \frac{-\mu^2}{2\lambda} = \frac{v^2}{2}. \tag{2.26}$$

Choosing one particular ground state $\Phi_3 = v, \Phi_1 = \Phi_2 = \Phi_4 = 0$, which ensures that the electric charge is conserved in agreement with experiment, and expanding $\Phi(x)$ around it in the non-flat direction, leads to

$$\Phi(x) = \frac{1}{\sqrt{2}}\begin{pmatrix} 0 \\ v + \mathrm{H}(x) \end{pmatrix}. \tag{2.27}$$

The $O(4)$ symmetry of Eq. (2.26) has been broken down to an $O(1)$ symmetry corresponding to the $U(1)_{\mathrm{em}}$ group of electromagnetism. Three fields have been "gauged away". They become the longitudinal part of the $\mathrm{W}^\pm$ and Z bosons which are needed for massive gauge bosons. Investigating the first term in Eq. (2.25) at the vacuum state and inserting $Y = 1/2$ yields:

$$\begin{aligned} |(ig'YB_\mu + i\tfrac{g}{2}\vec{\tau}\vec{W}_\mu)\tfrac{1}{\sqrt{2}}\begin{pmatrix} 0 \\ v \end{pmatrix}|^2 &= \tfrac{1}{8}v^2g^2((W_\mu^1)^2 + (W_\mu^2)^2) + \tfrac{1}{8}v^2(g'B_\mu - gW_\mu^3)^2 \\ &= \left(\frac{1}{2}vg\right)^2 W_\mu^+W^{-\mu} + \left(\frac{1}{2}v\sqrt{g'^2+g^2}\right)^2 Z_\mu Z^\mu. \end{aligned} \tag{2.28}$$

In deriving the last line, the identities given by Eqs. (2.21), (2.23), (2.24) were used. The factors in front of the gauge fields are interpreted as masses. Therefore, the masses of the gauge bosons are given by

$$m_{\mathrm{W}} = \frac{1}{2}vg, \tag{2.29}$$

$$m_{\mathrm{Z}} = \frac{1}{2}v\sqrt{g'^2+g^2}, \tag{2.30}$$

and

$$m_\gamma = 0, \tag{2.31}$$

the last because there is no term of the form $A_\mu A^\mu$ in Eq. (2.28). Using Eq. (2.24), one can easily derive the relation between the boson masses with the weak mixing angle:

$$\cos\theta_{\mathrm{W}} = \frac{m_{\mathrm{W}}}{m_{\mathrm{Z}}} \tag{2.32}$$

A useful quantity which is often referred to is $\rho = m_{\mathrm{W}}/m_{\mathrm{Z}}\cos\theta_{\mathrm{W}}$. As can be seen from Eq. (2.32), the Standard Model predicts $\rho = 1$. The experimental values of the m_{W}, m_{Z} and $\sin^2\theta_{\mathrm{W}}$ have been precisely measured and yield $\rho = 1$.

The Higgs mass is predicted to be

$$m_{\mathrm{H}} = \sqrt{2\lambda}\cdot v. \tag{2.33}$$

The value of v (246 GeV) is known through its relation to the Fermi coupling constant G_F ($v = (\sqrt{2}G_F)^{-1/2}$), which is obtained to high precision from muon decay measurements. However, λ is unknown, and remains a free parameter of the theory.

The bosons and their quantum number assignments in the Standard Model are summarized in Tab. 2.4.

		T_3	Y	Q
Gauge Bosons	γ	0	0	0
	Z	0	0	0
	W^+	+1	0	+1
	W^-	-1	0	-1
Higgs	$\Phi = \begin{pmatrix} \phi^+ \\ \phi^0 \end{pmatrix}$	1/2 $-1/2$	1 1	1 0

Table 2.4: Quantum number assignments of the bosons in the Standard Model.

The fermion masses are generated by adding a $SU(2) \times U(1)$ gauge invariant Yukawa coupling term of the Higgs field with the fermion fields:

$$g_f \left[\bar{\psi}_{\rm L}\Phi\psi_{\rm R} + \bar{\psi}_{\rm R}\Phi^\dagger\psi_{\rm L}\right] \tag{2.34}$$

to the Lagrangian, where g_f is the Yukawa coupling of the fermion f represented by the field ψ to the Higgs field. For the first lepton family (and similarly for the other lepton flavors), the Yukawa coupling term is:

$$\mathcal{L}_{\rm Yukawa} = g_{\rm e}\left[(\bar{\nu}_{\rm e}, \bar{e})_{\rm L}\begin{pmatrix} \phi^+ \\ \phi^0 \end{pmatrix} e_{\rm R} + \bar{e}_{\rm R}(\phi^-, \bar{\phi}^0)\begin{pmatrix} \nu_{\rm e} \\ e \end{pmatrix}_{\rm L}\right]. \tag{2.35}$$

After spontaneous symmetry breaking (Eq. (2.27)), one obtains:

$$\mathcal{L}_{\rm Yukawa} = \frac{g_{\rm e}}{\sqrt{2}}v(\bar{e}_{\rm L}e_{\rm R} + \bar{e}_{\rm R}e_{\rm L}) + \frac{g_{\rm e}}{\sqrt{2}}(\bar{e}_{\rm L}e_{\rm R} + \bar{e}_{\rm R}e_{\rm L})H. \tag{2.36}$$

for which we can conclude that the electron mass is:

$$m_{\rm e} = \frac{g_{\rm e}v}{\sqrt{2}}, \tag{2.37}$$

whereas the neutrino remains massless.

Quark masses can be generated similarly. In order to allow masses for up-type quarks, the charge-conjugate Higgs doublet is used

$$\tilde{\Phi} = \begin{pmatrix} \phi^{0\dagger} \\ -\phi^- \end{pmatrix}. \tag{2.38}$$

The Yukawa term then becomes:

$$\begin{aligned}\mathcal{L}_{\rm Yukawa} = g_{\rm d}&\left[(\bar{u}, \bar{d})_{\rm L}\begin{pmatrix} \phi^+ \\ \phi^0 \end{pmatrix} d_{\rm R} + \bar{d}_{\rm R}(\phi^-, \bar{\phi}^0)\begin{pmatrix} u \\ d \end{pmatrix}_{\rm L}\right] \\ +g_{\rm u}&\left[(\bar{u}, \bar{d})_{\rm L}\begin{pmatrix} -\bar{\phi}^0 \\ \phi^- \end{pmatrix} d_{\rm R} + \bar{d}_{\rm R}(-\phi^0, \phi^+)\begin{pmatrix} u \\ d \end{pmatrix}_{\rm L}\right].\end{aligned} \tag{2.39}$$

after spontaneous symmetry breaking, this equation yields:

$$\mathcal{L}_{\rm Yukawa} = \frac{g_{\rm d}v}{\sqrt{2}}\bar{d}d + \frac{g_{\rm u}v}{\sqrt{2}}\bar{u}u + \frac{g_{\rm d}}{\sqrt{2}}\bar{d}dH + \frac{g_{\rm u}}{\sqrt{2}}\bar{u}uH, \tag{2.40}$$

from where the down- and up-quark masses $g_{\rm d}v/\sqrt{2}$ and $g_{\rm u}v/\sqrt{2}$ are derived. In general the mass of any given fermion f is proportional to the coupling constant g_f to the Higgs boson:

$$m_f = \frac{g_f v}{\sqrt{2}}. \tag{2.41}$$

This proportionality predicts that the Higgs boson prefers to decay to the heavier fermions - a property which is used in presently ongoing searches. It is also the property that decisively distinguishes a Higgs boson from any other particle.

2.5 Higgs Boson Phenomenology at LEP2

This section summarizes phenomenological issues relevant to Standard Model Higgs searches at the e^+e^- collider LEP2. Until the Higgs boson is discovered, its mass is unknown and remains a free parameter in the Standard Model. However, for a given mass, the relevant properties (*e.g.*, the production cross section) of the Higgs boson can be unambiguously determined. The range of masses relevant to LEP2 searches is from 60 to 120 GeV.

2.5.1 Production of the Standard Model Higgs Boson

The Higgs boson couples to massive fermions and the $W^\pm$ and Z bosons. It is possible for Higgs bosons to be produced radiatively from these particles. Alternatively, it can be produced via W^+W^- and ZZ fusion. The s-channel production of Higgs bosons from the annihilation of fermion-anti-fermion pairs is possible, but this process is negligible in e^+e^- collisions since the electron mass (and hence the Higgs-electron coupling) is very small. A gluon fusion production mechanism exists where two gluons couple to a massive fermion loop which produces a Higgs boson; but this is only relevant for searches at $p\bar{p}$ and pp colliders.

The main production process of the Standard Model Higgs boson in the context of e^+e^- interactions relevant to LEP2 searches is the so-called Higgs-strahlung (Fig. 2.2). In this process the electron and the positron annihilate into a virtual Z boson which then emits a Higgs boson. At tree level, the cross section of this process is:

$$\sigma(e^+e^- \to HZ) = \frac{g^4}{3072\pi \cos^4\theta_W s}[1 + (1 - 4\sin^2\theta_W)^2]\lambda^{\frac{1}{2}} \frac{\lambda + 12m_Z^2/s}{(1 - m_Z^2/s)^2}, \tag{2.42}$$

where $\lambda = (1 - m_H^2/s - m_Z^2/s)^2 - 4m_H^2 m_Z^2/s^2$ is a two-particle phase space factor [27]. This Higgs-strahlung cross section as obtained from the HZHA event generator [28] is shown in Fig. 2.3 as a function of the Higgs boson mass for various center-of-mass energies.

By going to higher center-of-mass energies, two more diagrams start to contribute a sizeable Higgs production rate: the W^+W^- and ZZ fusion diagrams (Fig. 2.4). The cross sections of Higgs boson production for the fusion processes as well as for Higgs-strahlung process at a fixed center-of-mass energy ($\sqrt{s} = 206.6$GeV) and as a function of the the Higgs boson mass are shown in Fig. 2.5.

2.5.2 Decay of the Standard Model Higgs Boson

The Higgs boson is not stable. It decays to massive fermions or gauge bosons. Its lifetime depends on its mass. The heavier the Higgs boson is, the more decay channels become open. Therefore, the lifetime decreases with increasing mass. At tree level, the partial width for the Higgs boson decaying into fermions is

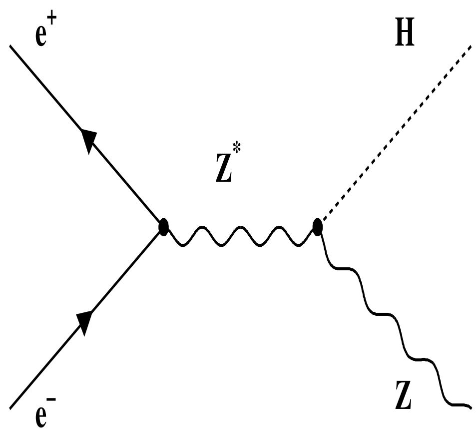

Figure 2.2: Higgs-strahlung process.

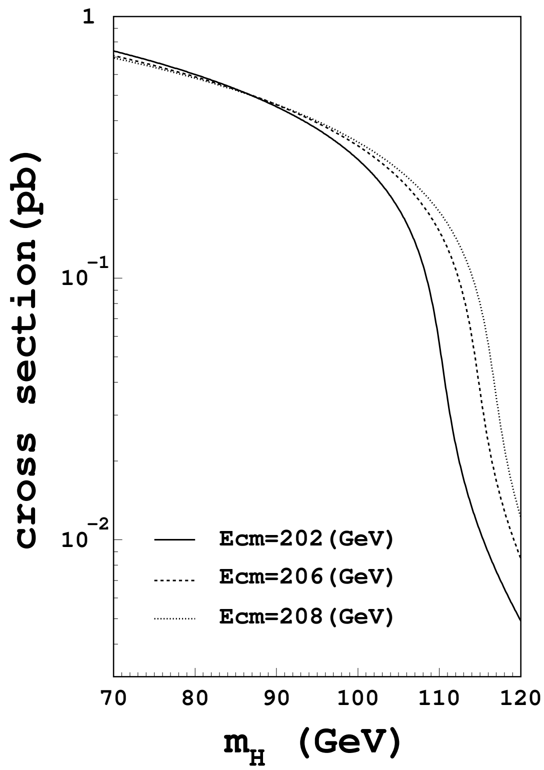

Figure 2.3: The Higgs-strahlung cross section as a function of the Higgs boson mass for various center-of-mass energies.

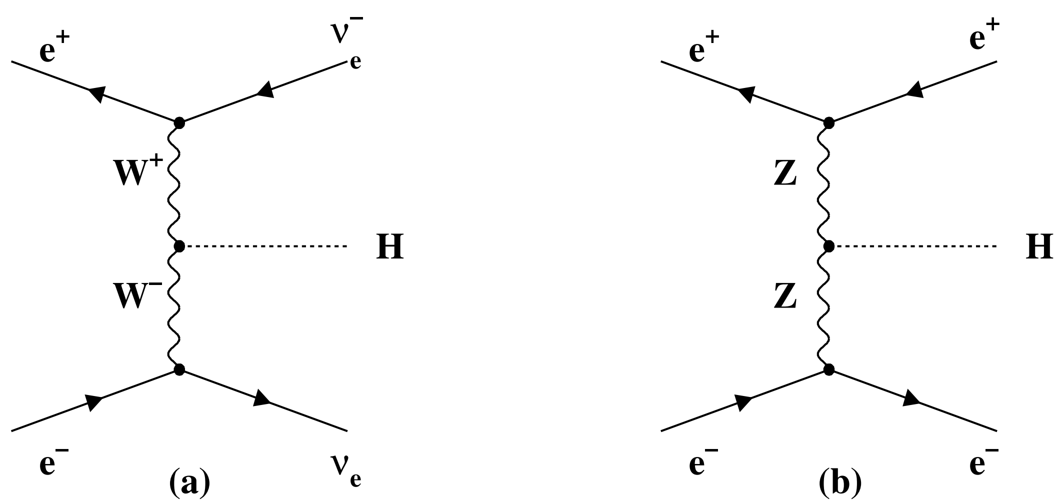

Figure 2.4: WW and ZZ fusion diagrams.

$$\Gamma(\mathrm{H} \to f\bar{f}) = N_{\mathrm{c}} \frac{G_{\mathrm{F}} m_f^2 m_{\mathrm{H}}}{4\pi\sqrt{2}} (1 - \frac{4m_f^2}{m_{\mathrm{H}}^2})^{3/2}, \tag{2.43}$$

where N_{c} is 1 for leptons and 3 for quarks [29].

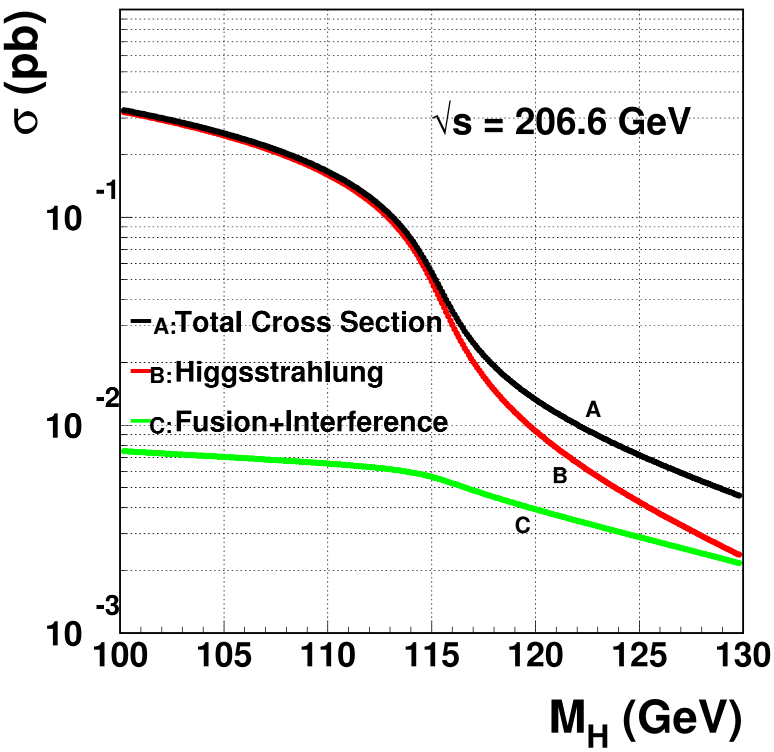

Figure 2.5: Higgs production cross sections for the fusion processes as well as for Higgs-strahlung process at $\sqrt{s} = 206.6\text{GeV}$.

The Higgs-fermion coupling is proportional to the fermion mass, while the couplings to the $\mathrm{W}^{\pm}$ and Z are proportional to the boson mass squared. The Higgs boson therefore decays preferentially into the heaviest particles which are kinematically accessible. Within the relevant Higgs boson mass range for LEP2, the Higgs boson decays predominantly to $\mathrm{b\bar{b}}$ pairs, ranging from roughly 87% to 70% with increasing Higgs boson mass. The next most prevalent decays are to $\tau^+\tau^-$ and $\mathrm{c\bar{c}}$ pairs with branching ratios of roughly 7% and 3%, respectively. The branching ratio of Higgs boson decaying to gluons through intermediate massive quark loops ranges from 2% to 6%. At high masses the Higgs can decay into WW^* and ZZ^*, however, with a very small branching fraction due to the heaviness of the gauge bosons. The Higgs decay width into virtual W bosons is given by [27]:

$$\Gamma(\mathrm{H} \rightarrow \mathrm{WW}^*) = \frac{3G_{\mathrm{F}}^2 m_{\mathrm{W}}^4}{16\pi^3} m_{\mathrm{H}} R(x), \tag{2.44}$$

where $R(x)$ is a function of the ratio $x = m_{\mathrm{W}}^2/m_{\mathrm{H}}^2$. The decay into ZZ^* is further suppressed due to the mass of the Z boson and the reduced neutral current couplings with respect to the charged current couplings.

Higgs boson decays to $\gamma\gamma$ and $\mathrm{Z}\gamma$ are possible through intermediate $\mathrm{W}^{\pm}$ loops or massive fermion loops [29].

The diagrams of the Higgs boson decay are indicated in Fig. 2.6, and the branching ratios of the Higgs boson as a function of the Higgs mass are shown in Fig. 2.7.

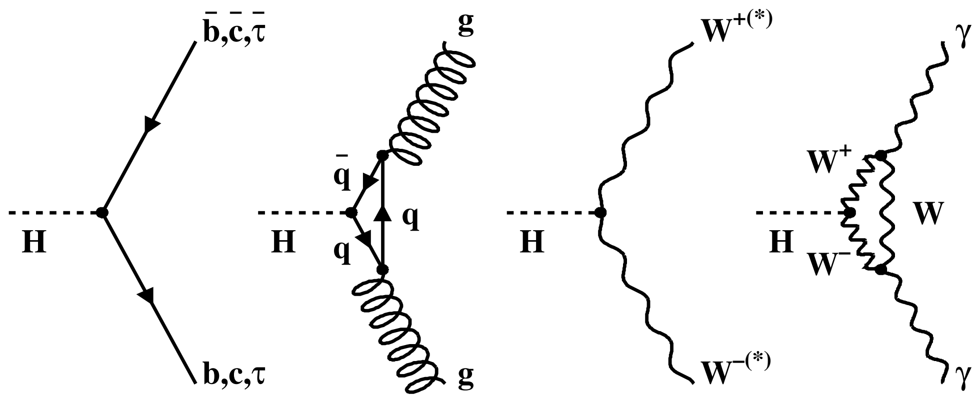

Figure 2.6: The Higgs decay modes.

2.5.3 Higgs Boson Mass Bounds

Various theoretical arguments have been used to constrain the mass of the Higgs boson. Precision electroweak measurements can also be used to determine the most consistent Higgs boson mass and to derive an upper limit. However, the final arbiter will be the direct experimental observation of the Higgs boson and the measurement of its mass.

Theoretical Bounds

Theoretical considerations teach us that the Standard Model is not the ultimate theory of the fundamental particles and their interactions, though the global analysis of electroweak observables provides a superb fit to the Standard Model predictions. At an energy scale above the Planck scale, $m_{\mathrm{PL}} \simeq 10^{19}$ GeV, quantum gravitational effects become significant and the Standard Model must be replaced by a more fundamental theory that incorporates gravity. The self-interacting complex doublet of scalar fields which is employed by the Standard Model for the explanation of electroweak symmetry breaking should also be replaced by other approaches of electroweak symmetry breaking. It is also possible that the Standard Model breaks down at some energy scale (called Λ) below the Planck scale. In this case, the Standard Model degrees of freedom are no longer adequate for describing the theory above Λ and new physics must become relevant. The Higgs mass m_{H} is the key parameter for constraining Λ, the scale at which that Standard Model breaks down [30]. Given a value of Λ, one can compute the maximum and minimum Higgs mass allowed by taking into account the triviality argument and vacuum stability argument, respectively. The triviality argument requires the Higgs self-coupling λ (Eq. 1.33) to remain finite up to the cut-off scale Λ, and this puts a constraint on the value of λ at electroweak scale (v), and therefore, as the upper limit of Higgs mass [32]. On the other hand, the vacuum stability argument requires that λ should be positive up to a scale Λ to keep the Higgs potential bounded from below. Otherwise, there would be no minimum of the Higgs potential, and no consistent theory could be constructed. This requirement puts a lower

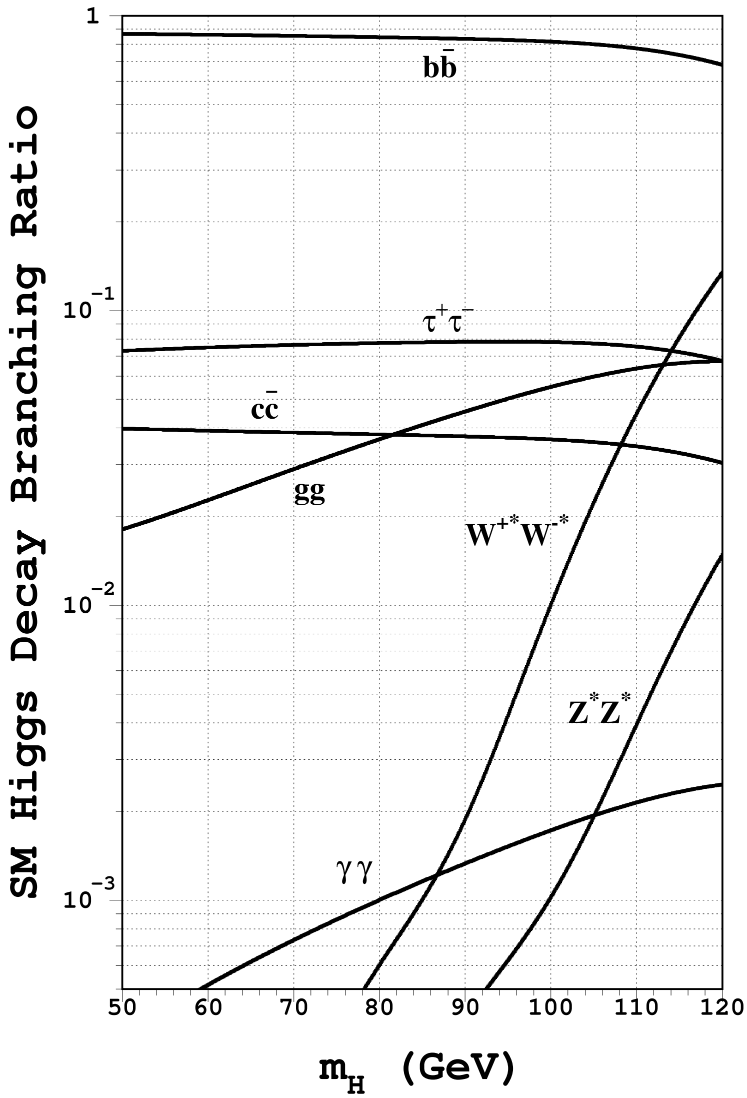

Figure 2.7: The branching ratios of the Standard Model Higgs boson decay as a function of the Higgs mass.

limit on the value of λ at electroweak scale (v), and thus gives a lower limit of Higgs mass [33]. The results of the computation (with shaded bands indicating the theoretical uncertainty of the results) are illustrated in Fig. 2.8 [31]. If the Higgs mass m_{H} is either too large or too small, new physics beyond the Standard Model must enter at a scale Λ or below.

Limits from Indirect Measurements

The Higgs boson influences observed electroweak processes via higher order processes. Hence, if electroweak observables are precisely measured, it is possible to determine the Higgs boson mass via the radiative correction. To demonstrate this, the Fermi coupling constant G_{F} can be rewritten with radiative correction terms included [34]:

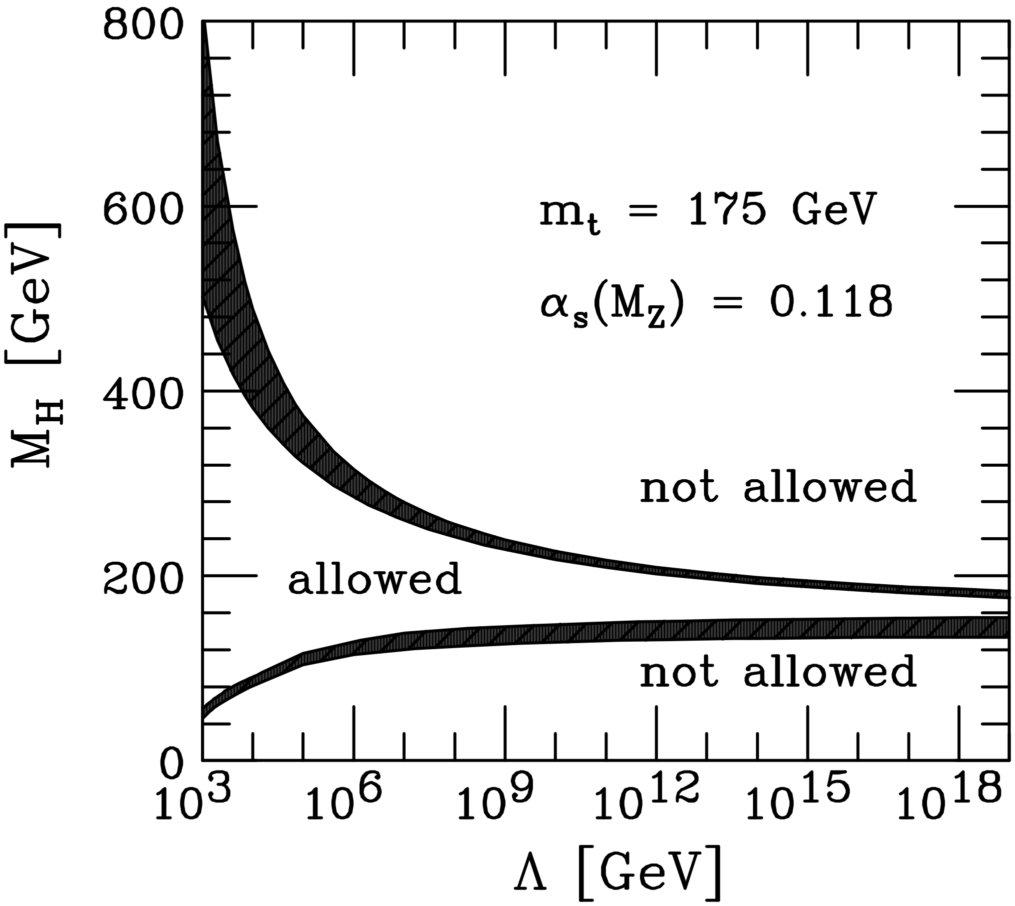

Figure 2.8: The lower and upper Higgs mass bounds as a function of the energy scale Λ at which the Standard Model breaks down, assuming $m_{\rm t} = 175$ GeV, and $\alpha(m_{\rm Z}^2) = 0.118$. The shaded areas above reflect the theoretical uncertainties in the calculations of the Higgs mass bounds[11].

$$\frac{G_{\rm F}}{\sqrt{2}} = \frac{2\pi\alpha}{\sin^2(2\theta_{\rm W})m_{\rm Z}^2}(1 + \Delta r_\alpha + \Delta r_t + \Delta r_{\rm H}), \tag{2.45}$$

where α is the electromagnetic coupling, Δr_α represents the difference between $\alpha(m_{\rm Z}^2)$ and $\alpha(0)$, and Δr_t represents the top radiative corrections to the $\rm W^\pm$ and Z masses. The $\Delta r_{\rm H}$ represents the radiative corrections to the $\rm W^\pm$ and Z masses from the Higgs boson; and this term is in the next-leading order proportional to $\log(m_{\rm H}^2)$. Measurements of electroweak observables from the four LEP experiments (ALEPH, DELPHI, L3, and OPAL), the SLD experiment at the Stanford Linear Collider (SLC), and the two Tevatron experiments (CDF and DØ) are combined, and a fit to these data is performed. The Higgs boson mass is determined from the minimum χ^2 of the fit [35].

The error on the fit result is currently dominated by the uncertainty in $\alpha(m_{\rm Z}^2)$. The uncertainty in $\alpha(m_{\rm Z}^2)$ arises from the contribution of light quarks to the photon vacuum polarization($\Delta\alpha_{\rm had}^{(5)}(m_{\rm Z}^2)$):

$$\alpha(m_{\rm Z}^2) = \frac{\alpha(0)}{1 - \Delta\alpha_l(m_{\rm Z}^2) - \Delta\alpha_{\rm had}^{(5)}(m_{\rm Z}^2) - \Delta\alpha_{\rm top}(m_{\rm Z}^2)}, \tag{2.46}$$

where $\alpha(0) = 1/137.036$, $\Delta\alpha_l(m_Z^2)$ is the leptonic contribution and $\Delta\alpha_{\rm top}(m_Z^2)$ is top contribution which depends on the mass of top quark. There are several evaluations of the hadronic contribution $\Delta\alpha^{(5)}_{\rm had}(m_Z^2)$.

Fig. 2.9 shows the value of $\Delta\chi^2 = \chi^2 - \chi^2_{min}$ as a function of $m_{\rm H}$ (solid curve) and the shaded band represents the theoretical uncertainty due to uncalculated higher-order corrections (in case the $\Delta\alpha^{(5)}_{\rm had}(m_Z^2) = 0.02761 \pm 0.00036$ is obtained by a model independent approach). The one-sided 95% confidence level upper limit on the mass of the Higgs boson at $\Delta\chi^2 = 2.7$ (taking the band into account) is given by

$$m_{\rm H} < 196 \text{ GeV}. \tag{2.47}$$

If one of the most recent evaluations: $\Delta\alpha^{(5)}_{\rm had}(m_Z^2) = 0.02738 \pm 0.00020$, which is more theory-driven, is used for fit, one finds $\log(m_{\rm H}/\text{GeV}) = 2.03 \pm 0.19$ corresponding to

$$m_{\rm H} = (106^{+57}_{-38}) \text{ GeV}, \tag{2.48}$$

and an upper limit on $m_{\rm H}$ at 95% confidence level of

$$m_{\rm H} < 222 \text{ GeV}. \tag{2.49}$$

Limits from Direct Searches

A variety of searches have been conducted for the Higgs boson in a variety of quantum mechanical systems. The evolution of the searches from extremely low energies to the highest energy regimes that are currently experimentally accessible reflects the fact that the Higgs boson mass is a free parameter in the Standard Model.

An extremely light Higgs boson ($m_{\rm H} < 15$ MeV) has been excluded by experiments searching for indirect evidence in atomic and nuclear systems via a Higgs-nucleon coupling [36]. Searches for unexpected decays of pions [37], kaons [38], B mesons [39], and Υ's [40] have excluded a light Higgs boson ($m_{\rm H} < 5$ GeV).

A search for the Standard Model Higgs boson in $\rm p\bar{p}$ collisions at a center-of-mass energy of 1.8 TeV has been conducted with the CDF and DØ experiments at the Tevatron. The integrated luminosities of the data samples (110 $\rm pb^{-1}$ for CDF and 100 $\rm pb^{-1}$ for DØ) are insufficient to set any significant lower limits on the Higgs boson mass since cross sections and signal detection efficiencies are very small; however, in the absence of evidence of an unexpected signal, upper limits on the Higgs boson production cross section can be determined. The Standard Model expectation for the cross section is less than 1 pb for Higgs boson masses above 70 GeV [41]. No evidence of a signal was detected. CDF set a 95% confidence level upper limit on the cross section for a Higgs boson with mass between 70 and 120 GeV in the range from 14 to 19 pb [42]. Limits in the range from 20 to 50 pb are set by DØ [43]. The sensitivity of Tevatron Higgs boson searches is expected to improve after the currently completed upgrade, such that Higgs boson masses up to 190 GeV become accessible for detection.

From 1989 to 1995, the four LEP experiments searched for direct evidence of Higgs boson production via the Higgs-strahlung process in $\rm e^+e^-$ collisions at a center-of-mass energy of 91.2 GeV (*i.e.*, LEP1). Due to the enormous background from Z$\rightarrow$ hadrons, only the final states where the Z decays to $\nu\bar{\nu}$ and l^+l^- (where $l^\pm$ denotes either $\rm e^\pm$ or $\mu^\pm$) were considered. ALEPH, DELPHI, L3, and OPAL set 95% confidence level lower limits on the mass of the Higgs boson of 63.9, 55.7, 60.2 and 59.6 GeV respectively [44–47].

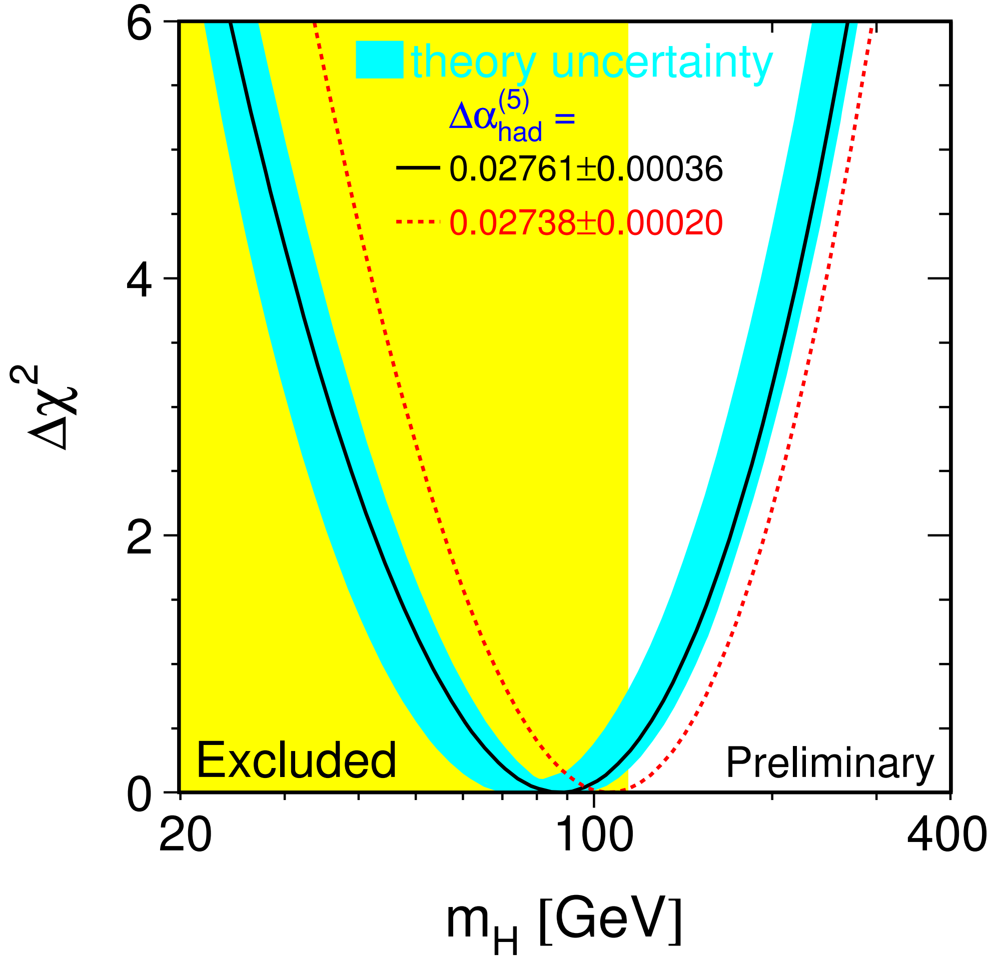

Figure 2.9: $\Delta\chi^2 = \chi^2 - \chi^2_{\rm min}$ versus $m_{\rm H}$ from a fit to precision electroweak measurements[15].

With the advent of LEP2, the four LEP experiments again searched for direct evidence of the Standard Model Higgs boson production via the Higgs-strahlung process at center-of-mass energies above 161 GeV. Before the work of this thesis was started, there was a 95% confidence level lower limit on the mass of the standard Model Higgs boson of 107.0 GeV [48], which was obtained by the search results from the L3 experiment up to a center-of-mass energy of 202 GeV, while the lower limit obtained from the combination of the four LEP experiments was set at 107.9 GeV [49].

2.5.4 Background Processes at LEP2

Several Standard Model Processes which do not involve Higgs boson production can mimic a potential Higgs signal. Hence, these processes are referred to as background processes for the Standard Model Higgs search. These background processes can be classified into two groups: two-fermion and various four-fermion processes. Since the Higgs signal processes considered in this thesis involve at least two quark jets, only background processes which could result in a multi-hadronic final state are relevant.

The Two-Fermion Process

The relevant two-fermion background process is the production of a quark/anti-quark pair from a Z or virtual photon: $e^+e^- \to Z^{(*)}/\gamma^* \to q\bar{q}(\gamma)$. A diagram contributing to this process is shown in Fig. 2.10. The (γ) denotes any initial state radiation (ISR) photon, if present, from the electron or positron. The quarks can produce hard gluons by bremsstrahlung, leading to events with more than two jets (*e.g.*, $q\bar{q}g$, $q\bar{q}gg$, $q\bar{q}q\bar{q}$, *etc.*). In the case of b or c quarks, leptons may be produced in b- or c-hadron decay. The so-called *radiative Z return* refers to the case when the invariant mass of the $q\bar{q}$ is equal to m_Z. In most of the cases, the ISR photons have low transverse momentum and escape undetected down the beam pipe. These events are characterised by an energy imbalance where the missing momentum vector points along the beam direction. For the generation of $e^+e^- \to q\bar{q}(\gamma)$ events, the Monte Carlo program KK2f version 4.13 [50] was used.

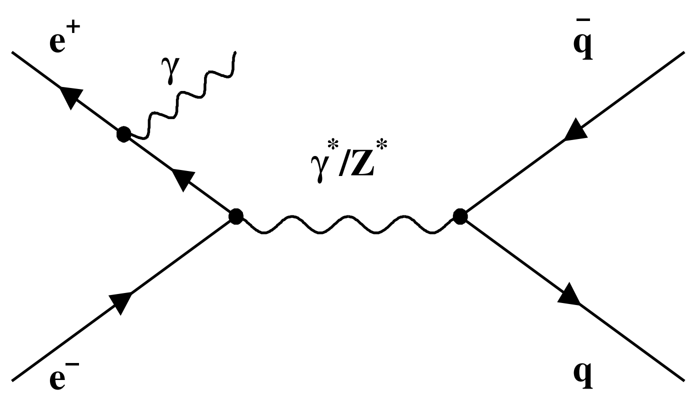

Figure 2.10: The background process $e^+e^- \to q\bar{q}(\gamma)$.

The W^+W^- Process

The pair production of $W^\pm$ bosons has a cross section of 17.5 pb at a center-of-mass energy of 207 GeV. This process has two s-channel (γ^* and Z^*) and one t-channel (ν_e exchange) production mechanisms. Fig. 2.11 shows diagrams contributing to these processes. The W boson can decay into a quark/anti-quark pair, *e.g.*, $W^+ \to u\bar{d}$ or $c\bar{s}$ or lepton/anti-lepton pair $l^+\bar{\nu}_l (l = e, \mu, \tau)$. For the generation of WW background, the Monte Carlo generator KORALW version 1.33 [51] was used.

The ZZ Process

The four-fermion process involving the pair-production of Z bosons shown in Fig. 2.12(a), includes the processes $e^+e^- \to \gamma^*\gamma^*, Z^{(*)}/\gamma^*$, and $Z^{(*)}Z^{(*)}$. These processes are collectively referred to as ZZ; hence "Z", in this context, denotes either an on-shell Z boson, Z^* or γ^*. This

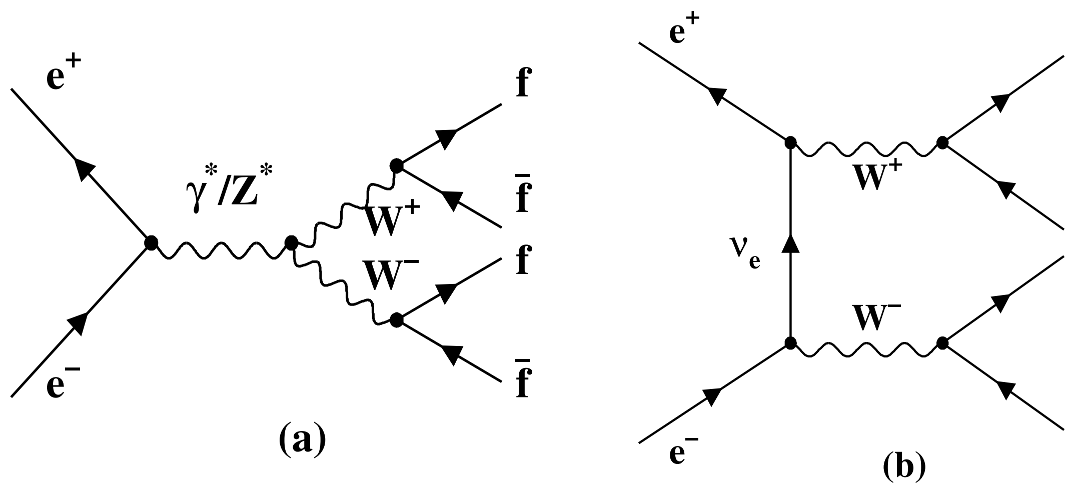

Figure 2.11: The background process $e^+e^- \rightarrow W^+W^-$: (a) s-channel; (b) t-channel.

process has a cross section of 1.3 pb at a center-of-mass energy of 207 GeV. For the generation of ZZ background, the Monte Carlo generator EXCALIBUR [52] was used.

The ZZ background is especially problematic for analyses designed to search for the Higgs boson at LEP2. If one Z deays to $b\bar{b}$ or $\tau^+\tau^-$, the resulting final state is indistinguishable from a Higgs-strahlung final state for a Higgs boson with a mass near m_Z; hence ZZ is an irreducible background in searches for the Standard Model Higgs boson in the region $m_H \simeq m_Z$.

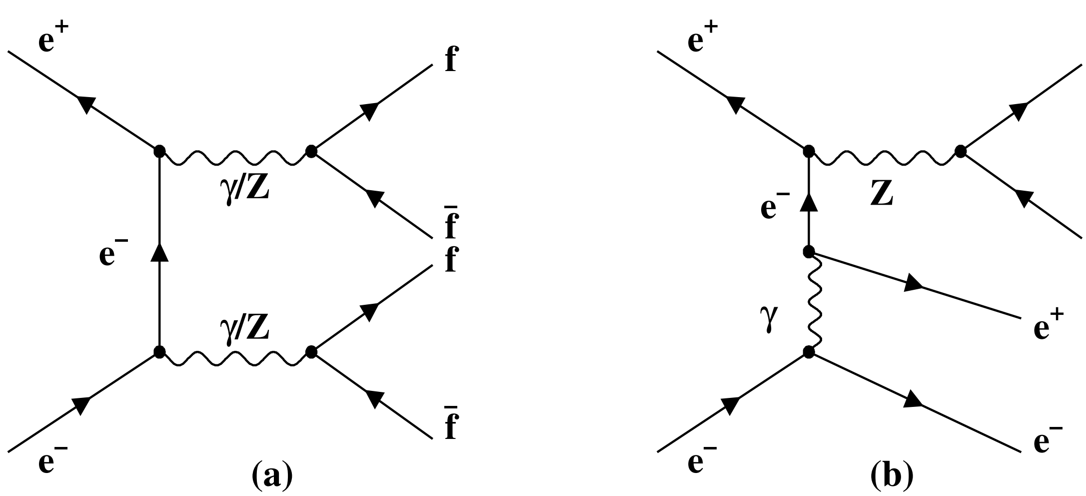

Figure 2.12: The background processes: (a) $e^+e^- \rightarrow ZZ$; (b) $e^+e^- \rightarrow Ze^+e^-$.

The Ze^+e^- Process

The lowest-order dominant t-channel diagram contributing to the four-fermion process involving the production of a single Z boson ($e^+e^- \to Ze^+e^-$) is shown in Fig. 2.12(b). The cross section for this process at a center-of-mass energy of 207 GeV is 3.6 pb. The Monte Carlo generator EXCALIBUR [52] was used for the generation of Ze^+e^- background.

There is one more relevant four-fermion process, which is referred to as the two photon interaction because of the virtual exchange of two photons (see diagram Fig. 2.13). This process has the highest cross section at LEP2 energies, but has little impact on the Higgs search. Usually, the electron and positron get slightly scattered in this process losing only a small fraction of their initial energy and remain undetected within the beampipe. The fermion pair which is observed in the detector has, therefore, extremely low visible energy and particle multiplicity. Hence they can be easily separated from the Higgs signal at the early stage of Higgs event selection. For the generation of two-photon background, the Monte Carlo generator PHOJET [53] was used.

Fig. 2.14 shows the cross sections of the background processes as a function of energy.

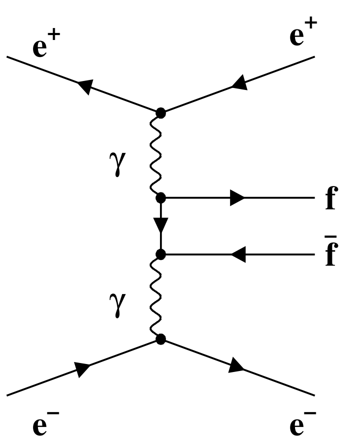

Figure 2.13: Two photon process.

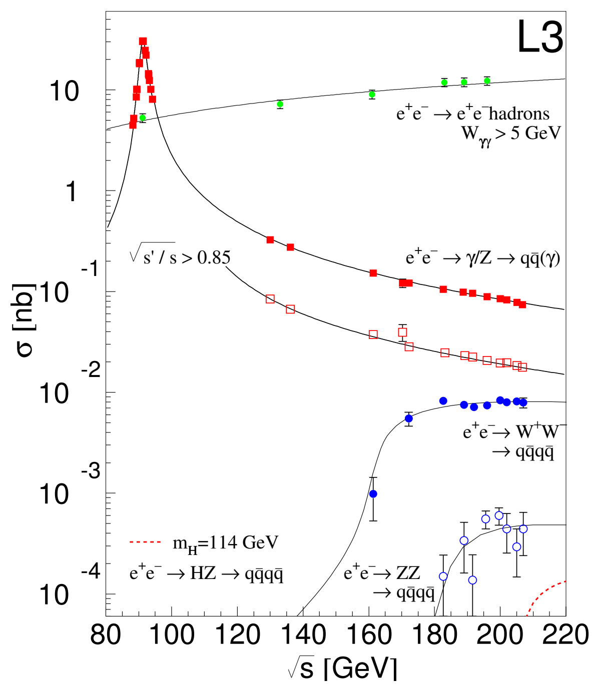

Figure 2.14: The cross sections of the main SM background processes as a function of center-of-mass energy.

Chapter 3

Analysis Methods

The searches for the Standard Model Higgs boson in L3 are mainly concentrated on the Higgs-strahlung process $e^+e^- \rightarrow HZ$, since it is the dominant production process of the Standard Model Higgs boson from an e^+e^- interaction at LEP2 energy (see section 1.5.1), and it constitutes the signal process for the discussions presented in this thesis.

There exists a variety of Higgs-strahlung final states when the specific decay modes of the Higgs boson and the Z boson are considered. Since the Standard Model Higgs boson couples to the fermions in proportion to their masses, the most likely decay of the Standard Model Higgs boson H, having a mass kinematically accessible at LEP2, would be $H\rightarrow b\bar{b}$ (about 75%). Some other decay modes of H that also offer opportunities to find the Higgs boson are $H\rightarrow \tau^+\tau^-$ (about 7.5%) and $H\rightarrow WW^*$ (about 8% at $m_H = 115$ GeV).

Combined with the main decay modes of the Z boson, which are $Z\rightarrow q\bar{q}$ (about 70%), $Z\rightarrow \nu\bar{\nu}$ (about 20%) and $Z\rightarrow \ell^+\ell^-$ (about 10%), the search for the Standard Model Higgs boson in L3 involves five distinct final state event topologies produced in the Higgs-strahlung process, namely, $q\bar{q}q\bar{q}$, $q\bar{q}\nu\bar{\nu}$, $q\bar{q}\ell^+\ell^-$ ($\ell = e, \mu, \tau$), $\tau^+\tau^-q\bar{q}$ and $WW^*f\bar{f}'$.

In this thesis, the so called leptonic channels are studied, which include two well separated leptons and two hadronic jets in the final state:

- the $HZ \rightarrow q\bar{q}e^+e^-$ channel,
- the $HZ \rightarrow q\bar{q}\mu^+\mu^-$ channel,
- the $HZ \rightarrow q\bar{q}\tau^+\tau^-$ channel and the $HZ \rightarrow \tau^+\tau^-q\bar{q}$ channel .

Although the branching ratios for these channels are small, the experimental signatures are very clear and (if found) the Higgs boson mass can be reconstructed with high resolution because of the more precise energy-momentum measurement of the leptons compared with those of quark jets that are often mixed with each other or of neutrinos that can not be measured at all. The evidence from the leptonic channels may therefore give the most convincing Higgs signal and the best measurement of the mass of the Standard Model Higgs boson.

This chapter will explain the main analysis strategies, and some common analysis techniques which were applied to the above mentioned channels.

The analysis is performed in 5 steps:

A. A high efficiency preselection. The aim of this step is to remove obvious background events that are very different from the signal. By making cuts on a set of variables, a lot of background events are removed while a very high signal efficiency for a broad range of possible signals is kept. As a consequence, the data sample is reduced dramatically for the continuing analysis steps. This analysis step is common for all leptonic channel analyses presented in this thesis and the subsequent analysis steps are specific for each channel.

B. An optimized selection based on lepton identification, topological and kinematic variables. According to the particular signature of the final state of the decay channel, a set of topological and kinematic variables, which have some distinguishing power between signal and background events, and the corresponding cuts are chosen to give the best analysis performance, *i.e.*, the best signal-to-background ratio, that allows a large sensitivity over a wide Higgs mass range (from 60 GeV up to the kinematic limit). Since the final state of each channel is composed of two leptons with two hadronic jets, the identification of leptons is very important for the analysis. This will be discussed in detail in the next section. The event topology is determined by the identified leptons and jets, where jet reconstruction will be explained in Sect. 3.3.

C. A kinematic fit taking into account energy and momentum conservation and the constraint that the lepton pair (or jet pair in the case of $\tau^+\tau^-\mathrm{q\bar{q}}$ channel) comes from a Z decay. At this step, the selected events have the topology of two well isolated leptons and two hadronic jets. Then a constrained kinematic fit is performed on the di-jet and di-lepton systems in order to improve the measurement resolution. This is accomplished by varying the four-momenta of the four reconstructed objects within their resolution while imposing the constraints, using the method of Lagrange multipliers, to minimize a χ^2 function which depends upon the measured values of the four objects' energies, angles and their assumed error matrix [57]. The constraints imposed by the kinematic fit are first a global four-momentum conservation in the event. This gives a four constraint or 4C fit. Adding the constraint on the di-lepton mass (or di-jet mass in the case of $\mathrm{HZ} \rightarrow \tau^+\tau^-\mathrm{q\bar{q}}$) to the Z boson mass makes it a 5C fit.

D. Construction of a powerful final discriminant variable to distinguish signal from background. The method to construct the binned likelihood final discriminant variable will be introduced in detail in Sect. 3.5. The Standard Model Higgs boson that is kinematically accessible at LEP2 will mostly decay into a pair of b quarks, while well known background processes have a much lower production rate of b quarks. Hence, whether or not the hadronic jets are from b hadrons is very powerful in characterizing Higgs events and is used to construct the final discriminant variable. The so-called "b-tagging" method to label and identify b quark jets is quite important for searching Higgs events and will be explained in Sect. 3.3.

E. Interpretation of data using the full spectrum of the discriminant variables. This will be discussed in the next chapter.

In order to make the analyses in a fast and straight forward way, a pre-processing method has been applied by the New Particles (NP) Group in the L3 experiment to reduce the complicated raw data to a more simple and convenient form called the NP Ntuple. The searches for the Standard Model Higgs boson described in this thesis are based on the information provided by this NP Ntuple.

3.1 Lepton identification

Five categories of leptons are identified. They are: **Electrons and Photons, Muons, Taus, Gap Electrons and Photons, MIPs (Minimum Ionizing Particles)**.

However, this information is obtained by quite loose requirements, and the accuracy of the identification of leptons is low, therefore, the contamination from background processes by mis-reconstruction is quite large. In order to get rid of more background and keep the selection with high purity, according to the signal characteristics of each investigated channel, more strict requirements are applied to identify the so called "good leptons" in order to make the lepton identification with more separation power between signal and background processes. So, two definitions for each lepton will be used for the lepton identification in the analyses.

3.1.1 Electron Identification

Electrons (or positrons) and photons are identified by narrow electromagnetic showers in the electromagnetic calorimeter. The energy is deposited in only a small number of adjacent crystals around the impact point of the particle, while hadrons cause a much wider shower shape (Fig. 3.1). To quantify the lateral shape of the shower, first the local maxima in the energy depositions are found and each associated with a so-called bump. A bump consists of the crystal with the local maximum energy and crystals around it above a certain threshold to avoid spurious noise contributions. The energy weighted position of the bump is thought to be the interaction point of a particle in the electromagnetic calorimeter. The lateral spread of the bump is measured by taking the ratio of the energy in a 3×3 crystal array centered on the bump center, E_9, and in concentric 5×5 crystal array, E_{25}. The variables E_9 and E_{25} are corrected for energy leakage of an electromagnetic shower:

$$E_{9\mathrm{cor}} = \frac{E_9}{b_0 \cdot \frac{E_1}{E_9} + b_1} \tag{3.1}$$

$$E_{25\mathrm{cor}} = \frac{E_{25}}{c_0 \cdot \frac{E_1}{E_{25}} + c_1}, \tag{3.2}$$

where b_0, b_1, c_0, c_1 are correction constants that depend on the different regions in the electromagnetic calorimeter and E_1 is the energy deposited in the central crystal. The ratio $E_{9\mathrm{cor}}/E_{25\mathrm{cor}}$ is usually close to one for electrons and photons, but much smaller for hadrons. Furthermore, a χ^2_{em} is defined that is a measure of the electron(photon)-likeness of the energy deposition. It is calculated by comparing the shower profile in a 3×3 crystal map around the most energetic crystal to that of an electron reference profile obtained in test beam measurements.

Since electrons, unlike photons,are charged, they interact with the gas in the central tracking chamber causing tracks which point to the bump measured in the BGO. This is the only difference used to distinguish between electrons and photons [54].

The so-called "good electron" is defined as passing the following requirements on electromagnetic shower shape in the BGO, on bump-track matching and on isolation:

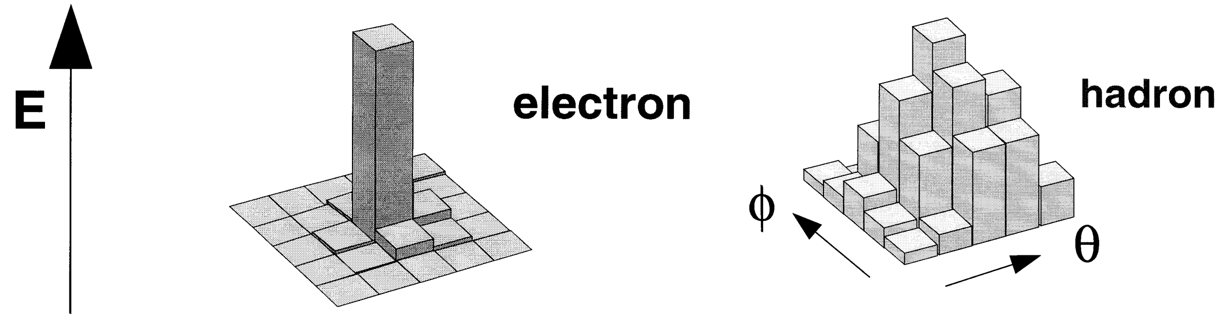

Figure 3.1: Typical shower shapes of an electron and a hadron in BGO.

- The energy ratio $E_{9\text{cor}}/E_{25\text{cor}}$ must be bigger than 0.98, the energy shower profile is electron(photon)-like and χ^2_{em} must be smaller than 35.
- A track must be matched to the bump within 20 mrad in ϕ and 200 mrad in θ, and the matched track should have a distance of closest approach to the interaction vertex (DCA) smaller than 10 mm.
- The bump energy measured in the BGO (E_{ECAL}) within a 10° cone of the matched track should be bigger than 1 GeV and the energy measured in the HCAL (E_{HCAL}) behind the bump should be less than 20% of the energy measured in the BGO (E_{ECAL}). The matched track should also have an absolute momentum value of at least 0.5 GeV.
- As isolation criteria, no additional tracks are allowed within a 100 mrad cone and no additional energy deposition in excess of 5 GeV within a 10° cone around the bump.

The above requirements for "good electron" are comparatively tight, and may cause a low signal efficiency. For example, if an electron impacts on a non-homogeneous region of the detector, the shower shape may deviate from a typical electromagnetic one. Furthermore, we may lose the track due to mismatches in the reconstruction or due to insensitivity of the TEC for tracks which are produced, for instance, at small angles with respect to the beampipe. In order to minimize the sensitivity loss due to badly reconstructed electrons, loose requirements are set to define the so-called "loose electron".

Objects that meet the following conditions qualify as a "loose electron":

- The energy ratio $E_{9\text{cor}}/E_{25\text{cor}}$ must be greater than 0.93, the bump energy measured in the BGO (E_{ECAL}) within a 10° cone of the matched track should be larger than 2 GeV and the energy measured in the HCAL (E_{HCAL}) behind the bump should not exceed 20% of the bump energy measured in the BGO (E_{ECAL}). There should be exactly 1 track matched within a 10° cone around the center of the energy deposition.

Additionally, the clusters in the gap between barrel and endcap BGO can also be accepted as a "loose electron" if the deposited energy in the gap (E_{GAP}) is more than 10 GeV, and there is a matched TEC track, but the number of tracks within a 20° cone around the gap cluster must be lower than 3. The energy measured in the HCAL (E_{HCAL}) should not exceed 20% of the energy measured in all calorimeters (E_{CAL}) in a 20° cone around the gap cluster.

The performance of the electron identification can be found in Fig. 3.2 from the distributions of $E_{9\text{cor}}/E_{25\text{cor}}$ and the track-bump matching in $\Delta\phi$ for a reference sample $e^+e^- \to e^+e^-$ [54]. There is good agreement between the data and the MC.

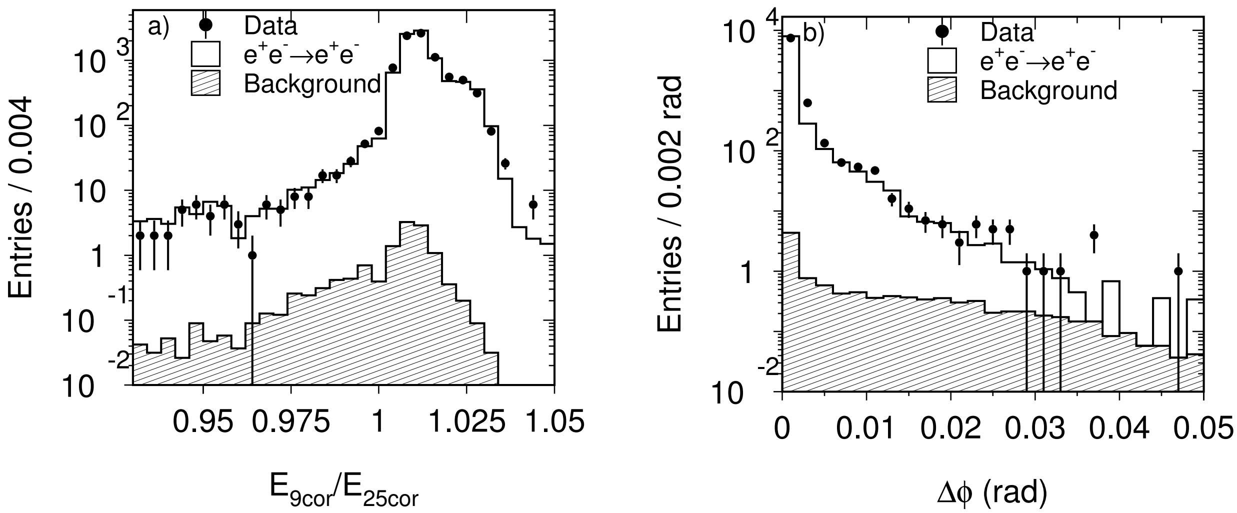

Figure 3.2: Distributions of a) corrected energy ratio $E_{9\mathrm{cor}}/E_{25\mathrm{cor}}$, b) track-bump matching in ϕ.

3.1.2 Muon Identification

Muons are characterized by tracks in the TEC and the muon chambers matching with a minimum ionizing signature in the calorimeters. The typical energy loss of muons in the BGO is about 200 to 300 MeV and in the hadron calorimeter about 2–3 GeV. This energy is localized in a very narrow cone involving only a small number of contiguous crystals and hits. Muons are the only observable particles that can penetrate the whole detector.

Similar to the electron identification, the "good muon" is defined as passing the following requirements on information of the muon chamber and track matching:

- At least one muon chamber track is required.
- This track must match one TEC track within 100 mrad in ϕ when it is traced back to the interaction point.
- The matching requirements for θ depends on the z information which is included in the TEC track fit. If both SMD and TEC-Z information are available, the matched track must be within 50 mrad in θ of a good TEC track. If only the SMD provides Z information, the matched track must be within 100 mrad in θ of a good TEC track. If both SMD and TEC-Z information are unavailable, the matched track must be within 200 mrad in θ of a good TEC track.
- In order to suppress cosmic ray contamination, the distance of closest approach to the interaction vertex in the plane perpendicular to the beam pipe, must not exceed 10 mm.

Muons that fail the above requirements can still be selected as a "loose muon" if the following conditions are met:

- Energy deposition in the calorimeter can be interpreted as arising from a minimum ionizing particle (MIP) comprising a small number (< 9) of clusters.
- There is exactly one matched TEC track within a $10°$ cone around the reconstructed direction.

- The calorimetric energy deposited between 10° and 30° around the reconstructed direction is less than 10% of the energy deposited within a 10° cone.

The possible induced contamination from WW $\rightarrow q\bar{q}\ell\nu(\ell = \mu, \tau)$ because of this loose selection can be suppressed by kinematic cuts, mass information and b-tagging in the analysis.

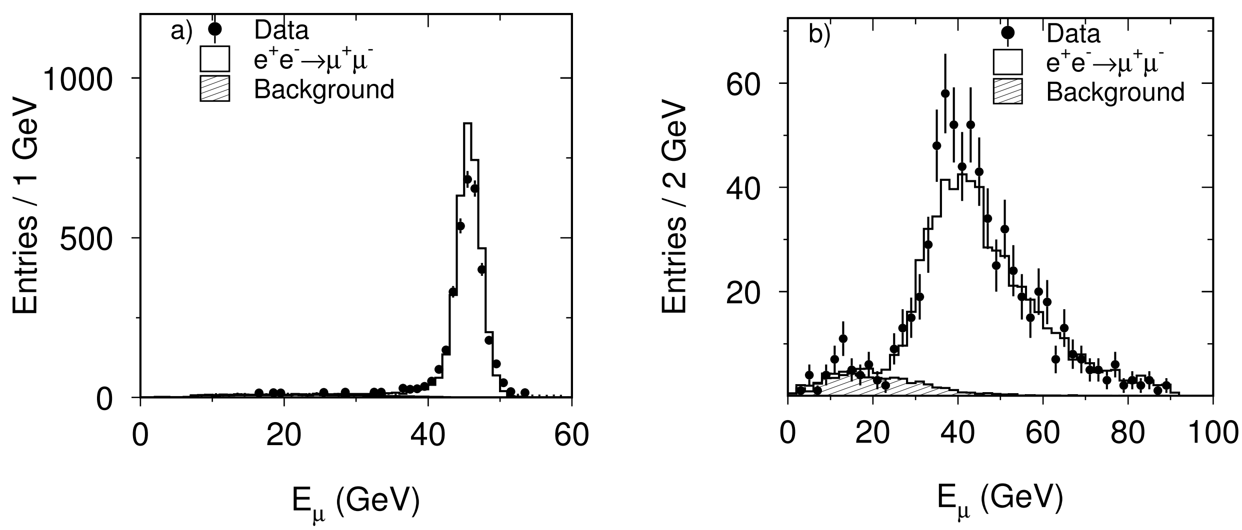

Figure 3.3: Distributions of muon energy for a) triplets, b) doublets of Z peak data.

Fig. 3.3 shows the energy distributions in the barrel for triplets (the muon is detected in all three muon chamber layers) and doublets (the muon is detected in only two muon chamber layers) [54]. The triplet muon is overestimated in the Monte Carlo simulation.

3.1.3 Tau Identification

Tau leptons have a short lifetime of about 290 fs, which, for a momentum of 45 GeV, corresponds to an average flight length of about 2 mm. Hence, they can be observed only through their visible decay products in the detector. These visible decay products carry part of the initial tau energy, while the other part goes into one or more neutrinos which escape undetected. Approximately 85% of the tau decays produce only one charged particle along with neutral decay products (1-prong decay), while approximately 15% of the decays produce three charged particles plus neutrals (3-prong decay). Each of the branching ratios of $\tau \rightarrow e\nu\nu$ and $\tau \rightarrow \mu\nu\nu$ are about 18% of the total tau decay.

Objects that are identified as "good electron" or "good muon" are also identified as tau leptons. In addition, low multiplicity jets are identified as tau leptons[1] if they meet the following requirements:

- There is only one or three tracks within a 10° cone around the reconstructed direction of the decay particles.

- The number of calorimetric clusters between 0° and 10° cone is limited to 8 and to 5 for the cone between 10° and 30°.

[1]The details of the jet clustering algorithm are discussed in the next section.

- The energy deposited in the 0° to 10° cone (E_{10}) must be greater than 2 GeV, and the calorimetric energy deposited between the 10° to 30° cone (E_{30}) must be smaller than 30% of E_{10}.
- The charge of the low multiplicity jets which is defined by summing up the signs of the track curvature, is ± 1.

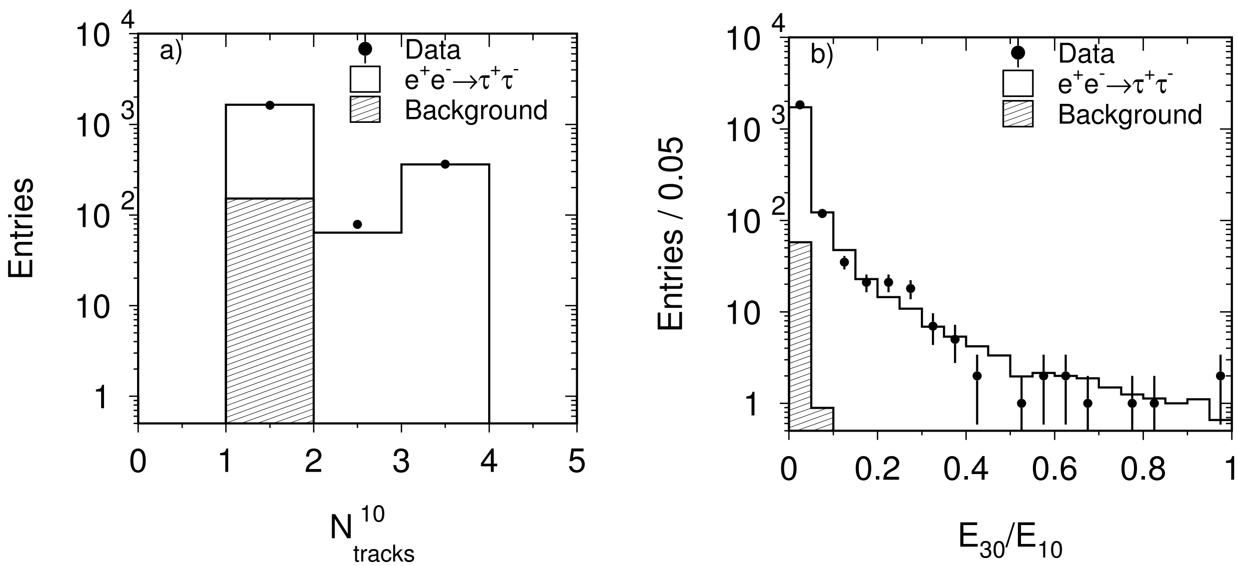

Figure 3.4: Distributions of a) number of tracks within a 10° cone around the reconstructed direction of τ, b) energy ratio E_{30}/E_{10} around the reconstructed direction of τ.

Fig. 3.4 shows the number of tracks in a 10° cone, N^{10}_{tracks} and the energy ratio E_{30}/E_{10} for a reference sample $\mathrm{e}^+\mathrm{e}^- \to \tau^+\tau^-$ [54]. The agreement between data and MC is good.

3.2 Durham Jet Clustering Algorithm

A Higgs boson with a mass relevant to LEP2 searches decays predominantly into a $\mathrm{b\bar{b}}$ quark pair. Quark pairs manifest themselves as jets of particles. Therefore, for the analyses dealing with hadronic events such as the search for the Higgs boson, it is very important to cluster, in an appropriate way, the final state charged and neutral particles to form jets which approximate the direction and energy of this initial parton. There are several algorithms for jet clustering, *e.g.*, the JADE [55] and Durham [56] algorithms, which are widely used in high energy physics studies. The Durham jet algorithm is used in this thesis, and has the advantage of a better treatment of low energy particles.

Using this algorithm, all possible energy measurements of particles (momentum measurements from the TEC+SMD, clusters of calorimeter energy, and momentum measurements from the muon chambers) are used to combine individual particles into pseudo-particles. Two particles, i and j, are combined into a pseudo-particle k if the parameter

$$y_{ij} = 2\frac{\min(E_i^2, E_j^2)}{E_{\mathrm{vis}}^2}(1 - \cos\theta_{ij}) \tag{3.3}$$

has the smallest value of all possible pairings, and also y_{ij} is below some fixed cutoff y_{cut}, where E_i and E_j are the energies of the particles, θ_{ij} is the opening angle between them and E_{vis} is the total visible energy in the event. The above procedure is then repeated until no value of y_{ij} is below the cutoff. The remaining pseudo-particles are called jets.

The value of $y_{\rm cut}$ where the configuration of the pseudo-particles changes from three to four is called $Y_{34}^{\rm D}$ and indicates how four-jet-like an event is.

3.3 B-tagging

In the Standard Model, a Higgs particle which is kinematically accessible at LEP is expected to decay into a pair of b quarks in at least 75% of the cases. On the other hand, background processes have a much lower production rate of b quarks. Hence, identifying that a jet is due to a b quark is a powerful tool to separate the Higgs event from background, and this information is used to construct the final discriminant variable. So, the so-called "b-tagging" technique to label and identify b quark jets is one of the most important analysis steps in the search for Higgs events.

B-tagging is mainly based on the fact that hadrons containing b quarks have relatively long lifetimes, typically about 1.5×10^{-12} s, while other hadrons containing only light quarks have either much shorter or much longer lifetimes, such as, for example, $\mathrm{K}_{\mathrm{s}}^0$ or Λ^0 that decay far away from the region where b hadrons typically decay.

Apart from lifetime, there are other aspects of b hadron decays that can be used to distinguish b hadrons from others, such as a higher charged particle multiplicity and the mass at the decay point, tertiary decay vertices from cascade decays, different jet shapes and prompt leptons from semileptonic b decays. The L3 b-tagging technique takes advantage of all of these distinguishing features of b decays to make a high purity, high efficiency b-tag. A detailed description of the b-tagging procedure can be found in references [58,59]. The main procedures are summarized in the following.

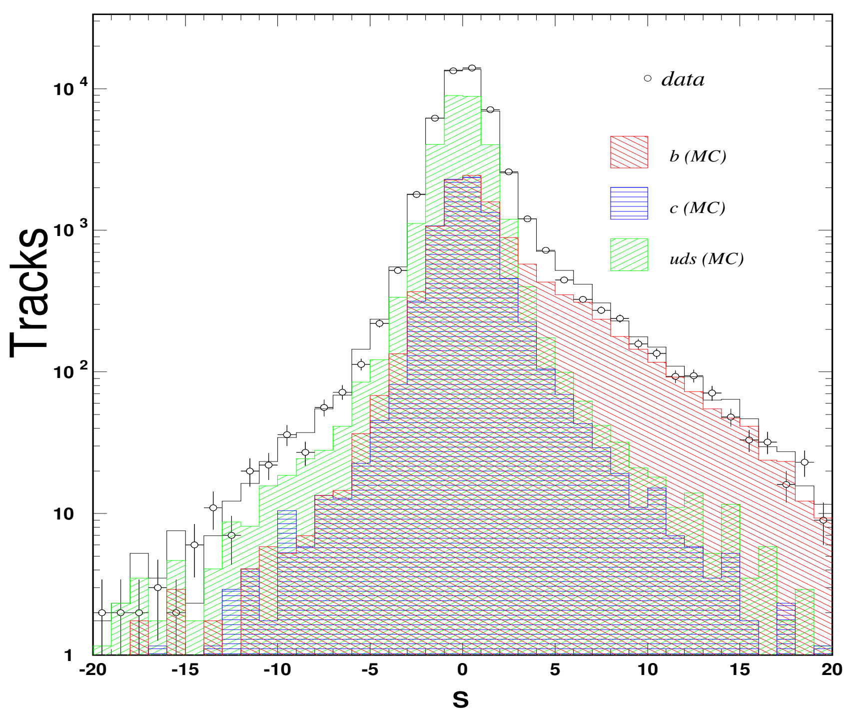

Figure 3.5: The decay length significance, $S = L/\sigma_L$, for tracks in the 1996 Z-peak data.

The first piece of tagging information comes from a discriminant based on the decay length and hence the lifetime information. Firstly, the 3-dimensional (3-D) primary vertex of the event is reconstructed. Secondly, for every track, the crossing point of the track with the axis of the jet containing it is calculated, and the decay length L of the track is evaluated by computing the distance between the crossing point and the primary vertex. This decay length is signed with the convention that it is positive if the crossing point lies along the jet axis in the supposed direction of flight of the original quark. Otherwise, it is negative. Then, in order to facilitate the combination of decay length information from more than one track in the event, the probability that a given track originates from the primary vertex is estimated using the distribution of decay length significance, $S = L/\sigma_{\mathrm{L}}$ (where σ_{L} is the error on decay length), for tracks which are assumed to have originated from the decays of particles with no discernible lifetime. The distribution of decay length significance is expected to be asymmetric for events with b quarks. The positive side of the distribution is enhanced due to the fact that not all tracks originate from the primary vertex. Fig. 3.5 shows the decay length significance for tracks of the 1996 data [59]. Assuming that tracks with negative S come from primary vertex and that the probability density function $f(S)$ is symmetric around zero, the negative side of significance distribution can be used to determine the probability density function $f(S)$. The confidence level that a track with a significance S originates from the primary vertex is:

$$P(S) = \frac{\int_S^\infty f(s')\mathrm{d}s'}{\int_0^\infty f(s')\mathrm{d}s'}. \tag{3.4}$$

A track originating from a b quark will have a large significance S and hence small $P(S)$. Finally, the individual track probabilities are weighted depending on the decay length resolution and their momenta, and are combined into a weighted probability P_n^{W}, where n denotes the number of tracks which are included in one jet. Jets with b quarks will have low values of P_n^{W}.

To further improve the b-tagging performance, an artificial neural network is used to take advantage of the distinguishing features of b decays, other than just lifetime information. The neural network input variables include the above lifetime information (which is the most powerful input variable), information about possible reconstructed secondary vertices, momenta of inclusive leptons and jet shape variables such as the boost and the sphericity.

The b-tagging neural network output spectrum for calibration data taken at the Z peak in 1997 can be seen in Fig. 3.6 [59]. The composition in terms of quark flavors for this sample of Z decays is known accurately from LEP1 analyses.

3.4 The Final Discriminant Variable

In this step of the analysis, a single, powerful discriminating variable is constructed from the most important variables that characterize a Higgs event using a binned likelihood technique.

The discriminant variable F_{HZ} of each event is determined as follows:

- Firstly, calculate the probability that an event belongs to the event class j,

  (j=(WW, qq, ZZ, Zee, HZ)), based solely on the value of the variable i :

$$p_j^i = \frac{f_j^i}{\Sigma_k f_k^i}, \tag{3.5}$$

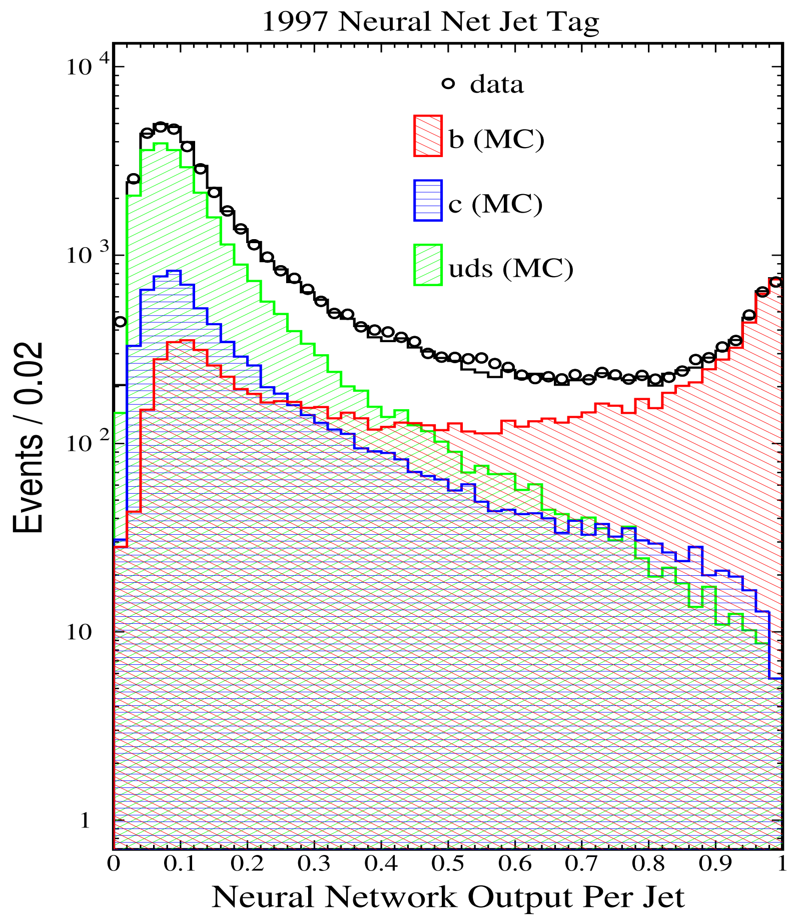

Figure 3.6: The output of the neural network for jet tag in 1997 Z-peak data.

in which f_j^i is the probability density function of variable i, which has discriminating power between the signal class and background classes, for a certain event class j. The functions f_j^i are derived from Monte Carlo simulations

- A likelihood F_{HZ} is made by combining the above probabilities for different variables i to describe the possibility that each event belongs to the signal class HZ:

$$F_{\text{HZ}} = \frac{\prod_i p^i_{\text{HZ}}}{\sum_j \prod_i p^i_j}, \tag{3.6}$$

where j runs over all event classes and i over all of the variables considered. It is easy to see that $0 \leq F_{\text{HZ}} \leq 1$.

In this thesis, the reconstructed Higgs mass and the b-tagging values of two hadronic jets are used to construct the final discriminant variable, except for the HZ$\rightarrow$ $\tau^+\tau^-\mathrm{q\bar{q}}$ channel, where only the reconstructed Higgs mass is used as the final discriminant variable because the Z boson does not decay predominately to $\mathrm{b\bar{b}}$ quark pair as the Higgs boson does.

The discriminant variable F_{HZ} can be used as an input parameter to estimate the confidence level to exclude the existence of a signal, and give the Higgs mass limit by combining all the information from different channels and different energies and even different experiments.

Chapter 4

Event Selections for the Leptonic Channels

The event selections described in this chapter are designed to find evidence of the Higgsstrahlung process with two highly energetic leptons in the final states (the leptonic channels) by rejecting the Standard Model background processes. As mentioned in chapter 3, the leptonic channels are defined to include the Higgs boson decaying to $\mathrm{q\bar{q}}$ (mostly $\mathrm{b\bar{b}}$) or gg and Z boson decaying to $\ell^+\ell^-$ (denoted as $\mathrm{H}\ell^+\ell^-$ or $\mathrm{q\bar{q}}\ell^+\ell^-$), and the Higgs boson decaying to $\tau^+\tau^-$ and Z boson decaying to $\mathrm{q\bar{q}}$ (denoted as $\tau^+\tau^-\mathrm{q\bar{q}}$). Apart from the two highly energetic leptons, there are two hadronic jets in the final states of these leptonic channels. For $\mathrm{H}\ell^+\ell^-$, the two hadronic jets mostly originate from the decay of a b quark and have high b-tagging probability. For $\tau^+\tau^-\mathrm{q\bar{q}}$, the primary quarks of these two hadronic jets come from a Z boson and thus the invariant mass of these two hadronic jets is close to the mass of the Z boson.

Processes that can mimic the leptonic channels will contaminate the selected sample. The important background processes that can contaminate the selection by having similar topologies are $\mathrm{e^+e^-} \to \mathrm{Z}^*/\gamma^* \to \mathrm{q\bar{q}}$, $\mathrm{e^+e^-} \to \mathrm{W^+W^-}$, $\mathrm{e^+e^-} \to \mathrm{ZZ}$ and $\mathrm{e^+e^-} \to \mathrm{Ze^+e^-}$.

For the $\mathrm{H}\ell^+\ell^-$ signal, the b-tagging helps to remove much of this contamination from the selected sample because the backgrounds have a much lower branching ratio into b quarks than the signal.

After describing the data and Monte Carlo samples for this analysis in Sect. 4.1, the event selection will be discussed in Sect. 4.2 together with a preselection to eliminate the large amount of dissimilar background processes. In Sects. 4.3 − 4.5, the individual optimized selections of the different signal processes are discussed. Finally, the statistical and systematic uncertainties for the event selections are estimated in Sect. 4.6.

4.1 Data and Monte Carlo Samples

During the year 2000, LEP ran at several center-of-mass energies. Fig. 4.1 shows the luminosity distribution for the data collected by L3 in the year 2000. The data are grouped into seven samples corresponding to average center-of-mass energies between 202.8 GeV and 208.6 GeV. The integrated luminosities corresponding to these samples are given in Tab. 4.1. The total integrated luminosity is 217.3 pb^{-1}.

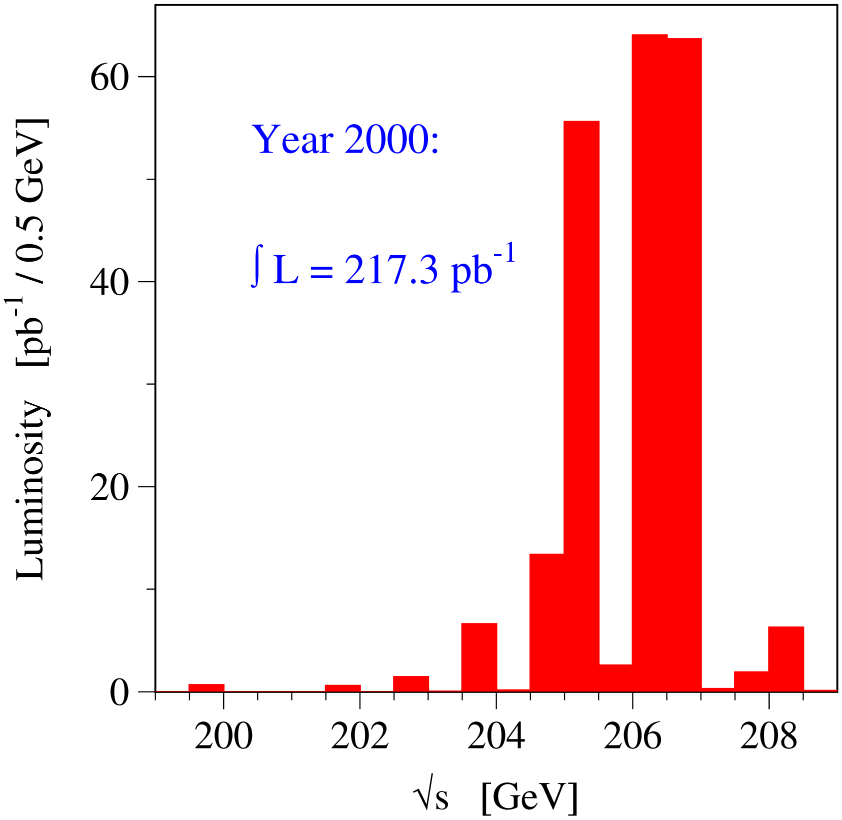

Figure 4.1: The luminosity distribution for the data obtained in the year 2000 with the L3 detector

average $\sqrt{s}$ (GeV)	202.8	203.8	205.1	206.3	206.6	208.0	208.6
Luminosity (pb^{-1})	2.7	7.6	68.1	66.9	63.7	8.2	0.1

Table 4.1: The average center-of-mass energies and the corresponding integrated luminosities of the data samples collected by L3 detector in the year 2000.

The Higgs production cross sections and branching ratios are calculated using the HZHA generator [28]. The Monte Carlo samples for signal events are simulated with PYTHIA [60] at each center-of-mass energy as shown in Tab. 4.1, for a Higgs mass (m_{H}) between 60 GeV and 100 GeV, in steps of 5 GeV, and for m_{H} between 100 GeV and 120 GeV, in steps of 1 GeV. For each Higgs mass and search channel, between 1000 and 10000 events are generated.

The Standard Model background samples are simulated using the following Monte Carlo programs: KK2f [50] for $\mathrm{e^+e^-} \rightarrow \mathrm{q\bar{q}}(\gamma)$, KORALW [51] for $\mathrm{e^+e^-} \rightarrow \mathrm{W^+W^-}$, EXCALIBUR [52] for $\mathrm{e^+e^-} \rightarrow \mathrm{ZZ}$ and $\mathrm{e^+e^-} \rightarrow \mathrm{Ze^+e^-}$ processes. As an example, the numbers of generated events for these backgrounds, as well as the cross section of each process, corresponding to the center-of-mass energy of 206.6 GeV, are shown in Tab. 4.2.

The GEANT program [19] is used to simulate the response of the L3 detector, taking into account the effects of multiple scattering, energy loss and showering in the detector. Hadronic

Background Process	$e^+e^- \to q\bar{q}(\gamma)$	$e^+e^- \to W^+W^-$	$e^+e^- \to ZZ$	$e^+e^- \to Ze^+e^-$
Monte Carlo Generator	KK2f	KORALW	EXCALIBUR	EXCALIBUR
Cross Section (pb)	81.1	17.5	1.33	3.58
Number of Simulated Events	909400	407750	62792	79767

Table 4.2: Cross sections and number of Monte Carlo simulated events for main background processes at the center-of-mass energy 206.6 GeV.

interactions in the detector are modelled using the GHEISHA program [20]. Time dependent detector inefficiencies, as monitored during the data taking period, are also simulated [67].

All of the event selections in this analysis are based on the information in the L3 New Particle (NP) Ntuple containing data in reduced format after pre-processing of the raw data.

In the following description of the event selection, only the data taken at the center-of-mass energy range 206.5 GeV$< \sqrt{s} <$ 207.5 GeV (average energy 206.6, see Tab. 4.1) and the corresponding signal and background samples are discussed as the selection applied for other energy bins are the same. As a reference, a signal process with a Higgs mass hypothesis of $m_H = 115$ GeV is used.

4.2 Preselection

The preselection corresponds to the first step outlined in Sect. 3.1, and has the basic aim of removing the "obvious" background events. Background events from the two-photon process have very low particle multiplicity and low visible energy. This is also true for four-fermion processes without hadronic jets (*i.e.*, $ZZ \to \ell^+\ell^-\ell^+\ell^-$, $W^+W^- \to \ell^+\bar{\nu}\ell^-\nu$). Radiative Z return ($q\bar{q}\gamma$) background events in which the initial state radiation (ISR) photons escape into the beam pipe have a large amount of missing energy and can be rejected by a requirement on the visible energy. Therefore, hadronic events are selected by placing requirements on the number of good charged tracks and on the fraction of visible energy over the available invariant mass.

For this preselection, at least 5 charged tracks, 15 calorimeter clusters and 4 scintillator hits between the BGO and HCAL are required. The fraction of visible energy to the center-of-mass energy must exceed 0.45. Fig. 4.2 shows the distributions of the number of scintillator hits (NSCT), the number of charged tracks (NGTK), the number of calorimeter clusters (NCLCA) and the fraction of visible energy (XVIS) for data, background processes, and the signal after other cuts are applied. The corresponding cut criteria are also displayed on the plots.

All the leptonic channels have the same topologies with two well-separated highly energetic lepton particles. A very basic requirement applied at this stage is that at least two leptons are found in the final state or that there are at least two hadronic jets with multiplicity not exceeding 3 tracks when the event is forced into 4 jets, to take into account the possible hadronic decays of τ leptons (see Fig. 4.3).

This preselection removes virtually almost two-photon events and leaves only two- and four-fermion background processes that contain jets from at least two primary quarks, while it maintains a high signal efficiency over a broad range of possible Higgs masses. The preselection efficiencies for various Higgs masses of each signal process are listed in the Tab. 4.3.

After preselection, 4219 events remain in the data, and in the Monte Carlo, 2978.4 events from $q\bar{q}\gamma$, 688.9 events from W^+W^-, 46.9 events from ZZ and 73.2 events from Ze^+e^- background processes respectively. In total there are 3787.4 events from background processes.

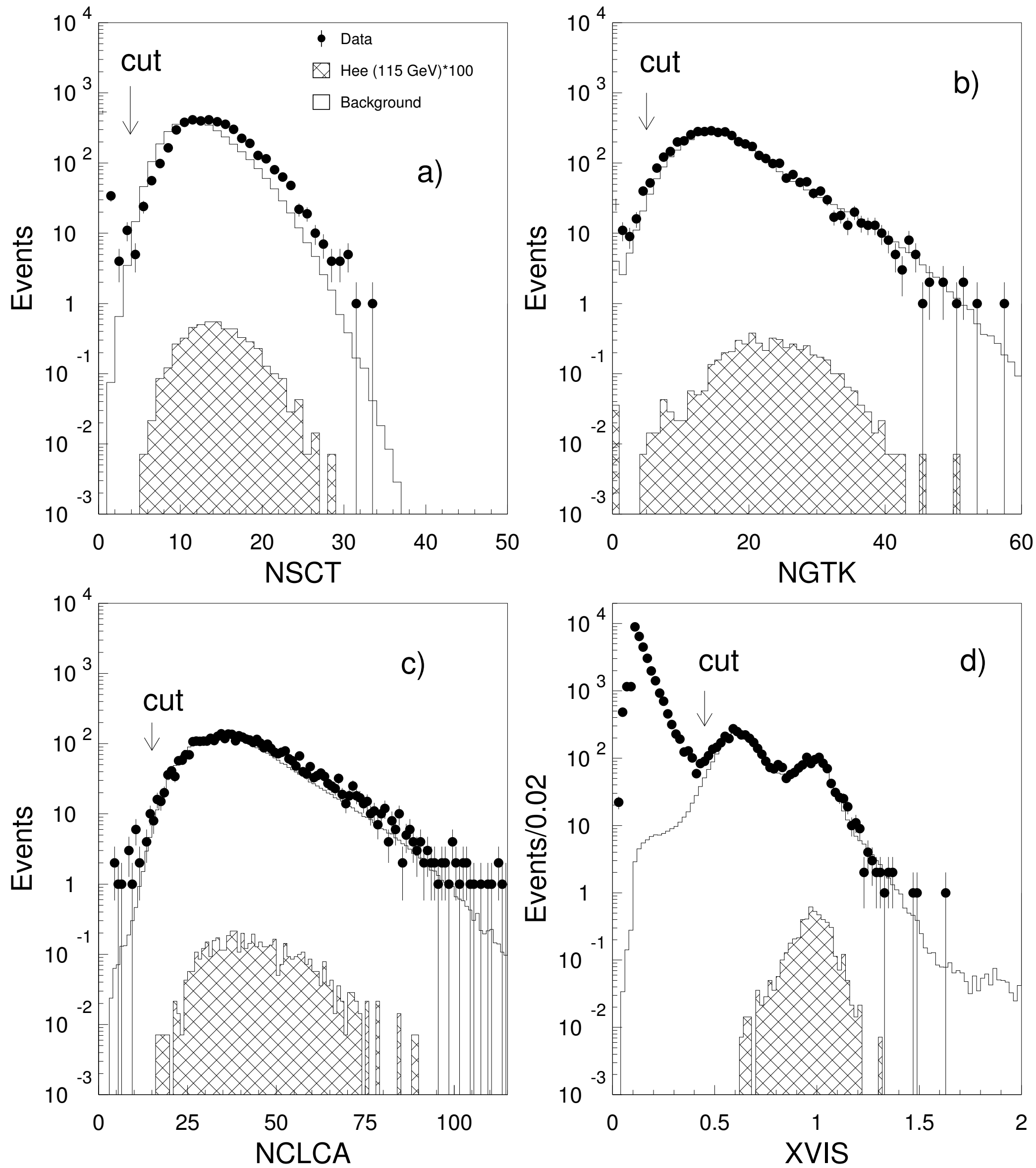

Figure 4.2: The distributions of a) number of scintillator hits (NSCT), b) number of charged tracks (NGTK), c) number of calorimeter clusters (NCLCA) and d) the fraction of visible energy (XVIS), after other cuts are applied .

The existing data discrepancy at this stage comes from the remains of two-photon processes, which are not considered in the Monte Carlo samples, and will be eliminated by the optimized selections *e.g.*, by requiring events with highly energetic leptons and a four-jet topology. This discrepancy will not exist after the final of event selection and has no impact on our results. After this preselection, optimized cut based selections are applied to particular channels respectively.

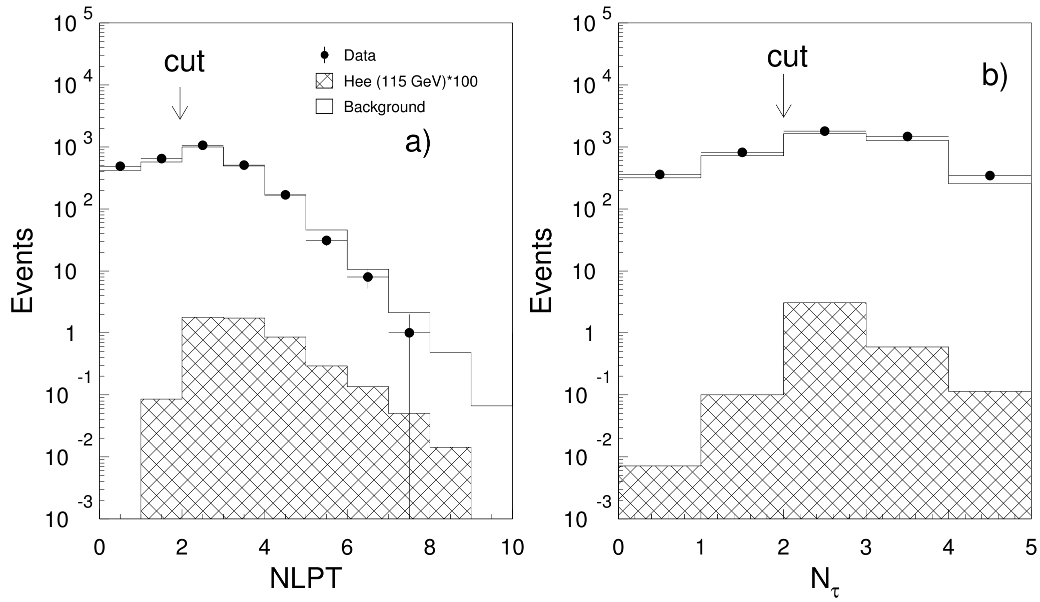

Figure 4.3: The distributions of a) number of leptons, b) number of jets with fewer than four tracks when the event is forced to 4 jets.

Signal process	Efficiency (%) on m_H = (GeV)									
	70	80	85	90	95	100	105	110	115	120
He^+e^-	98.6	98.3	98.6	98.4	97.5	98.6	97.6	97.4	96.8	97.9
$H\mu^+\mu^-$	96.1	96.4	96.3	95.0	94.7	94.7	93.4	93.2	93.1	95.1
$H\tau^+\tau^-$	94.5	92.8	93.1	90.9	89.7	89.9	90.6	88.9	88.8	85.7
$\tau^+\tau^- q\bar{q}$	95.1	95.2	95.2	93.9	94.5	93.2	92.8	92.9	91.6	92.4

Table 4.3: Preselection efficiencies for different signal processes of various Higgs masses at $\sqrt{s} = 206.6$ GeV

4.3 The HZ $\rightarrow q\bar{q}e^+e^-$ channel

The signature of the HZ$\rightarrow q\bar{q}e^+e^-$ process is a pair of well-separated highly energetic electrons with an invariant mass near the mass of the Z boson m_Z; accompanied by two hadronic jets which originate from the decay of the Higgs boson and usually contain b-quarks.

The process ZZ $\rightarrow q\bar{q}e^+e^-$ has a very similar topology as the signal and can not very well be separated from the signal. So it contributes the largest fraction of the background. This process becomes especially severe for a Higgs mass hypothesis near the mass of the Z boson. Other background sources are $e^+e^- \rightarrow Ze^+e^-$, $e^+e^- \rightarrow q\bar{q}$ and $e^+e^- \rightarrow W^+W^-$. The latter two contribute for a sizeable fraction to the background in the case of misidentified electrons, although they have different topologies from the signal.

After the preselection stage, for the selection of He^+e^- events, at least two well identified electrons with opposite charge are required. If there are more than 2 electron candidates in one event, the pair, of which the invariant mass is closest to m_Z, is chosen. Furthermore, at least one of the selected electrons should be a "good electron" to suppress more background. The other one can be either a "good electron" or a "loose electron" in order to keep the efficiency high. The "loose electron" obviously opens a gate for background processes such as radiative $q\bar{q}(\gamma)$ and WW $\rightarrow q\bar{q}'\ell\nu(\ell = e, \tau)$. However, these processes can be suppressed by other kinematic cuts, mass information and b-tagging. As we know that both electrons come from the Z boson, we can make the requirement that both electron's energies should be larger than 25 GeV. After that, most of the fully hadronic decays of WW and ZZ processes are rejected.

A cut on missing transverse momentum is placed to further reduce the WW $\rightarrow q\bar{q}'e\nu$ and $q\bar{q}(\gamma)$ background.

The particles left after removing the two electrons are clustered into two jets using the Durham algorithm. Here the logarithm of the Durham jet algorithm parameter $Y_{34}^{\rm D}$ should be larger than -7. There should be a separation between the leptons with the jets of at least 5°.

The opening angle of the electron pair is demanded to be larger than 50°, and that of the jet pair also larger than 50°. These two cuts are set loosely and allow a good sensitivity over a wide range of hypothetical Higgs masses.

A kinematic fit (4C fit) is performed which imposes energy and momentum conservation to determine the invariant mass of the two electron system. This must be around $m_{\rm Z}$, *i.e.*, 60 GeV$\leq m_{\rm ee} \leq$ 110 GeV.

The full set of cuts and the corresponding events left over for real data and background MC, together with the selection efficiency for signal MC can be found in Tab. 4.4. The distributions of some variables and the corresponding cuts used for the selection are displayed in Fig. 4.4.

Definition of selection steps	Data	Background Processes					Signal Efficiency
		WW	QQ	ZZ	Zee	Total	$(m_{\rm H} = 115$ GeV$)(\%)$
$N_{\rm tracks} \geq 5$,$N_{\rm clusters} \geq 15$, $E_{\rm vis}/\sqrt{s} \geq 0.45$	4219	688.9	2978.4	46.9	73.2	3787.4	96.8
2 Electrons	157	76.6	59.2	6.8	4.2	146.7	82.5
$E_{\rm el2} \geq 25$ GeV , $P_{\rm T}^{\rm Missing}/E_{\rm vis} < 0.2$	15	6.8	1.8	3.7	0.7	13.0	76.8
$\alpha_{\rm ee} \geq 50°$, $\alpha_{\rm qq} \geq 50°$	12	3.4	1.8	3.7	0.7	9.6	76.1
$\ln(Y_{34}^{\rm D}) \geq -7$	7	1.4	0.8	3.1	0.5	5.8	75.2
$60 \leq m_{\rm ee}^{\rm 4c} \leq 110$ GeV, $m_{\rm qq}^{\rm 5c}/m_{\rm qq}^{\rm 4c} \geq 0.7$	5	0.8	0.5	2.8	0.2	4.3	72.1

Table 4.4: Comparisons of data with expectations from the Standard Model background processes for each selection step of the HZ$\rightarrow q\bar{q}e^+e^-$ channel. The signal efficiency is given for Higgs mass hypothesis $m_{\rm H} = 115$ GeV.

At this stage, 5 candidates were observed with a background expectation of 4.3 events. The background is mostly contributed by ZZ(65.1%), while smaller contributions come from $q\bar{q}$(11.6%), WW (18.6%) and Zee (4.7%). A typical candidate is shown in Fig. 4.5.

As the most important variables, the b-tagging variable of the two hadronic jets and the Higgs mass are exploited to construct a final discriminant variable using the technique described in the previous chapter. Fig. 4.6 shows the b-tagging and the reconstructed Higgs mass (recoil mass of the two electron system) distributions.

The final discriminant variable distribution for a Higgs mass hypothesis of 115 GeV is shown in Fig. 4.7(a), for data, expected background and signal. The same distribution is obtained for a series of Higgs mass hypotheses (in steps of 1 GeV from 70 GeV to 90 GeV, step of 100MeV from 90 GeV to 120 GeV).

No deviation from the background expectation is observed. No significant candidate is observed with a high final discriminant variable value. By integrating from right to left, one

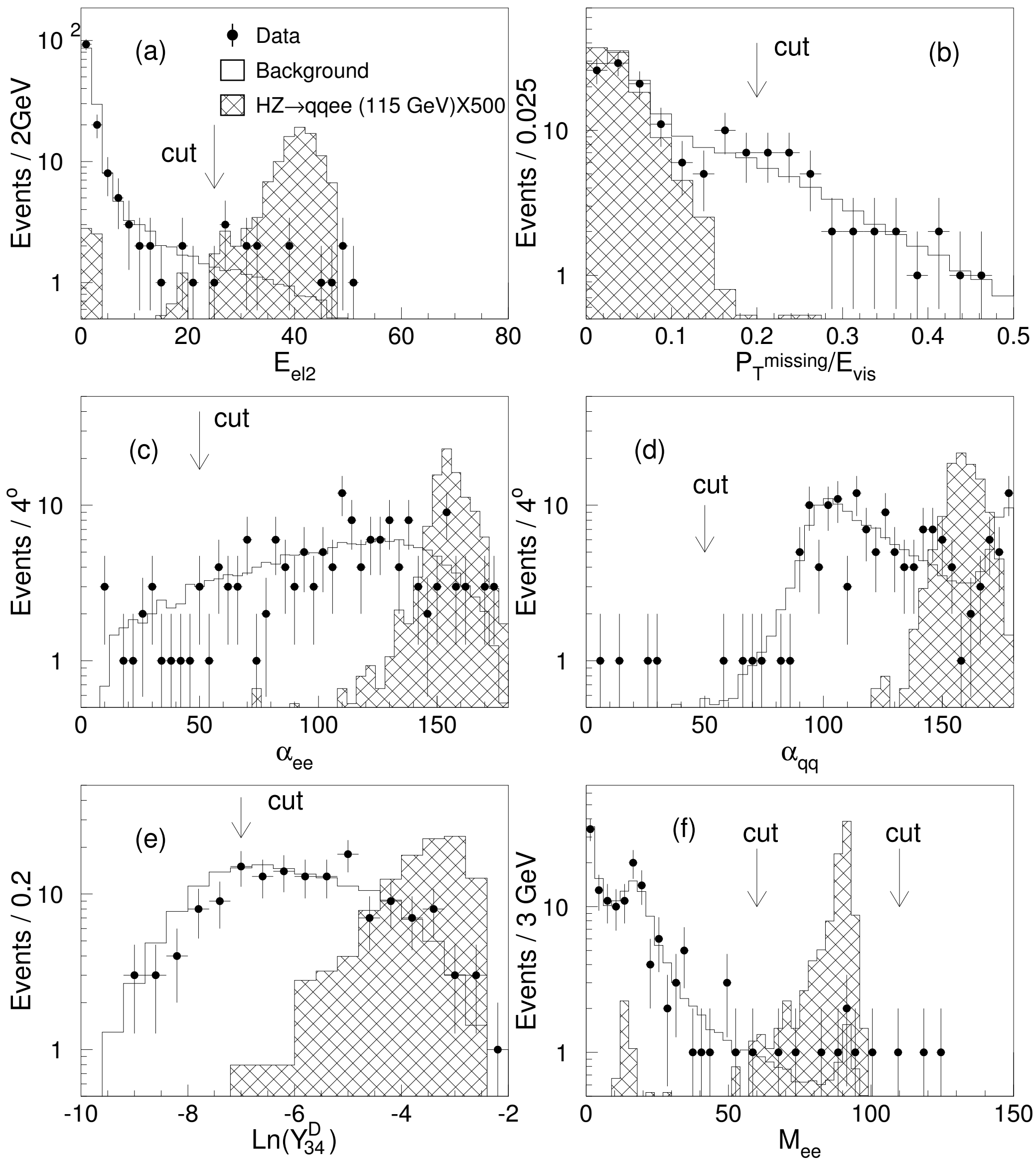

Figure 4.4: The distributions of (a) the energy of the second most energetic electron, (b) the transverse imbalance, (c) the opening angle of the elctron pair, (d) the opening angle of the jet pair, (e) the logarithm of the Durham jet algorithm parameter Y_{34}^{D}, (f) the invariant mass of the electron pair after imposing energy and momentum conservation, for the HZ→ $\mathrm{q\bar{q}e^+e^-}$ channel after the two candidates of electron from Z boson are determined and the corresponding particles are clustered into two jets as described in the text.

can get an impression of the analysis performance. In this way, Fig. 4.7 (b) is obtained, plotting the number of background events expected versus the expected number of signal events. At corresponding cut values of the final discriminant variable, the observed number of data events is plotted as well.

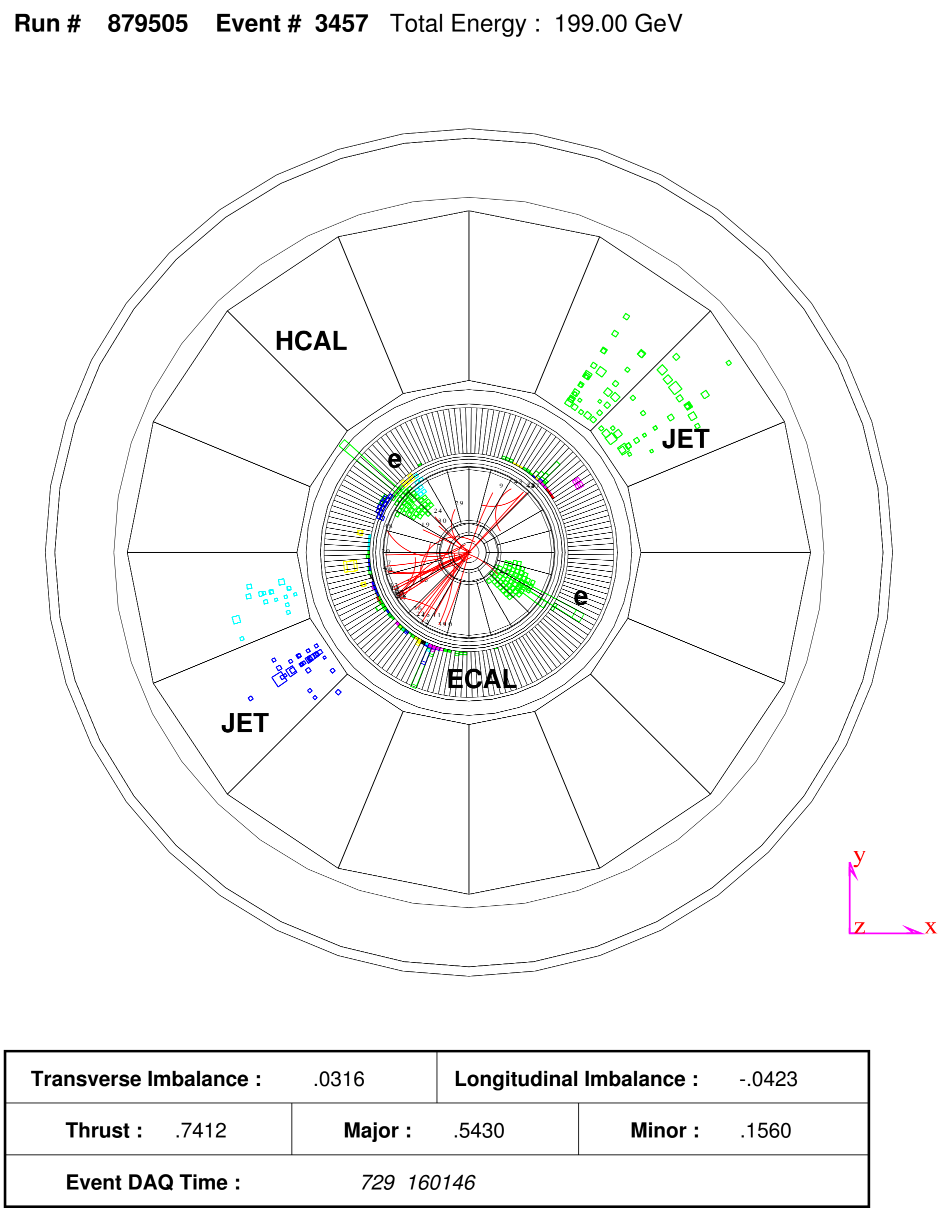

Figure 4.5: A candidate event for the HZ→ $q\bar{q}e^+e^-$ channel. The invariant mass of the electron-positron system is 91.2 GeV, and the recoil mass for the jet system is 98.3 GeV.

4.4 The HZ $\rightarrow q\bar{q}\mu^+\mu^-$ channel

This channel is quite similar to the HZ $\rightarrow q\bar{q}e^+e^-$ channel, and a similar method is applied for its analysis.

The signature for this channel is a pair of highly energetic muons, with an invariant mass close to m_Z, accompanied by two hadronic jets, mostly from b-quarks .

The main Standard Model background processes are: $e^+e^- \rightarrow q\bar{q}$, $e^+e^- \rightarrow W^+W^-$, and

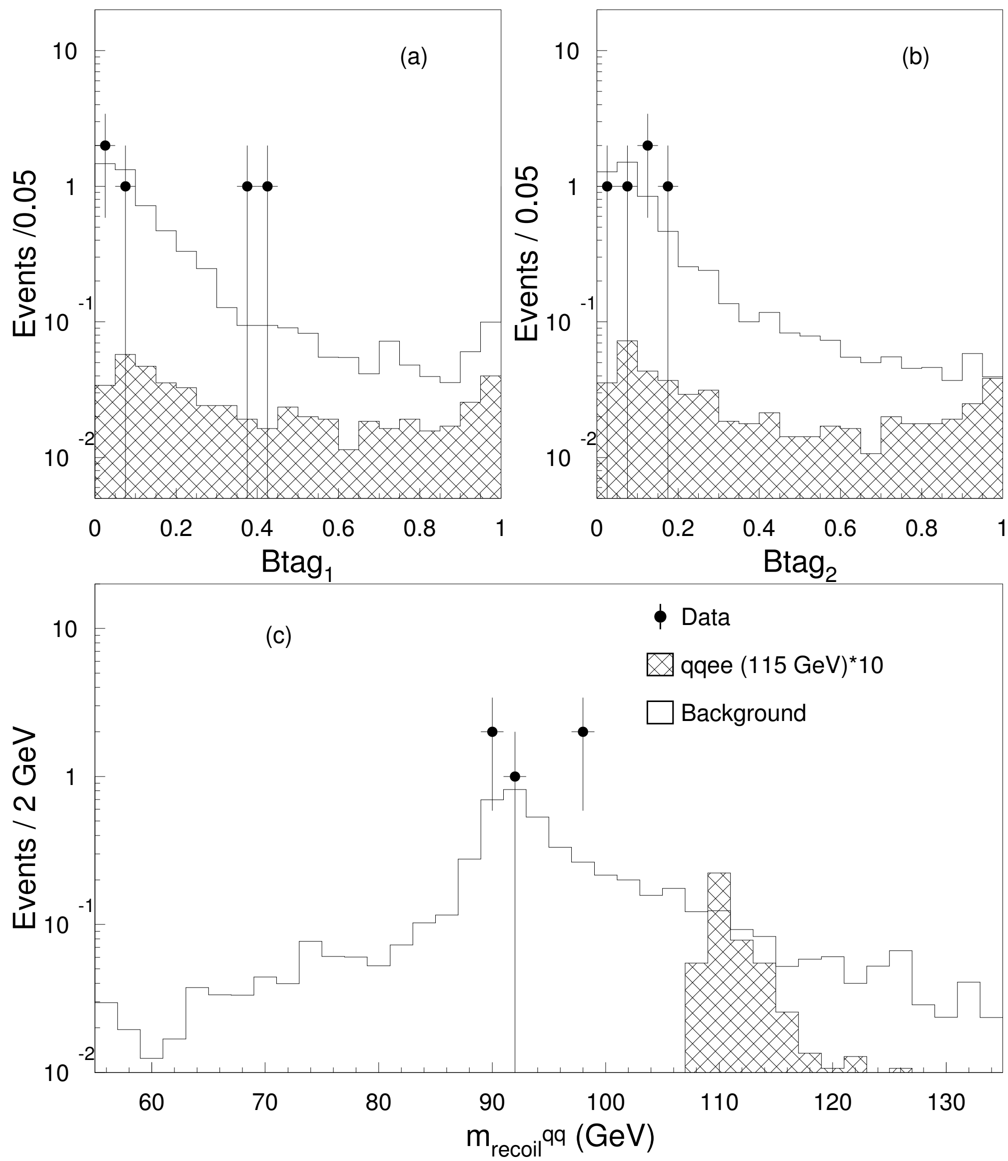

Figure 4.6: Distributions of (a) the b-tagging variable of the most energetic jet, (b) the b-tagging variable of the second jet, (c) the recoil mass of the electron-positron system after imposing energy and momentum conservation. These 3 variables are used to construct the final discriminant variable in the HZ→ $q\bar{q}e^+e^-$ channel.

$e^+e^- \rightarrow$ ZZ. The process ZZ $\rightarrow q\bar{q}\mu^+\mu^-$ has a topology very similar to that of the signal, and contributes the largest fraction to the background.

A hadronic event pre-selection is applied requiring at least 5 charged tracks, 15 calorimetric clusters and a visible energy of more than $0.45\sqrt{s}$.

Then, at least two well identified muons with different charges are required. If there are more than 2 muon candidates in one event, the pair having the invariant mass closest to m_Z is chosen. Furthermore, at least one of the selected muons should be a "good muon". The other one could be a "loose muon". After the above requirements, 14 events remain in the data whereas 15.8 are expected from Standard Model background processes. The signal efficiency

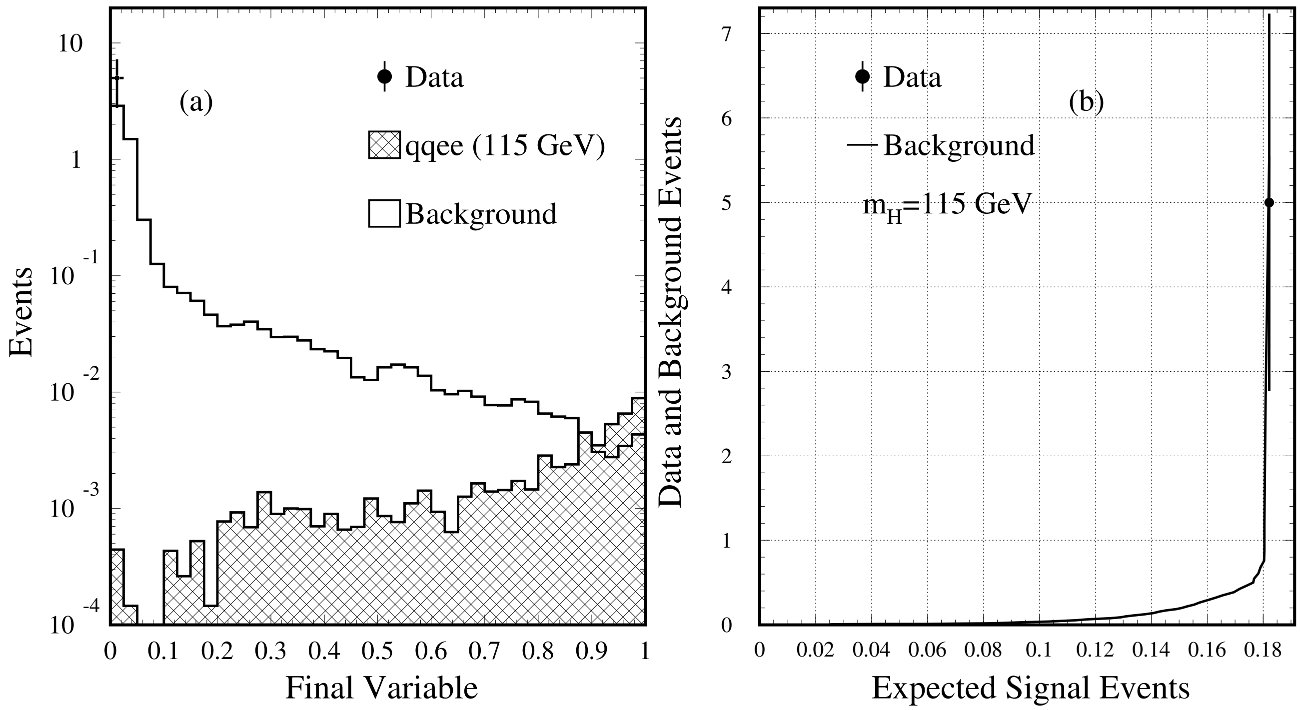

Figure 4.7: (a): The final discriminant variable distribution for the HZ→ $q\bar{q}e^+e^-$ channel for a Higgs mass hypothesis of 115 GeV. (b): Number of data events and background expectation versus the expected number of signal events for various cuts on the final discriminant variable.

for a 115 GeV Higgs boson is 65.2%.

The particles left after taking away the two muons are clustered into two jets using the Durham jet algorithm.

In order to remove the punch-through $q\bar{q}$ background, where leakage of the hadronic shower at the back of the hadronic calorimeter from highly energetic jets fakes a muon signal in the muon chamber, there is a requirement that the energy of a "good muon" should be larger than 15 GeV, and the energy of a MIP should be larger than 6 GeV.

As the two muons come from the Z boson, the invariant mass of the two muon system after performing a kinematic fit imposing energy and momentum conservation must be around m_{Z}, *i.e.*, 50 GeV $\leq \mathrm{m}_{\mu\mu} \leq$ 125 GeV, and the opening angle of the muon pair is required to be larger than 50°.

WW → $q\bar{q}\mu\nu$ and other background are reduced by setting an upper cut on the transverse momentum imbalance that will be there due to the presence of a neutrino.

A "four jet likeness" requirement is made by requiring the logarithm of the Durham jet algorithm parameter Y_{34}^{D} to be larger than -7.

The main cuts and the corresponding events left for data and expected background MC, and the selection efficiency for signal MC can be found in Tab. 4.5. Some of the variables used for event selection are displayed in Fig. 4.8 with a comparison between data and background.

After the above selection, 3 candidates were observed with a background expectation of 2.7 events. The signal efficiency is 58.2 % at 115 GeV. The background is dominated by ZZ (86.0%), and a smaller contribution comes from $q\bar{q}(\gamma)$ (1.8%) and WW (12.1%). A typical candidate event is shown in Fig. 4.9.

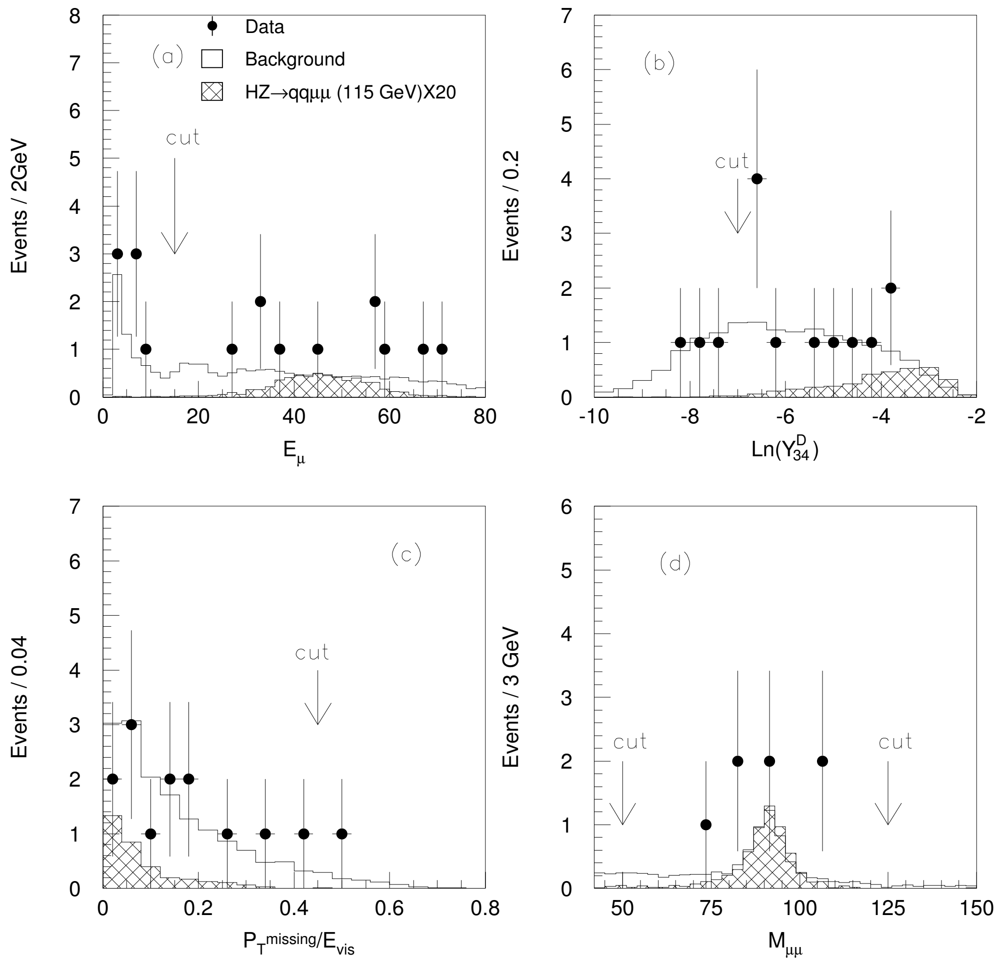

Figure 4.8: The distributions of (a) the energy of the "good muon " assumed to come from the decay of a Z boson, (b) the logarithm of the Durham jet algorithm parameter Y_{34}^{D}, (c) the transverse momentum imbalance, (d) the invariant mass of the muon pair after imposing energy and momentum conservation, for the HZ→ $\mathrm{q\bar{q}}\mu^+\mu^-$ channel after the two muon candidates from the Z decay are determined and the remaining particles are clustered into two jets as described in the text.

Fig. 4.10 shows the distributions of the most discriminating variables: b-tagging and the reconstructed Higgs mass after the 5C kinematic fit (requiring energy-momentum conservation and the mass of the two muon system to be m_{Z}). These variables are used to determine the final discriminant variable. The final discriminant variable distribution for a Higgs mass hypothesis of 115 GeV is shown in Fig. 4.11(a).

No deviation from the background expectation is observed. No significant candidate is observed with a high final discriminant variable value. The analysis performance for the HZ→ $\mathrm{q\bar{q}}\mu^+\mu^-$ channel can be seen in Fig. 4.11(b): the number of data events and the background expectation versus the expected number of signal events is obtained by integrating from right to left in Fig. 4.11(a).

Definition of selection steps	Data	Background Processes				Signal Efficiency
		WW	QQ	ZZ	Total	($\mathrm{m_H} = 115$GeV)(%)
$N_{\mathrm{tracks}} \geq 5$,$N_{\mathrm{clusters}} \geq 15$, $E_{\mathrm{vis}}/\sqrt{s} \geq 0.45$	4219	688.9	2978.4	46.9	3787.4	93.1
2 Muons	14	7.5	4.4	3.9	15.8	65.2
$E_\mu \geq 15$ GeV , $E_{\mathrm{Mip}} \geq 6$ GeV	5	2.6	0.9	3.3	6.8	63.8
50 GeV $\leq m^{4c}_{\mu\mu} \leq$ 125 GeV	4	0.9	0.2	2.6	3.7	58.6
$P_{\mathrm{T}}^{\mathrm{Missing}}/E_{\mathrm{vis}} < 0.4$	3	0.7	0.2	2.5	3.4	58.5
$\ln(Y^{\mathrm{D}}_{34}) \geq -7$	3	0.3	0.1	2.3	2.7	58.2

Table 4.5: Comparison of data with expectations from the Standard Model background processes for each selection step of the HZ→ $\mathrm{q\bar{q}}\mu^+\mu^-$ channel. The signal efficiency is given for a Higgs mass hypothesis $m_{\mathrm{H}} = 115$ GeV.

4.5 The HZ $\rightarrow \mathrm{q\bar{q}}\tau^+\tau^-$ and HZ $\rightarrow \tau^+\tau^-\mathrm{q\bar{q}}$ channels

The HZ $\rightarrow \mathrm{q\bar{q}}\tau^+\tau^-$ and HZ $\rightarrow \tau^+\tau^-\mathrm{q\bar{q}}$ channels (together referred to as $\tau^+\tau^-$ channels in the following) have similar signatures: a pair of well separated tau leptons which are observed as electrons, muons or low multiplicity jets with 1 or 3 tracks and unit charge, accompanied by two hadronic jets. The only difference between them is the mass information and b-tag information of the two hadronic jets.

After the common preselection stage, for the selection of $\tau^+\tau^-$ channels, the fraction of visible energy should be smaller than 0.95, since some of the energy must disappear with the production of neutrinos in the τ decay.

The background contribution from $\mathrm{q\bar{q}}(\gamma)$ is reduced by rejecting events containing photons with energies greater than 40 GeV. The background contributions from the WW→ $\mathrm{q\bar{q}}\ell\nu$ ($\ell = \mathrm{e}, \mu$) and the $\mathrm{Ze^+e^-}$ processes are reduced by requiring the energy of electrons and muons to be smaller than 45 GeV.

There are two methods used to identify tau leptons. The first method is based on the lepton identification information in the NP Ntuple. Tau leptons are identified via their decay into electrons or muons, or as an isolated low-multiplicity jet with 1 or 3 tracks and unit charge as described in Sect. 3.3.4. At least two tau leptons are required. If there are more than two τ leptons, all possible combinations of two τ's are taken and the rest of the event is forced into two jets. For both the two τ's and the two jets, the effective mass is calculated. The combination that has the effective mass (in either the τ's or the jets) closest to the m_{Z} is selected. This tau identification is rather strict and leads to low signal efficiency, especially for the tau leptons with hadronic decay mode. The second method to identify tau leptons is to consider jets with less than four tracks as the candidates of tau leptons when the event is forced into four jets using the Durham jet algorithm. At least two tau candidates are required, and if there are more than two candidates, a similar choice as in the first method is applied to choose the best pairing of candidates. Furthermore, at least one of the candidates must coincide with a tau candidate defined in the first method within a 3° cone.

As the probability that both tau leptons decay into 3 or more charged tracks is quite low, those events with both taus decaying into 3 or more charged tracks are rejected in order to reduce the background contamination from fully hadronic decay of the WW process.

The “Four jet likeness” requirement is set by requiring the logarithm of the Durham jet algorithm parameter Y^{D}_{34} to be larger than -7.

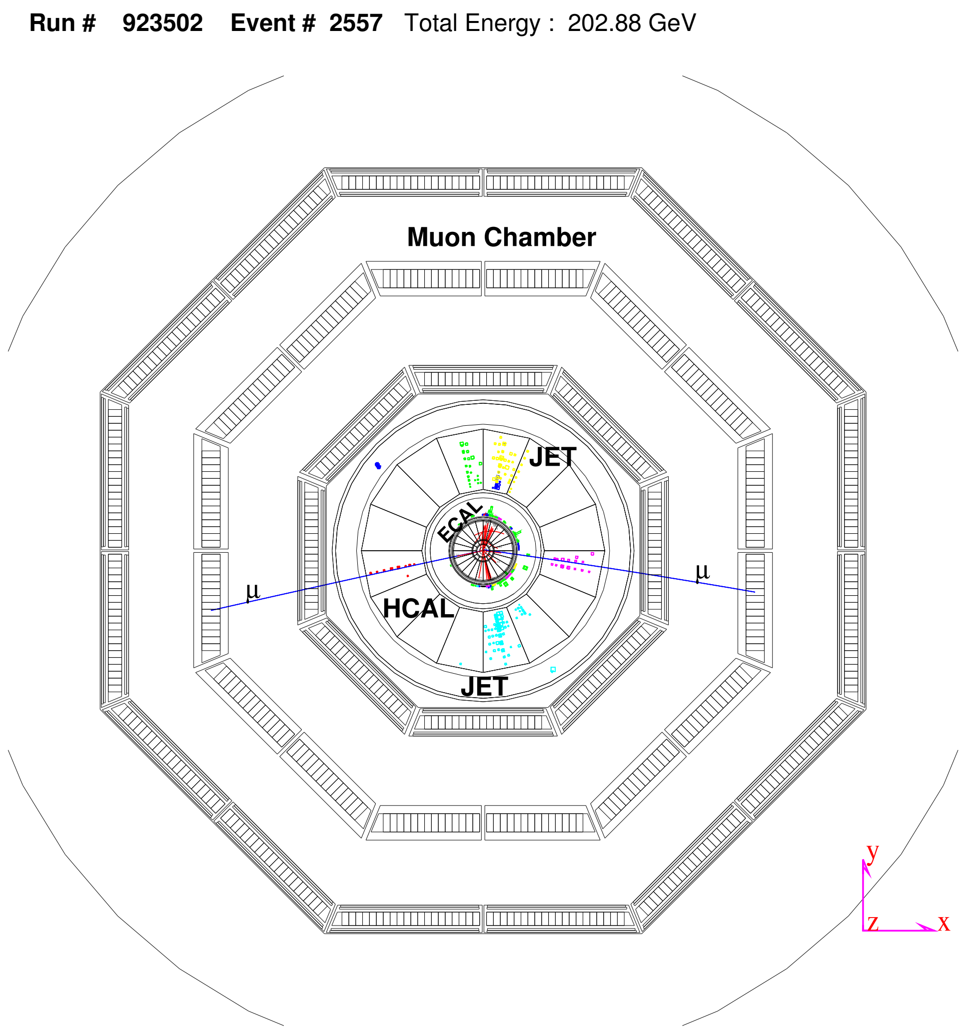

Transverse Imbalance :	.1004		Longitudinal Imbalance :	-.0444	
Thrust :	.7368	Major :	.5757	Minor :	.1260
Event DAQ Time :	1004 1310				

Figure 4.9: A candidate event for the HZ→ $q\bar{q}\mu^+\mu^-$ channel. The invariant mass of the two muon system is 91.2 GeV, and the reconstructed mass for the jet system is 103.8 GeV.

The background contributions from (semi-)leptonic decays of WW can be further reduced by requiring the missing momentum of the event to be less than 50 GeV. A large fraction of the $q\bar{q}(\gamma)$ background can be reduced by requiring $|\cos\theta_{\mathrm{miss}}| < 0.95$, where θ_{miss} is the polar angle of the missing momentum.

An event qualifies for the HZ $\rightarrow q\bar{q}\tau^+\tau^-$ channel if the mass of the tau-tau system after a 4C (energy-momentum conservation) fit is consistent with the Z mass, the opening angle of the jets assigned to the Higgs boson must be larger than 50° and the opening angle between the tau's must also be larger than 50°.

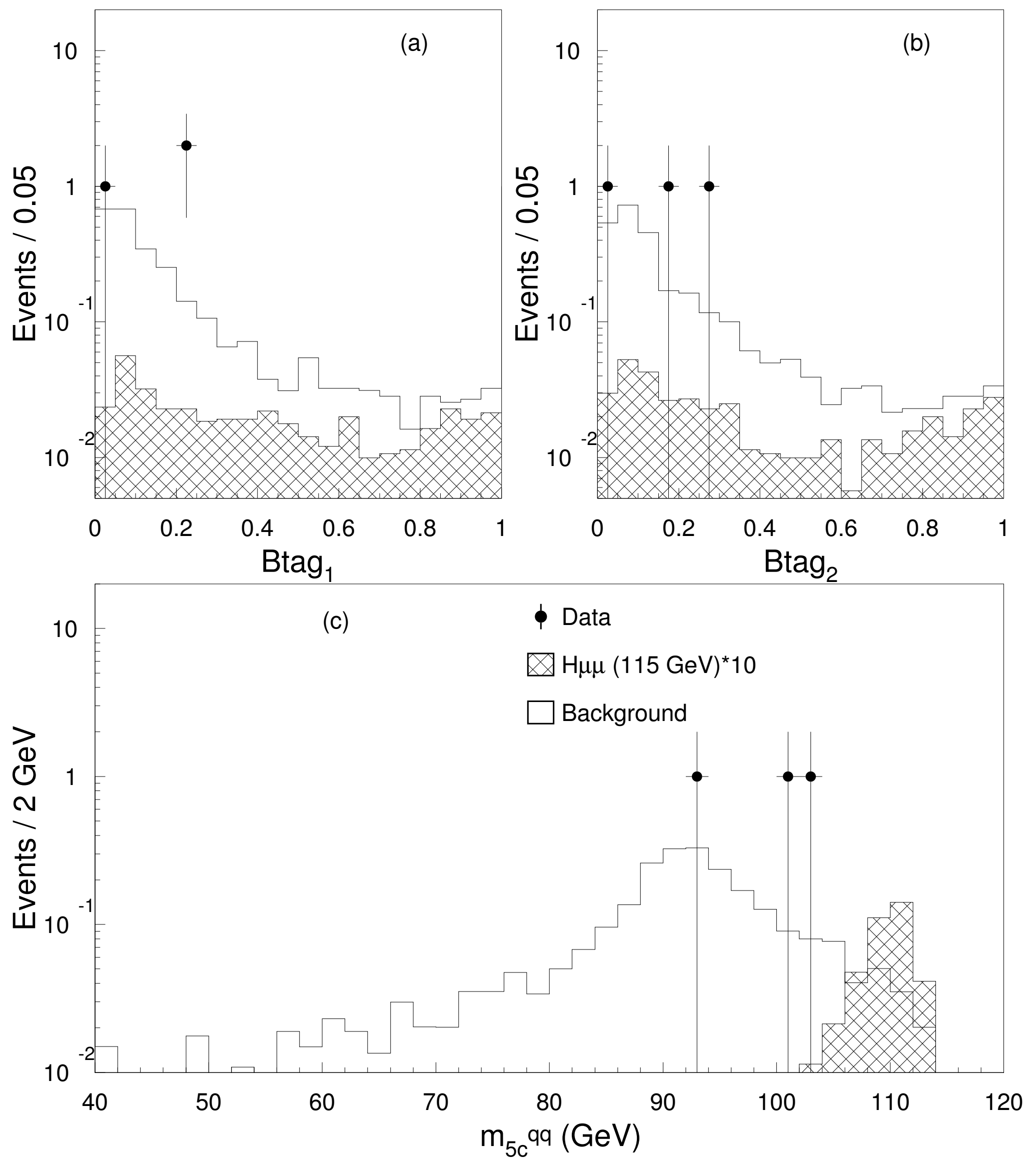

Figure 4.10: Distributions of (a) the b-tagging variable of the most energetic jet, (b) the b-tagging variable of the second jet, (c) the reconstructed mass of the two jet system after imposing energy and momentum conservation, and constraining the mass of the two muons to the mass of Z boson. These 3 variables are used to construct the final discriminant variable in the HZ$\rightarrow$ q$\bar{\text{q}}\mu^+\mu^-$ channel.

An event qualifies for the HZ $\rightarrow \tau^+\tau^-$q$\bar{\text{q}}$ channel if the 4C fitted mass of the jet-jet system is consistent with the Z mass, the opening angle of the jets assigned to the Z boson must be larger than than 50° and the opening angle between the tau's must be larger than than 50°.

The main cuts and the corresponding number of events after each cut for data and background MC, and the selection efficiency for signal MC can be found in Tab. 4.5. Some of the variables used for event selection are displayed in Fig. 4.12 with a comparison between data and background MC.

After the above selection, 7 events were observed as HZ$\rightarrow$ q$\bar{\text{q}}\tau^+\tau^-$ candidates with a back-

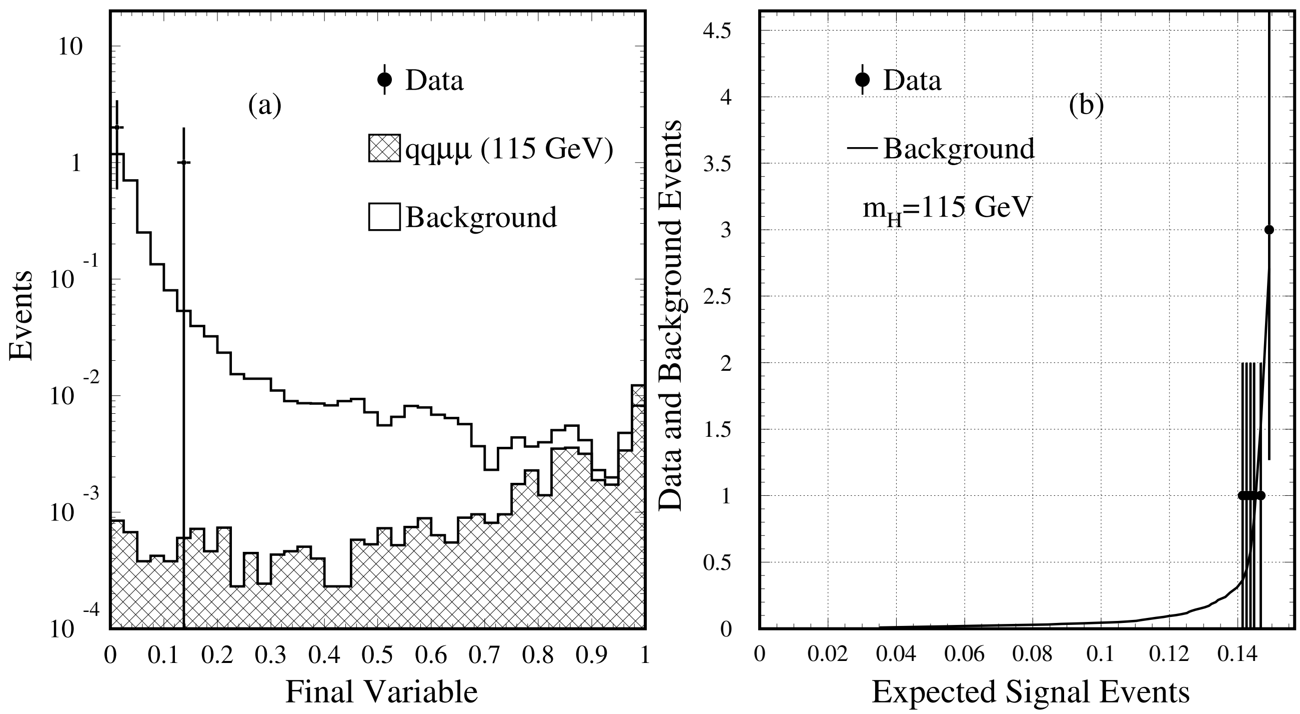

Figure 4.11: (a) The final discriminant variable distribution of the HZ→ $\mathrm{q\bar{q}}\mu^+\mu^-$ channel for a Higgs mass hypothesis of 115 GeV, (b) number of data events and background expectations versus the expected number of signal events.

Definition of selection steps	Data	Background Processes					HZ $\rightarrow \mathrm{q\bar{q}}\tau^+\tau^-$	HZ $\rightarrow \tau^+\tau^-\mathrm{q\bar{q}}$
		WW	QQ	ZZ	Zee	Total	Efficiency(%)	Efficiency(%)
$N_{\mathrm{tracks}} \geq 5$, $N_{\mathrm{clusters}} \geq 15$, $0.95 \geq \frac{E_{\mathrm{vis}}}{\sqrt{s}} \geq 0.45$	4219	688.9	2978.4	46.9	73.2	3787.4	88.8	91.6
$E_\gamma \geq 40$ GeV, $E_{\mathrm{e}} \geq 45$ GeV, $E_\mu \geq 45$ GeV	2262	264.3	2386.2	19.1	49.5	2719.1	74.6	68.0
2 Taus, no 3-3 prong	250	94.6	134.0	5.3	14.3	248.2	48.4	48.1
$\ln(Y_{34}^{\mathrm{D}}) \geq -7$	174	74.7	74.8	5.0	10.8	165.3	47.7	46.7
$E_{\mathrm{miss}} \leq 50$ GeV	75	41.9	22.9	3.9	3.9	72.6	47.0	44.6
$\lvert\cos\theta_{\mathrm{miss}}\rvert \leq 0.95$	46	31.0	8.8	3.4	0.6	43.8	44.34	41.90
HZ→ $\mathrm{q\bar{q}}\tau^+\tau^-$	7	4.3	0.7	1.5	0.1	6.6	29.6	23.9
HZ→ $\tau^+\tau^-\mathrm{q\bar{q}}$	6	5.1	0.9	1.6	0.2	7.8	28.0	28.2
both $\tau^+\tau^-$ channels	9	7.12	1.20	1.84	0.24	10.40	29.93	29.1

Table 4.6: Comparison of data with expectations from the Standard Model background processes after each selection step for the HZ→ $\mathrm{q\bar{q}}\tau^+\tau^-$ and HZ→ $\tau^+\tau^-\mathrm{q\bar{q}}$ channel. The signal efficiency is given for Higgs mass hypothesis $m_{\mathrm{H}} = 115$ GeV.

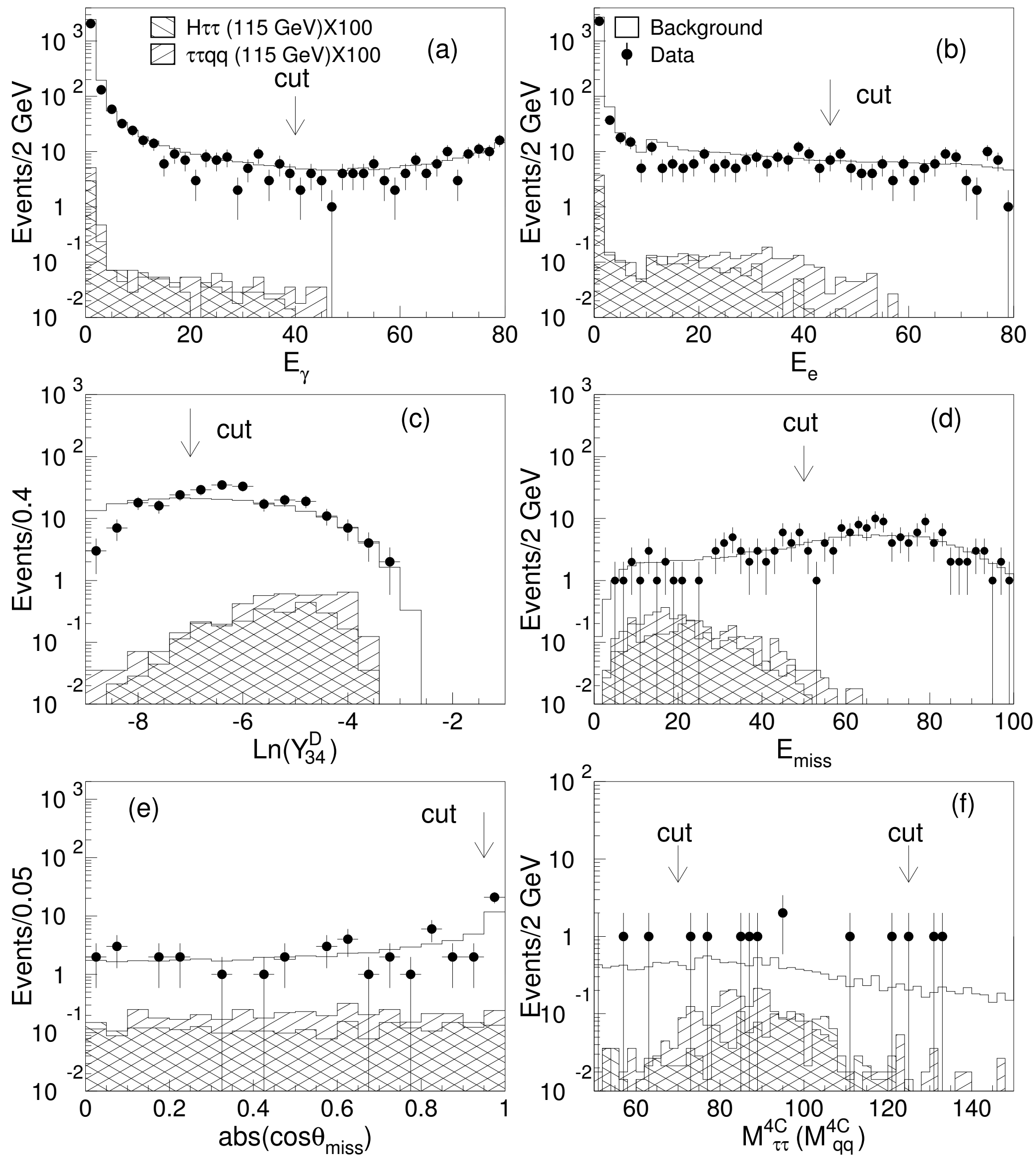

Figure 4.12: Distributions for the HZ $\rightarrow$ q$\bar{\text{q}}\tau^+\tau^-$ and HZ $\rightarrow \tau^+\tau^-$q$\bar{\text{q}}$ channels of (a) the energy of the most energetic photon, (b) the energy of the most energetic electron, (c) the logarithm of the Durham jet algorithm parameter Y_{34}^{D}, (d) the missing energy of the event (e) the cosine value of the polar angle of the missing momentum vector, (f) the reconstructed mass of the tau pair (or jet pair in case of HZ $\rightarrow \tau^+\tau^-$q$\bar{\text{q}}$) after imposing the energy and momentum conservation constraint. The last four distributions are after the two tau pair are determined and the particles left are clustered into two jets as described in the text.

ground expectation of 6.6 events. The signal efficiency is 29.6% at 115 GeV. The background is dominated by WW (65.4%), with additional contributions from q$\bar{\text{q}}(\gamma)$ (10.6%), ZZ (22.4%) and a small one from Zee (1.7%). For HZ$\rightarrow$ q$\bar{\text{q}}\tau^+\tau^-$, 6 events were observed with a background expectation of 7.9 events. The signal efficiency is 28.2% at 115 GeV. WW is the dominant background process (65.5%), other contributions are q$\bar{\text{q}}(\gamma)$ (11.5%), ZZ (20.4%) and Zee (2.7%). A

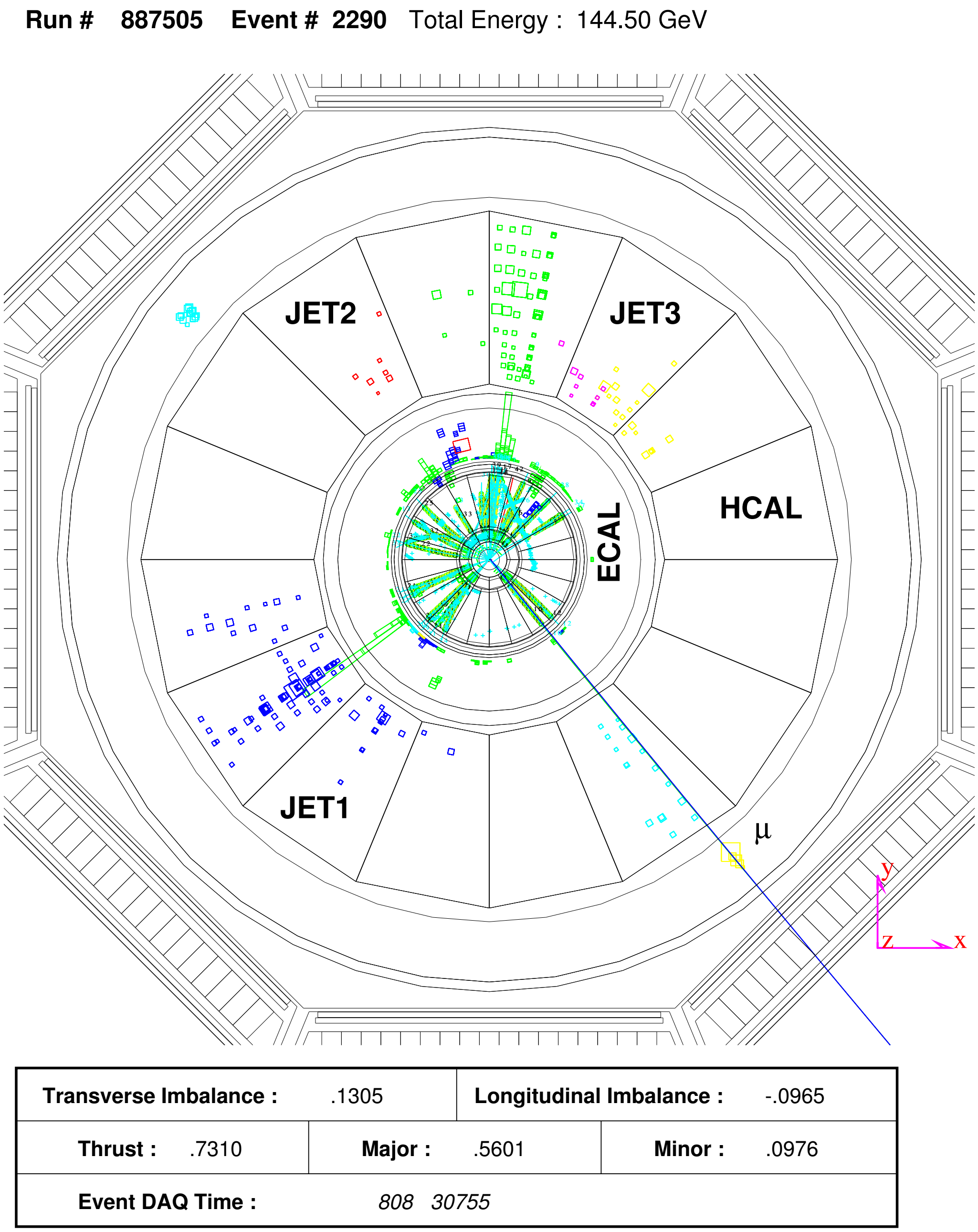

Figure 4.13: A candidate event for the HZ→ $q\bar{q}\tau^+\tau^-$ channel. The μ lepton and Jet 2 are selected as the τ candidates. The invariant mass of the 2 τ's is 91.2 GeV, and the reconstructed mass for the jet system is 96.1 GeV.

typical candidate event is shown in Fig. 4.13.

For the HZ→ $q\bar{q}\tau^+\tau^-$ channel, the most discriminating variables: b-tagging and the reconstructed Higgs mass, after a 5C kinematic fit (requiring energy-momentum conservation and the mass of the 2 tau system is m_Z), (see Fig. 4.14), are used to construct a final discriminant variable. The final discriminant variable distribution for a Higgs mass hypothesis of 115 GeV is shown in Fig. 4.16(a).

For the HZ→ $\tau^+\tau^- q\bar{q}$ channel, only the reconstructed Higgs mass after imposing energy and momentum conservation and the constraint on the mass of the two jets to m_Z (Fig. 4.15)

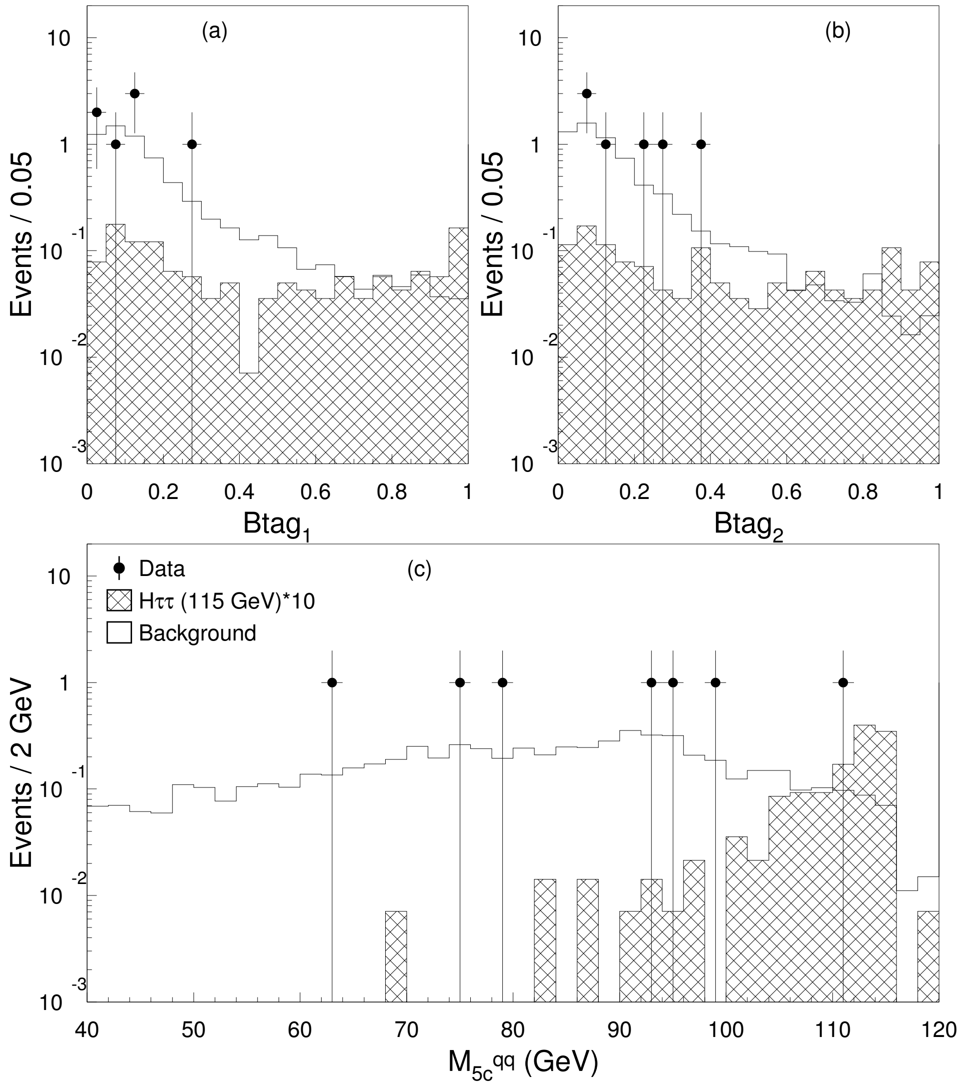

Figure 4.14: Distributions of (a) the b-tagging variable of the most energetic jet, (b) the b-tagging variable of the second jet, (c) the reconstructed mass of the two jet system after imposing the energy and momentum conservation, and adding the constraint on the mass of the two tau's to the mass of Z boson. These three variables are used to construct the final discriminant variable in the HZ→ $q\bar{q}\tau^+\tau^-$ channel.

is used to construct the final discriminant variable. The final discriminant variable distribution and the analysis performance for a Higgs mass hypothesis of 115 GeV are shown in Fig. 4.17.

It is obvious from Tab. 4.6 that these two channels have large cross selection efficiencies, about 23.9% of HZ→ $\tau^+\tau^- q\bar{q}$ signal events were selected as HZ→ $q\bar{q}\tau^+\tau^-$ candidates, while about 28.0% of HZ→ $q\bar{q}\tau^+\tau^-$ signal events were selected as HZ→ $\tau^+\tau^- q\bar{q}$ candidates, since they have quite similar final states. There are 4 observed events that pass both the HZ→ $q\bar{q}\tau^+\tau^-$ and the HZ→ $\tau^+\tau^- q\bar{q}$ selections. They will be assigned to either of these two channels according to their values of the final discriminant variables. If, for each of these events assigned to

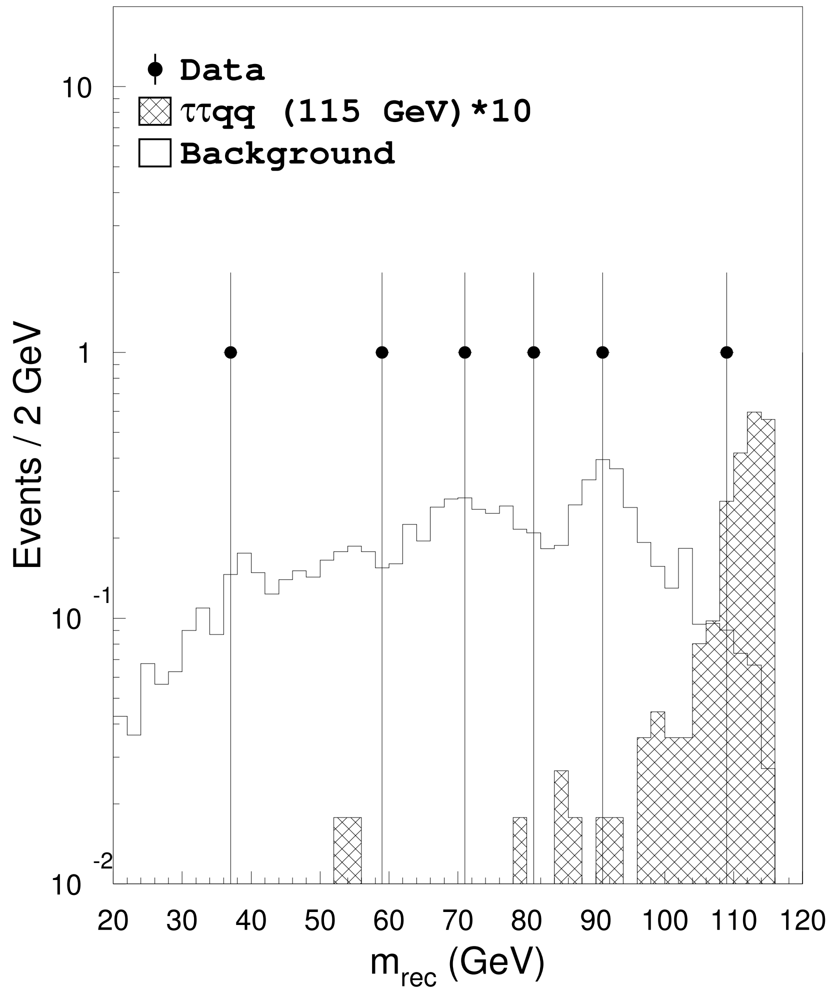

Figure 4.15: Distributions of the reconstructed mass of the two tau system after imposing energy and momentum conservation, and adding the constraint on the mass of the two jets to the Z boson mass.

two channels, the final discriminant variable $F_{\mathrm{HZ}\to \mathrm{q\bar{q}}\tau^+\tau^-}$ is larger than $F_{\mathrm{HZ}\to\tau^+\tau^-\mathrm{q\bar{q}}}$, the event will be taken as a HZ→ $\mathrm{q\bar{q}}\tau^+\tau^-$ candidate, otherwise, it is a HZ→ $\tau^+\tau^-\mathrm{q\bar{q}}$ candidate. The same treatment is applied to the background and signal expectations. As the final discriminant variable depends on the Higgs mass hypothesis, the relative ratio of observed candidate (and background) between these two channels changes with the variation of the Higgs mass hypothesis.

4.6 Systematic Uncertainties

Systematic uncertainties on the number of expected background and signal events can arise from two sources: the uncertainties on the detector response due to the misunderstanding of the detector and missimulation in the Monte Carlo, and the uncertainties on the theory evaluated by the Monte Carlo. This section summarizes the estimation of the systematic uncertainties.

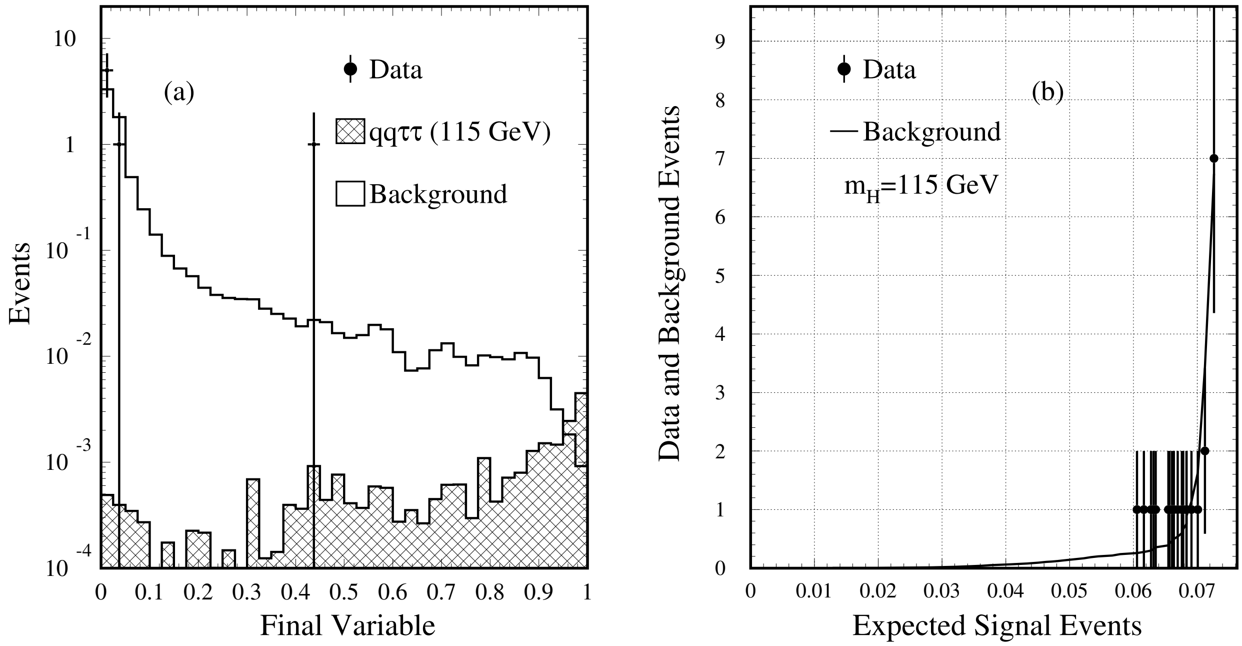

Figure 4.16: (a) The final discriminant variable distribution of the HZ→ $q\bar{q}\tau^+\tau^-$ channel for a Higgs mass hypothesis of 115 GeV, (b) number of data events and background expectations versus the expected number of signal events.

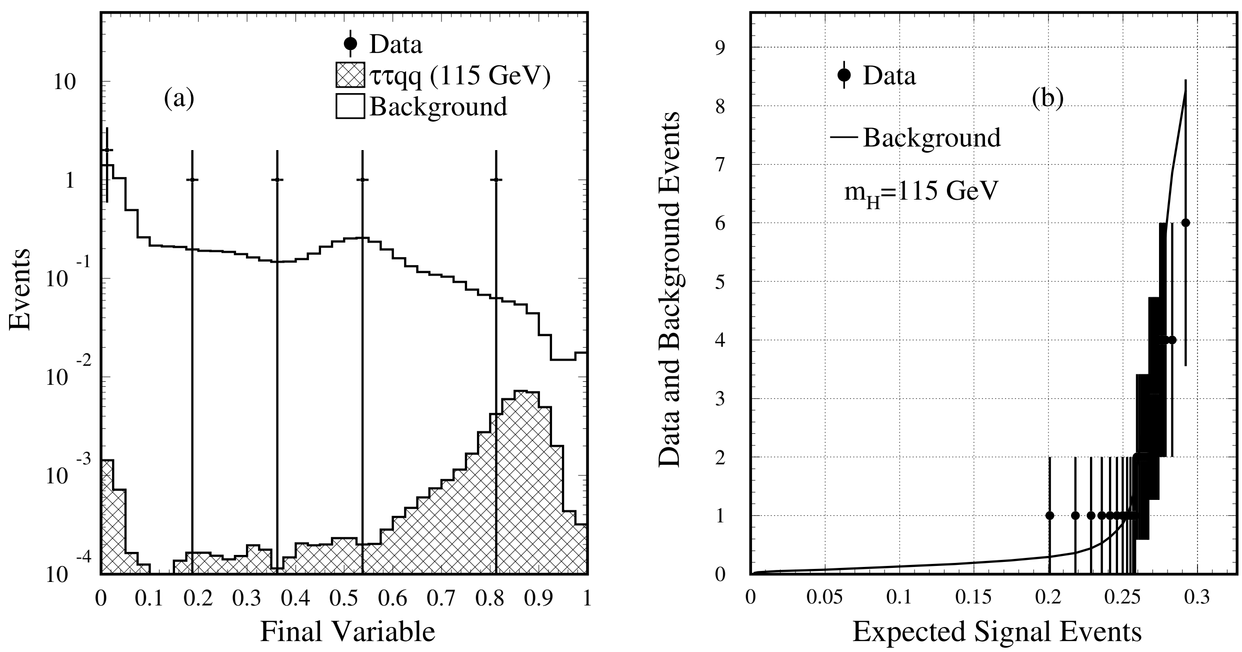

Figure 4.17: (a) The final discriminant variable distribution of the HZ→ $\tau^+\tau^-q\bar{q}$ channel for a Higgs mass hypothesis of 115 GeV, (b) number of data events and background expectations versus the expected number of signal events.

A. **Lepton Identification:**

The systematic uncertainty due to the lepton identification is estimated by studying high statistics reference samples: $e^+e^- \to e^+e^-$, $e^+e^- \to \mu^+\mu^-$, $e^+e^- \to \tau^+\tau^-$, both for data and Monte Carlo [54]. The lepton identification criteria are applied to the samples, and the event acceptance is determined both for data and Monte Carlo. The distributions of some of the variables are shown in Fig.s 3.2 - 3.4. The systematic uncertainty in the lepton identification is determined by summing the relative acceptance difference in quadrature with the relative statistical error of the reference sample. The uncertainty assigned to the signal efficiency and the background expectation ranges from 1% to 5%, depending on the investigated channel.

B. **B-tagging:**

B-tagging is used to construct the final discriminant variable and its uncertainty translates directly into the final discriminant variable, which is used to evaluate the mass limit. The systematic uncertainty due to the b-tagging is estimated using the calibration sample of hadronic events at 91 GeV (see the neural network output for jet tag in Fig. 3.6). Assuming that the difference between the data and Monte Carlo distributions is entirely due to the systematic effects, the uncertainty assigned to the signal efficiency is 4% [61].

C. **Energy Scale:**

The systematic uncertainty arising from uncertainty on the energy scale has been evaluated by smearing the calibration constants used to determine the energy scale of the tracking, electromagnetic and hadronic calorimeters, as well as shifting the global energy [59]. The uncertainty on the number of background expectation is about 2.5%.

D. **Luminosity Measurement:**

Experimental uncertainty in the luminosity measurement accounts for 1% systematic error on the number of expected signal events [61].

E. **Theoretical uncertainty:**

The theoretical uncertainty on the Higgs boson production cross section due to the uncertainties in m_{top} and α_s [62] (0.1%), interference effects [63] (1%) and quark masses [64] (1%) amounts to 1% in total.

F. **Background normalisation:**

The background normalisation error due to the uncertainty on the background cross sections contributes up to 10% relative uncertainty to the background expectation [61].

Assuming these uncertainties are independent, the overall systematic error on the number of signal events is estimated to range from 3% to 6% for m_{H} close to and beyond the HZ kinematic limit, and on the number of background events is estimated to be from 6% to 15% for m_{H} close to or beyond the HZ kinematic limit. The statistical uncertainties on the signal and background predictions, arising from the finite number of generated Monte Carlo events, are evaluated to be up to 4% for the signal and 8% for background [67]. These uncertainties will be included in the calculation of confidence level and mass limit presented in the next chapter.

Chapter 5

Combination of Results and Higgs Mass Limit

In the previous chapter, the results of the searches for the evidence of the production of the Standard Model Higgs boson via the Higgsstrahlung process in the channels with leptons in the final states were presented. No evidence of a significant excess was observed in the data sample. Searches for the Standard Model Higgs in two other channels were also performed within L3. No apparent hint of a signal was found either in the $\mathrm{q\bar{q}q\bar{q}}$ or in the $\mathrm{q\bar{q}}\nu\bar{\nu}$ channels [67]. At LEP energy, the cross section for the production of the Standard Model Higgs boson via the Higgsstrahlung process being quite small, a possible deviation from the background expectation may only become apparent in the combination instead of in any individual channel. Furthermore, datasets from different LEP energies and experiments can also be added to give a better overall sensitivity. If no Higgs is present in the mass range investigated, a lower limit on the mass of the Standard Model Higgs boson can be set using a confidence level calculation method in which the different final state analyses are combined. For this purpose, a globe *test-statistic* is constructed which allows the experimental result to be used to test two hypotheses: the *background-only* ("b") hypothesis, which assumes no Higgs boson is present in the mass range, and the *signal + background* ("s+b") hypothesis, where the Higgs boson is assumed to be produced according to the Standard Model. The test-statistic takes into account experimental details such as detection efficiencies, signal-to-background ratios, resolution functions, and provides a single value for a given Higgs mass hypothesis. The observed value and the expected distributions of the test-statistic for the *background-only* and the *signal + background* hypotheses are used to evaluate confidence levels for the two hypotheses as a function of m_{H}. Based on the confidence levels for the two hypotheses, the 95% confidence level lower limit for the Standard Model Higgs boson mass can be set. It can then be said that for any Higgs mass below this limit, the probability that a Higgs boson with that mass exists is less than 5%. For many Higgs masses well below the limit, this probability is in fact much smaller.

5.1 Test-Statistic

The test-statistic adopted in the present combination of results is the ratio of the likelihood function for the "s+b" hypothesis to the likelihood function for the "b" hypothesis [65]:

$$Q(m_{\mathrm{H}}) = \frac{\mathcal{L}(s(m_{\mathrm{H}}) + b)}{\mathcal{L}(b)}, \tag{5.1}$$

where the binned likelihood function based on Poisson statistics is given by

$$\mathcal{L}(s(m_{\mathrm{H}})+b)=\prod_i \frac{e^{-(s_i(m_{\mathrm{H}})+b_i)}(s_i(m_{\mathrm{H}})+b_i)^{n_i}}{n_i!} \tag{5.2}$$

The index i runs over the bins of the distribution of the final discriminant variable from all independent contributions to the combined searched result: search channels of an experiment, searches at different centre-of-mass energies, and channels from different experiments. The variables s_i (Higgs mass dependent), b_i and n_i represent the numbers of the expected signal, the expected background and the observed candidates, respectively, of the i-th bin in the individual search channel.

By taking the logarithm of the likelihood ratio, one obtains the so-called log-likelihood ratio which is practically used as the test-statistic [67]:

$$-2\ln Q(m_{\mathrm{H}}) = 2\Sigma_i[s_i(m_{\mathrm{H}}) - n_i \ln(1+s_i(m_{\mathrm{H}})/b_i)]. \tag{5.3}$$

In this expression, each candidate in the sum has a weight $\ln(1+s/b)$ which depends on the signal-to-background ratio, s/b, in the bin where it is found. This weight also depends on the Higgs mass hypothesis, m_{H}.

In order to take into account the possibility of background and signal fluctuations, for arbitrary Higgs mass hypothesis, a large number of Monte Carlo experiments are performed based on Poisson statistics for two hypotheses:

- background only, which takes the b_i as the mean value of this Possion distribution,
- signal+background, which takes the s_i+b_i as the mean value of this Possion distribution.

Then the log-likelihood ratio is calculated by replacing the data set in Eq. (5.3) by fictitious Monte Carlo sets of *background only* and *signal+background* hypotheses. Fig. 5.1 illustrates the behavior of the log-likelihood ratio, depending on the Higgs mass hypothesis, for observed data, *background only* hypothesis ("b") and *signal+background* hypothesis ("s+b"). The two shaded bands around the "b" curve give the 1σ (dark shadow) and 2σ (light shadow) statistical spread, respectively. A 2σ excess of observed data over *background only* hypothesis at a certain mass point may indicate the presence of Higgs around that mass point. For the "s+b" hypothesis, similar 1σ and 2σ bands can be calculated, but are not indicated for clarity in the figure.

Fig. 5.2 (a)$-$(c) shows the results of the log-likelihood ratio as a function of Higgs mass, for the search channels which were discussed in this thesis, and for the whole data set which was taken in the year 2000 by the L3 experiment. The combined result for all four search channels is displayed in Fig. 5.2 (d). The data are consistent with the *background only* hypothesis. Hence, there is no evidence of a Higgs boson in these four channels.

For each given m_{H}, the value of the log-likelihood ratio in the data is compared to the expected distributions of the log-likelihood ratio, $-2\ln Q(m_{\mathrm{H}})$, in a large number of simulated experiments under the *background only* and *signal+background* hypotheses. The confidence levels can be obtained from these distributions.

5.2 Confidence Level

To set the confidence level that the signal with a certain Higgs mass is absent (or present), the distributions of the log-likelihood ratio, separately for the "b" and the "s+b" hypotheses, at

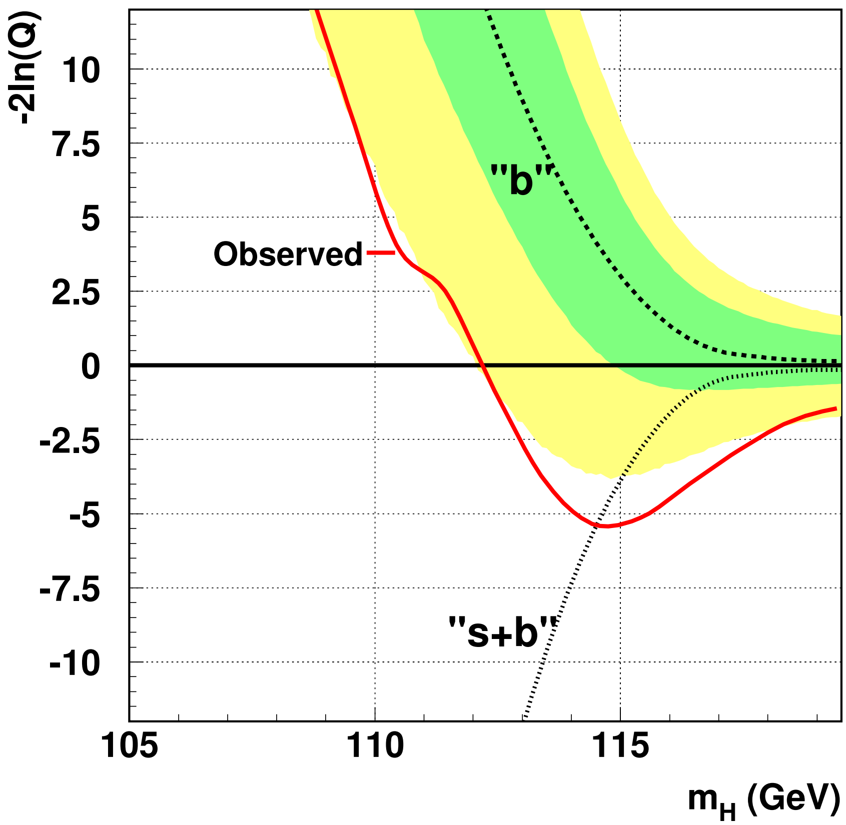

Figure 5.1: The illustration plot of the log-likelihood ratio (*test-statistic*) as a function of Higgs mass,m_{H}. The solid curve is the result from observed data, the dashed curve shows the expected median value of $-2\ln Q$ for the *background only* hypothesis, and the dotted curve shows the expected median value of $-2\ln Q$ for the *signal+background* hypothesis. The shaded bands show the 1σ (dark) and 2σ (light) spread centered on the background expected median value. From Ref. [66].

each hypothetical Higgs mass point, are normalised to become probability density functions, and integrated to form the confidence levels $CL_{\mathrm{b}}(m_{\mathrm{H}})$ and $CL_{\mathrm{s+b}}(m_{\mathrm{H}})$. The integration starts in both cases from the b-like end (high values of $-2\ln Q$) and runs up to the actually observed value in the data. (This is illustrated in Fig. 5.3). Thus $CL_{\mathrm{b}}(m_{\mathrm{H}})$ and $CL_{\mathrm{s+b}}(m_{\mathrm{H}})$ express the probabilities that the log-likelihood ratio of a Monte Carlo experiment is more *background*-like or less *signal+background*-like, respectively, than the observed log-likelihood ratio. On the contrary, the quantity $1 - CL_{\mathrm{b}}(m_{\mathrm{H}})$ is an indicator for a possible signal, and it measures the compatibility between observed results with the *background only* hypothesis. The distribution of $1-CL_{\mathrm{b}}(m_{\mathrm{H}})$ in a large sample of simulated *background only* experiments is uniform between 0 and 1, thus its median expected value is 0.5. A Standard Model Higgs boson with true mass m_0 would produce a pronounced drop in this quantity for $m_{\mathrm{H}} \approx m_0$, and an observed value of $1 - CL_{\mathrm{b}}(m_{\mathrm{H}})$ lower than 0.5 indicates an excess of events in data compared to the expected background.

The background confidence level $1 - CL_{\mathrm{b}}$ as a function of the Higgs mass hypothesis, m_{H}, for the combination of four discussed leptonic channels, and for the data sample collected by the L3 detector during the year 2000, is shown in Fig. 5.4 (a). There is no significant deviation of the observation from the *background only* hypothesis.

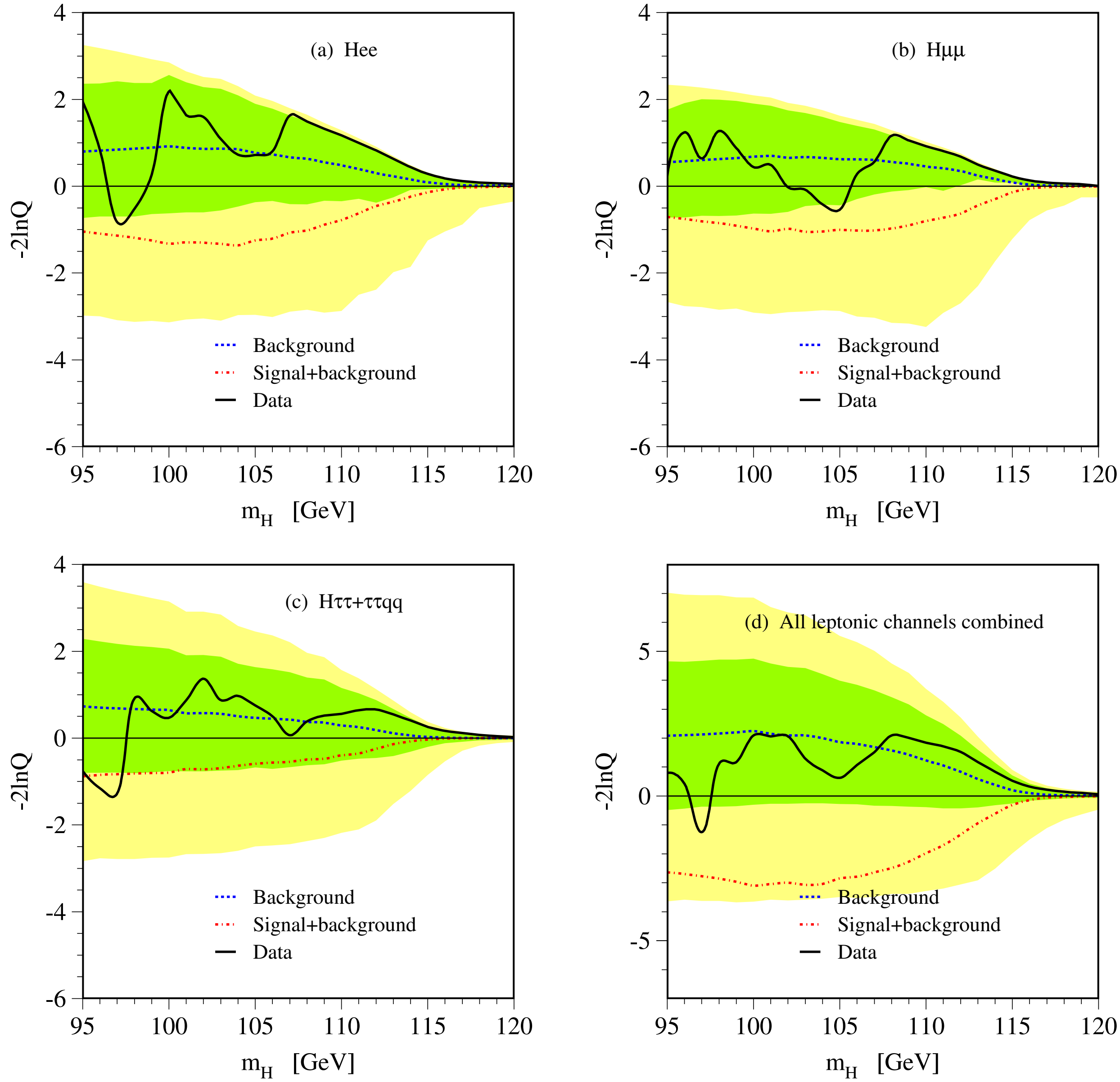

Figure 5.2: The log-likelihood ratio, $-2\ln Q$, as a function of the Higgs mass hypothesis, m_{H}, for the search channel (a) $\mathrm{He^+e^-}$, (b) $\mathrm{H}\mu^+\mu^-$, (c) $\mathrm{H}\tau^+\tau^-$ and $\tau^+\tau^-\mathrm{q\bar{q}}$, (d) the combination of the above 4 channels. The solid curve is the result from the observed data, the dashed curve shows the expected median value of $-2\ln Q$ for the *background only* hypothesis, and the dotted curve shows the expected median value of $-2\ln Q$ for the *signal+background* hypothesis. The shaded bands show the 1σ (dark) and 2σ (light) spread centered on the background expected median value.

To exclude a signal, an additional quantity is defined as

$$CL_{\mathrm{s}}(m_{\mathrm{H}}) = CL_{\mathrm{s+b}}(m_{\mathrm{H}})/CL_{\mathrm{b}}(m_{\mathrm{H}}), \tag{5.4}$$

to indicate the signal confidence one might have obtained in the absence of background. The signal hypothesis is excluded at 95% confidence level when $CL_{\mathrm{s}}(m_{\mathrm{H}})$ has a value smaller than

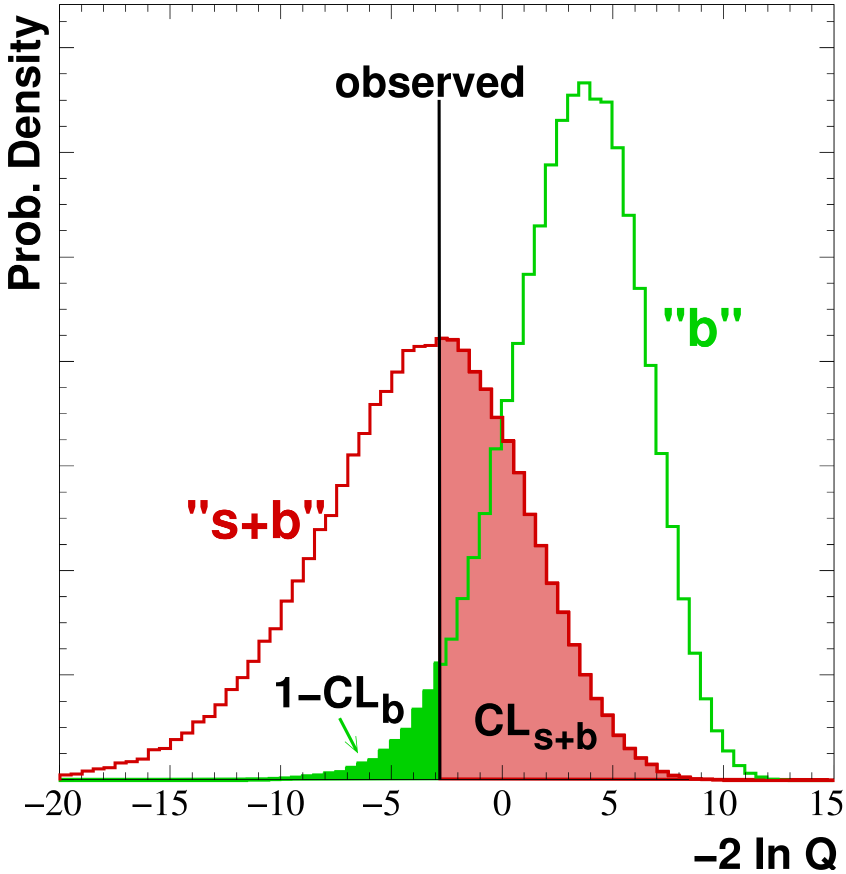

Figure 5.3: Illustration of the probability density distributions for the test statistics in a large number of simulated experiments based on the *background only* and *signal+background* hypotheses, respectively. The shaded integrated areas define the confidence levels: $1 - CL_{\mathrm{b}}(m_{\mathrm{H}})$ and $CL_{\mathrm{s+b}}(m_{\mathrm{H}})$. From Ref. [66].

or equal to 5%. The 95%CL lower limit for the Higgs mass is defined as the lowest value of the test mass m_{H} which yields $CL_{\mathrm{s}}(m_{\mathrm{H}}) = 0.05$. The so-called observed lower limit comes from the observed curve, while the expected median value comes from the *background only* hypothesis. The signal confidence level CL_{s}, as a function of the Higgs mass hypothesis, m_{H}, for the combination of four leptonic channels discussed in provious chapter is shown in Fig. 5.4 (b). At the 95% confidence level, the observed lower limit on the Higgs mass is 88.2 GeV, with an expected median value of 86.3 GeV.

5.3 Combined Results of L3

Searches for the Standard Model Higgs boson with the other two channels: HZ→ $\mathrm{q\bar{q}q\bar{q}}$ and HZ→ $\mathrm{q\bar{q}}\nu\bar{\nu}$ are also performed in L3 [67]. The general search strategy is similar to the one described in this thesis. Mass independent selections and kinematic fits are performed and a mass dependent discriminating variable is constructed. Though there is a slight excess of events above one standard deviation from the background in the $\mathrm{H}\nu\bar{\nu}$ channel for m_{H} above 100 GeV, the combined results from all search channels has a good agreement between the observation and the expected background within one standard deviation from the background expectation,

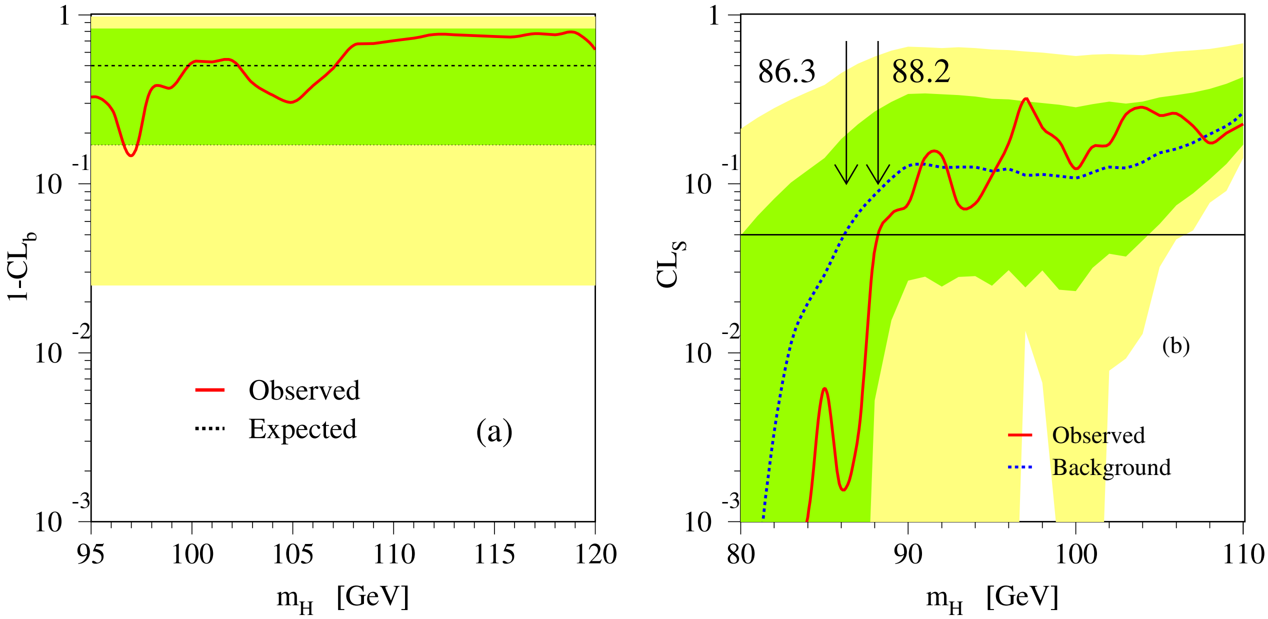

Figure 5.4: (a) The background confidence level $1-CL_\mathrm{b}$ and (b) the signal confidence level, CL_s, as a function of the Higgs mass hypothesis, m_H, combining the results of the four leptonic channels discussed in previous chapters, for all the data collected by the L3 detector during the year 2000. The solid line shows the observed value, the dashed line shows the median expected value in a large number of simulated *background-only* experiments. the dark and light shaded bands show the expected 68% and 95% probability intervals centered on the background expected median value. The observed lower limit on the Higgs mass is 88.2 GeV, with an expected median value of 86.3 GeV, at the 95% confidence level.

see Fig. 5.5. The confidence level for the "background only" hypothesis $1-CL_\mathrm{b}$ and the confidence level for the "signal+background" hypothesis CL_s as a function of m_H are shown in Fig. 5.6. The results of the L3 Standard Model Higgs boson searches at lower center-of-mass energies [68, 69] are included in the calculation of these confidence levels. The observed lower limit on m_H is 112.0 GeV at the 95% confidence level, for an expected lower limit of 112.4 GeV.

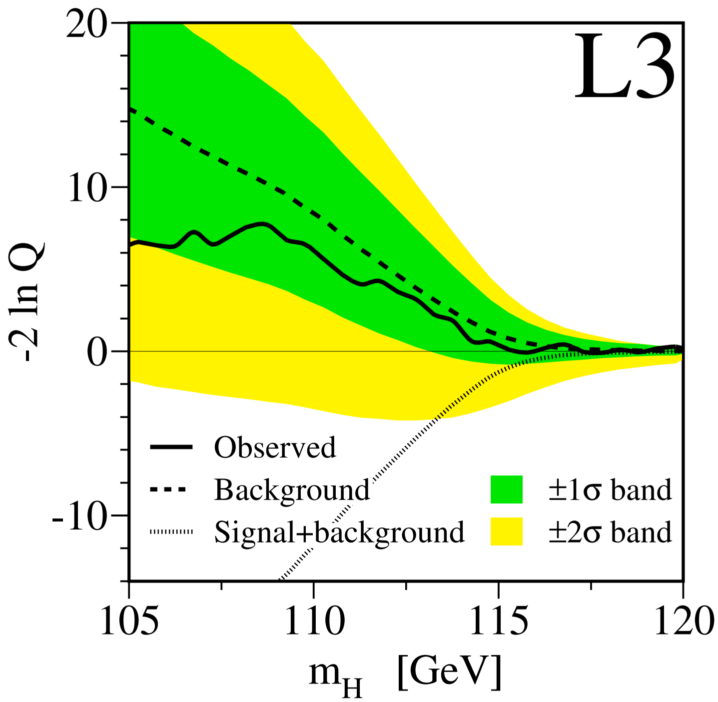

Figure 5.5: The log-likelihood ratio, $-2\ln Q$, as function of the Standard Model Higgs boson mass, m_{H}, combining all the search channels performed in L3. The observed value is indicated by the solid line, the dashed line and dotted line represent the results of *background only* hypothesis and *signal+background* hypothesis, respectively.

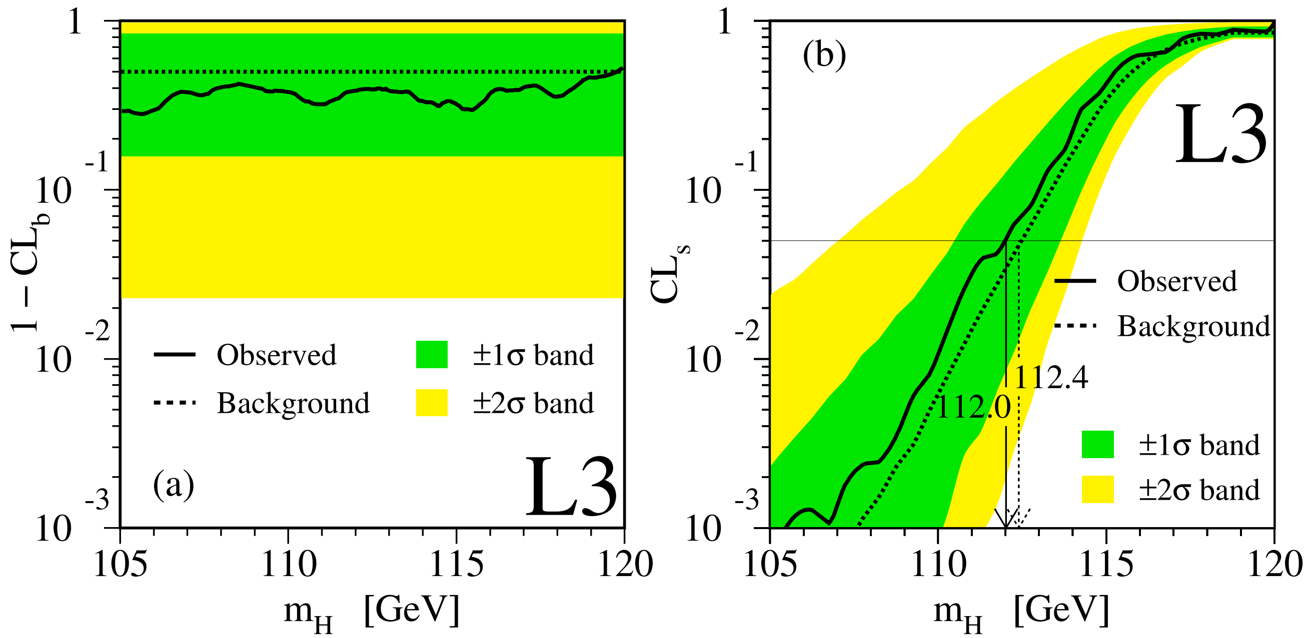

Figure 5.6: (a) The background confidence level $1-CL_{\rm b}$ and (b) the signal confidence level, $CL_{\rm s}$, as a function of the Higgs mass hypothesis, $m_{\rm H}$, combining all the search channels performed in L3. The data collected at lower center-of-mass energies are also included in the combination. The solid line shows the observed value, the dashed line shows the median expected value in a large number of simulated *background only* experiments. the dark and light shaded bands show the expected 68% and 95% probability intervals centered on the background expected median value. The observed lower limit on the Higgs mass is set at 112.0 GeV, with an expected median value of 112.4 GeV, at the 95% confidence level.

Chapter 6

Summary and Prospects

6.1 Summary

No evidence for the existence of a Standard Model Higgs boson has been found in the channels $\mathrm{HZ} \rightarrow \mathrm{q\bar{q}e^+e^-}$, $\mathrm{HZ} \rightarrow \mathrm{q\bar{q}}\mu^+\mu^-$, $\mathrm{HZ} \rightarrow \mathrm{q\bar{q}}\tau^+\tau^-$ and $\mathrm{HZ} \rightarrow \tau^+\tau^-\mathrm{q\bar{q}}$ using data collected by the L3 detector at center-of-mass energies from 200 GeV to 210 GeV in 2000. The observed lower limit on the mass of the Standard Model Higgs boson is 88.2 GeV at 95% confidence level, the expected lower limit is 86.3 GeV. A slight excess of events above one standard deviation from the background is observed in the $\mathrm{H}\nu\nu$ channel for m_{H} above 100 GeV [67]. For all channels combined, the observation is in agreement with the expected background within one standard deviation. The observed lower limit (including the results of L3 Standard Model Higgs boson searches at lower center-of-mass energies) on m_{H} is 112.0 GeV at the 95% confidence level, with an expected lower limit of 112.4 GeV. This is the L3 final result [67].

The other three LEP experiments also conducted searches for the Standard Model Higgs boson. ALEPH reported [70]the observation of a 3σ excess above the background expectation, which is consistent with the production of a Standard Model Higgs boson with a mass near 114 GeV. ALEPH's observed lower limit is 111.1 GeV at 95% confidence level with an expected lower limit of 114.2 GeV. No evidence for a Higgs signal is observed either from the DELPHI [71] or the OPAL [72] experiments. The observed lower mass limit of 114.3 GeV for the DELPHI experiment is set with an expected lower limit of 113.5 GeV, for the OPAL experiment, the two limits are 109.7 GeV and 112.5 GeV, respectively.

Combining the data from the four LEP experiments, the lower bound for the Standard Model Higgs mass has been derived, which is 114.1 GeV at the 95% confidence level, with 115.1 GeV as expected limit [73]. There is a 2.1σ excess beyond the background expectation which can be interpreted as production of a Standard Model Higgs with a mass higher than the quoted limit, and a preferred mass of about 115.6 GeV. However, the significance of the excess is not high enough to claim a discovery.

6.2 Prospects for the future

Following the closure of LEP at the end of 2000, the next possibilities to discover the Higgs boson will be the second phase (Run II) of the Tevatron collider at Fermilab, which has started at the beginning of 2001, the Large Hadron Collider (LHC) which is being constructed at CERN and is projected to start in 2007, and possibly a future high energy $\mathrm{e^+e^-}$ linear collider, which is currently in the planning stage.

6.2.1 Higgs Searches at the Tevatron

The Tevatron machine is a p$\bar{\text{p}}$ collider with a center-of-mass energy, in its Run II phase, of 2 TeV and with projected integrated luminosity of at least 2 fb^{-1} per experiment. There are two detectors, CDF and D$\emptyset$. Although gluon fusion is the dominant Higgs production process at the Tevatron, the more promising production processes for discovery are Higgs-strahlung: q$\bar{\text{q}}'$ →HW$^{\pm}$, with H→ b$\bar{\text{b}}$ and W$^{\pm}$ → $l\nu_l(l = \text{e}, \mu)$, and q$\bar{\text{q}}$ →HZ, with H→ b$\bar{\text{b}}$ and Z→ $\ell^+\ell^-(l = \text{e}, \mu)$ or q$\bar{\text{q}}$ [30]. A large fraction of the overwhelming QCD background can be suppressed by tagging leptons from the W and Z decays. These leptons are also vital to triggering the Higgs production events online.

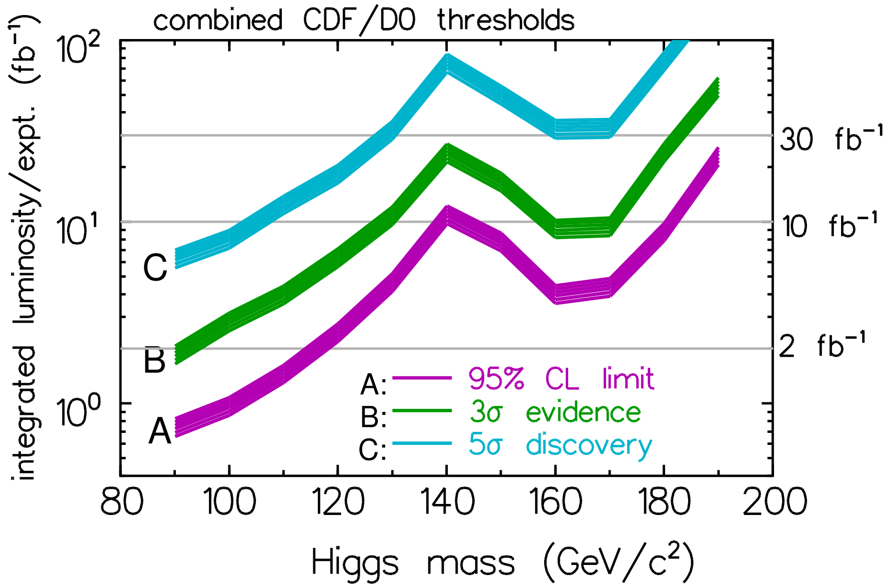

Figure 6.1: The required integrated luminosity per experiment, to either exclude a Standard Model Higgs boson at 95% confidence level or discover it at the 3σ and 5σ level, as a function of the Higgs mass.

Fig. 6.1 [30] shows the required integrated luminosity per experiment, to either exclude a Standard Model Higgs boson at 95% confidence level or discover it at the 3σ and 5σ level, as a function of the Higgs mass. It seems, unfortunately, that the integrated luminosity of RUN II will not be sufficient to discover, at a 5σ level, the Higgs boson beyond the sensitivity of LEP2, untill the time when the LHC will be running in 2007 or later. However, a Standard Model Higgs boson with mass up to 180 GeV could be discovered at a 3σ level with 20−30 fb^{-1} per experiment. A Tevatron Run IIb upgrade is in progress to reach these luminosities. However, no final results are expected to be available before 2007.

6.2.2 Future Higgs Searches at the LHC

The LHC that is presently being constructed will be a pp collider with a center-of-mass energy of 14 TeV and a peak design luminosity of $10^{34}\text{cm}^{-2}\text{s}^{-1}$ [74]. There will be two large detectors: A Toroidal LHC ApparatuS (ATLAS) [76] and the Compact Muon Solenoid (CMS) [75]. The LHC will offer the possibility to search for the Higgs boson with a mass up to 1 TeV.

The gluon fusion process pp→gg→H with a cross section ranging between 100 to 0.1 pb for Higgs boson masses between 100 GeV and 1 TeV will be the dominant Higgs boson production mechanism at the LHC. The quark fusion processes involving W$^{\pm}$ and Z boson will be the next most prevalent production process: $q\bar{q} \rightarrow Hq\bar{q}$ with a cross section between 10 and 0.1 pb. Diagrams contributing to Higgs boson production at the LHC are shown in Fig. 6.2, and the production cross sections are shown in Fig. 6.3 [77] .

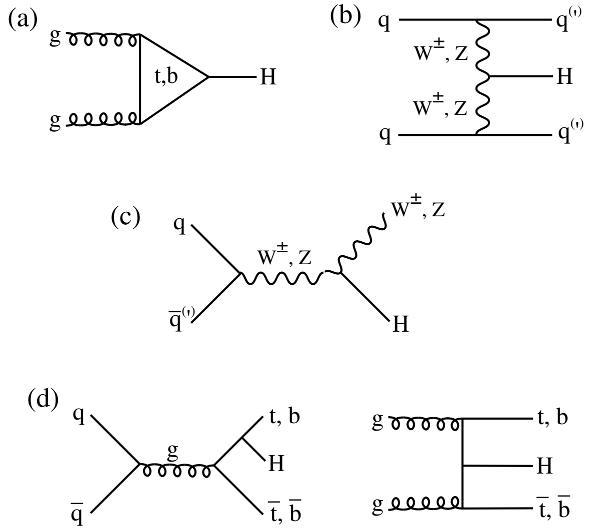

Figure 6.2: Diagrams contributing to Higgs boson production at the LHC: (a) $gg \rightarrow H$, (b) $q\bar{q} \rightarrow Hq\bar{q}$, (c) $q\bar{q}^{(\prime)} \rightarrow H(W^{\pm}, Z)$, and (d) $q\bar{q} \rightarrow H(b\bar{b}, t\bar{t})$.

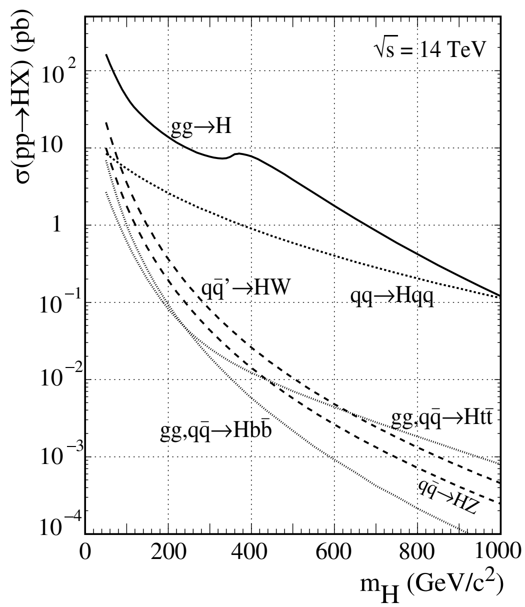

Figure 6.3: Higgs boson production cross sections at the LHC from Ref.[77].

The most sensitive range for the discovery of the Standard Model Higgs at LHC is the intermediate mass range [76]: from 140 GeV to roughly 800 GeV. In this range, the Higgs boson decays predominantly to W^+W^- and $ZZ^{(*)}$, The dominant decay mode, $H \rightarrow W^+W^-$, could be used but with large background. The most favorite channel with very low background would be $H \rightarrow ZZ^{(*)} \rightarrow \ell^+\ell^-\ell^+\ell^-$, and discovery of a Higgs boson in the intermediate mass range in this channel would only need a very small integrated luminosity of tens of fb^{-1} [78]. For the lower Higgs mass range, The Higgs boson decays mainly to $b\bar{b}$, but at the LHC, large QCD background will overwhelm this signal. The same is true for the decay mode $H \rightarrow \tau\tau$. The most promising mode for light Higgs boson searches would be $H \rightarrow \gamma\gamma$. CMS will be able to discover the Higgs boson in the mass range from 90 GeV to 140 GeV utilizing its high-resolution, high-granularity crystal calorimeter [75]. With the same integrated luminosity, ATLAS can search in the range from 110 GeV to 140 GeV, but needs more luminosity, on the order of 400 fb^{-1}, to reach down to 90 GeV [76]. On the other hand, for a heavy Higgs boson, with mass between 800 GeV and 1 TeV, the total width of the Higgs boson becomes large, between 100 and 600 GeV, and the channels having higher rates, such as $H \rightarrow (ZZ, W^+W^-) \rightarrow \ell^+\ell^-\nu\bar{\nu}$ are preferred.

6.2.3 Future Higgs Searches at e^+e^- Linear Colliders

There are several proposals for future high energy and high luminosity e^+e^- colliders: the Next Linear Collider (NLC) [79] and the Tera-electron-volt Energy Superconducting Linear Accelerator (TESLA) [80], with center-of-mass energies around 500 GeV or higher. The Higgs production mechanisms are similar to those at LEP2: the Higgsstrahlung, W^+W^-, and ZZ fusion processes. As shown in Fig.6.5, the W^+W^- fusion process dominates at high energies [81].

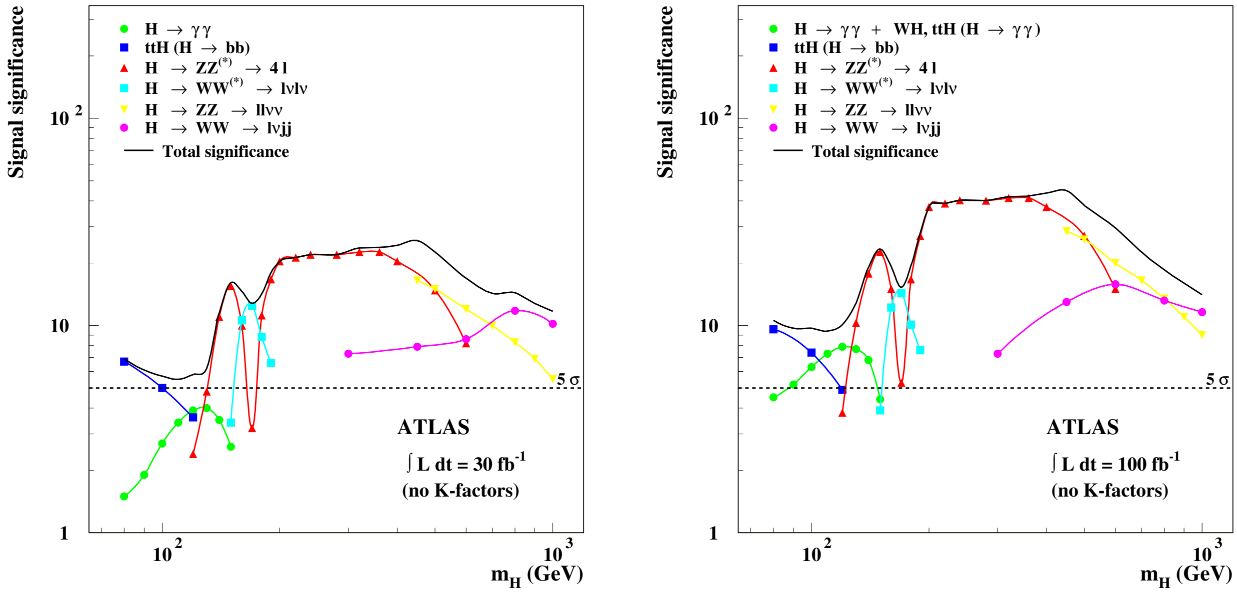

Figure 6.4: Sensitivity for the discovery of a Standard Model Higgs boson in the mass range from 80 GeV to 1 TeV with ATLAS at the LHC. The sensitivity is given in units of $S/\sqrt{B}$ for the individual channels as well as for the combination of the various channels, assuming the integrated luminosities of 30 (left) and 100 fb^{-1} (right).

Studies indicate that in e$^+$e$^-$ collisions at a center-of-mass energy of 500 GeV an integrated luminosity of 5 fb^{-1} would be needed to discover the Higgs boson with mass up to 180 GeV. To extend the discovery range up to 300 GeV would require about 50 fb^{-1} [82].

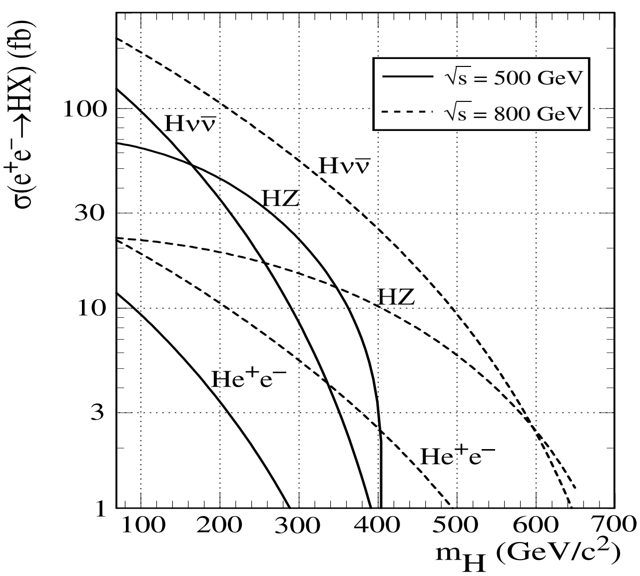

Figure 6.5: Higgs boson production cross sections at a future e$^+$e$^-$ linear collider from Ref.[81]. The HZ, H$\nu\bar{\nu}$, and He$^+$e$^-$ refer to the Higgsstrahlung, W$^+$W$^-$, and ZZ fusion processes, respectively.

These future e$^+$e$^-$ linear colliders could also be run in a $\gamma\gamma$ or e$^\pm\gamma$ collider mode, in which case the Higgs could be produced via $\gamma\gamma \rightarrow$ H, e$\gamma \rightarrow \nu$W$^\pm$H, and e$\gamma \rightarrow$eH processes [81].

Part II

Scaling Property of QCD Dynamical Fluctuations in Hadronic Z Decay

Chapter 7

Introduction

The electroweak sector of the Standard Model, gives a very successful description of the electroweak interaction between leptons, quarks and gauge bosons, even if the problem to confirm the existence of the Higgs still remains. Another sector of the Standard Model is Quantum ChromoDynamics (QCD) describing the strong interaction of quarks and gluons (partons) in color space. The gauge group of the theory is the non-abelian SU(3) group, the gauge bosons are eight gluons, and the fermions are the quarks with three degrees of "color" freedom.

Similarly to Eq. (2.6), the Lagrangian for the non-abelian SU(3) gauge theory has the form:

$$\mathcal{L} = i\bar{\psi}\gamma^{\mu}\mathcal{D}_{\mu}\psi - m\bar{\psi}\psi - \frac{1}{4}A^{j}_{\mu\nu}A^{\mu\nu}_{j}, \tag{7.1}$$

where ψ is now a fermion triplet:

$$\psi = \begin{pmatrix} \phi_1(x) \\ \phi_2(x) \\ \phi_3(x) \end{pmatrix}. \tag{7.2}$$

The index i of $\phi_i(x)$ $(i = 1, 2, 3)$ in Eq. (7.2) is the freedom in color space and x are the space and time coordinates. The covariant derivative $\mathcal{D}_{\mu}$ is given by

$$\mathcal{D}_{\mu} \equiv \partial_{\mu} + ig_{\mathrm{s}}\tau_i A^{i}_{\mu}(x). \tag{7.3}$$

The 3×3 matrices $\tau_i (i = 1, 2, ..., 8)$, called the Gell-Mann matrices, are the generators of the SU(3) group. For each of these eight generators, there is a corresponding massless vector gauge boson called the gluon, with specific color field $A^{i}_{\mu}(x)$. The field tensor is given by

$$A^{j}_{\mu\nu} \equiv \partial_{\mu}A^{j}_{\nu} - \partial_{\nu}A^{j}_{\mu} - g_{\mathrm{s}}f_{jkl}A^{k}_{\mu}A^{l}_{\nu}, \tag{7.4}$$

where f_{jkl} are the structure constants of the SU(3) gauge group. The variable g_s is the coupling constant, which is generally denoted in another form as $\alpha_{\mathrm{s}} \equiv g^2_{\mathrm{s}}/4\pi$ and depends on the energy scale. This important property of QCD, the so-called "running coupling constant", gives rise to two remarkable properties: "asymptotic freedom" and "color confinement". The first property means that at short distances, below the proton size (10^{-13}cm), the color interaction becomes weak, *i.e.*, the strong coupling constant α_{s} becomes small, and quarks are almost free particles. In this case, the interaction between quarks and gluons can be calculated perturbatively by QCD. On the other hand, color confinement means that, at distances comparable to or larger than the proton size, the color interaction becomes so strong that it confines quarks and gluons into composite color-neutral particles, such as pions, protons and neutrons. In this case, perturbative QCD calculations become impossible (non-perturbative regime of QCD).

If, for example, an electron and a positron collide at high energy and annihilate into a quark/anti-quark pair, the first stage is that this $q\bar{q}$ pair will cause the creation of new partons ($q\bar{q}$ pairs and gluons) in a shower-like manner. This so-called parton shower can be analyzed perturbatively by QCD. The next stage is the hadronization, the transition of partons to hadrons, which is strongly related to color confinement. The hadronization process can not be described by perturbative QCD because of the small transverse momentum and large α_s involved. Therefore, phenomenological studies have to be used to gain insight, and phenomenological models have to be developed.

There is another difficulty in forming a complete description of particles produced in an e^+e^- experiment. At high energies, this process is a multiparticle production process, *i.e.*, already at the perturbative stage a large number of partons is involved. Hence, many variables are necessary for the description of the process. For this reason, an exact treatment according to Feynman diagrams is a very difficult task even at tree level in perturbative theory.

Since QCD does not yield a full understanding of the multiparticle production process, it is the *experimental* study of multiparticle production where the essential information has to come from. In this study, e^+e^- collisions have the advantage of leading to the most simple and most clean intermediate $q\bar{q}$ system. Important information on the dynamics of the process is contained in the correlations between the produced particles. To high orders, these correlations can best be studied in terms of their integrals related to particle densities and their fluctuations.

In the last decade, particle density fluctuations of hadronic final states produced in high energy collisions have been extensively investigated, and dynamical (*i.e.*, non-statistical) fluctuations have been observed. For reviews, see [83, 84]. Recently, the study of fractal behavior of the dynamics responsible for local fluctuations has been started in high energy experiments. Parton branching in QCD [85], like other branching processes [86,87], naturally leads to fractal behavior [88]. Such fractal behavior manifests itself in the form of power-law scaling of final-state multiplicity fluctuations with improving resolution in phase space [89, 90]. Experimentally, approximate power-law scaling is observed in e^+e^- collisions [91–93], but, be it of reduced strength, also for all other types of collisions [84]. To be able to distinguish QCD branching expected to be present in e^+e^- collisions from the dynamics at work in hadron-hadron collisions, a better discriminator is needed. Such a discriminator will be applied here in the study of multiplicity fluctuations and fractal behavior in hadroproduction of e^+e^- annihilation using the high statistics data accumulated by the L3 experiment at LEP.

7.1 Hadron production in e^+e^- Collisions

Electron-positron scattering is one of the basic tools to study the QCD properties of the multiparticle production process. For a low center of mass energy, the multiparticle production process $e^+e^- \to q\bar{q}$ is dominated by single virtual photon exchange. When the center of mass energy of the Z resonance is reached ($\sqrt{s} \simeq 91.2$ GeV), Z exchange becomes the dominating process. Because of the large branching ratio of $Z \to q\bar{q}$, the most probable result of this Z exchange process is multihadron production.

Fig. 7.1 shows a schematic illustration of the process $e^+e^- \to q\bar{q} \to$hadrons, where the production mechanism of hadrons is believed to follow four distinct phases [94].

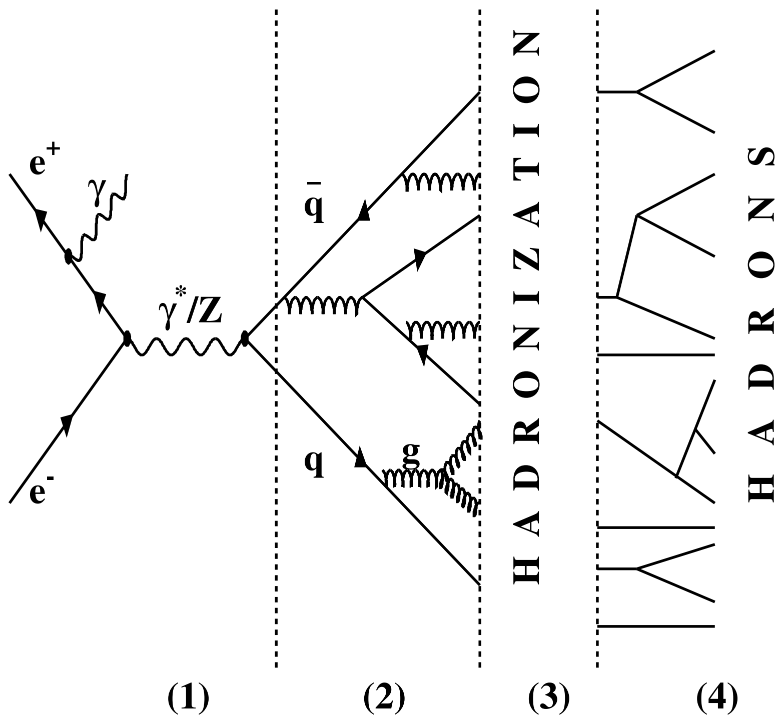

Figure 7.1: A schematic illustration of the process $e^+e^- \rightarrow q\bar{q} \rightarrow$ hadrons.

- **Phase 1:** The e^+e^- pair annihilates into a virtual γ^*/Z according to electroweak theory. The virtual γ^*/Z then decays into a $q\bar{q}$ pair, also following the electroweak theory. Before the annihilation, bremsstrahlung of a photon (initial-state radiation) may occur. This reduces the CMS energy of the e^+e^- collision and, therefore, the total effective mass of the hadronic final state.

- **Phase 2:** The primary quark/anti-quark produced in phase 1 may radiate gluons, which in turn may radiate quark/anti-quark pairs or gluons, thus giving rise to a parton shower. This phase can be described by perturbative QCD using two different approaches.

  The first approach is called the matrix element (ME) approach. Feynman diagrams are exactly calculated within QCD, order by order in the strong coupling constant α_s. In principle, these calculations take all interference terms into account. However, they become increasingly difficult for higher orders and up to now they have been carried out in full only up to the second order $O(\alpha_s^2)$ (*i.e.*, up to four partons in the final state).

  The second approach is called the parton shower (PS) approach. It is formulated in terms of a probabilistic picture where the probabilities for the three basic branchings, $q \rightarrow qg$, $g \rightarrow gg$ and $g \rightarrow q\bar{q}$, are obtained from the Dokshitzer-Gribov-Lipatov-Altarelli-Parisi (DGLAP) evolution equations [95], to describe the cascade process responsible for the jet structure of the event. The approach is based on the leading logarithmic approximation (LLA), where the leading terms and soft logarithm terms are summed to provide the answer in the perturbative QCD expansion. Several extensions of these approximations exist, such as DLLA (D for double), MLLA (M for modified), or NLLA (N for next-to-), all of which try to take some subleading corrections into account.

- **Phase 3:** This phase is called hadronization or fragmentation. The colored partons produced in phase 2 fragment into colorless hadrons. This transition must take place since QCD leads to color confinement and the colored partons cannot be observed as free particles. Due to the large value of α_s at small energy scale, perturbative QCD can not be used here. At present, this phase is explained by phenomenological models, to bridge the gap between colored partons and the colorless hadrons. There are three main types of phenomenological models used today: independent fragmentation (IF) [96], string fragmentation (SF) [97], and cluster fragmentation (CF) [98].

- **Phase 4:** The unstable hadrons produced in phase 3 decay into the experimentally observed hadrons (mostly pions). Again, QCD cannot be used and the experimental information on particle lifetimes and branching ratios is used to predict the outcome, although theoretical treatment is possible for weak decays of heavy quark mesons.

7.2 Monte Carlo generators

Phenomenological models are indispensable for the study of the multiparticle production process in QCD, especially for the hadronization process. Monte Carlo generators based on the models are used to generate the whole chain of the e^+e^- interaction process leading to a final state. Events are generated independently, and each property, such as quark flavor, particle direction, fragmentation function, branching ratio, is randomly generated according to its probability of occurrence as determined by the particular physics process. All of the dynamical and kinematical constraints and limitations imposed by the process are taken into account.

In this thesis, two Monte Carlo models, JETSET 7.4 [99] and HERWIG 5.9 [100] are used to simulate the hadron production process at the Z resonance in e^+e^- collisions.

The simulation of hadronic events is implemented in two main stages: the hard process in which electroweak and perturbative QCD calculations are used to produce partons, and the fragmentation in which the hadronization process and the decay of particles are treated phenomenologically. The main physical approaches used in the two Monte Carlo generators mentioned above to describe each of the stages are outlined in the following sub-sections.

7.2.1 Hard process

The hard process in hadron production in e^+e^- collision includes the first two phases described in Sect. 7.1. The production of a primary $q\bar{q}$ pair can be described by the electroweak interaction, while perturbative QCD is used for the final-state radiation of gluons and quarks. These high-order QCD corrections can be described in JETSET 7.4 either with the parton shower approach (JETSET 7.4 PS) or with the matrix element approach (JETSET 7.4 ME), the latter only allowing to choose between a maximum of 2, 3 or 4 partons in the final-state. The default of JETSET 7.4 is the parton shower. This parton shower implementation first generates partons according to the LLA framework, not taking into account the gluon interference (coherence) inherently. Gluon interference is introduced a-posteriori by requiring strict ordering in decreasing emission angles of partons. This makes the parton shower equivalent to the MLLA framework, but with exact energy and momentum conservation at each branching.

In HERWIG, the parton shower approach is based on the MLLA scheme, which takes coherence effects into account inherently, and energy and momentum conservation is applied at each branching.

7.2.2 Hadronization process

The basic hadronization scheme implemented in JETSET 7.4 is the Lund string model [97]. The physical picture for this model is that, at the end of the perturbative stage, the produced quarks and anti-quarks move out in opposite directions, losing energy. The color field between them is viewed as collapsing into a string-like configuration with uniform energy density. As the q and $\bar{\mathrm{q}}$ move apart, the string may break into two less energetic strings by the production of a colorless quark-antiquark pair. The resulting string pieces can break up similarly on their turn, until the mass of each resulting string piece has fallen to the hadronic mass scale. Each final $\mathrm{q\bar{q}}$ segment forms a meson, and baryon production can be introduced by allowing the production of diquark-antidiquark pairs. This model gives a very successful description of the data.

There is another hadronization scheme, the independent fragmentation model [96], available in JETSET 7.4 as an option. Supposing that each parton fragments into hadrons independently, this model was designed to reproduce the limited transverse momenta and has the great advantage of simplicity. However, it gives only a very approximate description of hadronization and can not be considered an alternative to the Lund string model.

The HERWIG generator uses a cluster fragmentation model which implements the idea of pre-confinement [101]. The physical picture is that all of the gluons resulting from the parton shower are split into light quark-antiquark or diquark-antidiquark pairs, which are then locally (in phase space) grouped into colorless clusters which then decay into hadrons while keeping the main properties of the partonic final state.

Very important is that there are several parameters which can be adjusted in both JETSET 7.4 and HERWIG 5.9 to ensure a good description of the experimental data.

7.2.3 Decay of unstable particles

As the last step of Monte Carlo simulation, unstable hadrons produced during the hadronization process decay into stable particles according to the experimental information on particle lifetimes and branching ratios.

7.3 Tools for local dynamical fluctuation analysis

After the discovery of very high multiplicity events with large local density fluctuations in the pseudo-rapidity (see definition in Sect. 7.5.2) distribution [102, 103], the following question arose: Are these fluctuation of dynamical or merely of statistical origin? Białas and Peschanski proposed a method to investigate these fluctuations in the particular case of events with fixed multiplicity [89]. A generalization of the method to inclusive distributions followed two years later [90]. The method is based on the noise-suppressing feature of factorial moments. The investigation of normalized factorial moments (NFM) in decreasing phase space intervals is, therefore, believed to be able to extract the information on non-statistical (*i.e.*, dynamical) fractal fluctuations in multiparticle production processes.

The normalized factorial moment $F_q(M)$ of order q is defined as

$$F_q(M) = \left[\frac{n_m^{[q]}}{\langle n_m\rangle^q}\right]_M , \qquad n_m^{[q]} = n_m(n_m-1)\cdots(n_m-q+1), \tag{7.5}$$

where n_m is the multiplicity in cell m of phase space, M is the number of cells into which the phase space Δ has been partitioned, $[\cdots]_M$ denotes an average over the M cells ($\frac{1}{M}\sum_{m=1}^{M}$), and $\langle\cdots\rangle$ denotes an average over the event sample. For M cells of equal size, the size of each cell is $\delta = \Delta/M$.

The NFM act as filters for particle spikes, allowing only contributions to F_q from bins with $n_m \geq q$. If particles are distributed independently in phase space, *i.e.*, according to a Poissonian distribution, then $F_q(M) = 1$. If there are non-statistical (*i.e.*, dynamical) fractal fluctuations in the event sample considered, the NFM rise with decreasing phase space size (or increasing number of cells) according to a power law:

$$F_q(\delta) \propto \delta^{-\phi_q} \qquad (\delta \to 0), \tag{7.6}$$

$$F_q(M) \propto M^{\phi_q} \qquad (M \to \infty). \tag{7.7}$$

This power law behavior, possibly an indication for a new scaling law, is called "intermittency", which is a phenomenon well-known in hydrodynamics. The exponent ϕ_q is called the q-th order intermittency index.

Since multiparticle production is a process in three-dimensional momentum space, one has to expect that part of the information about the underlying dynamics revealed by the power law behavior of NFM is lost when studying only one or two dimensions. Ochs [104] as well as Białas and Seixas [105] have pointed out independently the projection effect that intermittency, if present in three dimensions, can be lost in fewer dimensions. If one looks at the one-dimensional NFM, they will saturate due to projection. For example, the second-order NFM can be characterised [104] by the saturation formula

$$F_2(M_i) = A_i - B_i M_i^{-\gamma_i}, \tag{7.8}$$

in direction i instead of Eq. (7.7). To overcome this problem, it is necessary to study the NFM in three-dimensional momentum space.

When studying the NFM, one faces the difficulty that the particle density is not uniform in the usual single-particle variables, *e.g.*, (pseudo-)rapidity y, azimuthal angle φ, and transverse momentum p_{T}. The distribution in p_{T} in fact falls exponentially. Uniformity of the density is, however, an explicit assumption in the derivation of the power law (7.7). Violation of this condition renders an intermittency analysis useless.

To circumvent this problem, it has been proposed independently by Ochs [104, 106] and by Białas and Gazdzicki [107] to use domains in a transformed momentum space with almost constant density. This is accomplished by a transformation of the original variables to "cumulative" variables. For a single variable, say y, one defines the new variable $Y(y)$ as

$$Y(y) = \frac{\int_{y_{\min}}^{y} \rho(y')\mathrm{d}y'}{\int_{y_{\min}}^{y_{\max}} \rho(y')\mathrm{d}y'}, \tag{7.9}$$

where $y_{\min}$ and $y_{\max}$ are the lower and upper limits of the variable y. The variable $Y(y)$ has an uniform density distribution (by construction), since

$$\rho(y)\mathrm{d}y = \rho(y(Y)) \left| \frac{\partial y}{\partial Y} \right| \mathrm{d}Y = \rho(y(Y)) \left| \frac{\partial Y}{\partial y} \right|^{-1} \mathrm{d}Y = \rho'(Y)\mathrm{d}Y, \tag{7.10}$$

and from definition (7.9), the Jacobian is given as

$$\left| \frac{\partial Y}{\partial y} \right|^{-1} = \frac{\int_{y_{min}}^{y_{max}} \rho(y')\mathrm{d}y'}{\rho(y)}, \tag{7.11}$$

yielding

$$\rho'(Y) = \int_{y_{\min}}^{y_{\max}} \rho(y')\mathrm{d}y' = const. \tag{7.12}$$

From the definition (7.9), it also follows that

$$0 \leq Y(y) \leq 1.$$

For higher dimensions, the two treatments are different. It is assumed in [104,106] that the single-particle density, *e.g.* in three dimensions, factorizes as

$$\rho(y_1, y_2, y_3) = \rho_a(y_1)\rho_b(y_2)\rho_c(y_3). \tag{7.13}$$

Under this strong hypothesis, one can transform each of the three variables independently. However, the assumption can not be satisfied completely. In general, there is some residual structure visible in the density distribution of the combined three cumulant variables, indicating that the method is not perfect. The method proposed by Białas and Gazdzicki to perform the transformation in higher dimensions proceeds according to the following steps [107]:

$$(y_1, y_2, y_3) \to (Y_1, y_2, y_3) \to (Y_1, Y_2, y_3) \to (Y_1, Y_2, Y_3),$$

by using the density of particles in the corresponding set of variables at each step.

7.4 Fractality

A power-law dependence like (7.6) is typical for fractals [87]. Fractals widely range from purely mathematical ones (the Cantor set, the Koch curve (Fig. 7.2), snowflakes (Fig. 7.3), *etc.*,) to real objects of nature (coast-lines, clouds, polymers, *etc.*). It is argued in [88] that QCD is inherently fractal and in [108] that a simple connection $\phi_q = d_q(q-1)$ exists between the fractal (Rényi) dimensions $D_q = D - d_q$ (D is the topological dimension, d_q is the anomalous dimension of order q), defined in the context of fractal objects, and the intermittency indices ϕ_q. In other words, the underlying dynamics may have fractal structure.

When the underlying space is of dimension two or higher, there are two distinct kinds of fractals: self-similar and self-affine [87]. The difference between these two lies in the partitioning scales used in the different space directions. If the scales are the same in the different space directions, the fractal is called self-similar, otherwise it is called self-affine. Translated into the language of multiplicity fluctuations in phase space, if the power-law scaling of the NFM holds when the underlying space is partitioned equally in all directions (Fig. 7.4 (a) for a 2-dimensional case, $M_x = M_y = 2$), the dynamical fluctuations are isotropic and the

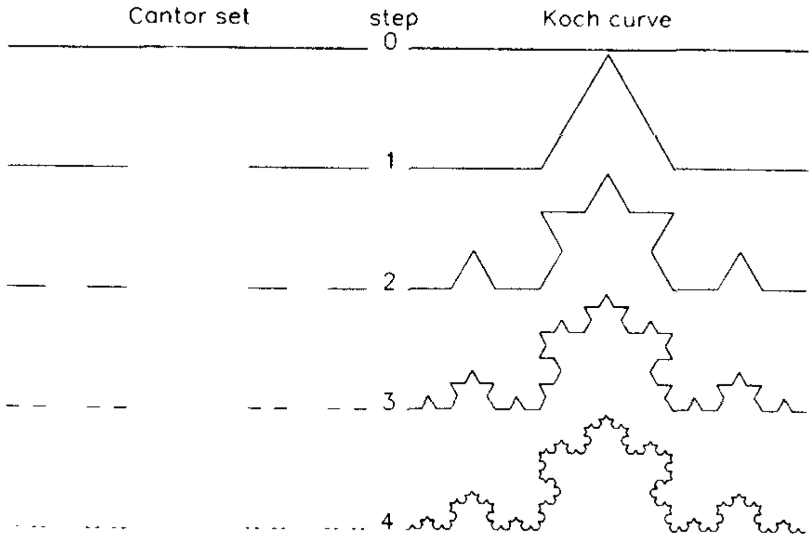

Figure 7.2: The Cantor set and the Koch curve.

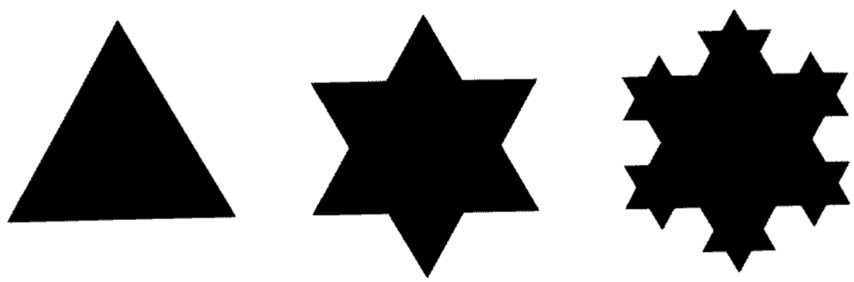

Figure 7.3: Snowflake

corresponding fractal is self-similar. On the other hand, if the power-law scaling of the NFM exists when and only when phase space is divided differently in different directions (Fig. 7.4 (b), $M_x = 3, M_y = 2$ or (c), $M_x = 2, M_y = 3$), the dynamical fluctuations are called anisotropic and the corresponding fractal is self-affine.

The degree of anisotropy can be characterised by a parameter called roughness or Hurst exponent [87], defined as the log-ratio[1]

$$H_{ij} = \frac{\ln M_i}{\ln M_j}, \tag{7.14}$$

with $M_i (i = x, y, z)$ being the partition number in direction i when the power-law scaling is observed. So, if all $H_{ij} = 1$, the dynamical fluctuations are isotropic, if not, they are anisotropic. The Hurst exponent is related to the exponent parameter in Eq. (7.8) by [109]

[1]In observing the power-law scaling property of a system, the phase space region in direction i is partitioned into λ_i bins, and then each bin is further partitioned into λ_i sub-bins,.... After ν steps, the partition number in direction i is $M_i = \lambda_i^\nu$. In this process, it is the log-ratio of M_i and M_j rather than their ratio itself that remains constant and can be used as a characteristic quantity.

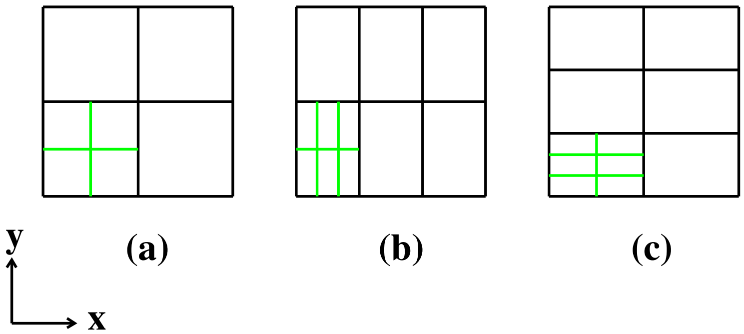

Figure 7.4: Schematic sketch of (a) isotropic and (b,c) anisotropic partitioning of phase space

$$H_{ij} = \frac{1+\gamma_j}{1+\gamma_i}. \tag{7.15}$$

As mentioned above, the multiparticle final state of a high energy collision is a three-dimensional object. The phase space in multiparticle production might be anisotropic, as indicated by the term “longitudinal phase space” first introduced by Van Hove [110]. It has, therefore, been argued that the multiplicity fluctuations might be self-affine fractals in the phase space of multiparticle production [111]. The experimental observations [112, 113] in hadron-hadron collisions at low energies indeed indicate that the multiplicity fluctuations can be interpreted in terms of a *self-affine* fractal behavior.

However, using published Z-decay data [91] and JETSET [99], it has been observed [114] that QCD branching may correspond to a *self-similar* fractal. In other words, the 3-dimensional NFM of hadrons produced in e^+e^- collisions are expected to exhibit a power-law scaling property when phase space is partitioned *isotropically*.

In this thesis, the exact scaling property of the NFM in the hadronic final state of e^+e^- collisions is for the first time studied directly, using the hadronic Z decay data obtained in the L3 detector at LEP.

7.5 Description of final-state hadrons

7.5.1 Event-shape variables

The event-shape variables are defined to characterize the hadronic event as a whole. In order to be calculated in perturbation theory, these variables should be infrared and colinear safe. This means that, if a particle a with 3-momentum $\vec{p}_a$ splits into two new particles b and c with 3-momentum $\vec{p}_b$ and $\vec{p}_c$, respectively, then the corresponding event variables must be invariant under the branching

$$\vec{p}_a \to \vec{p}_b + \vec{p}_c \tag{7.16}$$

whenever $\vec{p}_b$ and $\vec{p}_c$ are parallel or one of them approaches zero.

Thrust

The thrust axis, $\vec{n}_1$, is defined as the axis along which the projected energy flow is maximized. Experimentally, it is used to approximate the direction of the outgoing primary $q\bar{q}$ pair produced in phase 1 of the hadron production process. The value of thrust T_{thrust} and the axis $\vec{n}_1$ are given by [115]

$$T_{\text{thrust}} = \max \frac{\sum_i |\vec{p}_i \cdot \vec{n}_1|}{\sum_i |\vec{p}_i|}, \tag{7.17}$$

where $\vec{p}_i$ is the momentum vector of particle i. The sum $\sum_i$ runs over all final-state particles. The value of T_{thrust} lies in [1/2,1], with $T_{\text{thrust}} = 1/2$ for a fully isotropic final state. The value of T_{thrust} approaches unity as the event configuration in the hadronic center-of-mass system becomes more two-jet like. As the direction of the $\vec{n}_1$ axis is defined by Eq. (7.17) only up to the sign, we randomly choose the positive direction of $\vec{n}_1$.

Major

The Major axis, $\vec{n}_2$, is defined in the plane perpendicular to the event thrust axis $\vec{n}_1$, in the same way as thrust, but is maximized in this perpendicular plane [116],

$$T_{\text{major}} = \max \frac{\sum_i |\vec{p}_i \cdot \vec{n}_2|}{\sum_i |\vec{p}_i|}, \qquad \vec{n}_2 \perp \vec{n}_1. \tag{7.18}$$

In the hadron production process in e^+e^- collisions, the major axis direction is identified with the direction of the first hard gluon emision [114].

Minor

The Minor axis, $\vec{n}_3$, is defined as orthogonal to both the thrust and the major axes, according to a right-handed coordinate system.

7.5.2 Single-particle variables

All of the variables discussed here are defined in the system defined by the axes described above, with z along the $\vec{n}_1$ axis and x along the $\vec{n}_2$ axis.

Rapidity y:

The rapidity of a charged particle is defined by

$$y = \frac{1}{2} \ln \left(\frac{E + p_z}{E - p_z} \right), \tag{7.19}$$

where E is the energy of the particle (usually assuming it is a pion) and p_z is the momentum component along the z-axis. The rapidity has the important property of being additive with respect to a Lorentz transformation along the z-axis; thus the shape of the rapidity distribution is invariant under such a transformation.

Azimuthal angle φ:

The azimuthal angle of a charged particle is defined with respect to the major axis ($\vec{n}_2$) as

$$\varphi = \arctan\left(\frac{p_y}{p_x}\right). \tag{7.20}$$

The variable φ is invariant under Lorentz transformation along the z-axis.

Transverse Momentum $\mathbf{p_T}$:

The transverse momentum

$$p_\mathrm{T} = \sqrt{{p_x}^2 + {p_y}^2} \tag{7.21}$$

is the component of the momentum in the plane transverse to the z-axis. It is invariant under Lorentz transformation along the z-axis.

7.6 The coordinate system

Since the only direction determined by the electro-weak interaction is the direction of the primary $\mathrm{q\bar{q}}$ pair produced in phase 1 of the hadron production process, the system has a cylindrical symmetry about this direction. It is therefore natural to use a cylindrical coordinate system with the z-axis along the $\mathrm{q\bar{q}}$ direction. Experimentally, the $\mathrm{q\bar{q}}$ direction is approximated by the thrust direction.

The so-called thrust frame, an orthonormal system for an event, is widely used in experimental analyses. In this system, $\vec{n}_1$, $\vec{n}_2$, $\vec{n}_3$ are chosen as the z, x, y axes, respectively.

However, for the goal of studying QCD dynamical fluctuations, it should be ensured that the coordinate system does not depend on the QCD dynamics. Otherwise, the dynamics dependent coordinate system will have the effect of reducing the observed dynamical fluctuations. In the thrust system, the choice of x-axis, and consequently y-axis, does depend on the QCD dynamics, which can be easily seen from Eq. (7.18). Thus the fluctuations of some of the variables used to study the dynamics, which are defined with respect to the x-axis, *e.g.*, the azimuthal angle as defined in Eq. (7.20) will be reduced. To observe the dynamical fluctuations fully, a QCD dynamics independent coordinate system should be chosen. This can be done to a very good approximation by rotating the x-axis to lie in the plane of the thrust axis and beam [114]. This coordinate system is called the rotated frame. However, this choice has potential experimental biases if the $\mathrm{q\bar{q}}$-pair is not produced uniformly or if the detector acceptance is not uniform in the azimuthal angle about the beam. A simpler method is to choose the x-axis direction randomly for each event in the plane perpendicular to the thrust axis. This coordinate system is refered to as the randomized frame.

The thrust axis is, however, only an approximation of the $\mathrm{q\bar{q}}$ direction. We will, therefore, also use a so-called $\mathrm{q\bar{q}}$ frame (see Sect. 9.4) where a correction for the bias introduced by the use of the thrust axis as an approximation of the $\mathrm{q\bar{q}}$ axis is applied as derived from Monte Carlo simulations.

Chapter 8

Event Selection

The analysis presented here is based on a high-quality and high-statistics sample of hadronic events at a center-of-mass energy of $\sqrt{s} \simeq 91.2$ GeV, obtained by the L3 detector during the 1994 LEP running period. The investigation of multiplicity fluctuations in ever smaller phase-space windows demands not only a high purity in hadronic events, but also a high degree of accuracy on the determination of the particle momentum and a good two-particle resolution. We shall restrict our analysis to charged particles, since neutral particles can only be detected in the calorimeters with a resolution lower than that for charged particles, which are detected both in the TEC and the SMD.

Hadronic events produced in an e^+e^- reaction are selected by a two-step procedure. In the first step, the energy deposition in the electro-magnetic and hadronic calorimeters is used to select hadronic events and to remove most of the background. The second step of this selection procedure is the selection of good tracks from the events which have passed the first step of this selection. It is based on the track momenta measured in the central tracking detector, including the information from the TEC and the SMD.

8.1 Calorimeter-based selection of hadronic events

The selection of hadronic events is based on the calorimeter information, with the purpose of rejecting background as much as possible while not influencing the measurement of the charged tracks in the TEC. Since the factorial moments are calculated from charged tracks, this method, which largely decouples the event selection from the charged track selection, is expected to reduce the systematic uncertainty due to event selection.

The background sources can be divided into two main categories: leptonic Z decays ($Z\to e^+e^-, \mu^+\mu^-, \tau^+\tau^-$) and non-resonant background such as two-photon processes, as well as beam-wall and beam-gas events.

First, to remove contamination by electronic noise, all calorimeter clusters are required to have an energy larger than 100 MeV. After that, hadronic events are selected by requiring

$$0.5 < \frac{E^{\mathrm{cal}}}{\sqrt{s}} < 1.5, \tag{8.1}$$

$$\frac{|E_{\parallel}^{\mathrm{cal}}|}{E^{\mathrm{cal}}} < 0.4, \tag{8.2}$$

$$\frac{|E_{\perp}^{\mathrm{cal}}|}{E^{\mathrm{cal}}} < 0.6, \tag{8.3}$$

$$N_{\mathrm{cl}} > 14, \tag{8.4}$$

where E^{cal} is the total calorimeter energy, $E_{\parallel}^{\mathrm{cal}}$ is the energy imbalance along the beam direction, $E_{\perp}^{\mathrm{cal}}$ is the energy imbalance perpendicular to the beam direction, and N_{cl} is the number of calorimeter clusters.

Selection on the total calorimeter energy

The signature of Z$\rightarrow$ q$\bar{\mathrm{q}}$ events is characterized by a total visible energy around the center-of-mass energy of the $\mathrm{e^+e^-}$ collision. The lower cut of Eq. (8.1) is applied to reject background events connected with loss of energy in non-sensitive regions of the detector, *e.g.*, with missing energy due to invisible neutrinos or the two-photon process in which an electron and a positron with large momentum escape through the beam pipe without being detected. On the other hand, the upper cut of Eq. (8.1) is applied to remove Bhabha events which are shifted to high visible energy region after applying the scaling factors (G-factors). Fig. 8.1 (a) shows the normalized distribution of the total calorimeter energy after application of the other cuts (8.2) – (8.4). Data are shown by solid dots and Monte Carlo (MC) by the histogram. Cut (8.1) is indicated by arrows. The peak on the left of the low-energy cut is caused by background events $\mathrm{e^+e^-} \rightarrow \tau^+\tau^-$, which are not included in the Monte Carlo sample.

Selection on the number of clusters

Hadronic events usually have a larger particle multiplicity than other processes. Hence, a cut on low multiplicity events can eliminate background contaminations such as Z$\rightarrow$ $\mathrm{e^+e^-}, \mu^+\mu^-, \tau^+\tau^-$; and also beam-gas events. Since the number of smallest resolvable clusters is proportional to the number of produced particles, the cut on low multiplicity can be realized by the requirement of a minimum number of clusters.

The normalized distribution of the number of SRCs after cuts (8.1) - (8.3) applied and cut criterion (8.4) are shown in Fig. 8.1 (b). As in Fig. 8.1 (a), a small peak to the left of the low-multiplicity cut is caused by $\tau^+\tau^-$ events. There is a disagreement between Monte Carlo and data for large multiplicity events. This is due to the incorrect description of hadronic showers in the BGO crystals of the ECAL, not to background contamination. Since we use only charged track information for the calculation of the factorial moments, there is no reason to cut on large cluster multiplicity.

Selection on the energy imbalance

Since at LEP the laboratory frame coincides with the center of mass frame, hadronic events must be well balanced in energy flow. Hence, cuts (8.2) and (8.3) reject background (uranium noise, beam-gas, beam-wall interaction) events which do not have balanced energy (see Figs. 8.2 (a) and (b)).

In addition to the selection criteria (8.1) - (8.4), events are required to be contained in the barrel region of the calorimeter, $35^\circ < \theta < 145^\circ$. This is achieved by the following requirement on the polar angle $\theta_{\mathrm{thr}}^{\mathrm{cal}}$ of the event thrust axis determined from calorimeter clusters

$$|\cos\theta_{\mathrm{thr}}^{\mathrm{cal}}| < 0.74. \tag{8.5}$$

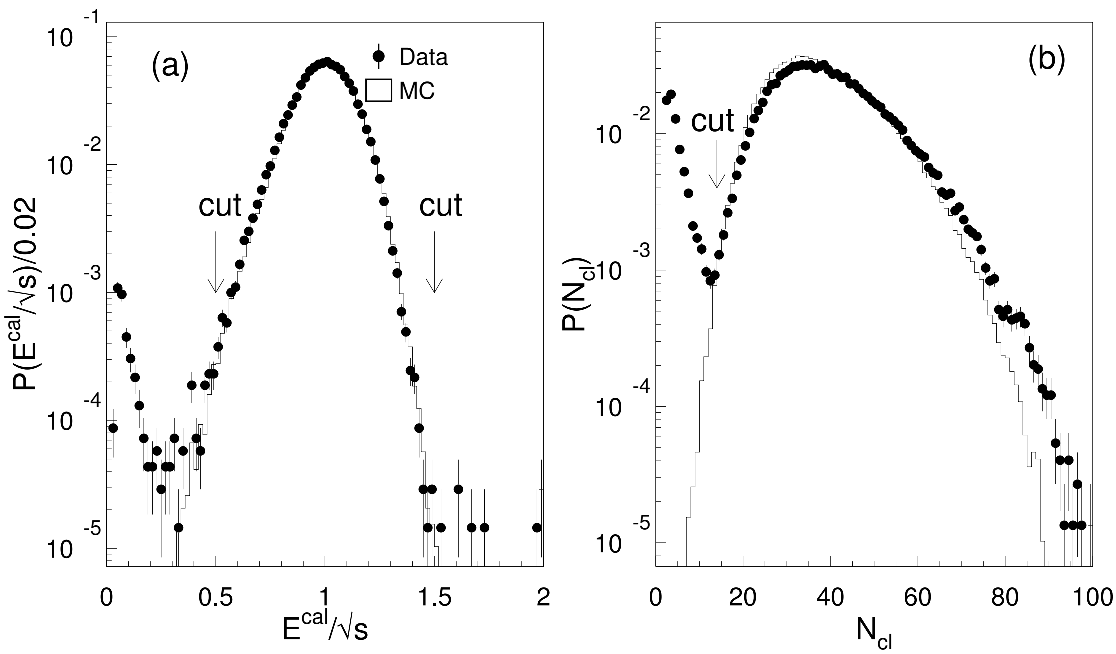

Figure 8.1: (a) Normalized distribution of total calorimeter energy of events compared with the corresponding Monte Carlo prediction, (b) normalized distribution of cluster-multiplicity of events compared with the corresponding Monte Carlo prediction, after other cuts have been applied. Data are represented by solid dots and Monte Carlo by the histogram.

8.2 Selection of charged particles

After the selection of good hadronic events, we consider selection procedures for good tracks within an event based on the information on charged particles from TEC and SMD.

Selection on the number of hits

A charged particle passing through a wire chamber causes ionization in the gas of the chamber. The ionization electron, drifting to the nearest anode wire, leads to an electric discharge ("hit") on this wire. Since the TEC contains 62 wires (8 in the inner sector and 54 in the outer sector), a charged particle can produce a maximum of 62 hits. The larger the number of hits, the better is the resolution of the transverse momentum, since the transverse momentum is calculated from the curvature of the track path formed by the subsequent hits. A mis-reconstructed track usually has a small number of hits. Especially, if there is no hit in the inner TEC, one cannot be sure that the track comes from the interaction region, and the possibility of mis-reconstruction of the track will be high. Therefore, at least one hit in the inner TEC is required to ensure that the track comes from the interaction region (see Fig. 8.3 (a)).

A discrepancy exists between MC and data in the distribution of the number of TEC hits (see Fig. 8.3 (b)). The reason is the MC underestimation of missing hits in the inner TEC. The cut is chosen to lie in the middle of a region where the variation of the disagreement between data and MC is stable and no big change from bin to bin in the disagreement is expected. Therefore, a charged track candidate is required to have at least 25 hits. Loss in

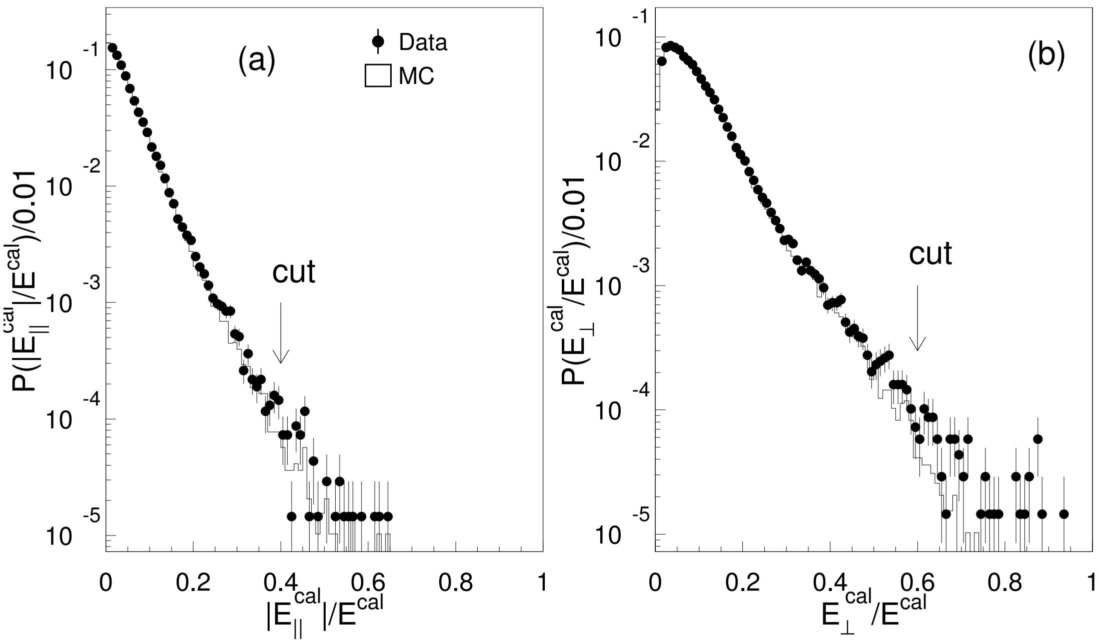

Figure 8.2: Normalized distributions of (a) longitudinal, (b) transverse energy imbalance of events, after other cuts applied. Data are represented by solid dots and Monte Carlo by the histogram.

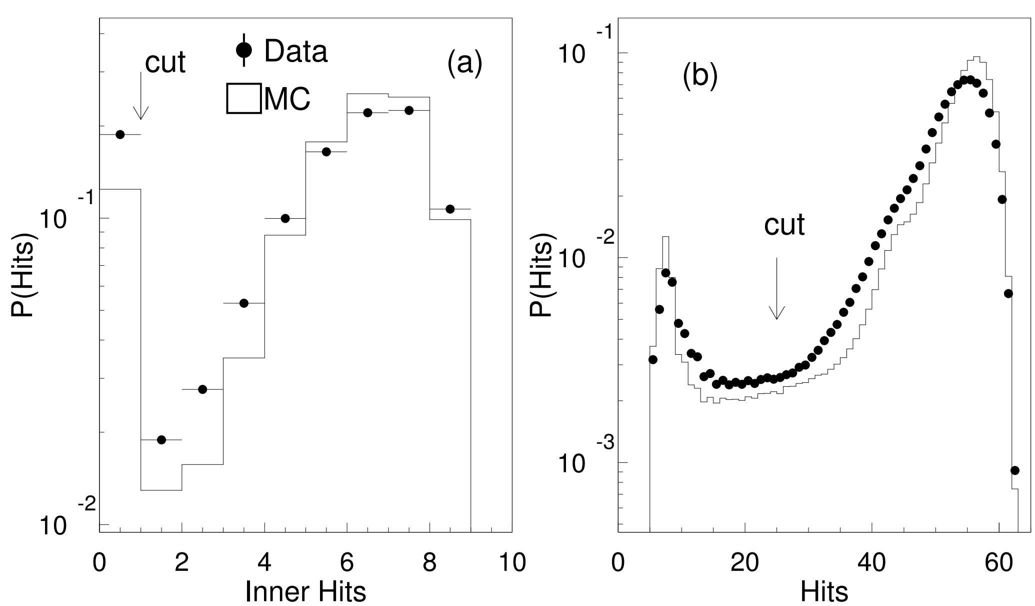

Figure 8.3: Normalized distributions of the number of hits on a track (a) in the inner TEC and (b) in the full TEC. Data are represented by solid dots and Monte Carlo by the histogram.

track momentum resolution, which could result from the use of such a low minimum requirement on the number of the TEC hits, is minimized by the requirement of at least one inner TEC hit and also by the choice of a rather large span (see below).

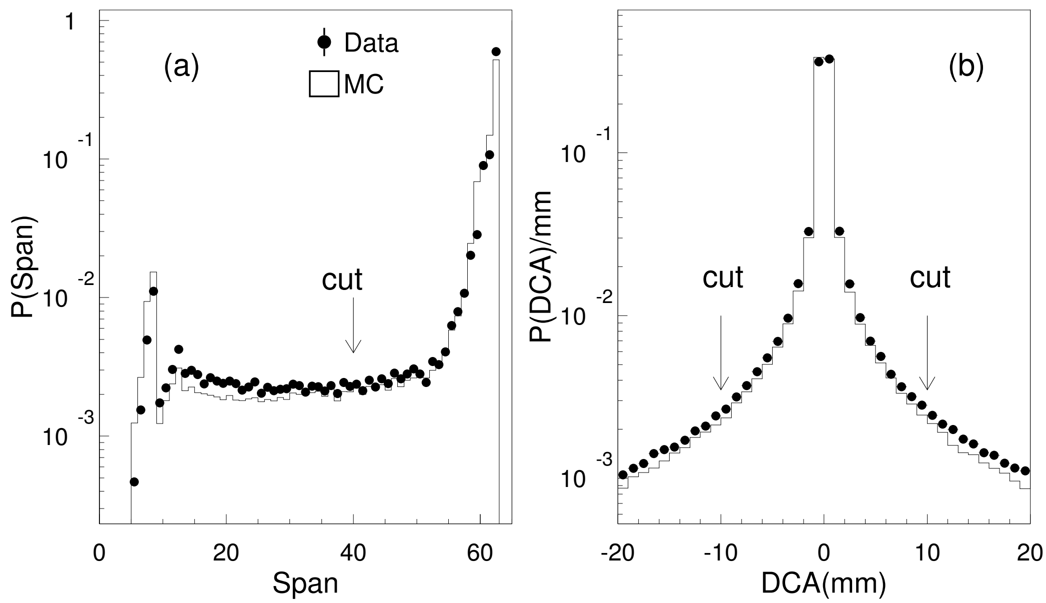

Figure 8.4: Normalized distributions of (a) the span of tracks and (b) the distance of closest approach (DCA) of tracks. Data are represented by solid dots and Monte Carlo by the histogram.

Selection on span

A track is reconstructed by combining hits. It can happen that the reconstruction program forms a track from hits belonging to different particles. In general, the mis-reconstructed track has a smaller length than that of a true particle. The length of a track in terms of hits is the so-called span. It is defined as

$$\text{Span} = W_{\text{out}} - W_{\text{in}} + 1, \tag{8.6}$$

where W_{out} is the wire number of the outermost hit and W_{in} is the wire number of the innermost hit. The requirement that a track have a span of at least 40 helps to reject mis-reconstructed tracks (see Fig. 8.4 (a)).

Selection on distance of closest approach (DCA)

Hadrons directly produced by Z decay must originate from the interaction vertex. A track can be extrapolated back to the interaction region. The distance of closest approach (DCA) for the track is defined as the distance of the track to the interaction point in the plane perpendicular to the beam direction. The requirement on the DCA is less than 10 mm (see Fig. 8.4 (b)) to ensure that a track originates from the interaction point.

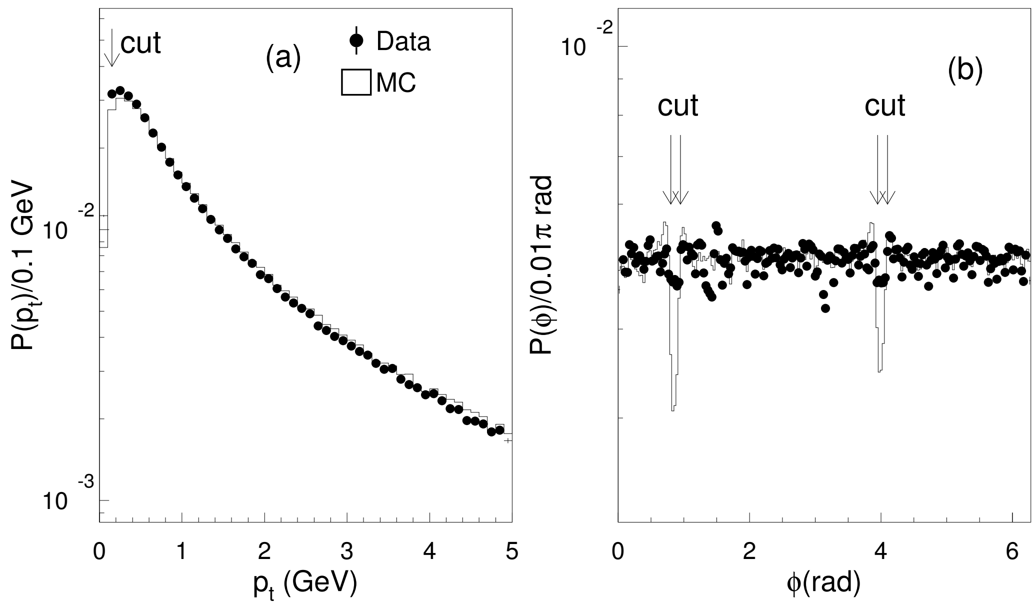

Figure 8.5: Normalized distributions of (a) transverse momentum of tracks and (b) the azimuthal angle of tracks. Data are represented by solid dots and Monte Carlo by the histogram.

Selection on transverse momentum $\mathbf{p_T}$

Tracks with low transverse momentum cannot be measured accurately in TEC and cannot enter the calorimeter. To avoid any reconstruction error, the measured transverse momentum with respect to the beam direction is required to be larger than 150 MeV (see Fig. 8.5 (a)).

Selection on azimuthal track angle φ

From Fig. 8.5 (b), we can see that large discrepancies between data and MC exist in the azimuthal angle distribution for two regions: $45° < \varphi < 52.5°$ and $225° < \varphi < 232.5°$. This is due to a wrong simulation of inefficiencies of the two corresponding TEC sectors. Tracks located in these two regions have, therefore, been removed from the analysis.

Selection on two-track resolution

The resolution of the opening angle between a pair of tracks is crucial for the study of fluctuations in small angular bins. A good reconstruction of the angle between the tracks is very important. However, when the opening angle between two like-sign tracks is less than 3°, the detector efficiency to resolve the two tracks drops sharply. This causes a large disagreement between data and MC simulation for relevant variables, such as the difference in the polar and azimuthal angles between two tracks, $\delta\theta$ and $\delta\varphi$. To resolve this problem, additional cuts on tracks are applied to remove the track when no hit in the Z-chamber is found and an energy deposit in the BGO is used to recover this missing hit. After this cut, there is a good consistency between data and MC simulation for the difference between two tracks in the polar and azimuthal angle with respect to the beam direction (see Fig. 8.6).

Together with the previous cuts, about 40% of the tracks are rejected, which results in an average charged-particle multiplicity of approximately 12.

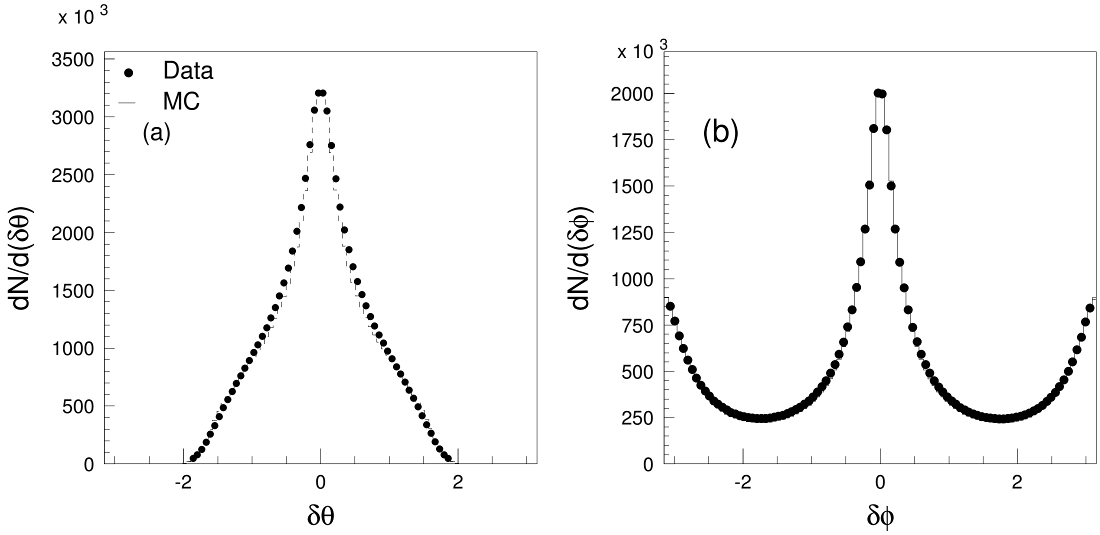

Figure 8.6: The distributions of the difference between two tracks in the (a) polar (b) azimuthal angle with respect to the beam direction. Data are represented by solid dots and Monte Carlo by the histogram.

8.3 Further event selection based on TEC information

In order to reject the remaining background, and increase the purity of the hadronic sample, we impose two more cuts based on the TEC information after having performed the track cut.

First, to reject residual $\tau^+\tau^-$ background, there is a cut on the second largest angle φ_2 between any two neighboring tracks in the $r - \varphi$ plane. Selected events are required to have their φ_2 angle between 20° and 170° [117].

Secondly, to ensure that tracks are in the barrel of the TEC, the polar angle of the event thrust axis $\theta_{\rm thr}^{\rm TEC}$ determined from the charged tracks is required to satisfy

$$|\cos\theta_{\rm thr}^{\rm TEC}| < 0.7 \quad . \tag{8.7}$$

After all the selections, about 820k events survive.

8.4 Resolution

The investigation of the multiplicity fluctuations using normalized factorial moments involves counting particles in small bins of phase space. To avoid systematic bias arising from limited detector resolution, we have to find, first of all, the resolution of the L3 detector. The knowledge of this quantity enables us to choose a minimum bin size for the study of multiplicity fluctuations.

Suppose the true value of the variable to be measured is X. However, what one actually measures with any real detector is not the true value X but X', the true value smeared with the detector resolution.

For the determination of the resolution in the various variables used in our analysis, we apply the Monte Carlo technique. An event is generated by Monte Carlo (generator level MC) giving the "true" value of the variable X. Then, all tracks resulting from this event are processed through a simulation of detector properties (detector level MC). In this stage, the L3 detector simulation program SIL3, based on the GEANT3 package, modifies the event, taking into account particle interactions with the detector material, resolution and acceptance of the detector, and various other detector imperfections. After the detector simulation, the event is reconstructed in the same way as a real data event. From the reconstructed MC events, we calculate the value X' of the same variable after distortion by detector effects. By histogramming the difference

$$\delta X = X - X' \tag{8.8}$$

from a sufficiently large sample of MC events, we can estimate the resolution for the variable X from the distribution of δX. This has been done [118] for the following two-particle distance variables defined with respect to the thrust axis:

1) rapidity difference $y_{12} = |y_1 - y_2|$ between two tracks;
2) azimuthal angle $\varphi_{12} = |\varphi_1 - \varphi_2|$ between two tracks;
3) transverse momentum difference $p_{\mathrm{T}12} = |p_{\mathrm{T}1} - p_{\mathrm{T}2}|$ between two tracks.

For each of the variables, the distribution of the difference between generator level of MC and detector level of MC is approximately Gaussian except for large tails. The value of the half-width at half-maximum (HWHM) HW_2, can be used as a characteristic of the resolution. For a Gaussian distribution, HW_2 is related to the standard deviation: $HW_2 = 1.18\sigma$. The HW_2 for the three variables is shown in Tab. 8.1.

y_{12}	φ_{12}(rad)	$p_{\mathrm{T}12}$(GeV)
0.05 ± 0.02	0.03 ± 0.01	0.031 ± 0.005

Table 8.1: HW_2 for different variables defined with respect to the thrust axis calculated from MC events for the 1994 running period.

The HWHMs shown in Tab. 8.1 are averages. There is a weak dependence of the resolution on the values of the variables themselves and on the location of the tracks in the detector.

Since the calculation of the NFM involves many particles in the same bin, we need to know the many-particle resolution. The easiest way to estimate the resolution of many tracks is to obtain the HWHM HW_i for i-particle resolution with the following formula according to the property of Gaussian distribution,

$$HW_i = \sqrt{(i-1)HW_2^2}. \tag{8.9}$$

The values of HW_i are listed in Tab. 8.2.

	HW_2	HW_3	HW_4	HW_5
y_{12}	0.05 ± 0.02	0.07 ± 0.03	0.09 ± 0.03	0.10 ± 0.04
φ_{12}(rad)	0.03 ± 0.01	0.04 ± 0.01	0.05 ± 0.02	0.06 ± 0.02
$p_{\mathrm{T}12}$(GeV)	0.031 ± 0.005	0.043 ± 0.007	0.054 ± 0.008	0.062 ± 0.01

Table 8.2: HW_i for different variables with respect to the thrust axis (MC events for 1994).

The smallest bin size in the following anlysis of NFM is chosen to be larger than these resolution values.

Chapter 9

Results

The experimental investigation of local dynamical fluctuations in the final-state hadron system presented in this chapter, is based on the samples of Z decays at $\sqrt{s} \simeq 91.2$ GeV recorded with the L3 detector during the 1994 LEP running period. After applying the event selections discussed in the previous chapter, approximately 820k hadronic events remain.

For comparison with the experimental data, two Monte Carlo (MC) samples of hadronic events are generated with the JETSET 7.4 Parton Shower Model with Bose-Einstein (B-E) correlations [1]. The first sample, without initial-state photon radiation (ISR), contains all charged final-state particles with a lifetime larger than 10^{-9} s (generator-level sample). The second, the detector-level sample, generated with ISR is passed through full detector simulation, including distortions due to detector effects, limited acceptance, resolution, long-lived resonances decaying within the detector and event and track selection. The events are processed with the same reconstruction program used for the data. Both generator-level and detector-level MC samples have the same statistics.

In the experimental analysis, the normalised factorial moments (NFM) calculated from the real data are corrected for detector effects by the following formula:

$$F_q = F_q^{\mathrm{raw}} \frac{F_q^{\mathrm{gen}}}{F_q^{\mathrm{det}}}, \tag{9.1}$$

where F_q^{gen} and F_q^{det} are the values of the NFM of order q calculated from the generator-level and detector-level MC samples, respectively, while F_q^{raw} is the NFM calculated directly from the raw data.

Before investigating the NFM, let us consider the single-particle inclusive distributions. A comparison between the inclusive distributions for uncorrected data and detector-level MC provides the first test of the validity of the selection procedure described in the previous chapter. Furthermore, the inclusive distributions will be used for the transformation of the variables into cumulative variables.

9.1 Inclusive distributions

The variables discussed here are the rapidity y, the transverse momentum p_{T} and the azimuthal angle φ, in first instance, all calculated with respect to the thrust axis which is determined by

[1]This model gives a better description of the data for the variables used in this study than JETSET without B-E or HERWIG. The so-called BE_0 algorithm is used in this model with parameters PARJ(92)=1.5 and PARJ(93)=0.33 GeV

using the information of electromagnetic and hadronic calorimeters. The inclusive distributions for these variables are presented in Fig. 9.1 and Fig. 9.2. As discussed in Sect. 7.3, it is better to use the variable φ defined in a randomized frame instead of that defined in the thrust frame, in order to fully reveal the dynamical fluctuations. The inclusive distribution of φ is shown both for the thrust frame and for the randomized frame in Fig. 9.2. All distributions for raw data are in reasonable agreement with detector-level MC.

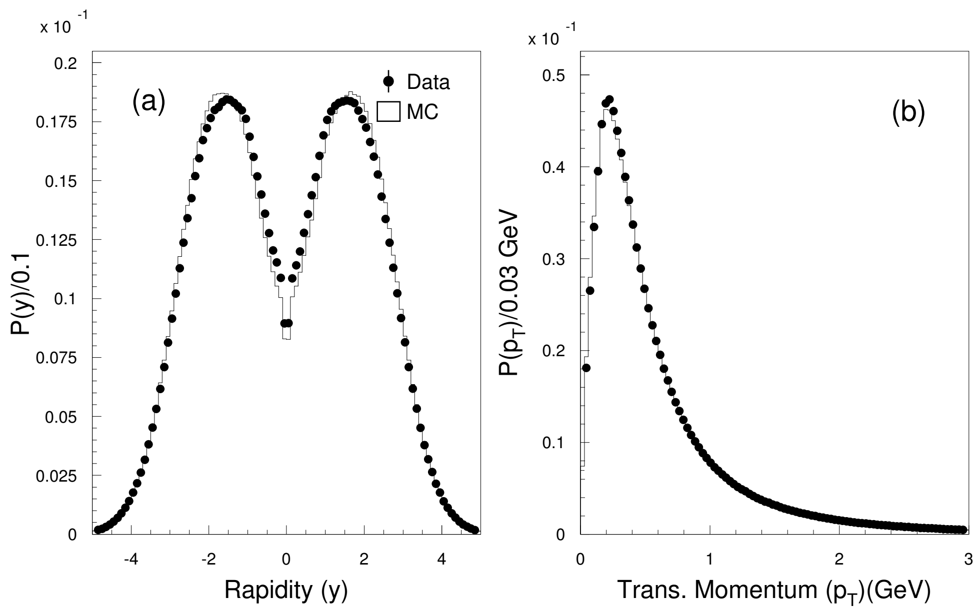

Figure 9.1: Normalized inclusive distribution of the variables (a) rapidity, (b) transverse momentum with respect to the thrust axis, for raw data and detector-level MC.

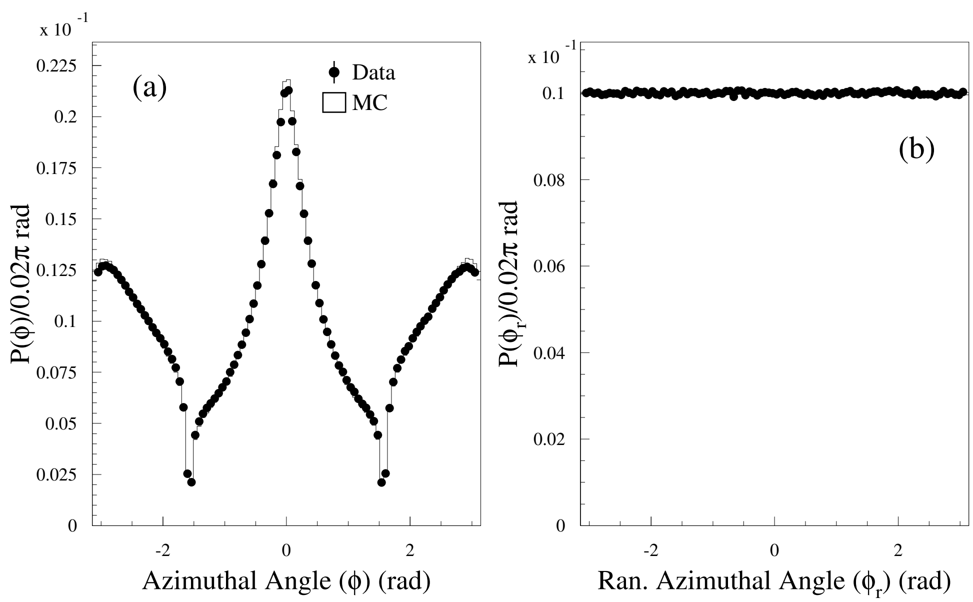

Figure 9.2: Normalized inclusive distribution of the azimuthal angle in (a) the thrust frame, (b) the randomized frame, for raw data and detector-level MC.

9.2 Transformation of variables

The NFM depend on the average local multiplicity $\langle n_m \rangle$ in the bin m, and, hence, on the shape of the inclusive density. As mentioned in Sect. 7.4, the scaling property of the NFM is derived from the assumption that the density is uniform in the variables considered. In practice, the inclusive density distribution of the variables used in our experimental study, *i.e.*, rapidity y, transverse momentum p_{T} and azimuthal angle φ, violate this condition strongly with non-flat phase space distributions. We, therefore, transform these one-dimensional variables to new "cumulative" variables having uniform single-particle distributions, using Eq. (7.9). Figs. 9.3 and 9.4 show the normalized distributions of one-dimensional cumulative variables, which will be used for the one-dimensional NFM calculation.

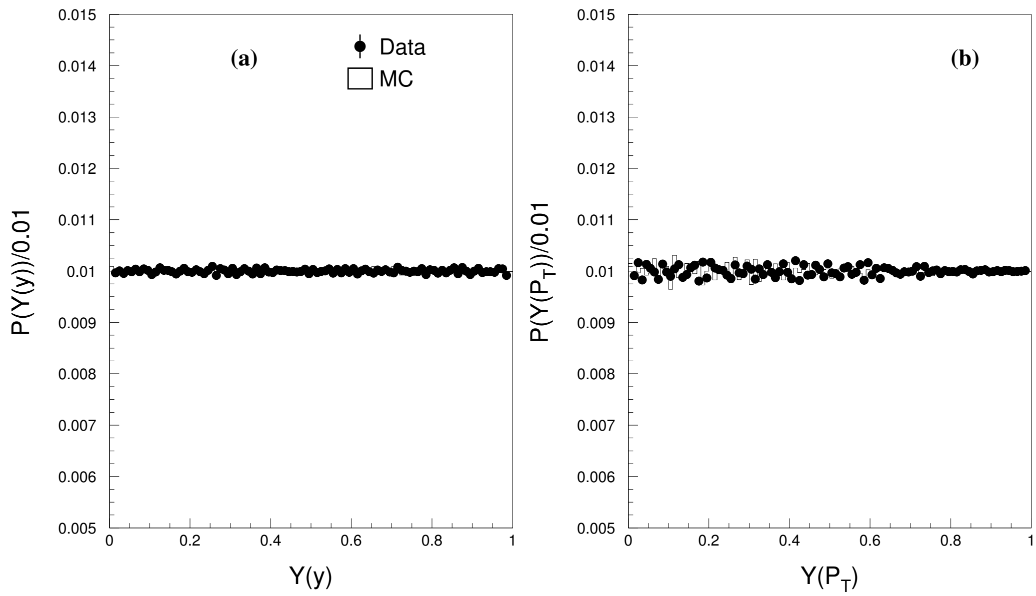

Figure 9.3: Normalized inclusive distribution of cumulative variables corresponding to (a) rapidity, (b) transverse momentum.

For the multi-dimensional cumulant transformation, both the Ochs method [104, 106] and the Białas-Gazdzicki method [107] (see Sect. 7.3) are investigated. As an example, Fig. 9.5 shows the density distribution of the two-dimensional "cumulative" variables obtained by the Ochs method and the Białas-Gazdzicki method. It is obvious that the Białas-Gazdzicki method gives a uniform distribution while the Ochs method does not. This is because the two variables are correlated. Therefore, the Białas-Gazdzicki method is used for the calculation of the three-dimensional NFM.

The Białas-Gazdzicki method is realized experimentally by determining the boundaries of the three-dimensional bins which contain the same number of particles. The method to determine the bin boundaries is as follows: firstly, all particles from all the events are sorted by rapidity y; then, the y range is divided into M_y bins of equal particle number and the corresponding bin boundaries of each bin in rapidity y are determined [2]; next, the particles in each bin of y are sorted in transverse momentum p_{T} and the boundaries of $M_{p_{\mathrm{T}}}$ bins which hold equal number of particles are determined. In general, the p_{T} bin boundaries are different in

[2]Thanks to W. Metzger for providing the sorting and bin-boundary determining code.

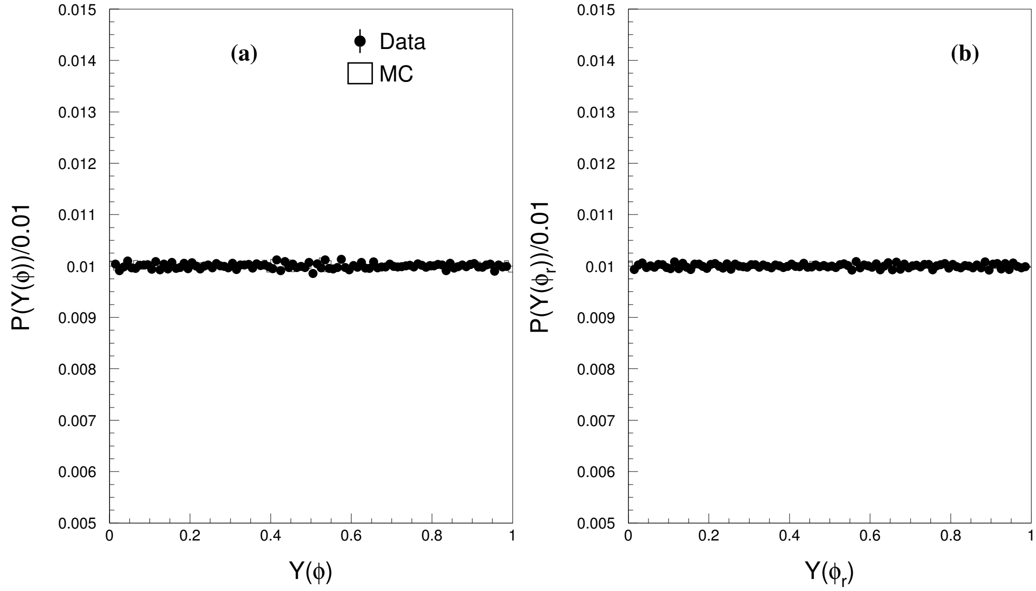

Figure 9.4: Normalized inclusive distribution of cumulative variables corresponding to the azimuthal angle in (a) the thrust frame, (b) the randomized frame.

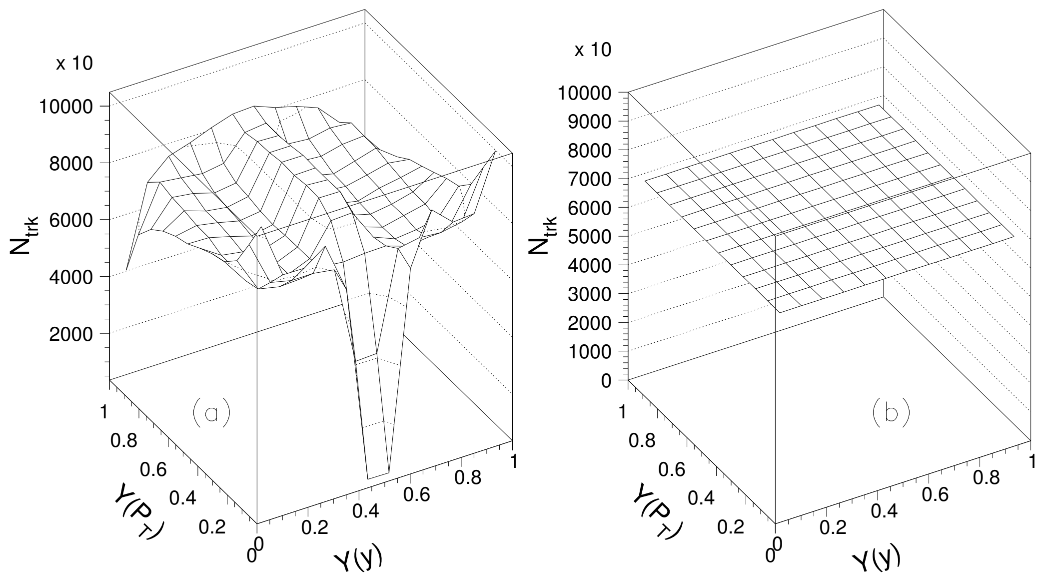

Figure 9.5: Two-dimensional ($y - p_{\mathrm{T}}$) cumulative variable distributions obtained by a) the Ochs method and b) the Białas-Gazdzicki method.

different y bins. Finally, the above procedure is applied to the particles in each of the $M_y M_{p_{\mathrm{T}}}$ bins, and the bin boundaries for the azimuthal angle φ are determined.

After the determination of bin boundaries, for each event the position of the particles in this three-dimensional grid is determined, and the number of particles in each bin is counted for the calculation of the NFM.

9.3 Systematic uncertainties

The sources of systematic uncertainty are grouped into two categories: One is for the NFM and the other one is for fitted results.

9.3.1 Systematic uncertainties on the NFM

The systematic uncertainties on the NFM are estimated from different cut criteria on track selection and event selection, and from different Monte Carlo models to correct for detector effects. Another systematic uncertainty for the three-dimensional NFM comes from the different order in which the three variables are transformed in the Białas-Gazdzicki method. This uncertainty, however, is found to be negligible compared to the statistical uncertainty.

Condsidering the bin-to-bin correlations between the NFM ($F_q(M)$) at different M, for the purpose of fit to NFM, the covariance matrices are also evaluated for each of the systematic uncertainty sources.

The track quality cuts

The influence of the track quality cuts is investigated by varying independently each cut parameter (Sect. 8.2) used to define a good track. For each cut parameter, p, the standard cut value is named C_0^p, and the corresponding q-th order NFM is $F_q^{C_0^p}$. Then we calculate the NFM the same way using both smaller, C_s^p, and larger, C_l^p, values of the cut parameter. The varied cut parameters are listed in Tab. 9.1. The corresponding values of the NFM are $F_q^{C_\mathrm{s}^p}$ and $F_q^{C_\mathrm{l}^p}$, respectively. The larger of the differences between the standard value of the NFM and the two varied NFM,

$$\delta F_q^{(p)}(M) = \max(|F_q^{C_\mathrm{s}^p} - F_q^{C_0^p}|, |F_q^{C_\mathrm{l}^p} - F_q^{C_0^p}|), \tag{9.2}$$

is taken as the contribution to the systematic uncertainty from cut parameter p. The systematic uncertainties from each of the track quality cuts are added in quadrature to give the total systematic error on F_q from the track quality cut:

$$\Delta_\mathrm{track}^\mathrm{syst} F_q(M) = \sqrt{\sum_p (\delta F_q^{(p)}(M))^2}. \tag{9.3}$$

This is the dominant contribution to the systematic error on the NFM.

cut parameters p	smaller value C_s^p	larger value C_l^p
$p_\mathrm{T} > C^p$	100 MeV/c	200 MeV/c
Span $\geq C^p$	32	48
$\mathrm{N_{innerHits}} \geq C^p$	0	2
$\mathrm{N_{Hits}} \geq C^p$	20	30
$\mid$ DCA $\mid < C^p$	5 mm	15 mm

Table 9.1: The varied values of each cut parameter used to determine the contributions to the systematic uncertainty from the track quality cuts.

The elements of the covariance matrix are estimated by

$$V^{\rm syst}_{\rm track}(M1,M2) = \rho(M1,M2)\Delta^{\rm syst}_{\rm track}F_q(M1)\Delta^{\rm syst}_{\rm track}F_q(M2) \tag{9.4}$$

where the correlation coefficient $\rho(M1, M2)$ can be calculated using:

$$\rho(M1,M2) = \frac{\overline{F_q^{(p)}(M1)F_q^{(p)}(M2)} - \overline{F_q^{(p)}(M1)}\cdot\overline{F_q^{(p)}(M2)}}{\sqrt{(\overline{(F_q^{(p)}(M1))^2} - \overline{F_q^{(p)}(M1)}^2)(\overline{(F_q^{(p)}(M2))^2} - \overline{F_q^{(p)}(M2)}^2)}}, \tag{9.5}$$

in which $\bar{x}$ denotes the average of x over all track selection cut parameters p.

The event selection cuts

The same technique as used to estimate the systematic uncertainty due to the track quality cuts, is applied to estimate the systematic uncertainty on the NFM $\Delta^{\rm syst}_{\rm eve-cut}F_q(M)$ and the covariance matrix $V^{\rm syst}_{\rm eve-cut}$ due to the event selection cuts (Sect. 8.1). The varied values of each cut parameter are listed in Tab. 9.2. This contribution to the systematic error on the NFM is very small since it only changes the size of the inclusive sample by a relatively small number, and after normalisation over the size of the inclusive sample the corresponding NFM value is quite close to the standard one.

cut parameters p	smaller value $C_{\rm s}^p$	larger value $C_{\rm l}^p$
$E^{\rm cal}/\sqrt{s} > C^p$	0.44	0.56
$E^{\rm cal}/\sqrt{s} < C^p$	1.42	1.55
$\mathrm{N}_{\rm clus} > C^p$	13	16
$\frac{\lvert E^{\rm cal}_{\parallel}\rvert}{E^{\rm cal}} < C^p$	0.35	0.45
$\frac{\lvert E^{\rm cal}_{\perp}\rvert}{E^{\rm cal}} < C^p$	0.55	0.64
$\lvert\cos\theta^{\rm cal}_{\rm thr}\rvert < C^p$	0.64	0.8
$\lvert\cos\theta^{\rm TEC}_{\rm thr}\rvert < C^p$	0.6	0.8

Table 9.2: The varied values of each cut parameter used to determine the systematic uncertainty from the event selection cut

Monte Carlo model uncertainties

As given in Eq. (9.1), the results from the raw data are corrected for detector effects using a Monte Carlo Model. An important source of systematic uncertainty comes from the influence of the model used to correct the data. This uncertainty is estimated by using two further Monte Carlo models, JETSET 7.4 without Bose-Einstein correlations and HERWIG 5.9, instead of JETSET 7.4 with Bose-Einstein correlations, which was used to determine the standard NFM. The larger of the differences between the standard NFM and the NFM corrected by these Monte Carlo models is taken as the systematic uncertainty on the NFM from the Monte Carlo model,

$$\Delta^{\rm syst}_{\rm MC}F_q(M) = \sqrt{\max((F_q^{\rm HERWIG} - F_q^{\rm JETSET})^2, (F_q^{\rm JETSET\_noBE} - F_q^{\rm JETSET})^2)}. \tag{9.6}$$

The corresponding covariance matrix can be obtained in the samilar way as Eqs. (9.4)−(9.5).

Combining the above three systematic uncertainties from track quality cuts, event selection cuts and different Monte Carlo models gives the total systematic uncertainty on the NFM:

$$\Delta^{\rm syst} F_q(M) = \sqrt{(\Delta^{\rm syst}_{\rm track} F_q(M))^2 + (\Delta^{\rm syst}_{\rm eve-cut} F_q(M))^2 + (\Delta^{\rm syst}_{\rm MC} F_q(M))^2} \tag{9.7}$$

and the total systematic covariance matrix:

$$V^{\rm syst} = V^{\rm syst}_{\rm track} + V^{\rm syst}_{\rm eve-cut} + V^{\rm syst}_{\rm MC} \tag{9.8}$$

For the $\mathrm{q\bar{q}}$ frame, there is an additional contribution to the systematic uncertainty of the NFM which comes from the influence of the MC model for the correction from the thrust axis to the $\mathrm{q\bar{q}}$ direction. This uncertainty is obtained similarly to the Monte Carlo model uncertainty for the detector effect correction.

9.3.2 Systematic uncertainties on fitted results

The NFM is the tool for our investigation. What we are interested in are the results of fits to the NFM. The standard values of the fitted intermittency index of the three-dimensional NFM as well as the fitted γ of the one-dimensional second-order NFM, and consequently, the Hurst exponent (generally, all fitted results are denoted as $R_{\rm fit}$) are obtained by fitting the F_q according to Eqs. (7.7) and (7.8). The systematic uncertainties for the fitted results are determined by using a different method for the event selection and for the determination of the thrust axis.

The event selection method

Instead of using the energy information from the electro-magnetic and hadronic calorimeters, hadronic events can also be selected on the basis of the charged-track information from TEC, including the total momentum sum of the charged particles, transverse and longitudinal momentum components of tracks, multiplicity of charged tracks, and the direction of the thrust axis determined from all charged tracks. This method has a selection efficiency and purity similar to that of the calorimeter-based method, and the corresponding results for one- and three- dimensional NFM, as well as the fitted results can also be obtained for this sample. The differences between the results from this event selection method and the standard values, $\Delta^{\rm syst}_{\rm eve-method} R_{\rm fit}$, is considered a systematic uncertainty on the fitted results.

The thrust determination method

Also the thrust axis can be determined from the charged-track information from TEC instead of using the energy information from the electro-magnetic and hadronic calorimeters. The difference between the fitted results from this thrust determination method and the standard values, $\Delta^{\rm syst}_{\rm thr-method} R_{\rm fit}$, is considered as another systematic uncertainty on the fitted results.

These two systematic uncertainties are summed quadratically to give the systematic uncertainty on the fitted results.

9.4 Three-dimensional NFM

Multiparticle production is a process in three-dimensional momentum space. Therefore, strict power-law scaling of the NFM should be studied in three-dimensional momentum space. To explore the possibly existing scaling property, we first study the three-dimensional NFM, F_q

($q = 2,3,4,5$) for an isotropic partitioning of phase space, $M_y = M_{p_T} = M_\varphi$ and $M = M_y M_{p_T} M_\varphi$. The NFM are calculated in three different coordinate systems (Sect. 7.6): the thrust frame, the randomized frame, and the q$\bar{\text{q}}$ frame. The range of the variables is $-5 < y < 5$, $0 < p_T < 3$GeV, $-\pi < \varphi < \pi$.

9.4.1 Thrust frame

In the thrust frame, the z-axis is defined along the direction of the thrust axis, which approximates the q$\bar{\text{q}}$ direction. The x-axis is along the major direction and the y-axis is along the minor direction. The F_q's are calculated using Eqs. (7.5) and (9.1). The resulting $\ln F_q(M)$ are plotted versus $\ln M$ in Fig. 9.6 (a). After omitting the first point to eliminate the influence of momentum conservation [119], the following function is fitted to the data

$$F_q(M) = b_q M^{\phi_q}. \tag{9.9}$$

To take into account the correlations between factorial moments at different M, the full covariance matrix, which is the sum of the statistical and systematic covariance matrix, is used for the fit. The elements of statistical covariance matrix are given by

$$V^{\text{stat}}(M1, M2) = \frac{1}{N-1}\left(\left\langle \left[\frac{n_{m1}^{[q]}}{\langle n_{m1}\rangle^q}\right]_{M1} \left[\frac{n_{m2}^{[q]}}{\langle n_{m2}\rangle^q}\right]_{M2}\right\rangle - \left\langle \left[\frac{n_{m1}^{[q]}}{\langle n_{m1}\rangle^q}\right]_{M1}\right\rangle \left\langle \left[\frac{n_{m2}^{[q]}}{\langle n_{m2}\rangle^q}\right]_{M2}\right\rangle\right), \tag{9.10}$$

in which $[\cdots]_M$ and $\langle\cdots\rangle$ have the same definitions as in Eq. (7.5). The elements of systematic covariance matrix are obtained according to Eq. (9.8).

The fitted lines are also shown in Fig. 9.6 (a) and the fitted intermittency index in Tab. 9.3. The data show good consistency with the fitted straight lines (*cf.* the χ^2 of the fits listed in the upper part of Tab. 9.3) and power-law scaling is observed.

For comparison, the expectations of Monte Carlo models, JETSET with Bose-Einstein correlations and HERWIG, are also shown in Fig. 9.6 (a). Both models agree very well with the data.

Frame	order	ϕ_q	b_q	χ^2/dof
Thrust	2	$0.187 \pm 0.004 \pm 0.015$	$0.790 \pm 0.012 \pm 0.011$	7.4/9
	3	$0.512 \pm 0.012 \pm 0.029$	$0.547 \pm 0.020 \pm 0.051$	7.7/9
	4	$0.954 \pm 0.030 \pm 0.049$	$0.341 \pm 0.030 \pm 0.028$	5.8/9
	5	$1.463 \pm 0.051 \pm 0.003$	$0.211 \pm 0.032 \pm 0.055$	6.6/9
Randomized	2	$0.212 \pm 0.005 \pm 0.004$	$0.752 \pm 0.012 \pm 0.017$	10.3/9
	3	$0.632 \pm 0.016 \pm 0.014$	$0.427 \pm 0.023 \pm 0.040$	9.9/9
	4	$1.215 \pm 0.028 \pm 0.016$	$0.197 \pm 0.020 \pm 0.021$	9.6/9
	5	$1.847 \pm 0.042 \pm 0.036$	$0.096 \pm 0.014 \pm 0.004$	7.0/9
q$\bar{\text{q}}$	2	$0.234 \pm 0.007 \pm 0.003$	$0.735 \pm 0.020 \pm 0.005$	5.6/9
	3	$0.730 \pm 0.013 \pm 0.020$	$0.364 \pm 0.033 \pm 0.013$	7.0/9
	4	$1.437 \pm 0.035 \pm 0.020$	$0.129 \pm 0.022 \pm 0.017$	10/9
	5	$2.207 \pm 0.066 \pm 0.030$	$0.046 \pm 0.015 \pm 0.020$	8.9/9

Table 9.3: The fitted intermittency index ϕ_q and b_q of three-dimensional factorial moments in different frames.

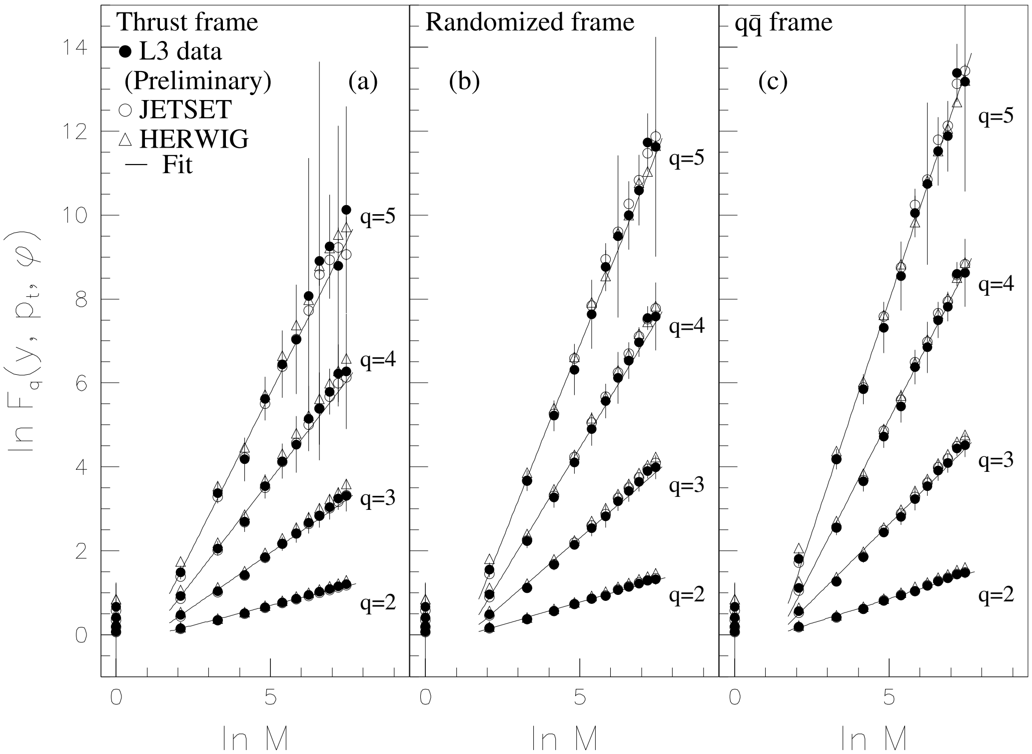

Figure 9.6: The logarithm of the three-dimensional factorial moments, $\ln F_q$, of order 2-5, as a function of the logarithm of the number of partitions, M, compared with the results of the Monte Carlo models, JETSET 7.4 with Bose-Einstein correlations and HERWIG, in the (a) thrust frame, (b) randomized frame and (c) q$\bar{\text{q}}$ frame. The lines are the fits to the data.

9.4.2 Randomized frame

To relax the limitation from the coordinate system in order to fully observe the fluctuations, the NFM are studied in the randomized frame, in which the z-axis is the same as in the thrust frame, the x-axis is chosed randomly on the plane perpendicular to the z-axis, the y-axis is then determined as perpendicular to both x-axis and z-axis.

The resulting $\ln F_q(M)$ versus $\ln M$, and the corresponding fitted results are plotted in Fig. 9.6 (b). The data show good consistency with the fitted straight lines. In other words, strict power-law scaling is observed. Since the three-dimensional phase space is partitioned isotropically along different directions, this strict power-law scaling suggests that the dynamical fluctuations of multiparticle production in e$^+$e$^-$ collosions are isotropic, *i.e.*, that the corresponding system is a self-similar fractal. It can be seen obviously from Tab. 9.3 that the fitted intermittency indices (ϕ_q) obtained in the randomized frame are larger than those in the thrust frame. The strength of the dynamical fluctuations displayed in the thrust frame is indeed reduced with respect to those of the randomized frame. The reason is that, as discussed in Sect. 7.6, the thrust frame is strongly dependent on the QCD dynamics we investigate and the fluctuations of some of the variables defined with respect to this frame are reduced.

9.4.3 q$\bar{\text{q}}$ frame

As mentioned in Sect. 7.6, the hadron production process in e$^+$e$^-$ collisions has a cylindrical symmetry about the primary q$\bar{\text{q}}$ pair direction. It is therefore natural to study the QCD dynamic fluctuation with respect to the q$\bar{\text{q}}$ pair direction. However, there is no possibility to access the q$\bar{\text{q}}$ pair direction experimentally, the best approximation being the thrust axis. Fig. 9.7 shows the distribution of the angle between the q$\bar{\text{q}}$ pair direction and the thrust axis as obtained from Monte Carlo simulation. The difference between the q$\bar{\text{q}}$ pair direction and the thrust axis is small but still considerable, and the result with respect to the q$\bar{\text{q}}$ pair direction should be more authentic. The results with respect to the thrust axis can be corrected to the q$\bar{\text{q}}$ pair direction using Monte Carlo simulation to determine a correction factor

$$C_q(M) = \frac{F_q^{\mathrm{q\bar{q}MC}}(M)}{F_q^{\mathrm{thrustMC}}(M)}. \tag{9.11}$$

The correction factors, C_q, are calculated using JETSET 7.4 with Bose-Einstein correlations. They are plotted as a function of M in Fig. 9.8 for the three-dimensional factorial moments.

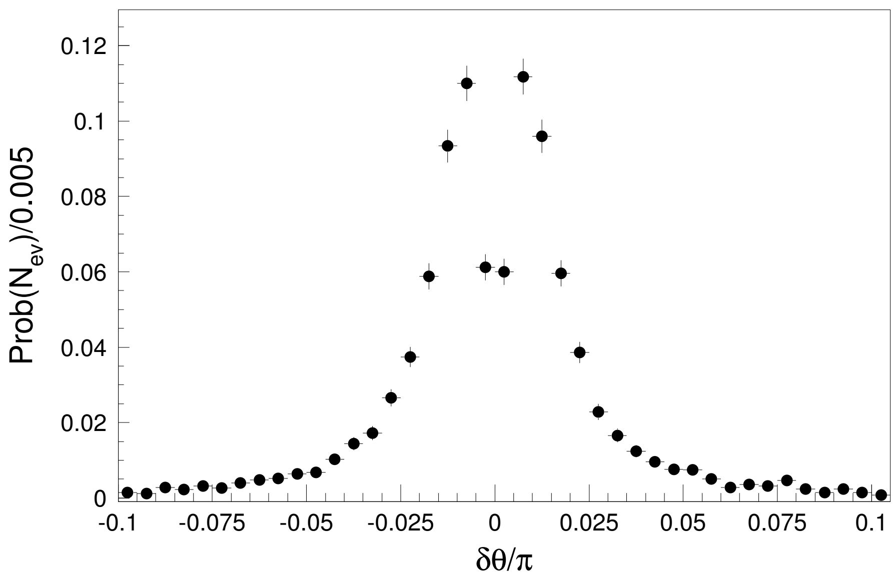

Figure 9.7: The distribution of the angle between q$\bar{\text{q}}$ pair direction and thrust axis, obtained by Monte Carlo using JETSET 7.4 with Bose-Einstein correlations.

The NFM in the q$\bar{\text{q}}$ frame, $F_q^{\mathrm{q\bar{q}}}$ are formed from

$$F_q^{\mathrm{q\bar{q}}}(M) = C_q(M) \cdot F_q^{\mathrm{thrust}}(M). \tag{9.12}$$

The resulting $\ln F_q(M)$ versus $\ln M$ and corresponding fit results are plotted in Fig. 9.6 (c). After this correction, the data still show very good consistency with the fitted straight lines and strict power-law scaling is observed. However, the fitted intermittency indices obtained in the q$\bar{\text{q}}$ frame are larger than those in the randomized frame (see lower part of Tab. 9.3). The use of the thrust axis instead of the q$\bar{\text{q}}$ direction thus appears to dilute the dynamical fluctuations.

9.5 F$_2$ in one dimension

The evidence for isotropy of the dynamical fluctuations of multiparticle production in e$^+$e$^-$ collisions corresponding to a self-similar fractal, can be quantified by the study of F_2 in the

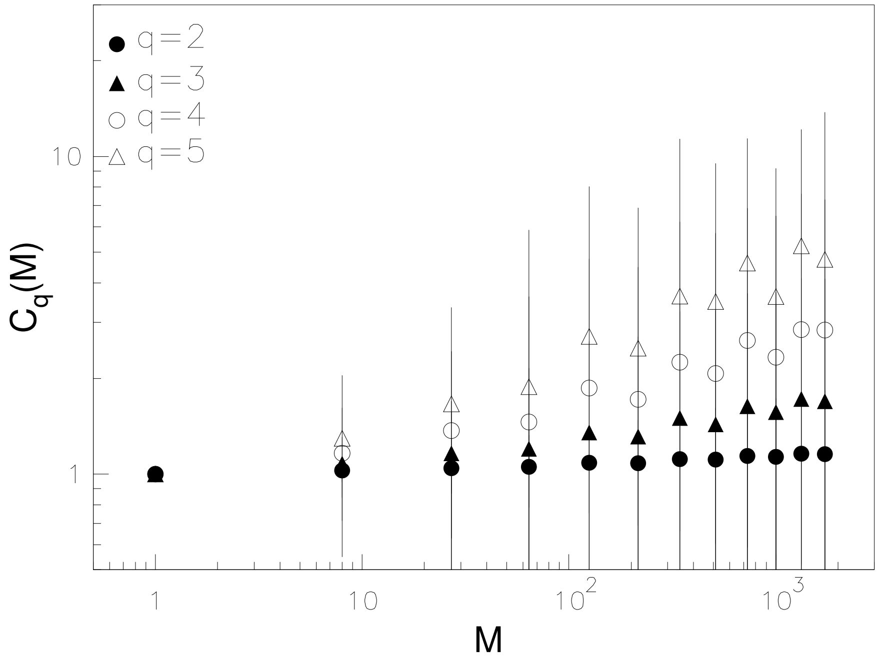

Figure 9.8: The correction factor $C_q(M)$ for three-dimensional factorial moments as a function of the number of bins M, for different order factorial moments. The JETSET 7.4 model with Bose-Einstein correlations is used for the Monte Carlo simulation.

three one-dimensional projections and the extraction of the Hurst exponents, describing the degree of (an-)isotropy of the underlying dynamical fluctuations.

The Hurst exponents can be obtained by fitting F_2 with Eq. (7.8) and calculating them by Eq. (7.15) [109].

9.5.1 Second-order factorial moments $\mathbf{F_2}$

The one-dimensional factorial moments, F_2, versus the number of partitions, M, in the thrust frame and in the randomized frame are plotted in Fig. 9.9 for the variables y, p_{T} and φ, respectively. Since the z-axes of both frames coincide, only $F_2(\varphi)$ depends on the frame used. It is clear from the figure that the fluctuations in φ are strikingly different in the two frames, being nearly absent in the thrust frame. This difference is attributed to the limitation, in the thrust frame, of the direction of the first hard gluon emission to the x axis, as discussed in Sect. 7.5 and 7.6. As a consequence of the reduced fluctuations in φ, the fluctuations in three dimensions are also reduced, resulting in the lower values of the intermittency indices in the thrust frame listed in the upper part of Tab. 9.3. The results obtained in the randomized frame are further corrected to the $\mathrm{q\bar{q}}$ frame. These results are shown in Fig. 9.10.

For comparison, the expectations from the Monte Carlo models JETSET and HERWIG are also shown in Fig. 9.9 and Fig. 9.10. JETSET, both with and without Bose-Einstein correlations gives fair agreement with the data. HERWIG has somewhat more fluctuations than the data, but, nevertheless, shows qualitatively similar behavior.

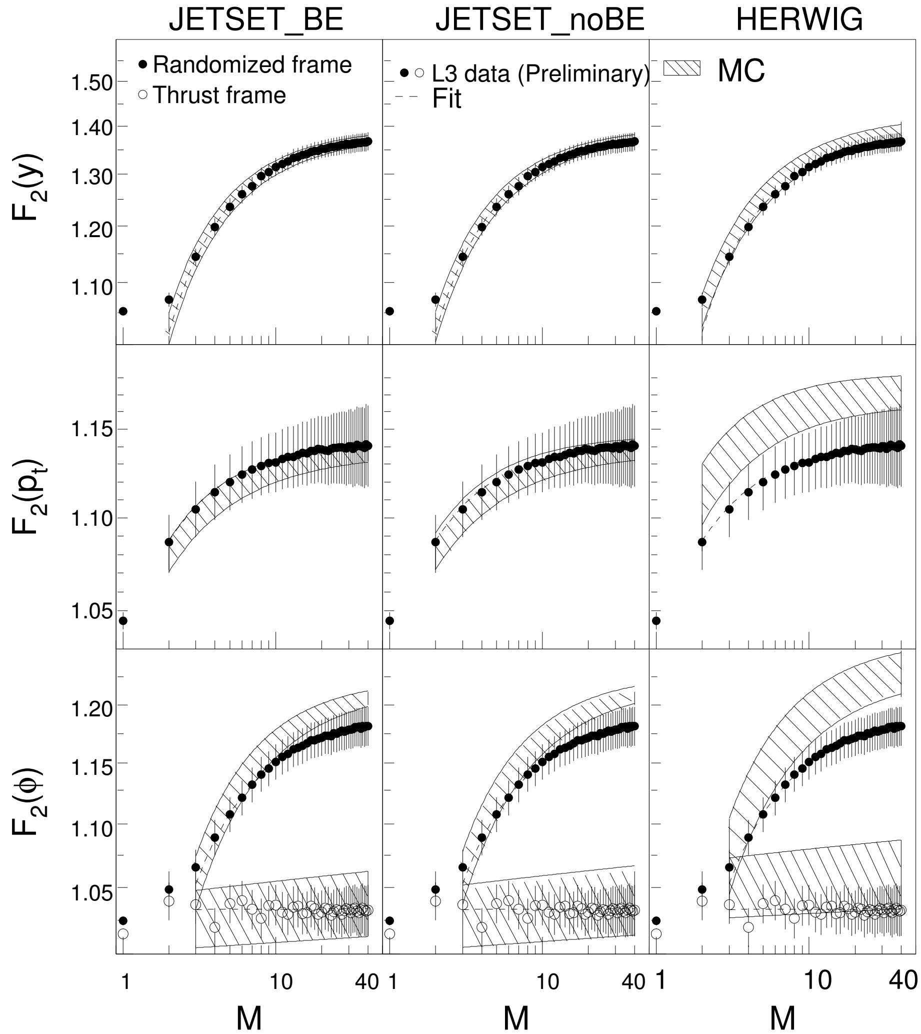

Figure 9.9: The one-dimensional second-order factorial moments as a function of the partition number M in the thrust frame and the randomized frame, compared to the Monte Carlo results of JETSET 7.4 with and without Bose-Einstein correlations and HERWIG.

9.5.2 Fit results

The one-dimensional factorial moments are fitted using Eq. (7.8) with the full covariance matrix, after omitting the first $1-3$ points to eliminate the influence of momentum conservation [119]. The fitted values of γ as well as the χ^2 values are given in Tab. 9.4. The Hurst exponents are
calculated from the values of γ by Eq. (7.15). The resulting values are displayed in Tab. 9.5, where they are compared to the values obtained for JETSET and HERWIG. In both the randomized and $q\bar{q}$ frames, the three γ values agree with each other within one standard deviation and the Hurst exponents are all consistent with unity. This confirms that the underlying dynamical fluctuations are isotropic and that the multiparticle production process is a self-similar fractal.

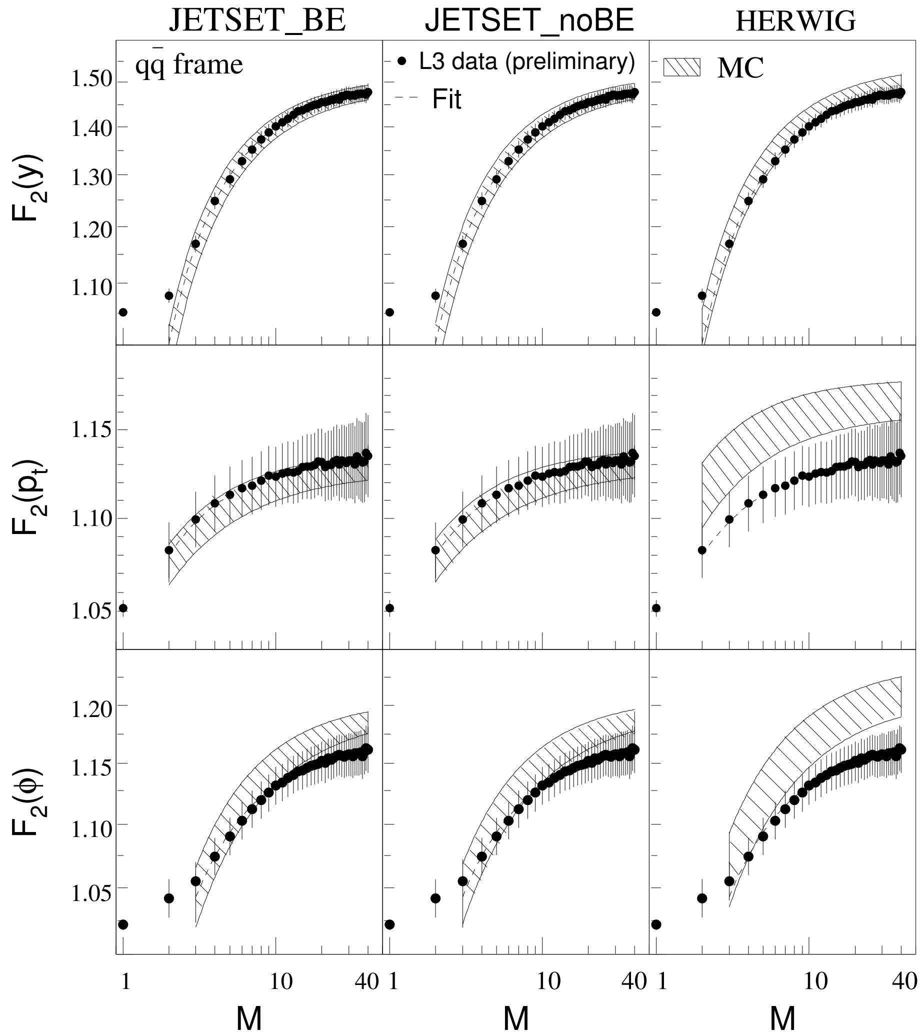

Figure 9.10: The one-dimensional second-order factorial moments as a function of the number of partitions M in the q$\bar{\text{q}}$ frame, compared to the Monte Carlo results of JETSET 7.4 with and without Bose-Einstein correlations and HERWIG.

frame	Variable	γ	χ^2/dof
Randomized	y	$0.992 \pm 0.014 \pm 0.028$	36/36
	p_{T}	$0.986 \pm 0.022 \pm 0.032$	29/37
	φ	$0.993 \pm 0.024 \pm 0.033$	25/35
q$\bar{\text{q}}$	y	$0.966 \pm 0.019 \pm 0.018$	35/36
	p_{T}	$0.972 \pm 0.042 \pm 0.030$	31/37
	φ	$0.967 \pm 0.034 \pm 0.024$	27/35

Table 9.4: The fitted γ values of one-dimensional factorial moments using $F_2(M_i) = A_i - B_i M_i^{-\gamma_i}$.

9.6 Comparison to other experiments

In L3, one-dimensional second-order factorial moments have been studied [118,120]. The aim of the study presented in this thesis is, however, to investigate the isotropy of the scaling property

$H_{yp_{\mathrm{T}}}$	$0.997 \pm 0.018 \pm 0.030$	Data - Randomized frame
	$1.003 \pm 0.031 \pm 0.024$	Data - $\mathrm{q\bar{q}}$ frame
	$0.978 \pm 0.016 \pm 0.042$	JETSET
	$1.079 \pm 0.026 \pm 0.058$	HERWIG
$H_{y\varphi}$	$1.001 \pm 0.019 \pm 0.031$	Data - Randomized frame
	$1.001 \pm 0.027 \pm 0.021$	Data - $\mathrm{q\bar{q}}$ frame
	$0.991 \pm 0.014 \pm 0.033$	JETSET
	$1.015 \pm 0.025 \pm 0.033$	HERWIG
$H_{p_{\mathrm{T}}\varphi}$	$1.003 \pm 0.023 \pm 0.033$	Data - Randomized frame
	$0.996 \pm 0.038 \pm 0.027$	Data - $\mathrm{q\bar{q}}$ frame
	$1.014 \pm 0.017 \pm 0.055$	JETSET
	$0.940 \pm 0.022 \pm 0.047$	HERWIG

Table 9.5: The extracted Hurst exponents.

of NFM in three dimensions and the fractal behavior of the dynamical fluctuations in hadronic Z decay.

DELPHI [91] used the sphericity coordinate system to do 1-D, 2-D and 3-D NFM analyses. The rapidity region used is also $[-5, 5]$. The second eigenvector of the momentum tensor, which is similar to the major axis in the thrust system, was used as the origin for the azimuthal angle φ. The 3-D $\ln F_2$ vs. $\ln M$ plot is well fitted by a straight line, provided the first point is neglected [114]. The three 1-D F_2 saturate and the smaller values of $F_2(\varphi)$ relative to $F_2(y)$ and $F_2(p_{\mathrm{T}})$ can clearly be seen from Fig. 8 of [91]. As discussed in Sect. 7.6, this is a consequence of the dependence of the origin for the azimuthal angle φ, the second eigenvector of the momentum tensor, on the QCD dynamics. The DELPHI results are qualitatively consistent with ours. However, the Hurst exponents have not been extracted for DELPHI and, therefore, no quantitative comparison can be made.

Recently, OPAL [92] published results on 1-D, 2-D and 3-D analyses using an alternative definition of the NFM. A more restricted phase space region was used. Despite these differences in the method of analysis, the log-log plots of the three-dimensional NFM approximately follow straight lines, consistent with the isotropy of dynamical fluctuations.

Full Hurst analyses have, however, been performed on hadron-hadron data [112, 113]. The three-dimensional results show isotropy in the transverse plane ($H_{p_{\mathrm{T}}\varphi} \approx 1$) but anisotropy in longitudinal-transverse directions ($H_{yp_{\mathrm{T}}} \approx H_{y\varphi} \neq 1$), corresponding to self-affine fractal. In contrast, three-dimensional isotropy ($H_{yp_{\mathrm{T}}} \approx H_{y\varphi} \approx H_{p_{\mathrm{T}}\varphi} \approx 1$) is observed in this experiment, which corresponds to self-similar fractal.

Chapter 10

Conclusions and Outlook of Part II

For the first time, the exact type of scaling property of the three-dimensional factorial moments of the hadronic system produced in Z decay is studied. The moments exhibit power-law scaling when phase space is partitioned isotropically in both the thrust frame with a randomized φ origin and after correcting the thrust axis to the $q\bar{q}$ direction. This isotropy is quantitatively confirmed by studies of the three one-dimensional second-order factorial moments. This indicates that the dynamical fluctuations are self-similar (isotropic). This is in sharp contrast to the self-affine (anisotropic) fluctuations observed in hadron-hadron collisions.

As discussed in the introduction, the multihadron production process in e^+e^- collisions at LEP energy can be roughly considered as a perturbative stage of QCD branching (parton shower) followed by a subsequent non-perturbative stage of hadronization. On the other hand, the situation in hadron-hadron collisions can only be treated in a non-perturbative way, particularly below collider energies. Therefore, the difference of dynamical fluctuations in e^+e^- collisions and hadron-hadron collisions may display the difference of dynamical fluctuations between the perturbative process and the non-perturbative process. This conjecture can be tested by studying the scaling property of 2-jet sub-samples in e^+e^- collisions. The strictly defined 2-jet sub-sample should be dominated by the hadronization process, and consequently be anisotropic. As the definition of the 2-jet sample is made looser, more parton branchings are included into the jets, and the fluctuations should become more isotropic, reaching full isotropy when all events are classified as 2-jet events.

Summary

In this thesis, two types of investigation are presented on the e^+e^- data taken with the L3 detector at LEP. One is the search for the Standard Model Higgs boson, the other a study of the scaling property of QCD dynamical fluctuations in hadronic Z decay.

The Standard Model of particle physics is a gauge invariant theory in which electroweak symmetry is spontaneously broken. In a specific way, the Higgs mechanism, and consequently, the Higgs boson is introduced into the Standard Model to give rise to the masses of particles. To probe the existence of the Standard Model Higgs boson is crucial to the final experimental verification of the Standard Model, even though its other predictions agree with the experimental observations precisely. Since the Standard Model does not predict the mass of the Higgs boson, direct searches for the Higgs boson have been performed in a variety of experiments from low energies to the currently accessible energies. The upgraded Large Electron Positron collider (LEP2) at CERN has provided an opportunity to search for the Higgs boson at center-of-mass energies up to 210 GeV.

The L3 experiment, like the other three experiments at LEP, has carried out searches for the Standard Model Higgs boson in a large data sample collected at ever increasing center-of-mass energies and luminosities, thus greatly extending the Higgs mass range investigated. The first part of this thesis is devoted to searches for the Standard Model Higgs boson in the data collected by L3 at center-of-mass energies between 200 and 210 GeV in the year 2000, with a luminosity amounting to 217.3 pb^{-1}.

At LEP2 energy, the Standard Model Higgs boson is produced mainly via the Higgs-strahlung process: $e^+e^- \rightarrow HZ$, with a cross section below 1 pb, depending on the center-of-mass energy and the hypothetical Higgs mass. The Higgs boson is unstable and decays with a branching ratio of around 80% into $b\bar{b}$ and about 7% into $\tau^+\tau^-$. Combining with the decay modes of the Z boson, the main final states of the Higgs-strahlung process are: $q\bar{q}q\bar{q}$ (roughly 60%), $q\bar{q}\nu\bar{\nu}$ (18%), $q\bar{q}\ell^+\ell^-(\ell = e, \mu)$ (5%), $q\bar{q}\tau^+\tau^-$ and $\tau^+\tau^-q\bar{q}$ (8%). The searches described in this thesis are performed in the last two kinds of final states, the so-called leptonic channels, characterised by two high energetic leptons in the final state.

The advantage of searching for the Higgs boson in the leptonic channels is that the experimental signatures are very clear and that they are expected to provide the Higgs boson mass with the best measurement resolution, even though the branching ratios for these channels are small. The important background processes that can contaminate the event selection because of similar topologies are $e^+e^- \rightarrow Z^*/\gamma^* \rightarrow q\bar{q}$, $e^+e^- \rightarrow W^+W^-$, $e^+e^- \rightarrow ZZ$ and $e^+e^- \rightarrow Ze^+e^-$.

Optimised cut-based event selection methods are evaluated, corresponding to the different signal processes, respectively. After event selection, a binned-likelihood final discriminating variable is constructed from the most important variables that characterize a Higgs event (*e.g.* the reconstructed Higgs mass, the B-tagging information) to distinguish signal from background. The observed candidates are, however, consistent with the expected background. No significant candidate event is observed with a high value of the final discriminating variable.

In order to grant a better overall sensitivity, the data sets originating from different energies and channels are combined by constructing a log-likelihood ratio. The experimental results are used to test two hypotheses: the *background-only* ("b") hypothesis, which assumes no Higgs boson to be present in the mass range, and the *signal + background* ("s+b") hypothesis, where the Higgs boson is assumed to be produced according to the Standard Model. The confidence levels for the two hypotheses are evaluated as a function of m_{H} on the basis of the log-likelihood ratio. Finally, the 95% confidence level lower limit for the Standard Model Higgs boson mass can be set.

Combining the results of the four leptonic channels presented in this thesis, there is no evidence for the existence of a Standard Model Higgs boson, and a lower mass limit for the Standard Model Higgs boson of 88.2 GeV is set at the 95% confidence level, with an expected lower limit of 86.3 GeV.

The combined results of all search channels performed in L3, demonstrate the agreement between observation and expected background within one standard deviation. The observed lower limit on m_{H} is 112.0 GeV at the 95% confidence level, with an expected lower limit of 112.4 GeV.

The second part of this thesis is devoted to the study of the scaling property of dynamical fluctuations and the fractal behavior expected from QCD for the multiparticle production process. For this study, we use the high statistics sample of hadronic Z decay data accumulated by the L3 experiment in 1994. Dynamical fluctuations are indeed observed, in the form of power-law scaling of the final-state multiplicity fluctuations with increasing resolution in phase space. This power-law scaling is a behavior typical for fractals. However, it is observed in all types of reactions ranging from $\mathrm{e}^+\mathrm{e}^-$ annihilation to nucleus-nucleus collisions, up to the highest attainable energies. So, a better discriminator is needed to distinguish between different sources.

The tools used for the investigation of dynamical fluctuations are the normalised factorial moments (NFM) F_q, which are able to filter out the statistical noise. If fractal-type dynamical fluctuations exist, the NFM rise with increasing number of cells (M) in phase space according to a power law: $F_q(M) \propto M^{\phi_q} \quad (M \to \infty)$. The exponent ϕ_q is called the q-th order intermittency index. It can be used to derive the various fractal dimensions and the fractal spectrum.

The hadronic Z decay process is a three-dimensional process. A strict power-law scaling of dynamical fluctuations may, therefore, only be observed in three-dimensional phase space, but will be lost in fewer-dimensional projections. If the power-law scaling holds when the underlying space is partitioned equally in all directions, the dynamical fluctuation is isotropic and the corresponding fractal is called *self-similar*. If, on the other hand, the power-law scaling holds when and only when the partitioning is different in different directions, the dynamical fluctuation is anisotropic and the corresponding fractal is called *self-affine*. The so-called Hurst exponent, which can be derived from the one-dimensional 2nd-order NFM, is used to label these two distinct fractal types: for self-similar fractals, $H = 1$; for self-affine fractals, $H \neq 1$.

Firstly, three-dimensional NFM are calculated using the variables: rapidity (y), transverse momentum (p_{T}), and azimuthal angle (φ) with respect to the event thrust axis, by dividing phase space equally in different directions. For the calculation of three-dimensional NFM's, the Białas and Gazdzicki method is implemented to obtain an exactly flat inclusive distribution, which is an explicit condition for the NFM method. A strict power-law scaling is observed for NFM from 2nd to 5th order. The intermittency indices are obtained. The result is that the multiproduction process in hadronic Z decay is self-similar, the involved dynamical fluctuation is isotropic.

The one-dimensional 2nd-order NFM are then computed to extract the Hurst exponents. The results that all Hs are equal to 1 within error, quantitatively confirms the observation in three-dimensional phase space that the dynamical fluctuation is isotropic and the multiproduction process is a self-similar fractal.

Similar analyses have been performed in hadron-hadron collisions at lower energies. The three-dimensional results show a cylindrical symmetry, *i.e.*, isotropy in the transverse plane ($H_{p_\mathrm{T}\varphi} \approx 1$) but anisotropy in longitudinal-transverse directions ($H_{yp_\mathrm{T}} \approx H_{y\varphi} \neq 1$), in contrast to the spherical symmetry, *i.e.*, three-dimensional isotropy ($H_{yp_\mathrm{T}} \approx H_{y\varphi} \approx H_{p_\mathrm{T}\varphi} \approx 1$), presented in this thesis. So, contrary to the self-similar behavior observed here for hadron production in e^+e^- annihilation, hadron-hadron collisions at lower energies lead to self-affine behavior. This discriminates between the fractal dynamics of perturbative QCD (which is considered the dominant process in the hadronic Z decay in e^+e^- collisions) and that of non-perturbative QCD (which is dominant in the hadron-hadron collisions studied so far).

Samenvatting

In dit proefschrift worden twee manieren van onderzoek beschreven op e^+e^- gegevens opgenomen met de L3 detector bij LEP. Een is de zoektocht naar het Higgsboson passend in het standaardmodel, de ander een studie van QCD-dynamische fluctuaties in het hadronische Z-verval.

Het standaardmodel van de elementaire deeltjes is een ijkinvariante theorie, waarin de electrozwakke symmetrie spontaan wordt gebroken. Meer specifiek, het Higgsmechanisme en bijgevolg het Higgsboson is geintroduceerd in het standaardmodel om de massa van deeltjes te verklaren. Het aantonen van het bestaan van een Higgsboson passend in het standaardmodel is essentieel voor de uiteindelijke experimentele verificatie van dit model, hoewel de andere voorspellingen hiervan precies overeenstemmen met de experimentele waarnemingen. Aangezien het standaardmodel de massa van het Higgsboson niet voorspelt, zijn er directe naspeuringen gedaan om het Higgsboson te vinden in een aantal experimenten bij energieën van laag tot de nu toegankelijke waarden. De opgevoerde grote electron-positronbotser bij het Cern (LEP2) maakt het mogelijk om naar het Higgsboson te zoeken bij massamiddelpuntsenergieën tot 210 GeV.

Het L3-experiment heeft, samen met de drie andere LEP-experimenten, naar het Higgsdeeltje verwacht in het standaardmodel gezocht en een grote gegevensverzameling bijeen gebracht voor voortdurend stijgende energieën en luminositeiten, daarbij het massagebied uitbreidend waar naar het Higgsdeeltje kan worden gezocht. Het eerste deel van het proefschrift is gewijd aan dit zoeken naar het Higgsboson in de meetresultaten verzameld in het jaar 2000 door L3 bij energieën tussen 200 en 210 GeV met een luminositeit gaande tot 217.3 pb^{-1} .

Bij de LEP2-energie wordt volgens het standaardmodel het Higgsboson voornamelijk geproduceerd via afstraling van het Higgsdeeltje in het proces $e^+e^- \to HZ$, met een werkzame doorsnede afhankelijk van energie en hypothetische Higgsmassa van minder dan 1 pb. Het Higgsboson is instabiel en vervalt met een vertakkingsverhouding van rond 80% naar $b\bar{b}$ en van ongeveer 7% naar $\tau^+\tau^-$. Gecombineerd met de vervalswijzen van het Z-boson worden de voornaamste eindtoestanden van het Higgsafstralingsproces: $q\bar{q}q\bar{q}$ (ruwweg 60%), $q\bar{q}\nu\bar{\nu}$ (18%), $q\bar{q}\ell^+\ell^-(\ell = e, \mu)$ (5%), $q\bar{q}\tau^+\tau^-$ en $\tau^+\tau^-q\bar{q}$ (8%). Het onderzoek gedaan in dit proefschrift heeft betrekking op de laatste twee eindtoestanden, de zogenaamde leptonische kanalen, gekarakteriseerd door twee hoogenergetische leptonen in de eindtoestand.

Het voordeel van het zoeken van het Higgsboson in de leptonische kanalen is, dat de experimentele kenmerken zeer helder zijn en ze een Higgsmassa zouden moeten opleveren met de beste meetprecisie, zelfs als de vertakkingsverhouding van dit kanaal klein is. De belangrijkste achtergrondprocessen, die na selectie voor contaminatie zorgen, omdat ze soortgelijke topologieën maken, zijn: $e^+e^- \to Z^*/\gamma^* \to q\bar{q}$, $e^+e^- \to W^+W^-$, $e^+e^- \to ZZ$ en $e^+e^- \to Ze^+e^-$.

Er zij op snedes gebaseerde geoptimaliseerde selectiemethodes ontwikkeld corresponderend met de respectievelijke signaalprocessen. Na de selectie wordt uiteindelijk een "likelyhood"-variabele geconstrueerd uit de belangrijkste variabelen, die het Higgsgeval karakteriseren (bijvoorbeeld: de gereconstrueerde Higgsmassa, de b-labeling informatie) om het signaal van de achtergrond te onderscheiden. De waargenomen kandidaten zijn niettemin in overeenstemming met de verwachte achtergrond. Er is geen significant kandidaatgeval waargenomen met een hoge waarde van de "likelyhood"-variabele.

Om een betere algehele gevoeligheid te bereiken zijn de gegevens van verschillende energieën en kanalen gecombineerd met behulp van de constructie van een "log-likelyhood" verhouding. De experimentele resultaten worden gebruikt om twee veronderstellingen te onderscheiden: de hypothese van *alleen achtergrond*, die aanneemt, dat er geen Higgsboson aanwezig is in het bekeken massagebied, en de hypothese met *signaal en achtergrond*, waarbij het Higgsboson verondersteld wordt te zijn geproduceerd volgens het standaardmodel. De aannemelijkheidsgraad wordt voor beide veronderstellingen ontwikkeld als functie van de Higgsmassa op basis van de "log-likelyhood"-verhouding. Uiteindelijk kan dan een lagere limiet van de Higgsmassa worden bepaald met een waarschijnlijkheidsniveau van 95%.

Combinatie van de resultaten van de vier leptonische kanalen gepresenteerd in dit proefschrift geeft geen aanwijzing voor het bestaan van een Higgsboson volgens het standaardmodel en een laagste massalimiet voor dit deeltje van 88.2 GeV met een waarschijnlijkheidsniveau van 95% bij een verwachte waarde voor deze limiet van 86.3 GeV. De gecombineerde resultaten van alle zoekkanalen, die in L3 zijn uitgevoerd laten een overeenstemming binnen een standaardafwijking zien tussen de waarneming en de verwachte achtergrond. Daar is de waargenomen lagere limiet voor de Higgsmassa 112.0 GeV (95% waarschijnlijkheid) bij een verwachte limiet van 112.4 GeV.

Het tweede deel van dit proefschrift is gewijd aan de studie van de schalingseigenschappen van dynamische fluctuaties en het fractale gedrag verwacht volgens QCD voor het veeldeeltjes productieproces. Voor deze studie gebruiken we de grote statistiek van meetgegevens bijeengezameld in 1994 in de hadronische Z-vervallen door het L3-experiment. Er worden inderdaad dynamische fluctuaties waargenomen in de vorm van een machtswetschaling van de eindtoestandmultipliciteitsvariaties bij een toenemende resolutie in de faseruimte. Deze machtswetschaling is een gedrag typisch voor fractalen. Dit wordt echter waargenomen in alle types interacties lopend van e^+e^- annihilaties tot kern-kernbotsingen tot aan de hoogst bereikbare energieën. Er is een variabele nodig om de verschillende bronnen te onderscheiden.

Het middel voor het onderzoek van dynamische fluctuaties is genormaliseerde factoriale momenten (NFM), gesymboliseerd door F_q, die in staat zijn de statistische ruis uit te filteren. Als er dynamische fluctuaties aanwezig zijn van het fractale type, nemen de NFM toe met toenemend aantal cellen (M) in de faseruimte volgens de machtswet: $F_q(M) \propto M^{\phi_q}(M \to \infty)$. De exponent ϕ_q heet de q-de orde intermittency index. Deze kan gebruikt worden om de verschillende fractale dimensies en het fractale spectrum af te leiden.

Het hadronisch Z-vervalsproces is een driedimensionaal proces. Een stricte machtswetschaling van dynamische fluctuaties kan daarom slechts worden waargenomen in een driedimensionale faseruimte, maar zal verloren raken in lagerdimensionale projecties. Als de machtswetschaling stand houdt, wanneer de onderliggende ruimte gelijkelijk verdeeld wordt in alle richtingen, is de dynamische fluctuatie isotroop en de erbij behorende fractaal wordt *zelfgelijkend* genoemd. Als anderzijds de machtswetschaling behouden blijft als en alleen als de verdeling in de verschillende richtingen verschillend is, is de dynamische fluctuatie anisotroop en de erbij behorende fractaal heet *zelfaffien*. De zogenaamde Hurstexponent, die afgeleid kan worden van een eendimensionale tweede orde NFM wordt gebruikt om de verschillend fractale types te onderscheiden: voor zelfgelijkende fractalen geldt $H = 1$, is de fractaal zelfaffien, dan is H ongelijk aan 1.

Eerst worden de drie dimensionale NFM's berekend met variabelen, rapiditeit (y), transverse impuls (p_{T}) en "thrust"azimuthhoek (φ), door de faseruimte gelijk te verdelen in de verschillende richtingen. Voor de berekening van driedimensionale NFM's is de methode van Białas en Gazdzicki gebruikt om een exact vlakke inclusieve distributie te krijgen, die een expliciete voorwaarde is voor de NFM-methode. Een stricte machtswetschaling wordt waargenomen voor NFM's van de tweede tot de vijfde orde. De intermittency-indices worden hiermee verkregen. Het resultaat is, dat het multiproductieproces in hadronisch Z-verval zelfgelijkend is, de betrokken dynamische fluctuatie is isotroop.

De eendimensionale tweede orde NFM's worden dan berekend om de Hurst exponenten af te leiden. De resultaten, dat alle H's binnen de fout gelijk zijn aan 1, bevestigt kwantitatief de waarneming in de driedimensionale faseruimte, dat de dynamische fluctuatie isotroop is en dat het multiproductieproces een zelfgelijkend fractaal is.

Soortgelijke analyses zijn uitgevoerd in hadron-hadron botsingen bij lagere energieën. De driedimensionale resultaten laten hier cylindersymmetrie zien, d.w.z. isotropie in het transverse vlak ($H_{p_\mathrm{T}\varphi} \approx 1$), maar anisotropie in de longitudinale-transverse richtingen ($H_{yp_\mathrm{T}} \approx H_{y\varphi} \neq 1$), in tegenstelling tot sferische symmetrie, d.w.z. drie dimensionale isotropie, ($H_{yp_\mathrm{T}} \approx H_{y\varphi} \approx H_{p_\mathrm{T}\varphi} \approx 1$), zoals in dit proefschrift wordt gepresenteerd. Dus in tegenstelling tot het zelfgelijkend gedrag, dat wordt waargenomen voor hadron productie in $\mathrm{e}^+\mathrm{e}^-$ annihilatie, leiden hadron-hadron botsingen bij lagere energieën tot een zelfaffien gedrag. Dit maakt onderscheid tussen het fractale gedrag van verstorings-QCD, dat als het dominante proces wordt beschouwd in hadronisch Z-verval uit $\mathrm{e}^+\mathrm{e}^-$ botsingen, en dat van de niet-verstorings-QCD, die tot nog toe overheerst in hadron-hadron botsingen.

Bibliography

[1] LEP design report volume I, CERN-LEP/TH/83-29(1983);
LEP design report volume II, CERN-LEP 84-01 (1984);
LEP design report volume III, CERN-AC 96-01 (1996).

[2] D. Decamp *et al.* (ALEPH Collab.), Nucl. Instr. Meth. **A294** (1990) 121.

[3] P. Aarnio *et al.* (DELPHI Collab.), Nucl. Instr. Meth. **A303** (1991) 233.

[4] B. Adeva *et al.* (L3 Collab.), Nucl. Instr. Meth. **A289** (1990) 35.

[5] J.A. Bakken *et al.* (L3 Collab.), Nucl. Instr. Meth. **A275** (1989) 81.

[6] O. Adriani *et al.* (L3 Collab.), Nucl. Instr. Meth. **A302** (1991) 53.

[7] B. Adeva *et al.* (L3 Collab.), Nucl. Instr. Meth. **A323** (1992) 109.

[8] K. Deiters *et al.* (L3 Collab.), Nucl. Instr. Meth. **A323** (1992) 162.

[9] M. Chemarin *et al.* (L3 Collab.), Nucl. Instr. Meth. **A349** (1994) 345.

[10] B. Acciari *et al.* (L3 Collab.), Nucl. Instr. Meth. **A351** (1994) 300.

[11] G. Basti *et al.* (L3 Collab.), Nucl. Instr. Meth. **A374** (1996) 293.

[12] I.C. Brock *et al.* (L3 Collab.), Nucl. Instr. Meth. **A381** (1996) 236.

[13] A. Adam *et al.* (L3 Collab.), Nucl. Instr. Meth. **A383** (1996) 342.

[14] K. Ahmet *et al.* (OPAL Collab.), Nucl. Instr. Meth. **A305** (1991) 275.

[15] A. Adam *et al.* (L3 Collab.), Nucl. Instr. Meth. **A344** (1994) 521.

[16] O. Adriani *et al.* (L3 Collab.), Phys. Rep. **236** (1993).

[17] U. Uwer, *The L3 Scintillation Counter System: Description and Status*, L3 Internal Note 2003, 1996.

[18] P. Béné *et al.*, Nucl. Instr. Meth. **A306** (1991) 151;
R. Bizzarri *et al.*, Nucl. Instr. Meth. **A283** (1989) 799; Nucl. Instr. Meth. **A317** (1992) 463;
P. Bagnaia *et al.*, Nucl. Instr. Meth. **A323** (1992) 528; Nucl. Instr. Meth. **A324** (1993) 101; Nucl. Instr. Meth. **A344** (1994) 212;
S.P. Beingessner *et al.*, Nucl. Instr. Meth. **A340** (1994) 322; Nucl. Instr. Meth. **A336** (1993) 78;
L. Tauscher *et al.*, L3 internal note 2016 (1996).

[19] R. Brun *et al.*, preprint CERN DD/EE/84-1 (Revised 1987).

[20] H. Fesefeldt, RWTH Aachen Report PITHA 85/02 (1985).

[21] S.L. Glashow, Nucl. Phys. **22** (1961) 579;
S. Weinberg, Phys. Rev. Lett. **19** (1967) 1264;
A. Salam, In *Proc. 8th Nobel Symposium, Asglaesgaden*, page 367. Almquist and Wiksell, Stockholm, 1968;
M. Veltman, Nucl. Phys. **B7** (1968) 637;
G. 't Hooft, Nucl. Phys. **B35** (1971) 167;
G. 't Hooft and M. Veltman, Nucl. Phys. **B50** (1972) 318.

[22] G. Arnison *et al.* (UA1 Collab.), Phys. Lett. **B122** (1983) 103.

[23] M. Banner *et al.* (UA2 Collab.), Phys. Lett. **B122** (1983) 476.

[24] P.W. Higgs, Phys. Lett. **12** (1964) 132;
F. Englert and R. Brout, Phys. Rev. Lett. **13** (1964) 321;
G.S. Guralnik *et al*, Phys. Rev. Lett. **13** (1964) 585.

[25] PDG group, K. Hagiwara *et al.*, Phys. Rev. D66 (2002) 010001.

[26] C.N. Yang and R.L. Mills, Phys. Rev. **96** (1954) 191.

[27] G. Altarelli, T. Sjöstrand, and F. Zwirner (eds.) *Physics at LEP2*, CERN 96-01 (1996).

[28] P. Janot, *"The HZHA generator" in Physics at LEP2*, Eds. G. Altarelli, T. Sjöstrand and F. Zwirner, CERN 96-01 (1996) Vol.2, 309.

[29] E. Leader and E. Predazzi, *An Introduction to Gauge Theories and Modern Particle Physics*(Cambridge University Press, 1996) Vol.1.

[30] Tevatron Higgs working group, *Report of Tevatron Higgs Working Group*, FERMILAB-Conf-00/279-T, hep-ph/0010338 (October, 2000).

[31] K. Riesselmann, DESY-97-222 (1997) [hep/hp/9711456].

[32] T. Hambye and K. Riesselmann, Phys. Rev. **D55** (1997) 7255.

[33] G. Altarelli and G. Isidori, Phys. Lett. **B337** (1994) 141;
J.A. Casas, J.R. Espinosa and M. Quirós, Phys.Lett.**B343** (1995) 171;**B382** (1996) 374.

[34] M. Spira and P.M. Zerwas, CERN-TH/97-379 (1997).

[35] The LEP Collabs. ALEPH, DELPHI, L3, OPAL, the LEP Electroweak Working Group and the SLD Heavy Flavour and Electroweak Groups, *A Combination of Preliminary Electroweak Measurements and Constraints on the Standard Model,* L3 Note 2723 (2001).

[36] D. Kohler, B.A. Watson and J.A. Becker, Phys. Rev. Lett. **33** (1974) 1628;
N.C. Mukhopadhyay, P.F.A. Goudsmit and A. Barroso, Phys. Rev. **D29** (1984) 565;
S.J. Freedman *et al.*, Phys. Rev. Lett. **52** (1984) 240;
R. Barbieri and T.E.O. Ericson, Phys. Lett. **B57** (1975) 270;
S. Alder, R. Dashen and S. Treiman, Phys. Rev. **D10** (1974) 3728.

[37] S. Egli *et al.* (SINDRUM Collab.), Phys. Lett. **B222** (1989) 533.

[38] G.D. Barr *et al.*, Phys. Lett. **B235** (1990) 356;
N.J. Baker *et al.*, Phys. Rev. Lett. **59** (1987) 2832.

[39] A. Snyder *et al.* (MARK II Collab.), Phys. Lett. **B229** (1989) 169;
M.S. Alam *et al.* (CLEO Collab.), Phys. Rev. **D40** (1989) 712.

[40] J. Lee-Franzini, *Update on Light Higgs' Searches* in *Proceedings of the XXIV International Conference on High Energy Physics* (Münich, 1988) 1432;
H. Albrecht *et al.*(ARGUS Collab.), Z. Phys. **C42**(1989) 349.

[41] L. Groer, HEP-EX/9707034 (1997).

[42] F. Abe *et al.* (CDF Collab.), Phys. Rev. Lett. **79** (1997) 3819.

[43] J. Valls, *MSSM and Higgs Search at Tevatron,* presentation at *the XXIX International Conference on High Energy Physics* (Vancouver, 1998).

[44] D. Buskulic *et al.* (ALEPH Collab.), Phys. Lett. **B384** (1996) 427.

[45] P. Abreu *et al.* (DELPHI Collab.), Nucl. Phys. **B421** (1994) 3.

[46] M. Acciarri *et al.* (L3 Collab.), Phys. Lett. **B385** (1996) 454.

[47] G. Alexander *et al.* (OPAL Collab.), Z. Phys. **C73** (1997) 189.

[48] M. Acciarri *et al.* (L3 Collab.), Phys. Lett. **B508** (2001) 225.

[49] ALEPH,DELPHI,L3,and OPAL Collabs., the LEP Electroweak Working Group, CERN-EP-2000-055.

[50] S. Jadach and Z. Was, Comp. Phys. Comm. **130** (2000) 260.

[51] M. Skrzypek *et al.*, Comp. Phys. Comm. **94** (1996) 216;
M. Skrzypek *et al.*, Phys. Lett. **B372** (1996) 289.

[52] F.A. Berends, R. Kleiss and R. Pittau, Nucl. Phys. **B 424** (1994) 308; Nucl. Phys. **B 426** (1994) 344; Nucl. Phys. (Proc. Suppl.) **B 37** (1994) 163; Phys. Lett. **B 335** (1994) 490;
R. Kleiss and R. Pittau, Comp. Phys. Comm. **83** (1994) 14.

[53] R. Engel, Z.Phys. **C66** (1995) 203;
R. Engel, J. Ranft and S. Roesler, Phys. Rev. **D52** (1995) 1459.

[54] A. Kopp, *Searches for Higgs Bosons using the L3 Detector at LEP*, PhD thesis, Deutsches Elektronen-Synchrotron laboratory (DESY), (2000).

[55] S. Catani *et al.*, Phys. Lett. **B 263** (1991) 491.

[56] S. Bethke *et al.*, Nucl. Phys. **B 370** (1992) 310.

[57] N.J. Kjaer and R. Moller, *Reconstruction of Invariant Masses in Multi-Jet Events,* DELPHI Internal Note 91-17, (1991).

[58] J. Branson, A. Dominguez, I. Fisk and G. Raven, *The UCSD B-Tag for 1996*, L3 internal Note 2108, (1997).

[59] A. Dominguez, *Search for Neutral Higgs Bosons in* e^+e^- *Interactions at Center-of-mass Energies between 130 GeV and 183 GeV*, PhD thesis, University of California, San Diego, (1998).

[60] T. Sjöstrand, Preprint CERN-TH/7112/93 (1993), revised August 1995; Comp. Phys. Comm. **82** (1994) 74; Preprint hep-ph/0001032 (2000).

[61] M. Acciarri *et al.* (L3 Collab.), Phys. Lett. **B411** (1997) 373.

[62] B.A. Kniehl, Phys.Rep. **C240** (1994) 211; E. Gross, B.A. Kniehl and G. Wolf, Z. Phys. **C63** (1994) 417, *erratum ibid* **C66** (1995) 321.

[63] M. Krämer, W. Kilian and P.M. Zerwas, Phys. Lett. **B373** (1996) 135.

[64] A. Djouadi *et al.*, Z. Phys. **C70** (1996) 427.

[65] The LEP Collabs. ALEPH, DELPHI, L3, OPAL, the LEP Working Group for Higgs boson searches, *Searches for Higgs bosons: preliminary combined results using LEP data collected at energies up to 202 GeV*, Preprint CERN-EP/2000-55 (2000).

[66] P. Igo-Kemenes, *Status of Higgs Boson Searches*, talk gived at LEP Seminar, Nov. 3, 2000.

[67] P. Achard *et al.* (L3 Collab.), Phys. Lett. **B 517** (2001) 319.

[68] M. Acciarri *et al.* (L3 Collab.), Phys. Lett. **B 461** (1999) 376.

[69] M. Acciarri *et al.* (L3 Collab.), Phys. Lett. **B 508** (2001) 225.

[70] R. Barate *et al.* (ALEPH Collab.), Phys. Lett. **B 495** (2000) 1.

[71] P. Abreu *et al.* (DELPHI Collab.), Phys. Lett. **B 499** (2001) 23.

[72] G. Abbiendi *et al.* (OPAL Collab.), Phys. Lett. **B 499** (2001) 38.

[73] ALEPH, DELPHI, L3 and OPAL Collabs., and the LEP Higgs Working Group, *Search for the Standard Model Higgs boson at LEP*, ALEPH 2001-066 CONF 2001-046, DELPHI 2001-113 CONF 536, L3 Note 2699, OPAL Physics Note PN479, CERN-EP/2001-055 (July 2001).

[74] The LHC Study Group, *The Large Hadron Collider: Conceptual Design*, CERN/AC/95-05(LHC) (1995).

[75] CMS Collab., *The Compact Muon Solenoid - Technical proposal* , CERN/LHCC/94-38 (1994).

[76] ATLAS Collab., *ATLAS, detector and physics performance, technical design report*, CERN/LHCC/99-14,-15, ATLAS TDR-14,-15 (1999).

[77] M. Spira, Fortsch. Phys. **46** (1998) 203.

[78] W. Lavrijsen, *COmBined muon Reconstruction for Atlas*, Ph.D. Thesis, Univ. of Nijmegen, 2002, The Netherlands.

[79] C. Adolphsen *et al.* (NLC Design Group), *Zeroth-Order Design Report for the Next Linear Collider*, SLAC-474 (1996).

[80] TESLA Collab., *TESLA Technical Design Report*, DESY 2001-11, TESLA Report 2001-23, TESLA-FEL 2001-05 (2001).

[81] E. Accomando *et al.*, (ECFA/DESY LC Physics Working Group), DESY 97-100 (hep-ph/9705442) (1997).

[82] S. Kuhlman *et al.*, (NLC Accelerator Design Group and NLC Physics Working Group), *Physics and Technology of the Next Linear Collider*, FERMILAB-PUB-96/112 (1996).

[83] P. Bożek, M.Płoszajczak and R.Botet, Phys. Reports **252** (1995) 101.

[84] E.A. De Wolf, I.M. Dremin and W. Kittel, Phys. Reports **270** (1996) 1.

[85] See for example Yu. Dokshitzer, V.A. Khoze, A.H. Mueller and S.I. Troyan, *Basics of Perturbative QCD* (Editions Frontières, Giv-sur-Yvette,1991)
G. Altarelli, *The Development of Perturbative QCD* (World Scientific, Singapore, 1994).

[86] B. Mandelbrot, *The Fractal Geometry of Nature* (W.H.Freeman, New York,1983).

[87] B. Mandelbrot, in *Dynamics of Fractal Surfaces,* eds. E. Family and T. Vicsek (World Scientific, Singapore, 1991).

[88] G. Veneziano, in *Proc. 3rd Workshop on Current Problems in High Energy Particle Theory*, Florence 1979, eds. R. Casalbnoni *et al.* (Johns Hopkins Univ. Press, Baltimore, 1979) p.45;
K. Konishi, A. Ukawa and G. Veneziano, Phys. Lett. **B78** (1978) 243;
A. Giovannini, in *Proc. Xth Int. Symp. on Multiparticle Dynamics*, Goa 1979, eds. S.N. Ganguli, P.K. Malhortra and A. Subramanian (Tata Inst.) p.364.

[89] A. Białas and R. Peschanski, Nucl. Phys. **B273** (1986) 703.

[90] A. Białas and R. Peschanski, Nucl. Phys. **B308** (1988) 857.

[91] P. Abreu *et al.* (DELPHI Collab.), Phys. Lett. **B247** (1990) 137; Nucl. Phys. **B386** (1992) 471.

[92] M.Z. Akrawy *et al.* (OPAL Collab.), Phys. Lett. **B262** (1991) 351;
G. Abbiendi *et al.* (OPAL Collab.), Eur. Phys. J. **C11** (1999) 239.

[93] D. Decamp *et al.* (ALEPH Collab.), Z. Phys.. **C53** (1992) 21;
R. Barate *et al.* (ALEPH Collab.), Phys. Rep. **294** (1997) 1.

[94] T. Sjöstrand, *et al.*, *Z Physics at LEP 1*, CERN Report CERN-89-08, Vol.III(1989)

[95] V.N. Gribov and L.N. Lipatov, Sov. J. Nucl. Phys. 15 (1972) 438;
G. Altarelli and G. Parisi, Nucl. Phys. **B126** (1977) 298;
Yu. Dokshitzer, Sov. Phys. JETP 46 (1977) 641.

[96] R.D. Field, R.P. Feynman, Nucl. Phys. **B136** (1978) 1.

[97] B. Andersson *et al.*, Phys. Rep. **97** (1983) 31;
X. Artru, Phys. Rep. **97** (1983) 147.

[98] G.C. Fox, S. Wolfram, Nucl. Phys. **B213** (1983) 65.

[99] T. Sjöstrand, Comp. Phys. Comm. **39** (1986) 347;
T. Sjöstrand and M. Bengtsson, Comp. Phys. Comm. **43** (1987) 367;
T. Sjöstrand, Comp. Phys. Comm. **82** (1994) 74.

[100] G. Marchesini and B. Webber, Nucl. Phys. **B310** (1988) 461;
G. Marchesini *et al.*, Comp. Phys. Comm. **67** (1992) 74.

[101] D. Amati and G. Veneziano, Phys. Lett **B83** (1979) 87;
G. Marchesini, L. Trentadue and G. Veneziano, Nucl. Phys. **B181** (1981) 335.

[102] T.H. Burnett, Phys. Rev. Lett. **50** (1983) 2062.

[103] M. Adamus *et al.* (NA22 Collab.), Phys. Lett. **B382** (1996) 305

[104] W. Ochs, Phys. Lett. **B247** (1990) 101.

[105] A. Białas and J. Seixas, Phys. Lett. **B250** (1990) 161.

[106] W. Ochs, Z. Phys. **C50** (1991) 339.

[107] A. Białas and M. Gazdzicki, Phys. Lett. **B252** (1990) 483.

[108] P. Lipa and B. Buschbeck, Phys. Lett. **B223** (1989) 465.

[109] Y.F. Wu and L.S. Liu, Science in China **A38** (1995) 435.

[110] L. Van Hove, Phys.Lett. **B28** (1969) 429.

[111] Y.F. Wu and L.S. Liu, Phys. Rev. Lett. **70** (1993) 3197.

[112] N.M. Agababyan *et al.* (NA22 Collab.), Phys. Lett. **B382** (1996) 305; Phys. Lett. **B431** (1998) 451.

[113] S. Wang, Z. Wang and C. Wu, Phys. Lett. **B410** (1997) 323.

[114] F. Liu, F.M. Liu and L.S. Liu, Phys. Rev. **D59** (1999) 114020.

[115] E. Fahri, Phys. Rev. Lett. **39** (1977) 1587.

[116] D.P. Barber *et al.* (MARK J.Collab.), Phys. Rev. Lett. **43** (1979) 830.

[117] D.J. Mangeol, *Correlations in the Charged-Particle Multiplicity Distribution*, Ph.D. Thesis, Univ. of Nijmegen, 2002, The Netherlands.

[118] S. Chekanov, *Local Multiplicity Fluctuations and Intermittent Structure inside Jets*,Ph.D. Thesis, Univ. of Nijmegen, 1997, The Netherlands.

[119] Y. Zhang, L.S. Liu and Y.F. Wu, Z. Phys. Lett. **C71** (1996) 499.

[120] M. Acciarri *et al.* (L3 Collab.), Phys. Lett. **B429** (1998) 563.

Acknowledgements

This thesis could not have been written without the help and support of many people. It would be difficult to thank them all individually. However, I would like to mention some of them explicitly.

First of all, I am deeply indebted to my supervisors, Prof. Dr. Sijbrand de Jong and Prof. Dr. Wolfram Kittel who offered me the opportunity to study at the L3 experiment as a Ph.D. student of the Experimental High Energy Physics Institute of the Katholieke Universiteit Nijmegen. With Sijbrand's expert guidance and warm encouragement, I really enjoyed the exciting time of Higgs hunting at LEP in 2000. The full chain of QCD fluctuations analysis under Wolfram's illuminating advice and ardent impelling largely widened my knowledge about different domains of particle physics. Their careful criticism on the contents and structure of this thesis is very much appreciated.

I would like to thank Dr. Jaap Schotanus, my co-supervisor, greatly, for all the helps he handed to me, especially for teaching me about the L3 experiment from beginning, and for patiently reading the crude version of this thesis. I would also like to thank Dr. Wes Metzger, who was practically acting as my co-supervisor, for his stimulating help for the completion of the QCD part in this thesis. His critical remarks greatly improved the quality of this thesis.

I want to express my sincere gratitude to Prof. Lianshou Liu, following him, I entered in the fascinating world of particle physics.

It is my pleasure to thank all members of the L3 collaboration for their combined effort to make the success of the experiment. My special thanks go to the members of the L3 Higgs working group. Without the help from Andreas Kopp, Andrei Kounine and Chris Tully, I could not have started my Higgs search analysis so quickly. I benefited quite a lot from the fruitful discussions with Ross Berbeco, Marta Felcini, Pablo Garcia-Abia, André Holzner, Wolfgang Lohmann, Alexei Raspereza, Daniel Teyssier, Jin Yamamoto, Haijun Yang. I wish to thank Gerjan Bobbink and Piet Duinker for their support when I studied at CERN.

I thank all the past and present members of Experimental High Energy Physics Institute in Nijmegen for providing a very pleasant working atmosphere. In particular, I would like to mention Martin van den Akker, Jorn van Dalen, Silke Duensing, Frank Filthaut, Cristina Galea, Rapheal Hakobyan, Wim Lavrijsen, Axel Naumann, Bert Peterson, Blandine Roux, Michiel Sanders, Charles Timmermans, Bram Wijngaarden, Henric Wilkens, for their friendship. Without the valuable help from Marjo van Wees-Mobertz, Hanneke Vos-van der Lugt and Annelies Oosterhof-Meij, as a foreigner from China, I could not have sat down quietly to concentrate myself on my study. So, I would send my big thanks to our secretaries. I acknowledge the innumerable help (not only for computer problems) from Peter Klok very much.

I am grateful to Gang Chen, who undertook part of the Factorial Moments calculations, for his collaboration.

I would like to dedicate this thesis to Yan Zhuge, my partner and wife, who lost her own favorite profession because of accompanying me, for her unconditional love and warm support in all the endeavors to make the completion of this thesis to be possible, and to Taige Hu, my beloved son, who filled my life with fun and color away from the stress at work.

Finally, I have to pay tribute to my parents, for their industrious bringing up, character influence and enthusiastic encouragement from early on in my life. This thesis is dedicated to them too.

Yuan Hu Nijmegen, August 2002

Curriculum Vitae

The author of this thesis was born on 4th of January 1967 in Huarong (Hunan province, China). After finishing his middel school education, from 1984, he studied as an undergraduate student in the Radio and Electronics Department of the University of Science and Technology of China (USTC) in Hefei. Five years later, he obtained Bachelor degree with the thesis about the study of the internal energy loss at the junction of alloy. Then the author moved to Wuhan, and studied on Nuclear Magnetic Resonance (NMR) as a graduate student in Wuhan Institute of Physics, Chinese Academy of Sciences in 1989. In 1992, he got his Master degree of Science and found a job of working as an assistant researcher in the Institute of Particle Physics of Huazhong Normal University in Wuhan. In 1994, he participated the BEijing Spectrometer (BES) Collaboration at Beijing Electron-Positron Collider (BEPC), and in 1998, he became the membership of NA49 Collaboration, which is an Ultra-relativistic Heavy Ion Physics experiment at CERN.

Within the exchange project, the author visited Experimental High Energy Physics Institute Nijmegen of the Katholieke Universiteit Nijmegen twice, in 1997 and in 1998, respectively. In 1999, he started to study as a Ph.D student (Onderzoeker in Opleiding) at the Katholieke Universiteit Nijmegen. The topics of his study are those presented in this thesis: Search for the Higgs particle and study of fractal properties of the QCD process using the L3 detector at LEP. During his studies, he took part in several graduate schools, namely the joint Belgian-Dutch-German graduate schools at Rolduc (The Netherlands) in 1999 and at Monschau (Germany) in 2000, the NATO Advanced Study Institute at Nijmegen in 1999. He also participated in some international conferences and meetings including the Meeting of the Division of Particles and Fields of the American Physical Society in 2000 at Columbus, Ohio (USA), the L3 Extended Analysis Meeting in 2001 at Balaton (Hungary) and in 2002 at Aachen (Germany), QCD 02 - High-Energy Physics International Conference in Quantum Chromodynamics in 2002 (Montpellier, France), ICHEP 2002 - XXXI International Conference on High Energy Physics (Amsterdam, The Netherlands).